Stresses and Strain in Silicon: 3-Dimensional Analytical Capabilities for the Non-invasive Evaluation of Strain Fields in Si Wafers and Packaged Chips.

DISSERTATION SUBMITTED IN FULFILMENT OF THE
REQUIREMENTS FOR THE AWARD OF
DOCTOR OF PHILOSOPHY (PH.D.)

DUBLIN CITY UNIVERSITY
SCHOOL OF ELECTRONIC ENGINEERING

Jennifer Stopford
B.A. Mod., M. Eng
October 2011

Supervisor: Prof. Patrick J. McNally

Declaration

I hereby certify that this material, which I now submit for assessment on the programme of study leading to the award of PhD. is entirely my own work, that I have exercised reasonable care to ensure that the work is original, and does not to the best of my knowledge breach any law of copyright, and has not been taken from the work of others save and to the extent that such work has been cited and acknowledged within the text of my work.

Signed:

ID No.:

Date:

Acknowledgements

I would like to thank my supervisor Patrick McNally for his advice and support while undertaking this study and to my colleagues in the NPL for their encouragement and good humour over the past 4 years. I would also like to thank Arthur Henry for his collaboration in work relating to 3DSM, and for continued helpful advice relating to 3D modelling.

Many thanks to Prof. Turkka Tuomi, Dr. Appo Lankinen and Dr. Pasi Kostamo for their tutoring and guidance while undertaking Synchrotron X-Ray Topography Studies at beamline F1, HASYLAB, and Dr. Andreas Danilewsky and Jochen Wittge for their guidance and support at the Topotomo beamline, ANKA.

This thesis would not have been possible without the provision of samples. To this end I would like to thank Dr. Dionysios Manessis, Mr. Lars Boettcher, Mr. Stefan Karaszkiewicz, IZM Fraunhofer, Berlin, for the QFN packges used in 3DSM, and the accompanying packaging and processing data.

Thanks to Science Foundation Ireland for funding this study under Project# 05/IN/I656, and EU-FP7 project no. 216382 SIDAM. This work was conducted under the framework of the INSPIRE programme, funded by the Irish Government's Programme for Research in Third Level Institutions, Cycle 4, National Development Plan 2007-2013. This work was also supported by the European Community— Research Infrastructure Action under the FP7 ‘‘Structuring the European Research Area’’ Programme. I am also grateful to Wayne Rasband and the *plugin* authors who have made their work on *ImageJ* freely available to the scientific community.

Abstract

IC manufacturing and chip embedding processes can induce stresses in Si, which have the potential to affect device functionality and reliability and ultimately lead to device failure. One of the challenges for the future of semiconductor manufacturing and chip packaging is the development of non-destructive metrology both at wafer level, and post-packaging. In this context this thesis proposes novel techniques for the *in situ* imaging of strain and internal damage in processed Si wafers and packaged Si chips.

X-Ray Diffraction Imaging (XRDI) is a powerful, non-destructive technique for the imaging of strain in crystalline materials. Traditionally, section transmission topography geometry has been used to image the crystal volume and obtain direct information on the depth of defects present; however these images provide information on only a small volume of the crystal and can be difficult to interpret. In this thesis two novel 3-dimensional characterisation techniques based on XRDI are presented; 3-dimensional x-ray diffraction imaging (3D-XRDI) and 3-dimensional surface modelling (3DSM). The development and application of 3D-XRDI and 3DSM for the *in situ* imaging of strain and internal damage in processed Si wafers and packaged Si chips is demonstrated.

Contents

Declaration ii

Acknowledgements iii

Abstract iv

Table of Acronyms ix

Table of Figures x

Introduction and Overview 1

- 1.1 Chip Packaging Technology 2
  - 1.1.1 Chip Scale Packages (CSP) 3
  - 1.1.2 Embedded Quad Flat Non-Lead (QFN) Packages 6
- 1.2 Scope of work 7
  - 1.2.1 3-Dimensional X-Ray Diffraction Imaging, (3D-XRDI) 7
  - 1.2.2 3-Dimensional Surface Modelling (3DSM) 8
  - 1.2.3 Photoacoustic Microscopy (PAM) 8
- 1.3 Thesis Organisation 9
- References 10

Theory 13

- 2.1 Introduction 13
- 2.2 Synchrotron X-Ray Topography (SXRT) / X-Ray Diffraction Imaging (XRDI) 13
  - 2.2.1 Kinematical Theory of X-Ray Diffraction (XRD) 14
  - 2.2.2 Dynamical Theory of XRD 19
  - 2.2.3 Defect Contrast Mechanisms 20
- 2.3 Photoacoustic Microscopy 26
  - 2.3.1 Photoacoustic Effect in Condensed Matter 27
  - 2.3.2 The Rosencwaig and Gersho (RG) Theory 29
  - 2.3.3 PAM Image Formation & Resolution 34

2.3.2 Light Source Diameter and Resolution 38

2.3.3 Scattering from Inhomogeneties 39

2.3.4 Semiconductors 41

2.4 Micro-Raman Spectroscopy 43

2.4.1 Rayleigh and Raman Scattering 44

2.4.2 Raman Scattering in Solids 45

2.4.4 Polarizability and Raman Selection Rules 49

2.4.5 Raman Peak Characteristics 49

2.5 Summary 51

References 52

Experimental Methodology 56

3.1 Introduction 56

3.2 Synchrotron X-Ray Diffraction (SXRT) / X-Ray Diffraction Imaging (XRDI) 56

3.2.1 Image Geometries 57

3.2.2 Synchrotron Sources 59

3.3 3-Dimensional X-Ray Diffraction Imaging (3D-XRDI) 64

3.3.1 *ImageJ* 67

3.3.2 3D Processing 67

3.3.3 Post-Rendering Image Processing 70

3.3.4 Slicing the 3D model 72

3.4 3-Dimensional Surface Modelling (3DSM) 73

3.4.1 XRDI Image Capture 74

3.4.2 Importing XRDI into *SolidWorks*® 75

3.4.3 Creating B-spline curves 76

3.4.4 Constructing the 3D Surface Model 78

3.5 Photoacoustic Microscopy (PAM) 80

3.5.1 PAM Schematic & Operation 80

3.5.2 System Operation 86

3.6 Micro-Raman Spectroscopy 87

3.6.1 LabRam® HR800 System 87

3.6.2 System Calibration & Error Compensation 90

Summary 91

References: 93

Evaluation of Plasma Arc Induced Damage on Silicon Wafers using 3D-XRDI, Micro-Raman Spectroscopy, and PAM. 96

4.1 Introduction 96

4.2 Experiment 97

4.3 Results & Discussion 101

4.3.1 Damage Regime 1 101

4.3.2 Damage Regime 2 106

4.3.3 Damage Regime 3 110

4.4 Summary 122

References 124

Analysis of Strain in Packaged Chips using 3DSM, XRDI and Micro-Raman Spectroscopy. 126

5.1 Introduction 126

5.1.1 IZM Fraunhofer Package 127

5.1.2 Chip Embedding Process 128

5.1.3 Preconditioning and Qualification Tests: 129

5.2 Experimental 131

5.3 Results 132

5.3.1 Stage 1: Chip Attach 133

5.3.2 Stage 3: Via Electroplating 139

5.3.3 Stage 5: Post Production 144

5.3.4 Stage 6: Preconditioning 153

5.3.5 Stage 7: Phase 2 Reliability Testing 159

5.4 Summary 165

References 168

Study of Warpage in Stacked Chip Scale Package (CSP) using XRDI and Micro-Raman Spectroscopy. 171

6.1 Introduction 171

6.2 Stacked Chip Scale Package (CSP) 172

6.3 Experiment 173

6.4 Results 174

6.5 Summary 185

References 187

Conclusions & Further Research 189

7.1 Conclusions 189

7.2 Further Research 191

Appendix A 194

K-Means Clustering 194

Appendix B 195

Noise in PAM Microphones 195

PAM Pre-Amplifier Circuit Diagrams 196

List of Publications 198

Conference Presentations 198

Posters 199

Table of Acronyms

3D	3-Dimensional
3DSM	3-Dimensional Surface Mapping
3D-XRDI	3-Dimensional X-Ray Diffraction Imaging
BGA	Ball Grid Array
ccd	Charge Coupled Device
CSP	Chip Scale Package
FEM	Finite Element Modelling
GUI	Graphical User Interface
ITRS	International Technology Roadmap for Semiconductors
PA	Photoacoustic
PAM	Photoacoustic Microscopy
PCB	Printed Circuit Board
QFN	Quad Flat Non-Lead
SEM	Scanning Electron Microscope
SiP	System in Package
SoC	System on Chip
ST	Section Transmission
SXRT	Synchrotron X-Ray Topography
XRDI	X-Ray Diffraction Imaging
XRT	X-Ray Topography

Table of Figures

Figure 1.1: Dual trends in semiconductor manufacturing: miniaturisation of digital functionalities “More than Moore” and functional diversification “More Moore” [2]. 1

Figure 1.2: Development of advanced IC packages with respect to functionality and packaging density [39]. 3

Figure 1.3: 4 forms of stacked CSPs [40]. 4

Figure 2.1: Bragg Diffraction. Conditions for Constructive Interference. 15

Figure 2.2(a):Schematic illustrating the zone axis, A, and parallel planes G. 16

Figure 2.2(b): Laue pattern for transmission geometry. Diffracted beams for reflections in a zone fall on a cone centred around the zone axis (A). Projection sphere and cone intersect to form an apex angle φ. 17

Figure 2.2(c): Laue pattern for back reflection geometry. Diffracted beams for reflections in a zone fall on a cone centred around the zone axis (A). Apex angle $\varphi > 45^{o}$ 18

Figure 2.3: Kinematical penetration depth, t_p for a diffracting plane in a crystal. 19

Figure 2.4: Graph of Photon Energy Versus X-Ray Attenuation Length [68]. 19

Figure 2.5 (a): Orientational contrast for a monochromatic, collimated x-ray beam. Diffraction occurs in regions A and C, but is missing in region B [2, 10]. 21

Figure 2.5 (b): Orientational contrast for white beam topography. Adjoining misoriented regions A and B and the resultant boundary leads to image contrast. 21

Figure 2.6(a) and (b): (a) Diagram of Si substrate illustrating nano-indents on surface. (b) Schematic of ST topograph showing series of five 500mN nano-indents on silicon substrate showing regions of high contrast corresponding to orientational contrast. 22

Figure 2.7 (a): Diffraction from a highly misoriented region in a crystal leading to x-rays appearing at different places on the film. 22

Figure 2.7(b): ST topograph of bottom right corner of QFN-A package 09-089 no. 047 showing highly misorientated regions resulting from orientational contrast. 22

Figure 2.8: Schematic rocking curves for perfect crystal and for imperfect crystal. The shaded area represents the integrated intensity, which is equal to the scattering power [71]. 23

Figure 2.9 (a): Formation of 3 types of extinction contrast in a sample with high strain gradient. (1) Direct image contrast (2) Dynamical image contrast (3) Intermediary image contrast. 24

Figure 2.9 (b): 2 2 0 ST topograph of silicon showing three types of extinction contrast; direct, dynamical and intermediate [67]. Diffraction vector, g is also indicated. ...25

Figure 2.10: Electronic processes involved in light absorption and decay. 28

Figure 2.11: Major processes which contribute to the photoacoustic effect. 28

Figure 2.12: Simple cylindrical photoacoustic cell. 29

Figure 2.13: Experimental results for Reflectance (R), Absorption (A) and Transmission (T) of Radiation in 600 μm thick Silicon Wafers [36] 36

Figure 2.14: Schematic of Si sample showing defect position with respect to the thermal diffusion length (207 μm), sample thickness (675 μm) and optical absorption length (100 μm) for an excitation laser wavelength of 810 nm. 36

Figure 2.15: Thermal diffusion length (microns) for modulation frequencies in the range 100 – 2000 Hz. 37

Figure 2.16: Graph showing the relationship between the wavelength of the excitation source (laser) and the optical absorption length of the sample (Si). 38

Figure 2.17: Coating-air gap-substrate sample system [33]. Subscripts 1, 2 and 3 refer to the coating, air and substrate, respectively. L is the layer thickness, ρ is the density, c is the specific heat capacity, k is the thermal conductivity. 40

Figure 2.18: Schematic of Optical Absorption, Intraband Relaxation and Nonradiative Recombination via Traps in a Semiconductor. 42

Figure 2.19: 2-dimensional crystal lattice with atomic bonds modelled as springs [70]. 45

Figure 2.20: Vibrational wave travelling through crystal lattice with wavelength indicated. Amplitude of the wave is given by the displacements of the atoms from their equilibrium positions. λ is the wavelength of the wave [69]. 45

Figure 2.21: Diagram of Raman and Rayleigh Scattering. Raman scattering differs from Rayleigh by ΔE, the energy of the first vibrational level of the ground state. The energy of the virtual state is defined by the energy of the incoming laser and the phonon properties. 46

Figure 3.1(a): Large-Area Transmission Topography. Sample was typically tilted at 18^o to optimise the imaging of the 2 2 0 and 1 1 1 reflections. L is the sample to film distance. 58

Figure 3.1(b): Transmission Section Topography. Sample was typically tilted at 18^o to optimise the imaging of the 2 2 0 and 1 1 1 reflections. L is the sample to film distance..58

Figure 3.1(c): Large Area Back Reflection Topography. L is the sample to film distance. 59

Figure 3.1(d): Back Reflection Section Topography. L is the sample to film distance..59

Figure 3.2: Topography Beamline at Synchrotron Radiation Facility [4]. 60

Figure 3.3: Schematic diagram showing the geometrical resolution set by the projected source height normal to the incident plane. 60

Figure 3.4: Main Parameters of the Synchrotron at DESY [8]......................................61

Figure 3.5: LABR Topography setup at DESY. Synchrotron X-Ray beam passes through the back of the film holder, and diffracts off the sample which is fixed to the sample holder. A Laue pattern of topographs is formed on the X-Ray Film....62

Figure 3.6: Main Parameters of the Synchrotron at ANKA [9].....................................62

Figure 3.7(a): Image of the XRDI setup at ANKA showing the LAT geometry...........63

Figure 3.7(b): Schematic of stage and sample holder at ANKA showing x, z and φ axes. 64

Figure 3.8: 3D-XRDI Image Acquisition and Processing Steps...................................66

Figure 3.9: Series of Section Topographs (ST) which are rendered together to form 3D XRDI. 69

Figure 3.10 (a): 3D-XRDI ‘raw’ image showing Si sample damaged by arcing. Image was rendered using *volume reconstruction* plugin...70

Figure 3.10 (b): 3D-XRDI image (Figure 3.10 (a)) after thresholding and transparency adjustments..70

Figure 3.11(a): 3D-XRDI image of arcing damaged sample with K-means clustering applied. 71

Figure 3.11(b): 3D-XRDI image of arcing damaged sample with Spectrum LUT applied after K-means clustering. 71

Figure 3.11(c): 3D-XRDI image of arcing damaged sample with HiLo LUT applied after K-means clustering. 72

Figure 3.12(a): The arcing damaged sample from the side view after a region has been removed using the rectangular selection tool...73

Figure 3.12(b): The arcing damaged sample from the side view after a region has been removed using the rectangular selection tool and K-means clustering has been applied. 73

Figure 3.13: Process flow of 3DSM technique. 74

Figure 3.14(a): QFN-A package. Red lines show the approximate positions where ST topographs where obtained. 75

Figure 3.14(b): Unpackaged chip from QFN-A package. Red arrows show the [011] and [1-10] crystal directions. 75

Figure 3.15: Construction of 3DSM showing 5 horizontal sketch planes with ST topographs intersected by front and top planes. 76

Figure 3.16: ST Topograph (black line) with b-spline curve fitted to the contour (blue line). Points which form spline and handles which control tangent vectors are indicated by black and red arrows respectively. 77

Figure 3.17: Horizontal topographs and corresponding horizontal B-Spline curves created in *SolidWorks*®. 77

Figure 3.18(a): Boundary surface formation showing splines and mesh detail. 78

Figure 3.18(b): Boundary surface formation showing curvature combs. 78

Figure 3.19: Schematic of Photoacoustic Microscope. 81

Figure 3.20: Photoacoustic Cell. 1 & 4, Gas inlet / outlet, 2, cell top plate, 3, spectrosil window, 5, microphone detector, 6, base plate. 83

Figure 3.21: Microphone Detector Head. 84

Figure 3.22: Schematic of Spectrometer System. Either Argon ion or HeCd laser can be selected, and Mirror 1 and Edge / Notch filter adjusted appropriately. 87

Figure 3.23: Raman Spectrograph Configuration. 88

Figure 3.24: Micro-Raman confocal focussing system. 90

Figure 4.1(a): Scanning Electron Microscope (SEM) image of damage regime 1. Image shows an approximate 1000 µm × 800 µm area of arcing damage on Si substrate. 97

Figure 4.1(b): SEM image of damage regime 2. Image shows 100 µm – 250 µm islands of arcing damage on Si substrate. Note the difference in scale compared to Figure 4.1(a). 97

Figure 4.1(c): SEM image of damage regime 3. Image shows 850 µm × 750 µm area of arcing damage on back side of patterned Si wafer. 98

Figure 4.1(d): SEM image of damage regime 3. Image shows melting and cracks on arcing damaged region. 98

Figure 4.2(a): LABR Laue pattern for Si crystal with L=80 mm, θ=0°, spot size = 2 mm x 2 mm. Numbers show index of reflections. Laue pattern simulated using LauePt [35]. -1 1 7, -1 1 9 and 2 2 12 reflections are circled in blue. 99

Figure 4.2(b): LAT Laue pattern for Si crystal with L=80 mm, θ=12°, spot size = 2 mm x 2 mm. Numbers show index of reflection. Laue pattern simulated using LauePt [35]. 2 2 0 reflection is circled in blue. 99

Figure 4.3: Series of Section Topographs (ST) which are rendered together to form 3D XRDI of damage regime 1. Changes in intensity and discontinuities at surface are a result of strain and related damage. Uniform grey area is bulk, unstrained Si. 100

Figure 4.4: 0 2 6 LABR topograph of damage regime 1. Boxed area corresponds to region analysed by micro-Raman. 101

Figure 4.5(a): 3D-XRDI of damage regime 1. All 3D images are rendered from 220 Transmission Section Topographs. 102

Figure 4.5(b): 3D-XRDI of damage regime 1 with K-means clustering applied.......... 102

Figure 4.6: 3D-XRDI of damage regime 1 which has been 'cut' down the centre and false colouring applied. Scale bar shows look up table (LUT) with red region corresponding to area with highest strain levels and orange / yellow region corresponding to lowest strain levels. 103

Figure 4.7(a): UV Micro-Raman 2D scan of region from damage regime 1 at d_p = 9 nm. Note area in compressive strain is above the dashed line, closest to main 'body' of damage site, and the area of tensile strain is largely below the dashed line, on the periphery of the damage site. Edge of damaged region is bordered in black. 104

Figure 4.7(b): 40x optical microscope image of region in Figures 4.7(a) and 4.8. Note scale is the same for both images. 105

Figure 4.7(c): UV Micro-Raman spectra from damage regime 1 at d_p = 9 nm, corresponding to the 2D matrix scan in Figure 4.7(a). Spectra were collected over an 80 μm × 80 μm area at a spacing of 5 μm and with 3 accumulations. Blue shift of 520 cm^{-1} peak indicates compressive strain. Peak at 575 cm^{-1} is indicative of Boron doping, peak at 330 cm^{-1} is also a Si peak, however the phase is not known. Smaller, sharp peaks can be attributed to cosmic rays. 105

Figure 4.8: Ar^+ laser micro-Raman 2D scan of region from damage regime 1 at d_p = 569 nm. Spectra were taken over a 90 μm × 90 μm area at a spacing of 2.5 μm and with

3 accumulations. Note the bulk of the damage site is in tensile strain, and surrounding region is in compressive strain. Edge of damaged region is bordered in black. 106

Figure 4.9: 0 2 6 LABR topograph of damage regime 2 showing arc induced islands containing networks of dislocation cells. 106

Figure 4.10(a): 3D-XRDI of damage regime 2. All 3D images are rendered from the 2 2 0 ST reflections. Region circled in red corresponds to largest area of damage which penetrates completely through the substrate. 107

Figure 4.10(b): 3D-XRDI of damage regime 2 with K-means clustering applied........107

Figure 4.11(a): UV Micro-Raman spectra from damage regime 2 at $d_p = 9$ nm, corresponding to the 2D matrix scan in Figures 4.11(b) and (c). Spectra were collected over a 70 µm × 70 µm area at a spacing of 2.5 µm and with 3 accumulations. Red Shift of 520 cm^{-1} peak indicates tensile stress. Peak at 469 cm^{-1} is indicative of amorphous Si, peak at 178 cm^{-1} may also be due to amorphous Si. Sharp peaks at ~100 cm^{-1} and 850 cm^{-1} are plasma lines. 108

Figure 4.11(b): UV Micro-Raman 2D scan of region from damage regime 2 at $d_p = 9$ nm. Spectra were taken over a 70 µm × 70 µm area at a spacing of 2.5 µm and with 3 accumulations. Plot shows 520 cm^{-1} peak shift and related strain....................109

Figure 4.11(c): UV Micro-Raman 2D scan of region from damage regime 2 at $d_p = 9$ nm. Plot shows 470 cm^{-1} (amorphous Si) peak which forms a ring around the periphery of the damage site. 109

Figure 4.12(a): Ar^+ Micro-Raman 2D scan of region from damage regime 2 at $d_p = 9$ nm. Spectra were taken over a 50 µm × 60 µm area at a spacing of 2.5 µm and with 3 accumulations. Plot shows 520 cm^{-1} peak shift and related strain....................110

Figure 4.12(b): 50× optical microscope image of region in Figures 4.11-4.12. 110

Figure 4.13: 20x Optical Microscope Image of the periphery of arcing damage on Sample 3...111

Figure 4.14: LAT topograph of the damage site, showing its distinctive shape. Image is recorded on CCD at ANKA. 111

Figure 4.15: Diagram illustrating the dislocation pile-up present at the periphery of the cells of single crystal Si as seen in LATs Figures 4.16(a)-(c). 112

Figure 4.16(a): LABRT of damage regime 3, -1 1 7 reflection at 100x magnification. t_p, = 40 µm. Image recorded on high resolution film at HASYLAB Synchrotron....112

Figure 4.16(b): LABRT of damage regime 3, -1 1 9 reflection at 100x magnification. t_p, = 75 µm. 112

Figure 4.16(c): LABRT of damage regime 3, 2 2 12 reflection at 100x magnification. t_p, = 190 µm. 112

Figure 4.17: 3D-XRDI of damage regime 3. Image is comprised of over 130 ST topographs from 2 2 0 reflection. 113

Figure 4.18 (a): Damage regime 3, which has been sectioned along central plane to enable internal damage to be viewed. 113

Figure 4.18(b): Damage regime 3, with phase and HiLo LUTs applied. Blue regions are regions of highest strain. 114

Figure 4.19 (a): Optical micrograph of region examined using Ar+ laser scan position image showing arcing from damage regime 3. 114

Figure 4.19 (b):Ar^+ Micro-Raman 2D scan of region from damage regime 3 at d_p=556 nm. Spectra were taken over a 60 µm × 60 µm area at a spacing of 2.5 µm. Plot shows 520.07 cm^{-1} peak shift and related strain in MPa. 115

Figure 4.19 (c): Ar^+ Micro-Raman spectra from damage regime 3 at d_p=556 nm, corresponding to the 2D matrix scan in Figures 4.19(b) and (d). Spectra were taken over a 60 µm × 60 µm area at a spacing of 2.5 µm. Plot shows a single peak centred on 518.08 cm^{-1}. 115

Figure 4.19 (d): Ar^+ Micro-Raman 2D scan of region from Figure 4.18(a), damage regime 3. Plot shows FWHM (cm^{-1}) measurements. 116

Figure 4.20 (a): UV Micro-Raman 2D scan of region from damage regime 3 at d_p=9 nm. Spectra were taken over a 60 µm × 60 µm area at a spacing of 2.5 µm. Plot shows 520.07 cm^{-1} peak shift and related strain. 117

Figure 4.20 (b): UV Micro-Raman spectra from damage regime 3 at d_p=9 nm, corresponding to the 2D line scan in Figure 4.19 (b). Spectra were taken over a 60 µm × 60 µm area at a spacing of 2.5 µm. Plot shows a single peak centred on 520.50 cm^{-1}. Peak centred on 520.5 cm^{-1} and a broad shoulder at ~450 cm^{-1}. 117

Figure 4.21(a): PAM Amplitude image of damage regime 3. Bright green area at edge of sample indicates the sample edge. Region circled in black is the arc damage site. Units are in mV, as recorded by the lock-in amplifier. 118

Figure 4.21 (b): PAM Phase Image of of damage regime 3. Lighter orange area at edge of sample indicates the sample edge. Region circled in black is the arc damage site. Units are in degrees, as recorded by the lock-in amplifier. 119

Figure 4.21(c): PAM amplitude image of damage regime 3, with profile at arcing point. Taken at 760 Hz, Time constant = 30 ms, 0.1 mm resolution. 119

Figure 4.21(d): PAM phase image of damage regime 3, with profile at arcing point. Taken at 760 Hz, Time constant = 30 ms, 0.1 mm resolution. 120

Figure 4.22(a): PA amplitude plot of damage regime 3 showing frequency scan at two different points. 121

Figure 4.22(b): PA phase plot of damage regime 3 showing frequency scan at two different points. 121

Figure 4.23(a): XRT image of damage regime 3. Damage site is circled in blue......... 122

Figure 4.23(b): PAM Image of damage regime 3 (green dot) superimposed on XRT signal. Note scale is same in both images. 122

Figure 5.1(a): Schematic of 5 major chip embedding steps for QFN-A package. QFN-A chips underwent preconditioning and reliability testing after assembly. 128

Figure 5.1(b): Process flow for 7 stages of chip embedding, preconditiong and test. .. 128

Figure 5.2: Sample reference numbers and process stages for QFN-A package analysis. 129

Figure 5.3: Table detailing sample numbers and the corresponding process stage / reliability test stages for QFN-A package analysis. 131

Figure 5.4: Positions of Raman matrix (2D) scans on Sample 4. 132

Figure 5.5 (a) & (b), (a) 2 2 0 LAT topograph from stage 1 chip showing central region of sample 4. White dots are artefacts from the CCD. The projection of the diffraction vector g onto the plane of the recording film is also indicated. (b) 3DSM of stage 1 chip showing misorientation of (2 2 0) Si planes of sample 4. Contours are shown to indicate degree of warpage of chip. 134

Figure 5.5 (c): 3DSM showing Δα, the relative misorientation of (2 2 0) Si planes of sample 4 viewed end on, with ST position corresponding to the upper edge of the chip facing the page. 134

Figure 5.6 (a): Heteroepitaxial growth results in strained overlayer. Δθ changes, and the lattice symmetry alters from cubic to tetragonal. 135

Figure 5.6 (b): Metal overlayer deposition causes tension in underlying Si leading to lattice distortion. 135

Figure 5.6 (c): Chip warpage results in lattice distortion through entire volume of chip. 135

Figure 5.7: 2 2 0 ST topograph of sample 4, number 1 in series of 10 ST topographs which combine to form images 5.4 (b)-(d). Yellow lines show maximum deviation in ST topograph, which is equal to ΔS. 136

Figure 5.8 (a): Micro-Raman spectra for top section (Scan 1) of Sample 4 as shown in Figure 5.4. Main peak, indicative of crystalline Si is centred on 521.6 cm^{-1}. 137

Figure 5.8 (b): Micro-Raman 2D scan for top section (Scan 1) of Sample 4 as shown in Figure 5.4. Entire region is in compressive stress, as indicated by scale on left side of image. Highest levels of stress are indicated in blue/black, and present at the edges of the scan. 137

Figure 5.9 (a): Micro-Raman spectra for middle section (Scan 2) of Sample 4 as shown in Figure 5.4. Main peak, indicative of crystalline Si is centred on 520.75 cm^{-1}. 138

Figure 5.9 (b): Micro-Raman 2D scan for middle section (Scan 1) of Sample 4 as shown in Figure 5.4. Lower ~2/3 of scan is in compressive stress, with low levels of tensile stress also present, as indicated by scale on left side of image. 138

Figure 5.10 (a): Micro-Raman spectra for top section (Scan 3) of Sample 4 as shown in Figure 5.4. Main peak, indicative of crystalline Si is centred on 521.75 cm^{-1}. 138

Figure 5.10 (b): Micro-Raman 2D scan for bottom section (Scan 3) of Sample 4 as shown in Figure 5.4. Entire region is in compressive stress, as indicated by scale on left side of image. Highest levels of stress are indicated in blue/black. 138

Figure 5.10: Stereo microscope image of die after stage 3, drilling of micro-vias to the Cu pads. 140

Figure 5.12: 2 2 0 LAT topographs reflection from central section of Atiotech 3a sample. Sample was oriented at 90° when LAT was recorded. 140

Figure 5.13: 2 2 0 LAT topographs from central section of Hitachi 3b sample. Sample was oriented at 90° when LAT was recorded. 140

Figure 5.14(a): 3DSM of misorientation of (2 2 0) Si planes inside Atiotech 3a sample. 3DSM illustrates bumps corresponding to peaks on LAT topograph. 10 ST topographs were taken vertically across sample, beginning at the top edge of the chip. Sample was oriented at 0° when ST were recorded. 141

Figure 5.14 (b): 3DSM of misorientation of (2 2 0) Si planes inside Atiotech 3a sample, showing $\Delta\alpha_{MAX}$. Sample was oriented at 0° when ST were recorded. 141

Figure 5.14(c): 3DSM of misorientation of (2 2 0) Si planes inside Atiotech 3a sample. Sample was oriented at 90° when ST were recorded. 142

Figure 5.14(d): 3DSM of misorientation of (2 2 0) Si planes inside Atiotech 3a sample. Sample was oriented at 90° when ST were recorded. 142

Figure 5.14(e): 3DSM of misorientation of (2 2 0) Si planes inside Atiotech 3a sample, showing $\Delta\alpha_{MAX}$. Sample was oriented at 90° when ST were recorded. 142

Figure 5.14(f): 3DSM of misorientation of (2 2 0) Si planes inside Atiotech 3a sample with LAT overlaid. For both images topographs were recorded with the sample rotated at 90°. Scale is same at that for Figure 5.11 142

Figure 5.15(a): 3DSM of misorientation of (2 2 0) Si planes inside Hitachi 3b sample. 3DSM illustrates bumps corresponding to peaks on LAT topograph. 10 ST topographs were taken horizontally across sample, beginning at the top edge of the chip. 143

Figure 5.15(b): 3DSM of misorientation of (2 2 0) Si planes inside Hitachi 3b sample, showing $\Delta\alpha_{MAX.}$ Sample was oriented at 0° when ST were recorded. 143

Figure 5.15(c): 3DSM of misorientation of (2 2 0) Si planes inside Hitachi 3b sample. 3DSM illustrates bumps corresponding to peaks on LAT topograph. 10 ST topographs were taken vertically across sample, beginning at the bottom edge of the chip. 143

Figure 5.15(d): 3DSM of misorientation of (2 2 0) Si planes inside Hitachi 3b sample, showing $\Delta\alpha_{MAX.}$ Sample was oriented at 90° when ST were recorded. 143

Figure 5.16(a): LAT topographs of sample 09-096, no 158. 2 2 0 reflection was recorded using a CCD camera. Region circled in red corresponds to region shown in Figure 5.16 (b). 145

Figure 5.16(b): 0 2 10 LABR topograph of elliptical region circled in Figure 5.16 (a). Image was recorded on film and the contrast inverted for ease of comparison.... 145

Figure 5.16 (c): Diagram illustrates how the x-rays diffract from the chip and diverge forming an elliptical shaped strain pattern. 146

Figure 5.16(d): LAT topographs of sample 09-096, no 158, as shown in Figure 5.16 (a), with image normalised to compensate for geometric distortion parallel to $\vec{g}$ 147

Figure 5.17 (a): Stereo-microscope image taken after drilling the vias to the copper pads with the UV laser. View shows drilled via focusing on the underliyng chip Copper pad. Scale bar is 100 μm, via diameter is 51 μm. 148

Figure 5.17 (b): Stereo-microscope image taken after drilling the vias to the copper pads with the UV laser. View shows drilled via focusing on the upper Cu layer of the package. Note distortion of via edges and surrpunding region, indicating the presence of stress and strain. Scale bar is 100 µm, via diameter is 69 µm. 148

Figure 5.18: Angular displacement (warpage) data for package 09-096 No. 158. Horizontal and Vertical ST topograph positions (P1 – P5) correspond to red lines in Figure 3.14. 149

Figure 5.19: Angular displacement (warpage) data for package 09-095 No. 136. Horizontal and Vertical ST topograph positions (P1 – P5) correspond to red lines in Figure 3.14. 149

Figures 5.20 (a), (b), (c): 3DSM maps of misorientation of (2 2 0) Si planes inside a completely sealed package 09-096 no. 158. ST topographs were taken with the package orientated at 0^{o}, i.e. in the horizontal position. Red circles correspond to the elliptical region in Figures 5.16 (a) & (b). 150

Figures 5.21 (a), (b): 3DSM maps of misorientation of (2 2 0) Si planes inside a completely sealed package 09-096 no. 158. ST topographs were taken with the package orientated at 90^{o}, i.e. in the vertical position. Red circles correspond to the elliptical region in Figures 5.16 (a) & (b). 151

Figure 5.22(a): LAT topographs of sample 09-096 no. 136. 2 2 0 reflection was recorded using a ccd camera. Region circled in red corresponds to region of high lattice distortion........ 152

Figure 5.22(a): LAT topographs of sample 09-096, no 136, as shown in Figure 5.22 (a), with image normalised to compensate for geometric distortion parallel to $\vec{g}$ 152

Figure 5.22(c) & (d): 3DSM maps of misorientation of (2 2 0) Si planes inside a completely sealed package 09-096 no. 136. ST topographs were taken with the package orientated at 0^{o}, (Figure 5.20 (b)) and 90^{o} (Figure 5.20 (c)). Red circles correspond to the elliptical region in Figure 5.20 (a). Relative positions of ST topographs which form basis of 3DSM are also shown........ 153

Figures 5.23(a): Formation of enlarged LAT topograph due to x-rays diffracting off convex lattice planes in the QFN-A package. Note diagram is to scale with the exception of lattice distortion, which has been exaggerated for ease of viewing. 154

Figures 5.23(b): Formation of reduced size LAT topograph due to x-rays diffracting off concave lattice planes in the QFN-A package. Note diagram is to scale with the exception of lattice distortion, which has been exaggerated for ease of viewing. 154

Figures 5.24 (a), (b), (c): 2 2 0 LAT topographs from package 09-095 No. 150. Topographs show how high levels of lattice misorientation can lead to distinct diffraction patterns when the package is moved up/down on the sample stage by ~1 μm. 155

Figure 5.25: Angular displacement (warpage) data for package 09-095 No. 150. Horizontal and Vertical ST topograph positions (P1 – P5) correspond to red lines in Figure 3.14. 155

Figure 5.26(a): 3DSM of misorientation of (2 2 0) Si planes of package 09-095 No. 150 viewed side on. 5 ST topographs were taken with the package orientated at 0°. . 156

Figure 5.26(b): High resolution 3DSM of misorientation of (2 2 0) Si planes of package 09-095 No. 150 viewed side on. 10 ST topographs were taken with the package orientated at 0°. 156

Figure 5.27(a): 2 2 0 LAT topograph of package 09-096 No. 008. Image is recorded with chip at 0°. 157

Figure 5.27(b): 2 2 0 LAT topograph of package 09-096 No. 008. Image is recorded with chip rotated to 90°. 157

Figure 5.28(a) and (b): 3DSM of package 09-096 No. 008, showing misorientation of (2 2 0) Si planes. 5 ST topographs were taken with the package orientated at 0°. Relative positions of ST topographs which form basis of 3DSM are also shown. 157

Figure 5.29 (a) & (b): High resolution 3DSM of package 09-096 N0. 008, showing misorientation of (2 2 0) Si planes. 10 ST topographs were taken with the package oriented at 0°. Relative positions of ST topographs wich form 3DSM are also shown. Figure 5.28 (c): 2 2 0 LAT topograph of package 09-096 N0. 008. Note correlation between LAT topograph and 3DSM as oriented in (a)......................158

Figure 5.30: Angular displacement (warpage) data for package 09-096 No. 008. Horizontal and Vertical ST topograph positions (P1 – P5) correspond to red lines in Figure 3.14. 159

Figure 5.31 (a) & (b): 2 2 0 LAT topographs of package 09-088 No. 241. Yellow circled area indicates strained region most likely originating from the lamination process. 160

Figure 5.32 (a) & (b): 3DSM of package 09-088 No. 241, showing misorientation of (2 2 0) Si planes. Yellow arrows point to strained region most likely originating from the lamination process. 161

Figure 5.33: Angular displacement (warpage) data for package 09-088 No. 241. Horizontal ST topograph positions (P1 – P5) correspond to red lines in Figure 3.14. 161

Figure 5.34(a): ST topographs of middle (P3) horizontal ST topograph from sample 09-088 No. 241, 2 2 0 reflection, showing distinctive 'rippled' profile Figure 5.33 (b): Top edge (P1) horizontal ST topograph from sample 09-096 No. 158 with similar 'rippled' features on profile. 161

Figures 5.35 (a) & (b): 2 2 0 LAT topographs of package 09-089 No. 047 showing fragmented images resulting from high levels of strain. Scale is the same for both topographs. 162

Figure 5.36: Diagram illustrating how topographic images of the areas of a sample with lattice planes misoriented with respect to "good" silicon appear at different spatial positions on film. 163

Figure 5.37: BRST from regions on package 09-089 No. 047, indicated by red lines. All ST shown are -1 1 9 reflections. Slit size was set to 4 mm long and ~15 μm high. 163

Figure 5.38(a): 2 2 0 LAT topograph reflection of package 09-089 No. 241. Image consists of 3 topographs patched together. 164

Figure 5.38 (b): 2 2 0 ST topograph of package 09-089 No. 241 at approximately the centre of the chip. 164

Figure 5.39 (a): 2 2 0 LAT topographs of package 09-088 No. 218. Image consists of 7 topographs patched together. 165

Figure 5.39 (b): Optical Image of package 09-088 No. 218 showing external damage, resulting from pressure cooker testing. 165

Figure 6.1 (a) & (b): 620 Large Area Back Reflection X-Ray Topographs (penetration depth into Si = 27 μm) showing the different strain fields and damage under two Au wedge bonds, (a) and (b), in a delidded 2764 8Kx8 EPROM [22]. 172

Figure 6.2: Diagram of triple stacked CSP (not to scale) showing main components including silicon die, adhesive, gold wire and solder balls with 0.8 mm pitch. ... 173

Figure 6.3(a): Optical cross section of stacked CSP enclosed in resin, showing 3-layer structure. Total package height ~675 µm (excluding BGA), die thickness ~100 µm. Die stack thickness ~350 µm. Bottom die is attached to substrate by adhesive. .. 173

Figure 6.3(b): Position of Raman line scan for each layer (die) on triple stacked CSP. Layers (die) are labelled with respect to Figure 6.3(a). 174

Figure 6.4: Image of package illustrating approximate positions of x-y stage steps (blue boxes) and corresponding topograph positions (yellow numbers). 175

Figure 6.5(a): 2 0 10 LABR topographs, t_p ~107 µm from stacked CSP. The first image (uppermost position) corresponds to position 1 in Figure 6.4, and the image second from the top to position 2, etc. 176

Figure 6.5(b): 2 0 6 / 4 0 12 LABR topographs, t_p ~18/206 µm from stacked CSP. The first image (uppermost position) corresponds to position 1 in Figure 6.4, and the image second from the top to position 2, etc. 177

Figure 6.6: Maximum lattice tilt, Δα, for diffracting planes for reflections (h k l), and x-ray penetration depths (t_p) shown.. 178

Figure 6.7: (1 –1 0) Cross-sectional surface of Si wafer / chip................................... 180

Figure 6.8: Summary of micro-Raman peak shift data for each die in layer stack. Data shows each layer to be in compressive stress... 181

Figure 6.9(a): Ar+ Laser Micro-Raman Spectrum for line scan with 5 micron steps. Bottom layer of sample. 182

Figure 6.9(b): Ar+ Laser Micro-Raman Plot of Peak Position versus Scan Position for Line Scan in Figure 7.3.6 above, Bottom layer of sample.................................. 183

Figure 6.10(a): Ar+ Laser Micro-Raman Spectrum for line scan with 5 micron steps. Middle layer of sample.. 183

Figure 6.10(b): Ar+ Laser Micro-Raman Plot of Peak Position versus Scan Position for Line Scan in Figure 7.3.8 above, Middle layer of sample. 184

Figure 6.11(a): Ar+ Laser Micro-Raman Spectrum for line scan with 5 micron steps. Top layer of sample.. 185

Figure 6.11(b): Ar+ Laser Micro-Raman Plot of Peak Position versus Scan Position for Line Scan in Figure 7.3.10 above, Top layer of sample. 185

Figure B1: Graph plotting the PA signal obtained from the empty 196

PAM cell with laser modulation frequency of 720 Hz. 196

Figure B2 : Pre-amplifier circuit diagram... 196

Figure B3 : Summer circuit diagram... 197

Introduction and Overview

The production of the integrated circuit (IC) is a dynamic technology, and as the demand for smaller, faster chips with improved performance continues, so too do the demands placed on every stage of the development process, from design through to manufacturing, yield and reliability.

In 1965 Gordon Moore first published his hypothesis that the number of components that could be incorporated per integrated circuit would increase exponentially over time [1]. Since then, downscaling of critical dimensions by a factor of 0.7 every two years has been the principal driver behind the growth of the semiconductor market. As transistor size comes closer to that of atoms, we are now nearing the basic physical limits of Complementary Metal Oxide Semiconductor (CMOS) scaling. Each new semiconductor technology node provides further miniaturisation and higher performance, however the cost associated with the continuous downscaling of critical dimensions below the 18 nm node is becoming prohibitive. Future advances in modern nanoelectronics will depend on "More than Moore" (MtM) approaches (Figure 1), through the functional diversification of semiconductor based devices [2, 3].

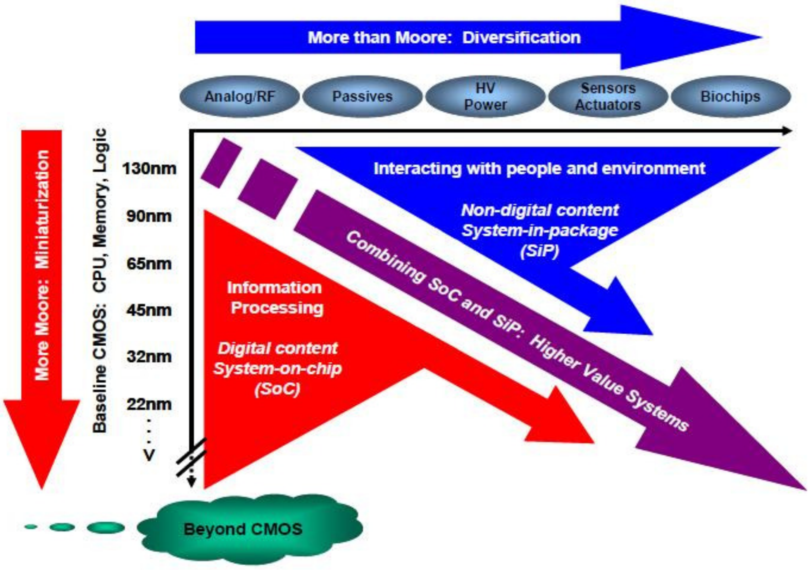

Figure 1.1: Dual trends in semiconductor manufacturing: miniaturisation of digital functionalities "More than Moore" and functional diversification "More Moore" [2].

Advanced IC packing and integration techniques such as system in package (SiP), systems on chip (SoC), and 3D integration provide a path for the higher density, performance, form factor and cost requirements of the next generation of electronic devices. However, these packages are still plagued by reliability problems, and none of today's available metrologies can non-destructively measure or image stress / strain, warpage or defects inside these advanced packages.

Progress goals in integrated circuit manufacturing are defined by the International Technology Roadmap for Semiconductors (ITRS) and particular issues related to packaged chips can be found in the chapter entitled "*Assembly & Packaging*" [3]. Specifically it states that *"… packaging is now the limiting factor in cost and performance for many types of devices*". This study examines different types of chips and packages: bare and patterned silicon wafers / die, embedded quad flat non-lead (QFN) packages and triple stacked chip scale packages (CSP), at various stages of the manufacturing and test processes. The metrology gap is addressed in this study through the development and demonstration of two novel tools for the non-destructive, *in situ* mapping of defects, stresses, strains and deformations in bare die and packaged chips:

- 3-Dimensional X-Ray Diffraction Imaging (3D-XRDI). A high spatial resolution synchrotron based (~3 µm x-y) diffraction imaging technique which enables visualization of the three-dimensional structure of crystal defects in semiconductor wafers and die.
- 3-Dimensional Surface Mapping (3DSM). A novel, non-destructive x-ray diffraction imaging technique to produce x-y mapping of the deformations and strain fields in packaged SiP.

A further, innovative technique, photoacoustic microscopy (PAM), is used in this study to image defects in silicon wafers / dies.

1.1 Chip Packaging Technology

IC packaging offers many benefits in terms of form factor, performance and cost improvements. Emerging MtM technologies have enabled packages to be eliminated completely, or reduced in size to the point where they take up little more than the size of the IC. Multiple die stacking, stacking of packages, or a combination of both can significantly reduce the package footprint, while functional integration enables the diverse range of technology applications, such as memory / logic and mixed signal devices for wireless communication and consumer electronics to be met. However implementation of these highly innovative technologies is only possible if new fabrication techniques can be developed to mass-produce the packages at an affordable price. Furthermore, form factor, size and function are market specific, and a "one size fits all" approach is not practical in terms of choosing the best type of package for a particular application. Figure 2 shows the main types of package relevant to this study and their evolution in terms of functionality and packaging density.

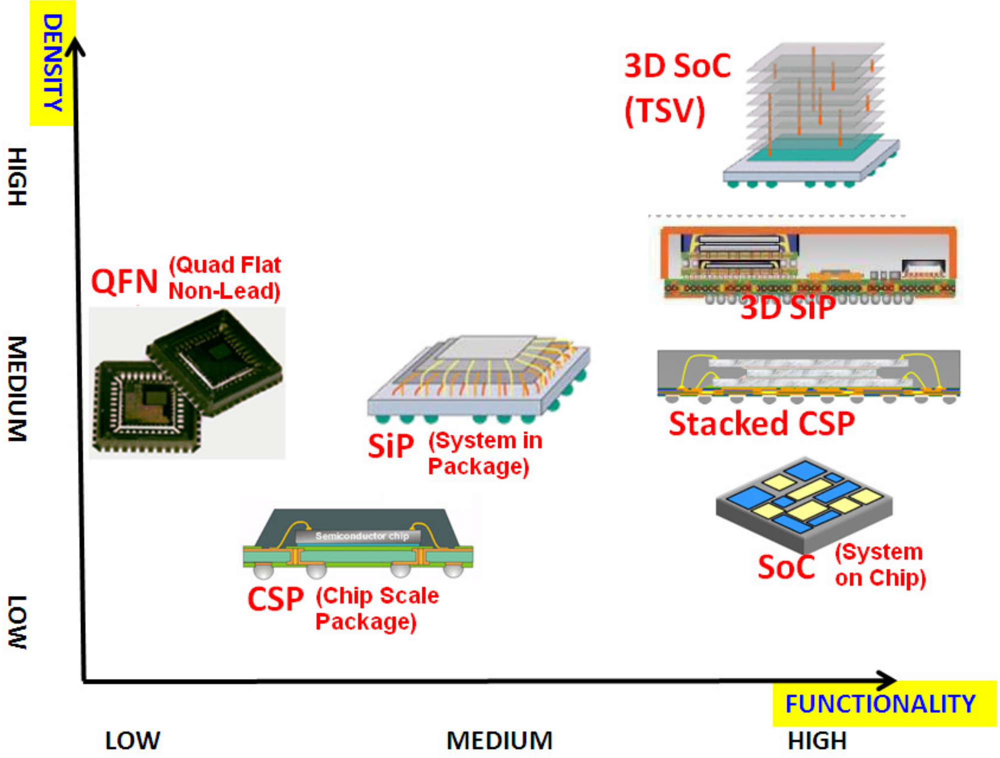

Figure 1.2: Development of advanced IC packages with respect to functionality and packaging density [39].

SEMI is the global industry association serving the manufacturing supply chain for the micro- and nano-electronics industries. SEMI standards are the internationally accepted standards for the semiconductor industry. There is no current SEMI definition for the deformation or warpage of a die inside a packaged chip. Package warpage is defined by the semi SEMI G54-93 standard, [22] as "*the loss of planarity of a plastic molded surface, excluding protrusions and intrusions*", and wafer warpage is defined as "*the distance between the maximum and minimum distance of the median surface of a wafer from a reference plane encountered during a scan pattern*", (SEMI M23), [22]. In this study the definition of package warpage is extended to include warpage of die inside a package, or in the case of SiP or SoC a package embedded inside a larger, external package.

1.1.1 Chip Scale Packages (CSP)

A chip scale package (CSP) is defined according to IPC/JEDEC J-STD-012 [4] as a direct surface mountable package of minimal size, no more than 1.2× the area of the original die size. This broad definition includes flip chip and wafer level packaging (WLP), with single die, multiple die side-by-side or multi-layer CSPs that incorporate several stacked active devices. CSP were originally developed for mobile phone applications, where space for surface mount components was at a premium, and the reduced footprint, thickness, and lesser weight were advantageous [5]. The small size of CSPs has primarily been achieved through ball grid array (BGA) design, which enables the number of interconnects to be increased while saving pcb mounting space. Furthermore the lack of leads and hence avoidance of coplanarity issues linked to bent leads has facilitated streamlining of pcb assembly and reflow processes. The popularity of CSPs has been largely linked to their flexibility in terms of manufacturing. Die size changes can be incorporated into standard size CSPs by modifying the interposer or substrate design. Furthermore, CSPs can combine the strengths of various packaging technologies, such as the size and performance advantages of bare die assembly and the reliability of encapsulated devices.

With the numerous advantages of CSPs it is no surprise that they have been developed as a platform for the first stacked packages. Stacked CSPs generally take one of 4 forms: stacked bare die, stacked packaged chips, stacked multichip modules, and stacked wafers (Figure 3) [6]. The stacked CSP (S-CSP) characterised for this study consists of multiple stacked die, interconnected via peripheral wire bonding.

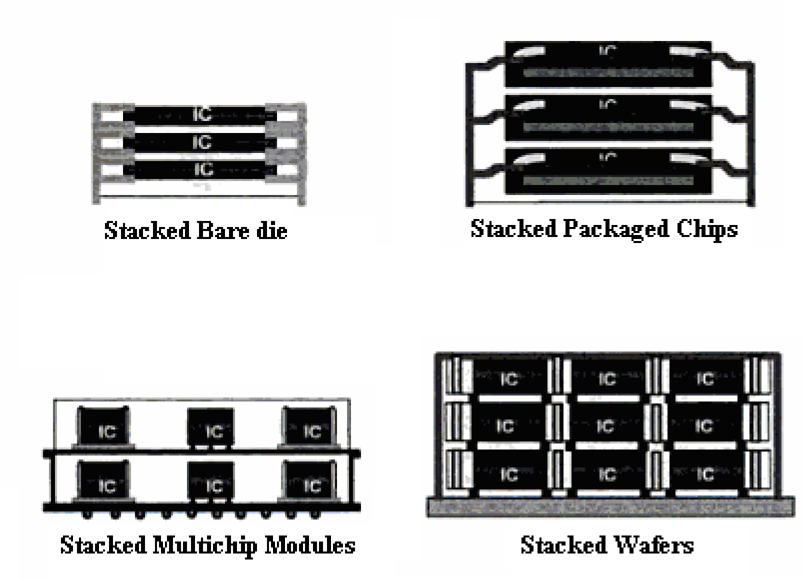

Figure 1.3: 4 forms of stacked CSPs [40].

Despite the advantages of CSPs, the technology is still young, and there remain many issues relating to package and device reliability. These include, but are not limited to interfacial delamination, solder ball / micro-joint reliability, and warpage due to CTE mismatch between the different materials used in IC manufacture and packaging [7 – 12] . To date considerable research has been undertaken in an effort to analyse the root causes and modes of failure of CSP / S-CSP. However, research relating to warpage in CSP / S-CSP has been largely confined to the use of finite element modelling (FEM), scanning electron microscopy (SEM), and the shadow Moiré method. FEM is a well established method for studying the effect of thermally induced stresses and deformations, such as warpage on semiconductors wafers, die and packages [13, 15], however as a modelling technique it is limited by the user input parameters, such as number of data points, stress profiles and boundary conditions which are supplied by the user. For many of the new materials used in CSPs and similar packages material data and correlation reliability data is still lacking, and FEM results are therefore only an estimation of the level of warpage present [13, 15]. SEM analysis is generally only performed on ICs and packages after potentially serious abnormalities, such as warpage, have been detected. Although SEM is considered a non-destructive technique, during analysis of ICs, a thin carbon layer may be deposited on the sample when the beam scans the surface; also, if the accelerating voltage is too high the electron beam can damage the device. In the case of warpage studies of CSPs, wafers, and die may need to be cross-sectioned in order to examine the internal structure or region of interest. The cross-sectioning, grinding and polishing processes have the potential to affect stresses and strains in the chip / package and thus any further analysis will measure these contributions in addition to the process / packaging induced stresses. SEM has been used as an analysis tool in the study of warpage on wafers and packages, however it is generally used in conjunction with either FEM or the shadow Moiré method [8, 16, 19]. The shadow Moiré method is an optical method that measures the topography of the surface of a solid object by means of a white light incident on a grating, the image of which is projected onto the surface of the sample. It is the most widely used means of measuring warpage of wafers and IC packages [12-14, 16, 17], and as such is described in the JEDEC standard No. 22B112 [20]. In spite of its widespread use, the shadow Moiré method is prone to errors, and can give erroneous results if not properly used [21]. Furthermore, it can only measure warpage directly on the surface at which it is looking, and thus is limited to characterising warpage on the external surfaces of single layer structures.

The advantages of CSPs, and specifically QFN CSPs has led to them becoming the fastest growing packaging segment. They offer a viable solution to IC package size reduction and performance improvement in many applications, however their advancement is limited by the need for a lead-frame interposer/substrate. The use of a lead frame makes QFNs bigger than necessary, and adds extra metal which reduces their electrical performance. It can also slow down fault diagnosis and testing. Additionally, high lead count designs are not practical using lead frame packaging, and the added height of the lead frame limits possibilities for vertical miniaturization.

1.1.2 Embedded Quad Flat Non-Lead (QFN) Packages

Embedded QFN packages offer many of the same advantages of lead frame CSPs, allowing for an equivalent footprint, reduced thickness and a lower manufacturing cost. Die embedding technology, based on PCB laminate infrastructure, combines the roles of the traditional disciplines of packaging, substrate manufacturing and assembly. It also offers the additional advantage of the possibility of employing 3D stacking to achieve high package density. Embedding of active chips and passive components using PCB manufacturing technology has been identified as a viable packaging technology for MtM heterogeneous integration, including System in Package (SiP) and System on Chip (SoC) technologies [23, 24, 25].

Systems on Chips integrate a large number of transistors and various mixed-signal active and passive components onto a single chip, leading to a single-chip complete system, referred to as SoC, while SiPs comprise of a number of similar of dissimilar chips stacked in a single package. Both types of package can utilize either traditional 2D or advanced 3D packaging (Figure 2), although SiPs are almost exclusively stacked. SoCs were initially seen as the solution to complete IC functional integration, however high wafer fabrication costs, test costs, mixed-signal processing complexities and intellectual property (IP) issues have imposed fundamental limits on their development [7, 28]. Simpler design and design verification, IC processing with minimal mask steps, minimal time-to-market, minimal IP issues, and the potential to reduce costs have resulted in the strongest initial uptake in the SiP package for mobile communications markets. Moreover, the ITRS has identified SiP technology as possibly the most important technology to address the key limitations of conventional packaging; interconnect density, thermal management, bandwidth and signal integrity [3, 7].

Today's ultra-thin Si chips and passive devices with thicknesses of < 50 μm are in the range of thickness levels of a typical build-up layer in a multilayer printed circuit board (PCB), and thus fit well into the build-up layers of a PCB. Manufacturing technologies such as drilling of laser via interconnects to chip pads, and precise die placement and bonding for accurate microvia alignment are key enablers in 2D and 3D chip embedding technology, and facilitate the construction of ever more complex, larger SiP modules connected on both sides of the active substrate [23, 26, 27]. However, in order for such technologies to be realized in high volume manufacturing environments, and for manufacturing costs to remain low, advanced process development is not sufficient. A detailed understanding of thermo-mechanical, thermal and electrical performance of SiP/SoC integrated systems has to be achieved, and designers will need to take into account how much stress a system can handle. The need to study packaging process steps to fully realize the requirements of future SoC/SiP components and systems is identified in [7]. Specifically, the identification of failure mechanisms, and improved failure analysing techniques and methods are listed as fundamental reliability challenges for SiP development and production.

IC manufacturing and packaging technology has evolved at a rapid pace over the past 10 years, and if advancements in MM and MtM technologies are to remain viable die and package reliability must keep pace with the changes. Analytical techniques capable of characterizing sub-surface damage and thermo-mechanical stress in die and packaged chips are therefore key enablers to these new technologies.

1.2 Scope of work

The primary aim of this study is to develop a non-destructive technique for the measurement and imaging of stress/strain and warpage in semiconductor die, and beneath the lid of SoC/SiP packages. This is achieved through the development and application of three novel, non-invasive analytical techniques – 3-Dimensional X-Ray Diffraction Imaging (3D-XRDI), 3-Dimensional Surface Mapping (3DSM), and Photoacoustic Microscopy (PAM).

Micro-Raman spectroscopy is an established characterisation technique; it is used in this study as a complementary technique to XRDI and PAM by providing quantitative values for strains and enabling crystalline, amorphous, and nano-crystalline phases to be distinguished.

1.2.1 3-Dimensional X-Ray Diffraction Imaging, (3D-XRDI).

Traditionally, for this x-ray diffraction technique, the section topography geometry has been used to image the crystal volume and obtain direct information on the depth of defects present [29], however these images provide information on only a small volume of the crystal and can be difficult to interpret. Stereo images were the first attempt by crystallographers to obtain three-dimensional (3D), information from diffraction images

[30, 31]. The information was limited by the stereo pair of topographs chosen, and did not enable information beyond the location and direction of crystal imperfections to be obtained. More recently 3D topography techniques have been developed which enable 3D modelling of the strain and defect distributions within crystals. This 3D modelling has taken three main forms: generation of 3D modelling/3D data by topo-tomography methods, where the sample is rotated around the diffraction vector while several images are recorded of the same Bragg reflection [32-34], generation of 3D models by using image processing software to combine section topographs taken at intervals along the sample surface, i.e. 3D x-ray diffraction imaging (3D-XRDI) [35, 36], and generation of 3D models by using image processing software and topographs obtained by v-shaped slit configurations [37]. 3D-XRDI is a high spatial resolution synchrotron based (<3 μm X-Y) diffraction imaging technique, it provides an improvement over conventional XRDI in that it makes it easier to distinguish damage sites, identify stress / strain regions both above and below the surface. It gives a 3D analysis of defects in semiconductor wafers, most usefully when in kinematical diffraction mode and delivers full 3D profiles of defects/strain inside semiconductor materials from top to back side.

1.2.2 3-Dimensional Surface Modelling (3DSM)

3-Dimensional Surface Modelling (3DSM) is a completely novel modelling technique which uses the high resolution (~3 μm) strain imaging capabilities of XRDI, combined with the advanced freeform modelling capabilities of *SolidWorks*® to build 3-dimensional profiles of crystalline misorientation across completely packaged chips. A small series of section topographs (ST) are initially taken at 0.5/1 mm intervals across the chip. In certain cases the chip is then rotated 90° and the process repeated. Data from each individual ST is then used to build a 3-dimensional profile of crystalline misorientation across the chip. The use of 3DSM has enabled non-destructive, *in situ* imaging of stresses, strains and deformations in these early packaged chips tested at different stages in the manufacturing and test process.

1.2.3 Photoacoustic Microscopy (PAM)

PAM is a non-invasive, non-contact technique which requires no pre-processing or sample preparation. Photoacoustic microscopy has been used to provide information about the mechanical, thermal, and electronic properties of materials and for imaging surface and subsurface defects in structures where the depth range depends on the thermal diffusion length [38]. In this report PAM is used to locate surface and sub-surface defects in silicon, caused during chip manufacturing.

1.3 Thesis Organisation

The organisation of the thesis is as follows:

Chapter 1, Provides a brief and contextual introduction.

Chapter 2 presents the theory behind the 3 main experimental techniques used in this study: X-Ray Diffraction Imaging (XRDI), Photoacoustic Microscopy and Micro-Raman Spectroscopy.

Chapter 3 provides a detailed explanation of the research methodology used in this study. The methodology describes the established experimental technique of XRDI, and how it has been developed to enable 3-Dimensional X-Ray Diffraction Imaging (3D-XRDI) and 3-Dimensional Surface Mapping (3DSM). The use of image processing algorithms to enhance XRDI is also discussed. The experimental equipment used for PAM is described in detail, and the system operation is explained. The final section describes the micro-Raman spectroscopy system used for materials characterisation in this study, and system calibration and error compensation techniques.

The next three chapters present the main parts of this research. Chapter 4 presents an evaluation of plasma arc induced damage on Si wafers using 3D-XRDI, and complemented by PAM and micro-Raman spectroscopy. Chapter 5 describes the implementation of 3DSM for the analysis of strain and die warpage in QFN packages. Chapter 6 is a study of warpage in a stacked CSP using conventional XRDI.

Finally a summary of the main conclusions and contributions and some suggestions for future work are presented in chapter 7.

References

[1] Moore G.E., *Electronics*, **38** (8) (April 19, 1965); reproduced in *Proc. IEEE*, **86**, 82 (1998).

[2] ITRS More than Moore White Paper 2010. http://www.itrs.net/Links/2010ITRS/IRC-ITRS-MtM-v2%203.pdf

[3] ITRS 2009, Chapter 2, *Assembly and Packaging*. http://www.itrs.net/links/2009ITRS/2009Chapters_2009Tables/2009_Assembly.pdf

[4] J-STD-012, Joint Industry Standard, Implementation of the Flip Chip and Chip Scale Technology, January 1996. http://www.ipc.org/ContentPage.aspx?Pageid=Standards

[5] Fukui, Y. Yano, Y. Juso H., Matsune, Y. Miyata, K. Narai A. Sota Y., Takeda, Y., Fujita K., Kada M., *Proceedings 50th Electronic Components and Technology Conference (ECTC)*, Las Vegas, USA, (2000), pp. 385 – 389.

[6] Charles A. Harper, Electronic Packaging and Interconnection Handbook, McGraw-Hill, 4th Edition, 2005.

[7] ITRS SiP White Paper, *The next Step in Assembly and Packaging: System Level Integration in the package (SiP)*, 2007, http://www.itrs.net/links/2007itrs/LinkedFiles/AP/AP_Paper.pdf

[8] Jihwan Hwang, Jongyeon Kim, Woonseong Kwon, Unbyoung Kang, Taeje Cho, and Sayoon Kang, *Proceedings 60th Electronic Components and Technology Conference (ECTC)*, (2010), pp.1399 – 1403.

[9] Ponlawat Pichitchaichan, Ajchara Simphlipan, Anocha Sriyarunya, *Proceedings 6th Electronics Packaging Technology Conference (EPTC)*, (2004), pp.72 – 75.

[10] E.R. Weltevreden, M. Erinc, S.J. Tesarski, A. Wymyslowski, A. Mavinkurve, A.W.J. Gielen, *12th Int. Conf on Thermal Mechanical and Multiphysics Simulation and Experiments in Microelectronics and Microsystem, (EuroSimE),* 2011.

[11] Cheng-Fu Chen and Daniel C. Peterson, *IEEE Transactions on Components, Packaging and Manufacturing Technology*, Vol. **1**, No. 3, March 2011.

[12] Wang, Y.Y., Hassell, P., *Proceedings of the 1st Electronic Packaging Technology Conference (EPTC)*, (1997), pp.283 – 289.

[13] Wei Tan, I. Charles Ume, Ying Hung, and C. F. Jeff Wu, *IEEE Transactions on Advanced Packaging*, Vol. **33**, No. 2, May 2010.

[14] F. Carson, S.M. Lee, and N. Vijayaragavan, *Electronic Components Technology Conference (ECTC)*, (2007) p. 737.

[15] Y. Suzuki, Y. Kayashima, T. Maeda, Y. Matsuura, T. Sekiguchi, A. Watanabe, *Electronic Components Technology Conference (ECTC) 2007*, Reno, Nv, June 2007, p.8.

[16] M. Dreiza, A. Yoshida, K. Ishibashi, *Electronic Components Technology Conference (ECTC) 2007*, Reno, Nevada, June 2007, p. 1397

[17] Wei Lin, Min Woo Lee, *2008 Electronic Components and Technology Conference*, pp. 1576 – 1581.

[18] Ng CS, Chua KY, Ong MT, Goh YC, Asundi AK, *Proc of SPIE*, vol. **6627**; 2007. p. 0301–11.

[19] Akito Yoshida, Jun Taniguchi, Katsumasa Murata, Morihiro Kada, Yusuke Yamamoto, Yoshinori Takagi, Takeru Notomi, Asako Fujita, *2006 Electronic Components and Technology Conference (ECTC)*, pp. 6.

[20] JEDEC STANDARD, “High Temperature Package Warpage Measurement Methodology”, JESD22B112, MAY 2005. http://www.akrometrix.com/industrydocs/JESD22B112_Warpage_Specification_2005.pdf

[21] Ding Hai and Ume Charles, “Error Analysis of Warpage Measurement on Electronic Structures Using Projection Moire”, *Society for Experimental Mechanics Annual Conference on Experimental and Applied Mechanics*, June 10-12, 2002, Milwaukee, Wisconsin.

[22] Semi international standards, compilation of terms, http://www.semi.org/cms/groups/public/documents/web_content/P007093.pdf

[23] Lars Boettcher, Dionysios Manessis, Andreas Ostmann, Stefan Karaszkiewicz and Herbert Reichl, *3rd International Microsystems, Packaging, Assembly & Circuits Technology Conference, 2008*, IMPACT 2008, pp 383 – 386.

[24] S. Norlyng, “Integrated component technologies: Opportunities, economics and trends”, *IMAPS Nordic*, October 2003.

[25] Ohshima D., Sasaki H., Mori K., Fujimura Y., Kikuchi K., Nakashima Y., Funaya T., Nishiyama T., Murakami T., Yamamichi S., *59th Electronic Components and Technology Conference, 2009,* (ECTC) 2009. pp. 482 – 488.

[26] Chien-Wei Chien, Li-Cheng Shen, Tao-Chih Chang, Chin-Yao Chang, Fang-Jun Leu, Tsung-Fu Yang, Cheng-Ta Ko, Ching-Kuan Lee, Chao-Kai Shu, Yuan-Chang Lee, Ying-Ching Shih, *57th Proceedings Electronic Components and Technology Conference, 2007*, ECTC '07, pp. 305 – 310.

[27] Dionysios Manessis, Lars Boettcher, Andreas Ostmann, Rolf Aschenbrenner, and Herbert Reichl, *2009 Electronic Components and Technology Conference (ECTC).* (2009), pp. 475 – 481.

[28] R.R. Tummala, *IEEE Trans. Advanced Packaging*, vol. **27**, no. 2, May 2004, pp. 241-249.

[29] D. Noonan et al., *J. Mater. Sci.: Mater. Electron.,* **10** (1999) 351–358.

[30] Kyoichi Haruta, *J. Appl. Phys.* **36** (1965) 1789–1790.

[31] A.R. Lang, *J. Appl. Phys*. **30** (1959) 11.

[32] W. Ludwig et al., J. *Appl. Cryst*. 34 (2001) 602–607.

[33] Seiji Kawado et al., *J. Synchrotron Radiat*. 11 (2004) 304–308.

[34] W. Ludwig et al., *Mater. Sci. Eng*., A 524 (2009) 69–76.

[35] V.V. Kvardakov et al., *Nucl. Instrum. Methods Phys. Res*. A 575 (2007) 140–143.

[36] Taihei Mukaide, Kentaro Kajiwara, Takashi Noma, Kazuhiro Takada, *J. Synchrotron Radiat.* **13** (2006) 484–488.

[37] R. Tanuma et al., *Phys. Status* Solidi (a), **204** (8) (2007) 2706–2713.

[38] Haruo Endoh, Katsuhiko Miyamoto, Yoichiro Hiwatashi and Tsutomu Hoshimiya, Jpn. *J. Appl. Phys.* Vol. **41** (2002) pp. 3361–3362.

[39] Rajiv Maheshwary, "3D Stacking: EDA Challenges & Opportunities", SEMATECH SymposiumTokyo, Japan, September 2009.

[40] John H. Lau, Ricky S.W. Lee and S.W. Ricky Lee, "Chip Scale Package: Design, Materials, Process, Reliability, and Applications", McGraw-Hill, Feb 28, 1999.

Theory

2.1 Introduction

In this chapter the main theories behind three non-destructive, high resolution, techniques utilised for the characterization and analysis of defects and strain in semiconductor materials and packaged chips are presented: synchrotron x-ray topography (SXRT), photoacoustic microscopy (PAM) and micro-Raman spectroscopy. SXRT, also known as x-ray diffraction imaging (XRDI) is a well established experimental technique, and in addition to being used in its traditional configuration, forms the basis of two novel techniques developed as part of this study: 3-dimensional x-ray diffraction imaging (3D-XRDI) and 3-dimensional surface mapping (3DSM). The two x-ray scattering theories concerning the formation of x-ray topographs are considered, and the image contrast mechanisms which enable imaging of the distribution of strain or defects in a crystal are outlined. In the case of PAM, a theoretical description of the photoacoustic effect in condensed matter is presented, and extended to consider defects and inhomogenties in semiconductors. Micro-Raman spectroscopy is utilised to obtain quantitative information on the magnitude of strain fields in semiconductor materials. The theory behind Raman spectroscopy is discussed in terms of both classical and quantum mechanical theories, the relationship between peak characteristics and strain measurements is also demonstrated.

2.2 Synchrotron X-Ray Topography (SXRT) / X-Ray Diffraction Imaging (XRDI)

X-Ray topography involves a crystalline sample being illuminated by an x-ray beam and the diffracted beams forming an image on a photographic film or other recording medium. Images of a perfect crystal are homogeneous, however strain induced by local imperfections in a crystal can modify the diffraction of x-rays, and cause defects to appear as contrasting regions or features on the topographic film.

X-ray topography was first developed by Berg in 1931 using x-rays from laboratory sources to study imperfections in large single crystals [1, 2]. The technique was further developed by Ramanchandran [3] and Wooster & Wooster [4], but it was not until 1945 that the first metallurgical specimens were examined by Barrett in his study of single crystals of silicon ferrite [5, 6]. Although not appreciated at the time, this was a great step forward for materials science and a highly significant discovery for the semiconductor industry.

Lang (1959) was the first to describe section and projection x-ray topography [7]. The next major advance in the development of x-ray topography was not until 1974 when Tuomi *et al*. showed that using the Laue technique white beam synchrotron radiation could be used to record excellent resolution topographs in a few seconds [8]. Prior to Tuomi's work, x-ray topography experiments had been undertaken using x-ray tubes as sources, composed of only brehmstrahlung and Kα (and Lα) wavelengths depending on the anode material. The continuous and high intensity spectrum of radiation obtained from a synchrotron beam means that there is no need for time consuming sample alignment, or sample preparation, exposure times for topographs were reduced to a matter of seconds, and multiple topographs could be obtained simultaneously. Synchrotron x-ray topography (SXRT) is now used in a range of geometries for the characterisation of materials, with each geometry providing information on a different part (surface, bulk, cross-section) of the crystal. This makes it far superior to conventional x-ray topography, however because of the requirement for a synchrotron radiation source SXRT cannot be easily commercialised and used as an industrial tool. This remains its greatest disadvantage.

2.2.1 Kinematical Theory of X-Ray Diffraction (XRD)

The kinematical or geometrical theory of x-ray diffraction goes back as far as 1912 when von Laue, Friedrich and Knipping first presented papers with a mathematical description of diffraction [9, 11]. Von Laue derived the amplitude diffracted by a 3-dimensional periodic assembly of atoms by adding the amplitudes of the waves diffracted by each atom, and simply taking into account the optical path differences between them. The basis of the theory was the assumption that, when a ray is incident on a crystal, each photon is scattered only once, and that the interaction of the x-rays with matter is so small that it can be neglected. The theory was expanded by Laue *et al.* in a second paper, published in the same year [12]. In this paper Laue gives the well known geometrical equations for the conditions to be satisfied by an incident wave to be diffracted by a crystal, and shows how to index the reflections. Around the same time, X-ray diffraction was discovered when the first of the well known diffraction equations was presented by W. L. Bragg. Bragg's paper described reflection of x-rays from mica plates, and explained how the cleavage faces of crystals appeared to reflect x-rays at certain angles of incidence. This experiment confirmed for many the electro-magnetic nature of x-rays.

Authier was the first to make a clear distinction between x-ray diffraction theories in terms of diffracted intensity. He identified geometric diffraction as relating to the directions of reflections, kinematical theory as relating to the intensities of reflections, and dynamical theory as multiple diffraction theory [2, 9] although geometric and kinematical theory are now generally considered together. The kinematical theory is a good approximation for small or thin, imperfect crystals; however for large, perfect or nearly perfect crystals it has a number of shortcomings. By failing to take into consideration the interaction of the wave with matter, or reflection of the wave, the law of conservation of energy is not obeyed. Laue's theory implies that for an infinitely large crystal the diffracted intensity would increase to infinity, which cannot be true [13]. Because of this, the kinematical theory is only valid when the strength of the interactions of the x-rays with matter is very weak, and scattered radiation can be ignored. Kinematical theory also fails to determine the intensity of the diffracted beam, or its phase.

2.2.1.1 Bragg's Law

Bragg's Law describes the conditions for constructive interference (Figure 2.1). Constructive interference occurs for certain angles (θ_B) correlating to an hkl plane, where hkl are indices of reflection.

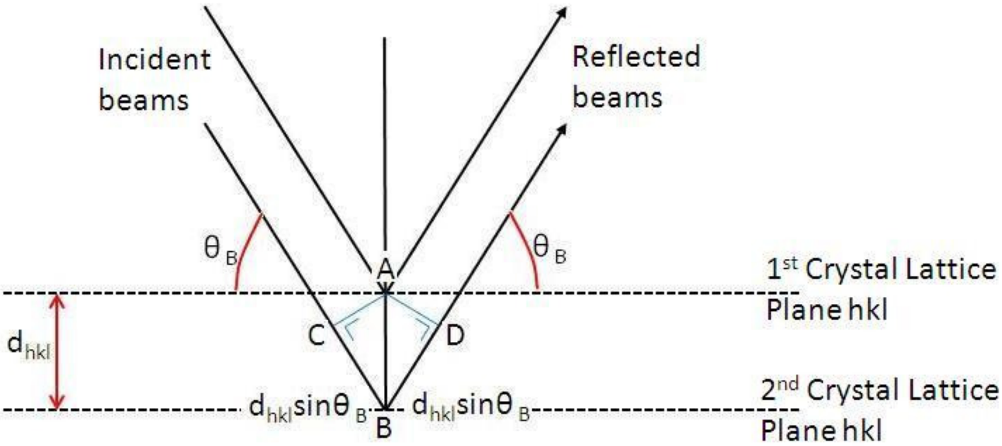

Figure 2.1: Bragg Diffraction. Conditions for Constructive Interference.

The rays of the incident beam are in phase and parallel. A and B are arbitrary scattering points on the first and second planes respectively. AB is normal to the planes. The incident and reflected beams pass through A on the first plane, and the second beam continues to the second plane where it is scattered by B. The second beam must travel the extra distance CB + BD if the two beams are to continue travelling adjacent and parallel. The path difference between waves reflected at A and B is: $CB + BD = 2d_{hkl}\sin\theta_B$. The two waves will be in phase when the path difference = nλ, where n = 1, 2, 3, 4, ….

$$\Rightarrow n\lambda = 2d_{hkl}\sin\theta_B \qquad (2.1)$$

where *d* is the interplanar spacing, θ_B is the Bragg angle, and λ is the wavelength of the incident beam. The white beam provides a continuous spectrum of wavelengths, which match certain Bragg criteria. This enables several topographs to be obtained on the same film, forming a Laue pattern. Each Laue spot is an x-ray topograph, arising from a different set of atomic planes.

2.2.1.2 Laue Conditions

When the synchrotron x-ray beam is incident on a crystal the lattice planes (hkl) act as a 3D grating. For white beam radiation, many reflections will simultaneously satisfy Bragg's law. Waves are reflected from the lattice planes in the crystal and can constructively interfere, creating a diffraction pattern. The array of spots formed is called a Laue pattern. The Laue Conditions describe the cone in reciprocal space about the lattice vectors $\vec{a_1}$, $\vec{a_2}$,$\vec{a_3}$. ν_1, ν_2, ν_3 are integer values of a reflection's reciprocal lattice indices (hkl) (Figure 2.2). k_i is the wavevector for the incoming (incident) beam, and $\vec{k_0}$ is the wavevector for the outgoing (diffracted) beam. The scattering vector, $\overrightarrow{\Delta k}$ measures the difference between the two wavevectors; $\overrightarrow{\Delta k} = \vec{k_0} - \vec{k_i}$. A crystal does not diffract x-rays unless:

$$\vec{a_1}\cdot\overrightarrow{\Delta k} = 2\pi\nu_1 \qquad (2.2)$$

$$\vec{a_2}\cdot\overrightarrow{\Delta k} = 2\pi\nu_2$$

$$\vec{a_3}\cdot\overrightarrow{\Delta k} = 2\pi\nu_3$$

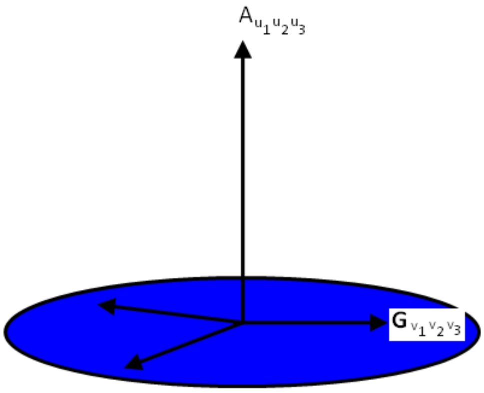

Figure 2.2(a):Schematic illustrating the zone axis, A, and parallel planes G.

$\vec{G}\cdot\vec{A}=0$ (Figure 2.2(a))

where $\vec{G}=v_1\vec{b_1}+v_2\vec{b_2}+v_3\vec{b_3}$, and $\vec{b_1}$, $\vec{b_2}$, $\vec{b_3}$ are reciprocal lattice vectors [72]

$\vec{A}=u_1\vec{a_1}+u_2\vec{a_2}+u_3\vec{a_3}$, and u_1, u_2, u_3, are integer values of the direct crystal lattice.

We know that: $\overrightarrow{\Delta k}=\vec{k_0}-\vec{k_i}$

and $\vec{G}=\overrightarrow{\Delta k}=\vec{k_0}-\vec{k_i}$

$\Rightarrow\vec{k_0}=\vec{G}-\vec{k_i}$

and $\vec{A}\cdot\vec{k_0}=\vec{A}\cdot\vec{G}+\vec{A}\cdot\vec{k_i}=\vec{A}\cdot\vec{k_i}$

$\Rightarrow\vec{k_0}$ should lie on the cone (Figure 2.2(b))

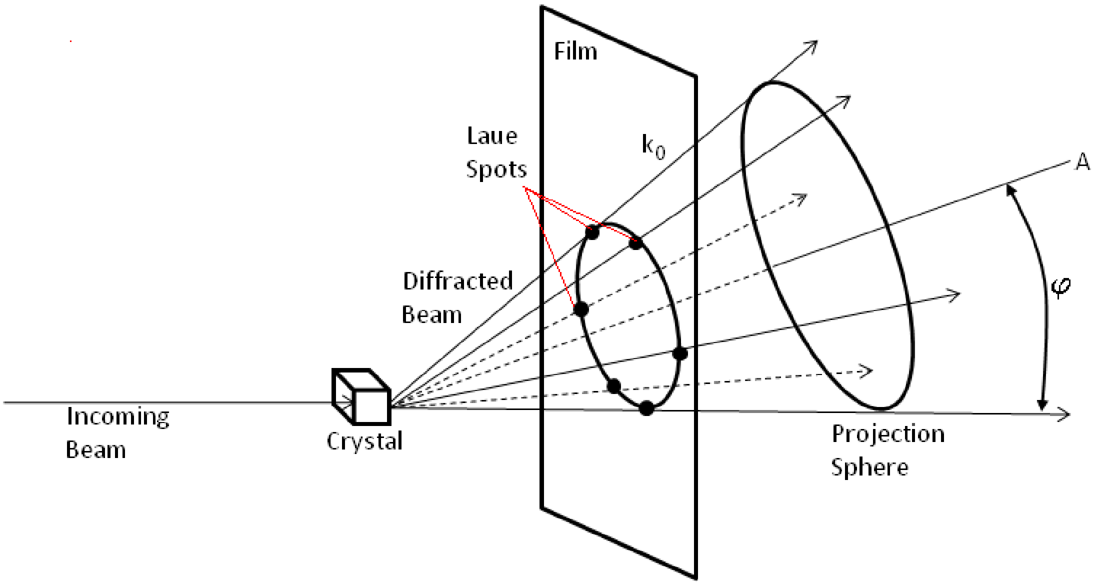

Figure 2.2(b): Laue pattern for transmission geometry. Diffracted beams for reflections in a zone fall on a cone centred around the zone axis (A). Projection sphere and cone intersect to form an apex angle φ.

In the case of the transmission Laue pattern, the angle φ between the zone axis and the incident x-ray, <45° (Figure 2.2(b)). For a back reflection Laue pattern the angle between the zone axis and the zone axis and the incident x-ray, φ, >45° (Figure 2.2(c)). When a sample is exposed to white beam radiation each diffraction vector which fulfils Bragg's law results in a diffraction spot (topograph). The result is a Laue pattern of topographs. These topographs can be imaged on x-ray film, and magnified using a conventional optical microscope.

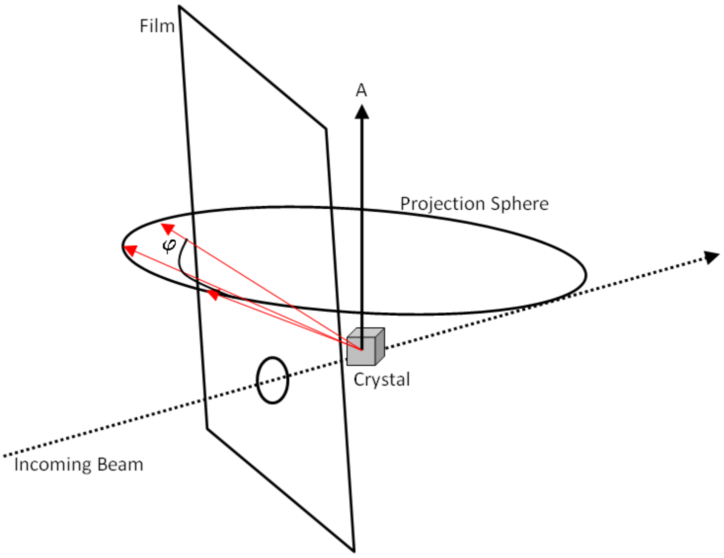

Figure 2.2(c): Laue pattern for back reflection geometry. Diffracted beams for reflections in a zone fall on a cone centred around the zone axis (A). Apex angle φ>45°.

2.2.1.3 Penetration Depths

Based on conventional kinematical theory, for imperfect crystalline materials such as strained silicon the kinematical penetration depth, t_p, of a particular reflection can be obtained from the equation [14]:

$$t_p = \left[\mu_0(\lambda) \left(\frac{1}{\sin \alpha_i} \right) + \left(\frac{1}{\sin \alpha_h} \right) \right] \tag{2.4}$$

where α_i, $\alpha_f >> \alpha_c$, the critical angle for total reflection, $\mu_0(\lambda)$ is the linear absorption coefficient for the material, and α_i and α_f are the incident and reflected angles (Figure 2.3).

For back reflection;

$\alpha_i = 90^0$, $\alpha_f = 90^0 - \tan^{-1}(H/L)$. (2.5)

where L is the film to sample distance, and H is the distance from centre of film. With these definitions equation 2.4 can be written as:

$$t_p = \left[1 + {}^{1}\!\!\diagup_{\sin \alpha_f} \right]^{-1} \tag{2.6}$$

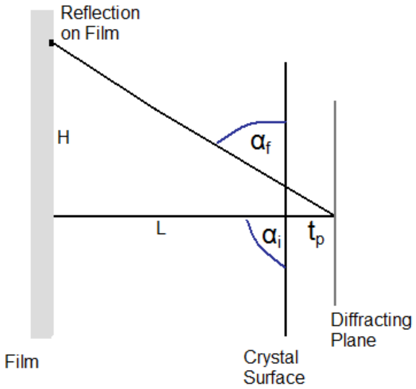

Figure 2.3: Kinematical penetration depth, t_p for a diffracting plane in a crystal.

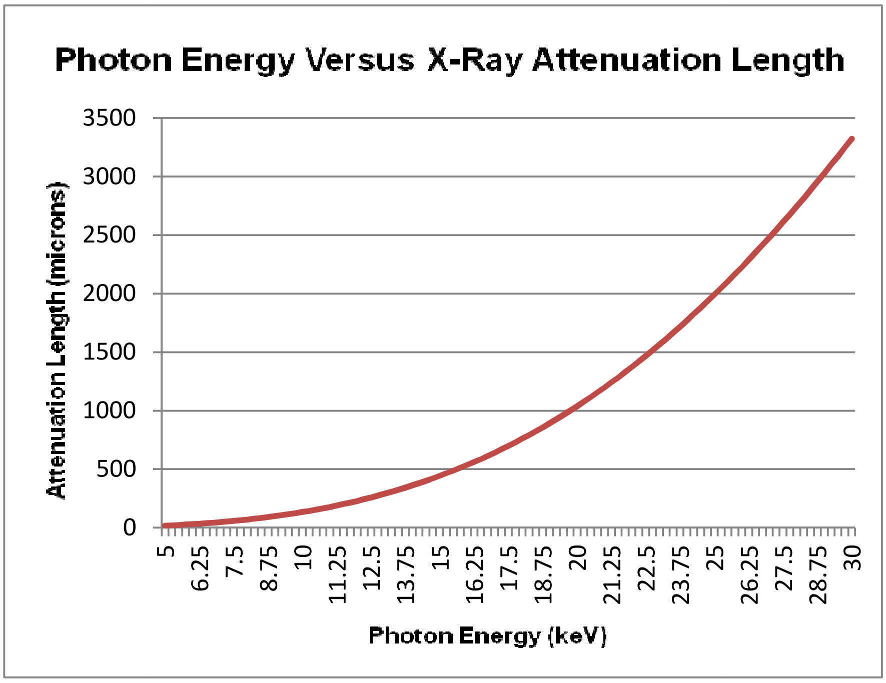

Figure 2.4: Graph of Photon Energy Versus X-Ray Attenuation Length [68].

We also know that [73]:

$$E(KeV) = \frac{12.4}{\lambda(\text{Å})} \tag{2.7}$$

Given the base wavelength, λ(Å), values for the attenuation length can be obtained from the graph in Figure 2.4 [68].

2.2.2 Dynamical Theory of XRD

In the case of large and perfect crystals the dynamical theory of XRD must be applied. In contrast to kinematical theory, dynamical theory takes into account interaction between incident waves and diffracted waves. The first of the dynamical theories was proposed back in 1914 by Darwin [15, 16]. Darwin based his initial theory on Bragg (reflection) geometry, and examined the interaction between transmitted and reflected waves at each atomic plane.

Ewald published his dynamical theory of x-ray diffraction in 1917, and introduced the concept of wavefields, which proved fundamental to the derivation of the main dynamical theory equations. Later, in 1920, Ewald [12, 19] used his theory to quantitatively interpret work by Stenstorm and Hjalmar, which observed systematic deviations from the Bragg angle for different orders of reflections in a crystal [2]. The theory was further developed by a number of scientists over the subsequent 10 years, however the form of the dynamical theory which is most widely used and accepted was developed by von Laue in 1931 [12], on the basis of Ewald's theory. Von Laue used Maxwell's equations to derive expressions for the diffracted intensities of an entire unit cell. The theory itself is complex, and includes multiple scattering, extinction, absorption and refraction for the case of large and/or perfect crystals. A detailed explanation of the theory will not be given here, however excellent explanations of the dynamical diffraction of x-rays by perfect crystals are given in [2, 9, 12].

2.2.3 Defect Contrast Mechanisms

When a perfect, uniform crystal is exposed to synchrotron radiation, and the image recorded on a photographic film, the resultant topographic image is uniform, and no contrast is visible. Contrast arises due to inhomogenities in the crystal lattice such as defects, strain, phase changes and crystal thickness changes. Image contrast on the recording films is generated via the difference in diffracted intensity between perfect and distorted regions in a single crystal sample and depends on the geometry used and on the spectrum of the incident radiation. Three types of image contrast are commonly observed in White Beam Synchroton X-Ray Topography: orientational contrast, extinction, and structure factor contrast [2, 9].

2.2.3.1 Orientational Contrast

Orientational contrast arises as a result of differences in the directions of reflections in the crystal lattice. When part of a crystal is oriented to satisfy Bragg's law, x-rays are diffracted. Areas in the same crystal can be misoriented due to features such as stacking faults and grain boundaries. If these parts of the crystal have sufficient misorientation such that they are outside the reflection range of the crystal, and cannot satisfy Bragg's law, they will not diffract (Figure 2.5(a)). The region of zero intensity corresponds geometrically to the misoriented region. This type of contrast occurs only in the case of monochromatic radiation [10].

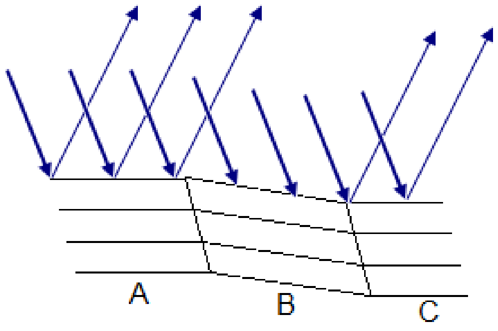

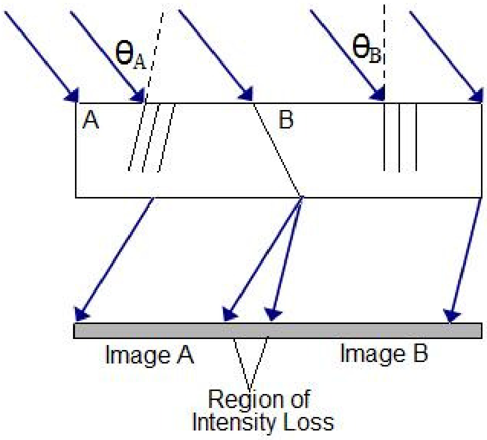

Figure 2.5 (a): Orientational contrast for a monochromatic, collimated x-ray beam. Diffraction occurs in regions A and C, but is missing in region B [2, 10].

Figure 2.5 (b): Orientational contrast for white beam topography. Adjoining misoriented regions A and B and the resultant boundary leads to image contrast.

In the case of white beam topography, the diffracted beams from the perfect and imperfect parts of the crystal emerge at different angles, and Bragg's law is satisfied only for certain wavelengths. Boundaries with misoriented regions show a gain or loss in intensity, depending on the angle of the diffracted beam. Boundaries producing divergent beams lead to a loss of intensity and thus stronger contrast than convergent boundaries. Depending on the misorientation of the area the resultant diffracted intensity can range from negligible to highly contrasting. Figure 2.5 (b) shows the region of intensity loss/gain at the boundary between regions A and B, the width of this region is dependent on the angle of misorientation and the sample to film distance [2, 9, 19]. This relationship enables the component of misorientation to be measured in the incidence plane of the misorientation across the boundary by simply taking topographs at different sample to film distances. Figure 2.6 (a) and (b) show orientational contrast formed from imaging nano-indents in (100) Si. Highly misoriented regions surrounding the indents show a gain in intensity due to orientational contrast mechanisms.

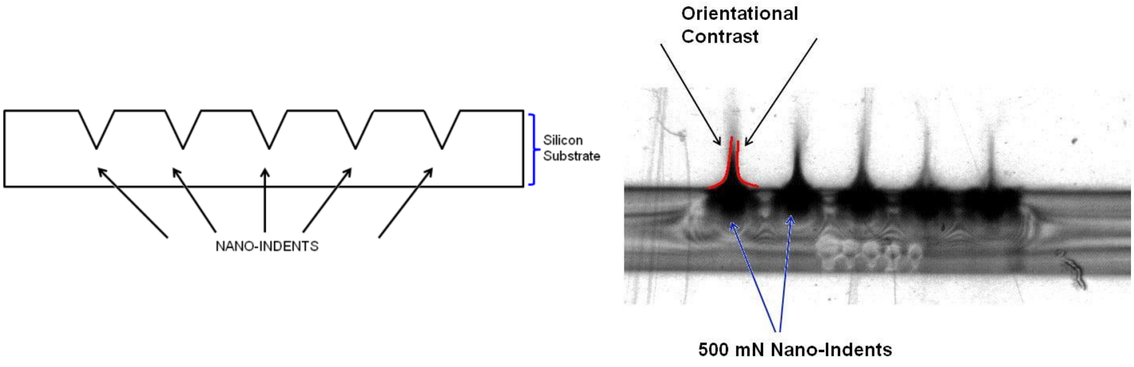

Figure 2.6(a) and (b): (a) Diagram of Si substrate illustrating nano-indents on surface. (b) Schematic of ST topograph showing series of five 500mN nano-indents on silicon substrate showing regions of high contrast corresponding to orientational contrast.

Extremely misorientated regions can appear at different places on the recording film [10, 20]. Figure 2.7 (a) shows parallel x-rays from a white beam source incident on a highly misorientated region of a crystal. The upper (green) ray interacts with the crystal lattice and the diffraction angle is equal to the angle of the incident ray minus twice the Bragg angle (180º-2θ_B). When the lower (red) ray interacts with the highly misorientated region, the ray is diffracted by 180º-2(θ_B+$\Delta\theta$). The additional diffraction angle, $\Delta\theta$, results in the ray appearing above the green ray when viewed on the recording film. Figure 2.7 (b) is an example of orientational contrast from a QFN-A package, where highly misorientated lattice planes have resulted in images appearing at different places on the x-ray film [10, 20].

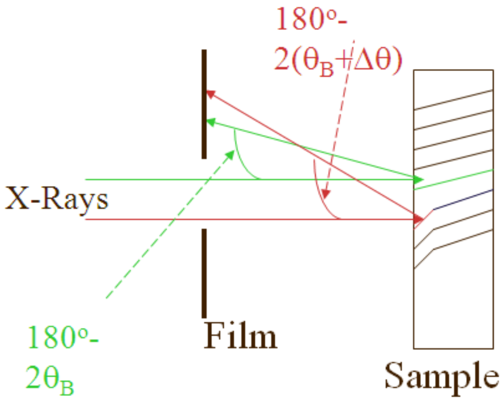

Figure 2.7 (a): Diffraction from a highly misoriented region in a crystal leading to x-rays appearing at different places on the film.

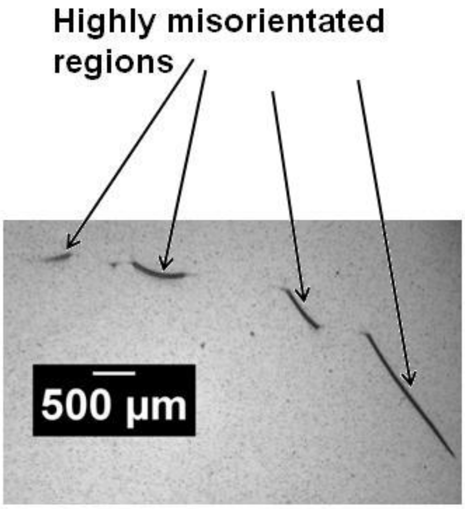

Figure 2.7 (b): ST topograph of bottom right corner of QFN-A package 09-089 no. 047 showing highly misorientated regions resulting from orientational contrast.

2.2.3.2 Extinction Contrast

As distinct from classical geometrical theory dynamical theory takes into account multiple interactions between the incident and diffracted waves in the sample, and thus is considerably more complex. A rocking curve gives the intensity of x-rays emerging from a sample as a function of the Bragg angle (Figure 2.8). In a perfect crystal the reflected x-ray intensity is high at the Bragg angle, however as the crystal is titled or rocked away from the Bragg angle the intensity of x-rays diminishes rapidly. In the case of an imperfect crystal the reflected x-ray intensity is maintained over a greater rocking curve, and one has to move relatively far away from the Bragg angle for the intensity to go to zero (Figure 2.8) [71]. The integrated area under the curves in Figure 2.8 represents the integrated reflected intensities, which is equal to the scattering power, P. In the case of a perfect crystal $P \propto |F|$, where F is the structure factor, whereas in an imperfect crystal $P \propto |F|^2$ [10]. The diffracted intensity for imperfect crystals is therefore much greater than for perfect crystals. Thus imperfect crystalline regions such as defects or dislocations appear black on the x-ray film, and the perfect crystal appears as white (lower intensity).

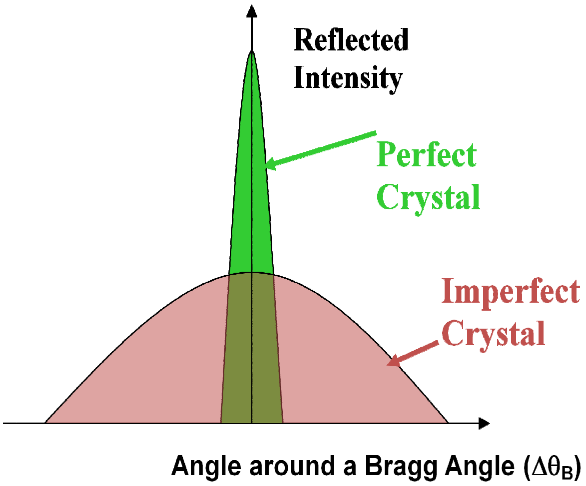

Figure 2.8: Schematic rocking curves for perfect crystal and for imperfect crystal. The shaded area represents the integrated intensity, which is equal to the scattering power [71].

Extinction contrast occurs in crystals with low defect density, where the scattering power in the region of the defect differs from that in the perfect crystal. In regions where the strain gradient is high, such as surrounding a dislocation, the dynamical diffraction of a perfect crystal is altered, and 3 types of extinction contrast are apparent [2]:

1. Direct image
2. Dynamical image
3. Intermediary image

The product of the linear absorption coefficient of the crystal, μ_0, and its thickness, t, define the absorption condition $\mu_0 t$ [21, 22]. The absorption condition indicates what type of extinction contrast can be observed. For topographs in transmission geometry, recorded under low absorption conditions, $\mu_0 t \leq 1\text{-}2$, direct image extinction dominates. Intermediate absorption conditions, where $5 \geq \mu_0 t \geq 1$, can lead to all three types of extinction occurring, while in the case of high absorption $\mu_0 t \geq 6$, the dynamical contribution is dominant [21]. A schematic of all three types of extinction contrast is shown in Figure 2.9 (a).

Direct Image Contrast

Direct image contrast occurs in the case of a perfect crystal, when the incident x-ray beam intercepts the defect within the crystal. The x-rays do not suffer extinction and for this reason their contrast is always higher than for a perfect crystal (Figure 2.9 (a) (1)). Direct images appear as dark lines against the white perfect crystal background, and are the most prevalent images seen in x-ray topographs.

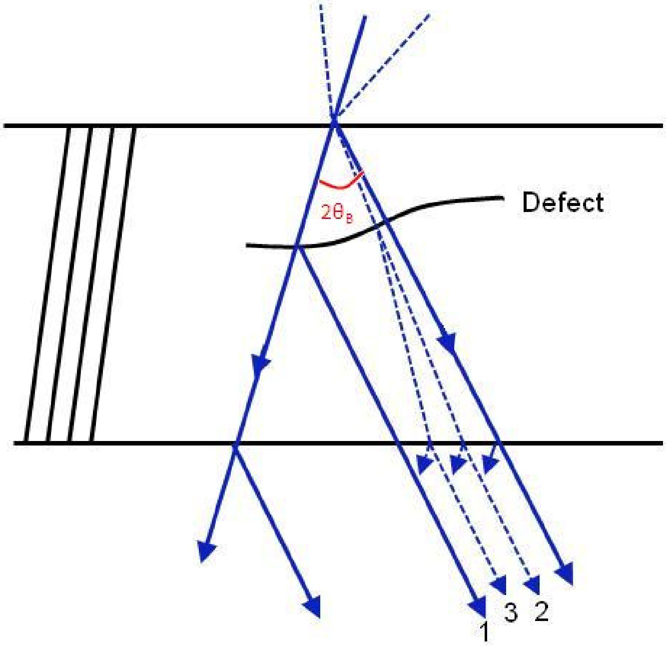

Figure 2.9 (a): Formation of 3 types of extinction contrast in a sample with high strain gradient. (1) Direct image contrast (2) Dynamical image contrast (3) Intermediary image contrast.

Dynamical Image Contrast

Dynamical image extinction occurs under high absorption conditions, as a result of a change in the wavefield intensity due to a defect. For a perfect crystal, in the case of a monochromatic plane wave, the wavefields propagate inside the crystal, and interfere at the defect site [20]. Outside the crystal the wavefield coupled waves decouple (Figure 2.9 (a) (2)). The characteristic coupling between wavefields results in extinction and a loss of intensity (white region) is recorded on the film [2, 19]. The extinction length (reflection geometry) or Pendellösung length (transmission geometry), ξ, gives the depth of the crystal which is imaged on the x-ray topograph [8, 19]:

$$\xi = \frac{\pi V_C \cos\theta_B}{\lambda C_p |F_h| r_0} \qquad (2.8)$$

where V_C is the unit cell volume, F_h is the structure factor of the Bragg reflection used, r_0 is the classical radius of the electron, $r_0 = \frac{e^2}{m_e c^2}$, where e is the electric charge of the electron, and m_e is the mass of the electron. c is the speed of light. C_p is the polarisation factor; $C_p=1$ if the electric vector of the x-ray wave is perpendicular to the dispersion plane. The lateral undulations along a standard undulator will produce linear polarization. $C_p=\cos 2\theta$, when the electric vector is parallel to the dispersion plane.

Intermediary Image Contrast

Intermediary image extinction is formed when the wavefields created in the dynamic case (above) interfere with new wavefields created at a defect site (Figure 2.9 (a) (3)). When the new wavefields exit at the defect boundary they can interfere with original wavefields propagating along other paths. Intermediary images can be difficult to identify on integrated wave topographic images, and appear as a bead like contrast along the direct image of the defect [20]. This type of image contrast is found in regions where the strain gradient is high.

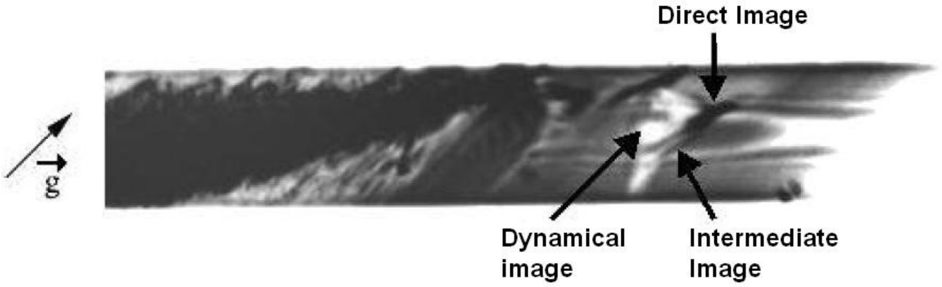

Figure 2.9 (b): 2 2 0 ST topograph of silicon showing three types of extinction contrast; direct, dynamical and intermediate [67]. Diffraction vector, g is also indicated.

2.2.3.3 Structure Factor Contrast

The structure factor, F, relates the number of atoms in a unit cell to the scattering angle, and thus the scattering vector. Differences in structure factors of a crystal can be a result of phase changes in the material, ferroelectric domains, or different materials in a sample.

When two regions in a crystal have different structure factors differences in the amplitude or phase of the structure factors can vary the intensity of the diffracted beam, and cause image contrast [9].

2.3 Photoacoustic Microscopy

Photoacoustic microscopy (PAM) is an imaging technique based on photothermal science and the photoacoustic effect. Although the use of the photoacoustic effect as an imaging technique is relatively new, the physical phenomenon of the photoacoustic effect was first observed by A.G. Bell in 1880 [23].

Bell used a beam of sunlight, which he interrupted by using a configuration of 2 perforated disks, one stationary and one rapidly rotated. The receiver in his experiment consisted of a parabolic reflector focussed on a glass vessel which contained selenium, and was connected to a hearing tube. Using this configuration Bell proved that sound was emitted from the action of the intermittent sunlight on a substance, and concluded that sonorousness under such conditions, was likely to be a universal property of matter. Further studies were undertaken on solids and liquids by Bell [24], and more extensively on gases by Tyndall [25], Roentgen [26] and Rayleigh [27]. As the basic gas laws were already well known at the time, the early scientists could correctly deduce that the signal was due to absorption of the chopped radiation by the gas, and the resultant periodic heat induced pressure and volume changes. These pressure and volume changes were transmitted to the observer via the diaphragm of a hearing tube. At the time both Bell and Rayleigh attributed the main source of the photoacoustic effect in solids to the uneven heating of the sample, caused by the chopped sunlight, and the mechanical vibration which it induced. However later studies showed that the vibrations were too small in magnitude to be the primary cause of the photoacoustic signal [28].

The further development of the photoacoustic effect lay more or less dormant until the first use of photoacoustic spectroscopy by Viengerov in 1938 [29], who used the technique to study light absorption in gases. Over the succeeding twenty years there were few significant developments in the study of the photoacoustic effect until several inventions in the late 1960’s and early 1970’s such as high-sensitivty microphones and the laser, and the advent of sensitive detection techniques such as the lock-in amplifier which enabled the major experimental limitations of the technique to be overcome. The first high sensitivity photoacoustic measurements were performed by Kreuzer in 1971, who used laser light sources for sensitive gas-phase analysis [30]. The high spectral brightness of lasers, and their spatial coherence enabled high energies to be delivered to the sample in small volumes. The smaller excitation volumes enabled enhanced signals to be obtained, reducing the problem of low signal to noise ratio, inherent in photoacoustic systems. Microphones enabled accurate pressure detection, and the lock-in amplifier enhanced the signal strength, filtering out unwanted noise.

Photoacoustic spectroscopy was not extended to liquid and solid phases until after Rosencwaig and Gersho developed the now well established one dimensional theoretical heat flow model for the photoacoustic effect [31, 32]. In this chapter the Rosencwaig-Gersho theory is reviewed, and later modifications and developments are discussed in its application to PAM and semiconductor materials.

2.3.1 Photoacoustic Effect in Condensed Matter

When light is incident on a solid sample confined within an enclosed cell, part of the optical energy may be absorbed by the sample and transferred to thermal energy, exciting internal energy levels. Subsequent relaxation of the excited states through non-radiative de-excitation processes (Figure 2.10) results in rapid heating of the sample. In a solid, the heat energy occurs as kinetic energy of the atoms, and the modulation of the light source generates thermal waves.

Thermal diffusion waves occur when a diffusion process couples with a periodic source. The depth a thermal wave penetrates into a sample depends on the thermal diffusivity of the sample, and the frequency of the thermal wave. For silicon with a high thermal diffusivity, Table 2.1, and a high frequency wave, the thermal wave will propagate deep into the material.

Material	Density (kg m^{-3})	Specific Heat (J kg^{-1} K^{-1})	Thermal Conductivity (W m^{-1} K^{-1})	Thermal Diffusivity (× 10^{-6} m^2 s^{-1})	Thermal Effusivity ($Ws^{1/2}$ m^{-2} K^{-1})
Silicon	2330	712	148	89.21	15669.27

Table 2.1: Thermal properties of Silicon [33]

In contrast to normal propagating waves, thermal diffusion waves are heavily damped, with a decay constant equal to the thermal diffusion length. For a diffusion wave

$\kappa_s = (1+i)\sqrt{2D/\omega}$, where l is the sample thickness (mm), κ_s is the thermal conductivity, (W m^{-1} K^{-1}), D is the thermal diffusion coefficient and ω is the chopping frequency of the incident light beam (radians / sec). These waves diffuse through the gas (air) in the cell and are detected acoustically using a microphone located within the cell walls (Figure 2.11). The amplitude and phase of the recorded photoacoustic signal are proportional to the amount of light absorbed by the sample.

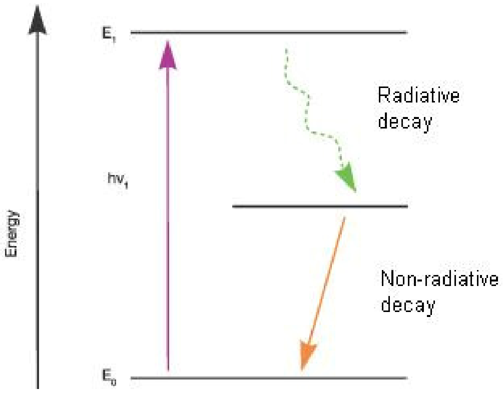

Figure 2.10: Electronic processes involved in light absorption and decay.

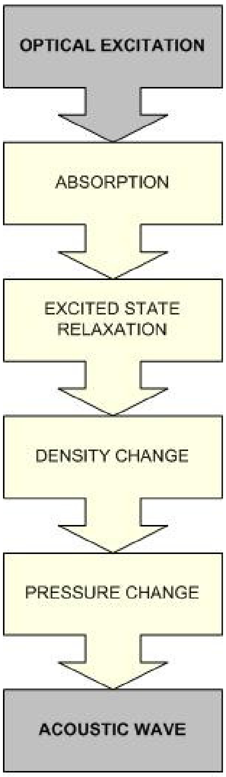

Figure 2.11: Major processes which contribute to the photoacoustic effect.

An advantage of this technique is that the photoacoustic signal is derived completely from the light energy absorbed by the sample. Scattered or reflected light does not contribute to the signal, making the technique ideally suited to highly scattering samples such as solids and interfaces [32].

In the case of photoacoustic microscopy a laser is used to generate thermal waves at a specific point on the surface of the sample. Raster scanning the laser across the surface of the sample enables spatially resolved thermal probing. As the photoacoustic signal is dependent on the optical, thermal, elastic and geometrical properties of the sample, photoacoustic images can be produced which give information on surface and sub-surface defects and structures in the sample.

2.3.2 The Rosencwaig and Gersho (RG) Theory

The Rosencwaig-Gersho theory considerers the case of a one-dimensional cylindrical cell (Figure 2.12) with diameter, D and length, L. Rowencwaig and Gersho [31, 32], propose that in the case of such a cell:

- the backing material is a poor thermal conductor,
- the cell length, L, >> the acoustic wavelength in the gas,
- the incident light is monochromatic and sinusoidally chopped,
- the gas and backing materials are non-light absorbing,
- the system is adiabatic,
- the window is optically and thermally transparent**.**

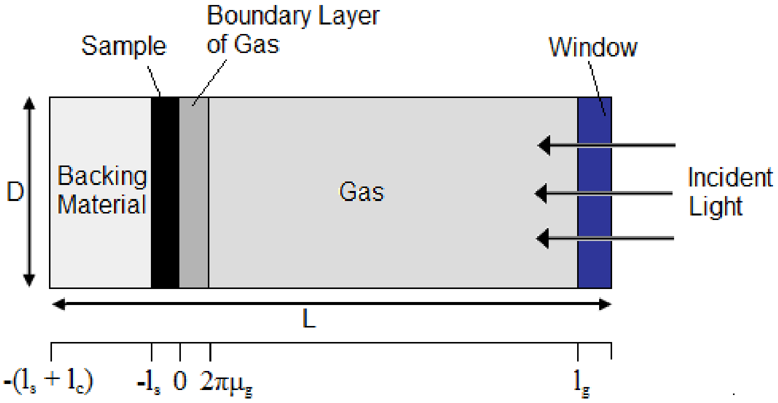

Figure 2.12: Simple cylindrical photoacoustic cell.

The photoacoustic effect is dependent on the relationship between three parameters of the sample: l_s, the thickness of the sample, β_s the absorption coefficient of the sample, its optical absorption length, l_β where $l_\beta = {}^{1}\!/_{\beta_s}$, and its thermal diffusion length, μ_s, where $\mu_s = \left({}^{2\alpha_s}\!/_{\omega}\right)^{1/2}$. For a 1D model [32], the thermal diffusion length, μ_s, can be calculated from

$$\alpha_s = {}^{\kappa_s}\!/_{\rho_s C_s} \qquad (2.9)$$

$$a_s = \left({}^{\omega}\!/_{2\alpha_s}\right)^{1/2} \qquad (2.10)$$

$$\mu_s = {}^{1}\!/_{a_s} \qquad (2.11)$$

where:

α_s = the thermal diffusivity (cm^2 / sec),

κ_s = the thermal conductivity, (W m^{-1} K^{-1}),

ω = chopping frequency of the incident light beam (radians / sec),

ρ_s = the density, (g / cm^3),

μ_s = the thermal diffusion length (cm), and

C_s = the specific heat (cal / g-^{0}C).

Subscripts denote parameters relating to the sample (s), gas (g) and cell backing materials (c), respectively.

When optical energy in the form of a sinusoidally modulated laser beam with intensity I_0 is applied to the solid sample with an absorption coefficient, β_s, a small amount of the energy is absorbed by the sample and converted to heat. The heat density generated due to the light absorbed by the sample at any point is given by:

$$\tfrac{1}{2}\beta_s I_0 e^{\beta_s x}\left(1+\cos\ \omega\, t\right) \qquad (2.12)$$

The thermal diffusion equation in the solid, taking into account the distributed heat source can be written as:

$$\frac{\delta^2\theta}{\delta x^2}=\frac{1}{\alpha_s}\frac{\delta\theta}{\delta t}-\frac{\beta_s I_0 \eta}{2k}e^{\beta_s x}\left(1+e^{i\omega\, t}\right) \qquad -l_s \leq x \leq 0 \qquad (2.13)$$

where θ is the temperature of the sample, and η is the efficiency at which the absorbed light is converted to heat.

Similarly, for the backing material and the gas, the heat diffusion equations are:

$$\frac{\delta^2\theta}{\delta x^2}=\frac{1}{\alpha_c}\frac{\delta\theta}{\delta t} \qquad -(l_c + l_s) \leq x \leq -l_s \qquad (2.14)$$

$$\frac{\delta^2\theta}{\delta x^2}=\frac{1}{\alpha_g}\frac{\delta\theta}{\delta t} \qquad \text{for } 0 \leq x \leq l_g \qquad (2.15)$$

The temperature in the cell relative to the ambient temperature as a function of position and time, is represented by the real part, $\theta(x, t)$ of equations 2.12 – 2.15.

To simplify the solutions to the expressions (2.13 – 2.15) above, a number of boundary conditions can be applied. For metallic walls it is a reasonable assumption that the temperature of the cell walls is at ambient. Also, for a small cell at steady-state conditions, convective heat flow in the gas ignored. Thus the solution of interest is the complex amplitude of the periodic temperature at the solid-gas boundary (x = 0, Figure 2.12), and is given by:

$$\theta_0 = \frac{\beta_s I_0}{2\kappa_s\left(\beta_s^{\,2} - \sigma_s^{\,2}\right)}\left[\frac{(r-1)(b+1)e^{\sigma_s l_s} - (r+1)(b-1)e^{-\sigma_s l_s} + 2(b-r)e^{-\beta_s l_s}}{(g+1)(b+1)e^{\sigma_s l_s} - (g-1)(b-1)e^{-\beta_s l_s}}\right] \quad (2.16)$$

where $b = {}^{\kappa_c a_c}\!\big/_{\kappa_s a_s}$, $g = {}^{\kappa_g a_g}\!\big/_{\kappa_s a_s}$, $r = {}^{(1-i)\beta_s}\!\big/_{2a_s}$, and $\sigma = (1+i)a$

The main source of the photoacoustic signal is due to the periodic heat flow from the sample to the surrounding boundary layer of gas, which acts as an acoustic piston, and induces a periodic pressure change in the column of gas above it.

Q, the pressure variation within the photoacoustic cell is dependent on thermal diffusion mechanisms and the densities and thermal properties of the gas, sample and cell backing materials.

$$Q = \frac{\beta_s I_0 \gamma \;\; P_0}{T_0 2\sqrt{2} T_0 \kappa_s l_g a_g \left(\beta^2 - \sigma^2\right)} \times \left[\frac{(r-1)(b+1)e^{\sigma_s l_s} - (r+1)(b-1)e^{-\sigma_s l_s} + 2(b-r)e^{-\beta_s l_s}}{(g+1)(b+1)e^{\sigma_s l_s} - (g-1)(b-1)e^{-\sigma_s l_s}}\right]$$

(2.17)

T_0 is the temperature at x=0 (Figure 2.12), P_0 is the ambient pressure within the cell; γ is the ratio of the specific heats of the gas and boundary layer.

The R-G theory gives several cases for the simplified calculation of Q. The appropriate expression depends on the optical opacity of the solid, which is determined by the relation of the optical absorption length, l_β to l_s, the thickness of the sample. The two main cases which should be considered when looking at the photoacoustic effect in condensed media are:

- Optically transparent solids, ($l_\beta > l_s$)
- Optically opaque solids, ($l_\beta << l_s$)

These cases are each further divided into three further categories, according to the magnitude of the thermal diffusion length, μ_s, with respect to the physical length, l_s, and the optical absorption length, l_β.

2.3.2.1 Optically Transparent Solids, ($l_\beta > l_s$)

For optically transparent solids the optical absorption length, l_β is larger than the sample thickness, l_s.

Thermally Thin Solids

A significant amount of light intensity can penetrate through the sample and light can be absorbed through the entire sample. As the thermal diffusion length is greater than the sample thickness $\mu_s > l_s$ or $\mu_s >> l_s$, heat can be transported back to the surface of the sample through the underlying regions.

Quantity	Definition	Quantity	Definition
μ_s	Thermal diffusion length in sample.	κ_c	The thermal conductivity of cell backing material.
β_s	Absorption coefficient of the sample.	μ_c	Thermal diffusion length in cell backing material.
l_s	Thickness of the sample.	ω	Chopping frequency of incident light.
l_β	Optical absorption length of sample.		

Table 2.2: Definition of parameters used in the simplified calculation of Q.

Case A: ($\mu_s >> l_s$; $\mu_s > l_\beta$)

Set $e^{-\beta_s l_s} \approx 1-\beta_s l_s$, $e^{\pm\sigma l_s} \approx 1$, and $|r| > 1$ in equation (2.17)

$$\Rightarrow Q = \frac{Y}{2a_g a_c \kappa_c}(\beta_s - 2ab - i\beta_s) \approx \frac{(1-i)\beta_s l_s}{2a_g}\left(\frac{\mu_c}{\kappa_c}\right)Y \qquad (2.18)$$

where $Y = \frac{\gamma \; P_0 I_0}{2\sqrt{2}T_0 l_g}$, for all cases. (2.19)

Case B: ($\mu_s > l_s$; $\mu_s < l_\beta$)

Set $e^{-\beta_s l_s} \approx 1-\beta_s l_s$, $e^{\pm\sigma l_s} \approx 1 \pm \sigma l_s$, and $|r| < 1$ in equation (2.17)

$$\Rightarrow Q = \frac{\beta_s l_s Y}{4\kappa_s a_g a_s^3 b}\left[\left(\beta_s^{\,2} + 2a_s^2\right) + i\left(\beta_s^{\,2} + 2a_s^2\right)\right] \approx \frac{(1-i)\beta_s l_s}{2a_g}\left(\frac{\mu_c}{\kappa_c}\right)Y \qquad (2.20)$$

In both of the above cases the acoustic signal is therefore proportional to βl_s, and since μ_c/a_g is proportional to $1/\omega$, the acoustic signal also has a ω^{-1} dependence. The thermal properties of the backing material, (denoted by subscript c), have an influence on the final value for Q.

Thermally Thick Solids

Case C: ($\mu_s < l_s$; $\mu_s << l_\beta$)

Although light can be absorbed throughout the length of the solid, because the thickness of the sample is greater than the thermal diffusion length, heat from underlying layers cannot reach the surface. The photoacoustic signal therefore comprises of only surface effects. The signal is proportional to β_s μ_s and has a $\omega^{-3/2}$ dependence.

Set $e^{-\beta_s l_s} \approx 1-\beta_s l_s$, $e^{-\sigma l_s} \approx 0$, and $|r| << 1$ in equation (2.17)

$$\Rightarrow Q \approx i\frac{\beta_s \mu_s}{2a_g}\left(\frac{\mu_s}{\kappa_s}\right)Y \qquad (2.21)$$

2.3.2.2 Optically Opaque Solids, ($l_\beta << l_s$)

In the case of optically opaque solids, $l_\beta << l_s$, most of the light is absorbed at the surface of the sample and effectively no light is transmitted.

Quantity	Definition	Quantity	Definition
μ_s	Thermal diffusion length in sample.	κ_c	The thermal conductivity of cell backing material.
β_s	Absorption coefficient of the sample.	μ_c	Thermal diffusion length in cell backing material.
l_s	Thickness of the sample.	ω	Chopping frequency of incident light.
l_β	Optical absorption length of sample.		

Table 2.3: Definition of parameters used in the simplified calculation of Q.

Case A: Thermally Thin Solids ($\mu_s >> l_s$; $\mu_s >> l_\beta$)

In theory because of the large thermal diffusion length, heat transport through the length of the sample is possible, however relatively little light intensity penetrates through the surface of the sample and therefore heat generation below the surface is minimal. The photoacoustic signal therefore comprises primarily of surface effects

Set $e^{-\beta_s l_s} \approx 0$, $e^{\pm\sigma l_s} \approx 1$, and $|r| >> 1$ in equation (2.17)

$$\Rightarrow Q \approx \frac{(1-i)}{2a_g}\left(\frac{\mu_c}{\kappa_c}\right)Y \tag{2.22}$$

The pressure variation within the cell is independent of β_s, the absorption coefficient, and is dependent on the thermal properties of the backing material. The acoustic signal varies as ω^{-1}.

Thermally Thick Solids

For optically and thermally thick solids the sample thickness is greater than the thermal diffusion length. Very little heat can penetrate through the sample due to the relatively small optical absorption length, and any small amount of heat generated in the underlying regions cannot reach the surface due to the relatively small thermal diffusion length. This results in the photoacoustic signal comprising mainly of surface effects.

Case B: ($\mu_s < l_s$; $\mu_s > l_\beta$)

Set $e^{-\beta l_s} \approx 0$, $e^{-\sigma l_s} \approx 0$, and $|r| > 1$ in equation (2.17)

$$\Rightarrow Q \approx \frac{Y}{2a_g a_s \kappa_s \beta_s}(\beta_s - 2a_s - i\beta_s) \approx \frac{(1-i)}{2a_g}\left(\frac{\mu_s}{\kappa_s}\right)Y \tag{2.23}$$

The photoacoustic signal depends on the properties of the sample, and as in the previous case is independent of β_s and varies with ω^{-1}.

Case C: ($\mu_s << l_s$; $\mu_s < l_\beta$)

Set $e^{-\beta l_s} \approx 0$, $e^{-\sigma l_s} \approx 0$, and $|r| < 1$ in equation (2.17)

$$\Rightarrow Q \approx \frac{-i\beta_s Y}{4a_g a_s^3 \kappa_s}(2a_s - \beta_s + i\beta_s) \approx \frac{-i\beta_s \mu_s}{2a_g}\left(\frac{\mu_s}{\kappa_s}\right)Y \tag{2.24}$$

Only the light absorbed within the first thermal diffusion length, μ_s contributes to the photoacoustic signal. The signal is proportional to β_s and has a $\omega^{-3/2}$ dependence.

2.3.3 PAM Image Formation & Resolution

It is well established [32-34], that the main factors which influence the degree of image contrast and spatial resolution of photoacoustic images are the diameter of the light probe, the excitation zone volume of a material, and the thermal diffusion length. The thermal diffusion length of a material has the greatest effect on the spatial resolution of the image obtained. R-G theory shows the dependence of the photoacoustic (PA) signal on the thermal diffusion length of the sample, (equation 2.11).

Engineering and software design features of the photoacoustic microscope can also heavily influence image resolution. Mechanical features such as the step size of the x-y stage, the quality of the focussing optics and data accumulation and analysis all play a large role in the final resolution of the image obtained. The great number of related aspects of signal formation and material properties which combine to influence image formation render the determination of the exact resolution of features in a PA image quite a complex process.

2.3.3.1 Thermal Diffusion Length

When light in the near-infrared region is incident on the sample, the light is transmitted, reflected, or absorbed. The thermal diffusion length of the material will indicate to what extent the thermal wave will propagate through the material. The R-G theory gives several cases for the calculation of Q, the pressure variation within the PA cell. The appropriate expression depends on the optical opaqueness of the solid, which is determined by the relation of the optical absorption length, l_β to l_s, the thickness of the sample. In the case of the samples studied in this report, the R-G equation (2.23) for optically opaque, thermally thick solids ($\mu_s < l_s$, $\mu_s > l_\beta$), is the closest approximation.

The reflectance, absorption and transmission values for 0.3 µm to 1.5 µm wavelength radiation and a Si wafer thickness of ~600 µm can also be determined by experiment [35]. It may be seen from the graph below (Figure 2.13) that for IR radiation at 0.8 µm wavelength, 0 % is transmitted, 32 % is reflected, and 67 % is absorbed, which are in agreement with the R-G theory, (section 2.3.2.)

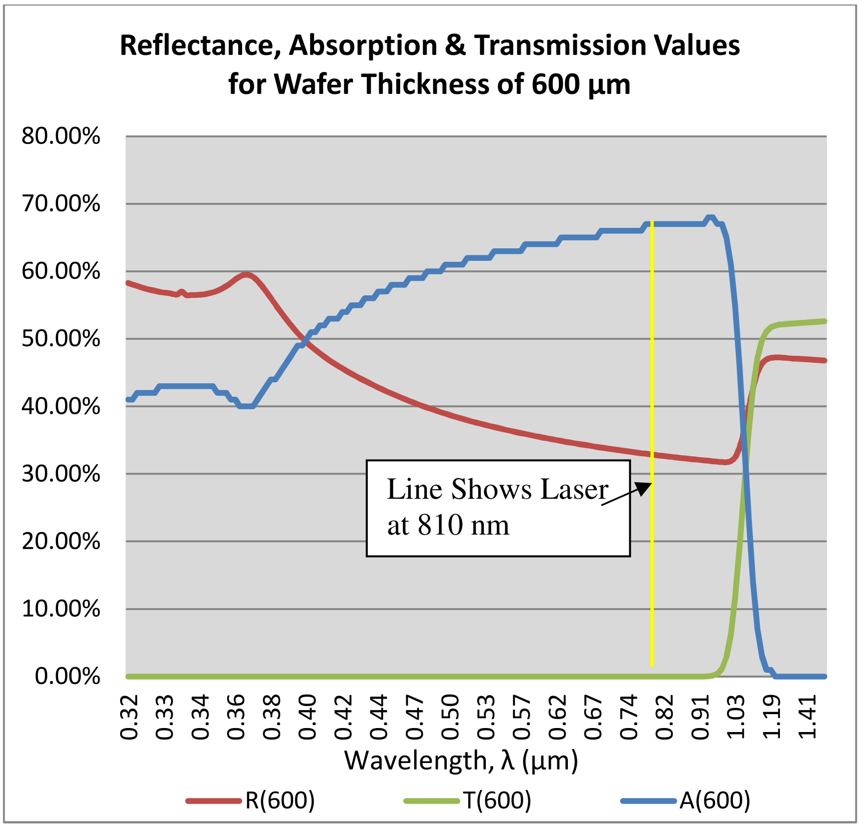

Figure 2.13: Experimental results for Reflectance (R), Absorption (A) and Transmission (T) of Radiation in 600 µm thick Silicon Wafers [36].

In the case of polished silicon (Table 2.1), the wavelength of the incident light is equivalent to that of the excitation laser, 810 nm. If the chopping frequency of the incident light beam is set to ~4398 rads / sec (700 Hz), the thermal diffusion length can be calculated as 207 µm.

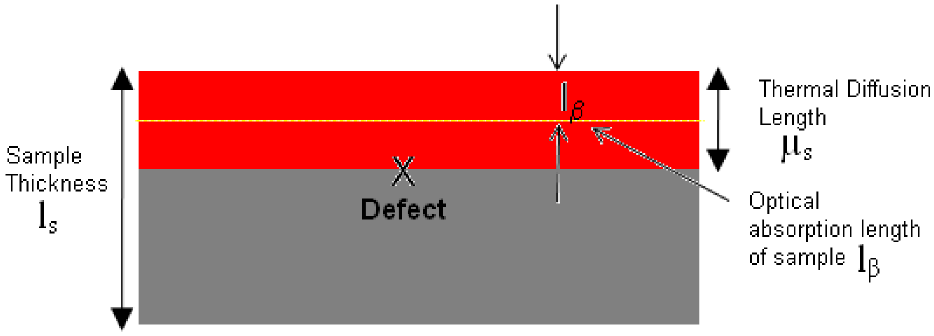

Figure 2.14: Schematic of Si sample showing defect position with respect to the thermal diffusion length (207 µm), sample thickness (675 µm) and optical absorption length (100 µm) for an excitation laser wavelength of 810 nm.

In photoacoustic microscopy the modulation frequency can be adjusted to correlate to a specific thermal diffusion length for a given material. When subsurface defects exist the thermal diffusion length must be sufficient for the thermal waves induced by the laser beam to propagate through the sample to the defect. Figure 2.15 shows the thermal diffusion length for single-crystal silicon for a range of modulation frequencies. The thermal diffusion length decreases with increasing modulation frequency. In the case of sub-surface defects it can be observed that the size of the image decreases with increasing modulation frequency, and is related to the decreased detection range at higher frequencies. By varying the laser modulation frequency and determining at what penetration depth defects are no longer visible the depth of defects can be established (Figure 2.14). The shape of sub-surface defects can also be estimated based on the obtained signal density distribution [35]

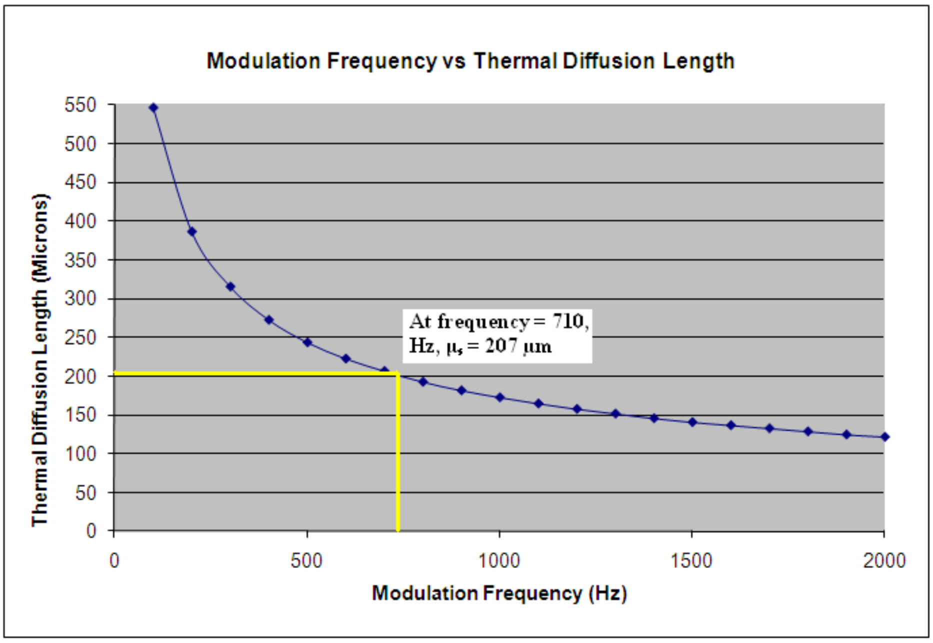

Figure 2.15: Thermal diffusion length (microns) for modulation frequencies in the range 100 – 2000 Hz.

In the case of this study a laser with wavelength, λ=810 nm was used, and all samples were Si, which has a thermal conductivity, κ_s= 148 W m^{-1} K^{-1} [33]. l_β the optical absorption length can therefore be calculated from:

$$l_\beta = 1/\beta_s \tag{2.25}$$

$$\beta_s = \frac{2\pi.\kappa_s}{\lambda} \tag{2.26}$$

$$l_\beta = \frac{\lambda}{2\pi.\kappa_s} \tag{2.27}$$

Figure 2.16 below shows the relationship between the wavelength of the laser, and the optical absorption length of the sample.

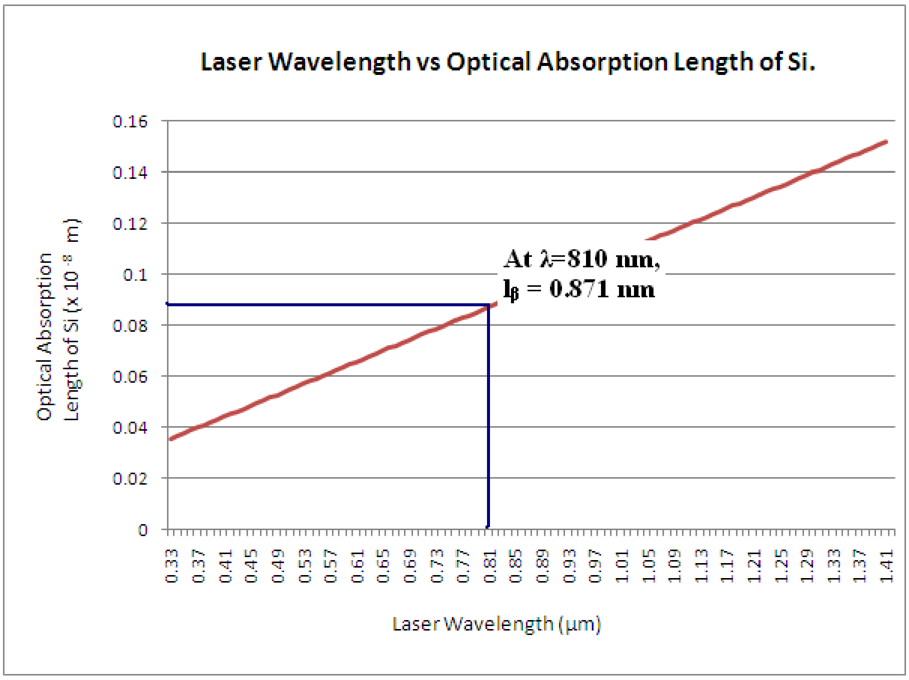

Figure 2.16: Graph showing the relationship between the wavelength of the excitation source (laser) and the optical absorption length of the sample (Si).

2.3.2 Light Source Diameter and Resolution

As a diode laser source is used the wavelength and power of the incident light is fixed, however the diameter of the light probe plays an important role in achieving the best resolution. Where the laser spot size is much larger than the thermal diffusion length, the lateral resolution is determined by the optical spot size. Collimating and focussing lens systems can be used to alter the optical density and spatial resolution of the laser beam, but lens imperfections and the resulting aberrations can negatively impact image resolution. It is therefore essential that lens quality is sufficiently high, while practical cost considerations are taken into account, as high quality lenses with low aberrations are costly.

The R-G theory is accurate for beam spot diameters >20 times the thermal diffusion length of material being studied [33]. However in the case of a PAM system, such as the one used here and described in Chapter 3, for highly focussed lasers (spot diameter ≤100 μm), thermal waves are generated from a point-like source and the 1D R-G model (Section 2.3.2) is not as accurate [33]. Conversely, it has been proven both theoretically and experimentally [38-40] that even when laser spot size is considered in a 3D model of the PA effect, the results are very similar to, or the same as the 1D R-G model as far as the PA signal frequency and phase dependencies are concerned. Spot size therefore plays a relatively insignificant role in determining the PA signal.

2.3.3 Scattering from Inhomogeneties

Photoacoustic microscopy has been proven to be a reliable technique for examining defects and inhomogenties in semiconductor materials. When optically invisible defects and inhomogeneities within a sample are imaged thermal wave generation, wave propagation, and scattering from inhomogeneities have an influence on photothermal signal formation [37]. When a laser spot is scanned across the surface of a sample, small inhomogenties (of the order of nm to µm in dimension), in the material, or changes in the material type or structure interrupt the propagation of thermal waves, and hence acoustic waves in the material, which result in changes in the photoacoustic signal. These changes appear as contrasting areas in the PAM image. The PA signal phase tends to have higher thermal wave sensitivity than the amplitude signal, and deeper flaws can be detected by the phase image than by the amplitude image when measured at the same laser modulation frequency. The phase image is not affected by the reflectivity of the sample surface, whereas the amplitude image is directly affected. Therefore the phase image has better resolution when subsurface characteristics and features such as stressed regions in samples and material inhomogeneities are being studied [41, 42].

Where defects such as inclusions, pores, cracks, and other inhomogeneities exist in semiconductor materials, the thermal wave is reflected at the boundary between the defect and the bulk material, resulting in the subsurface feature appearing in the photoacoustic image. A defect such as a crack or indent can be considered as an inhomogeneity where the buried air forms an additional layer where thermal waves can interfere. Thermal wave reflection can be modelled as a 3 layer system, with a coating, air gap, and substrate all in contact with each other (Figure 2.17), [33].

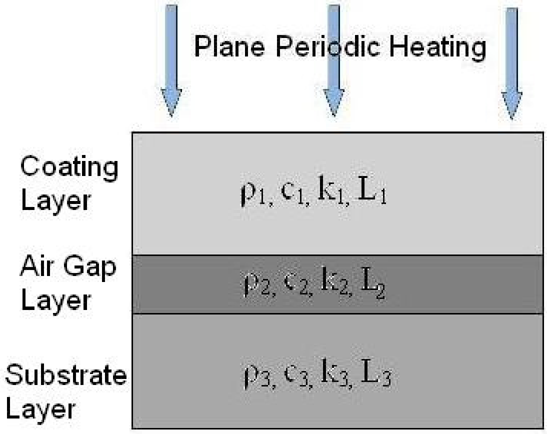

Figure 2.17: Coating-air gap-substrate sample system [33]. Subscripts 1, 2 and 3 refer to the coating, air and substrate, respectively. L is the layer thickness, ρ is the density, c is the specific heat capacity, k is the thermal conductivity.

As the size of the defect and hence the thickness of the air gap increases, the reflectivity increases. Thermal wave interference occurs in both the coating layer and the air gap. The effective reflection coefficient of the air layer can be shown to be [29, 34]:

$$\Gamma = \frac{\Gamma_1 + \Gamma_2 \exp(-2\sigma_{21}L)_2}{1 + \Gamma_1\Gamma_2 \exp(-2\sigma_{21}L)_2} \tag{2.28}$$

where: $\Gamma_1 = {}^{1-b_{21}}\!\big/\!{}_{1+b_{21}}$, $\Gamma_2 = {}^{1-b_{32}}\!\big/\!{}_{1+b_{32}}$, $b_{i+1/i} = {}^{k_{i+1}\sigma_{i+1}}\!\big/\!{}_{k_i\sigma_i}$ (2.29)

Subscripts 1, 2 and 3 refer to the media, coating, air and substrate respectively. L is the layer thickness, σ_{ij} is the thermal wavenumber for layer i = 1, 2, 3, Γ_1 and Γ_2, are the thermal wave reflecting coefficients for the 1/2 (coating/air) and 2/3 (air/substrate) media boundaries respectively.

Increasing the modulation frequency reduces the thermal wave length and the reflecting power of a particular layer of air, therefore lower modulation frequencies enable the detection of cracks. The effusivity of a material e, is given by, $e = \sqrt{\kappa.\rho.C_p}$ where κ is the thermal conductivity of the material, ρ is the density of the material and C_p is its heat capacity. Effusivity measures the rate at which a material can absorb heat. Silicon has a relatively high thermal effusivity, and hence the air layer presents a higher thermal contrast, and is therefore more reflective than a lower effusivity material. The detection ability of an air gap is therefore better in a higher effusivity material.

In a real situation where a defect is present, distinct layers are not distinguishable, and the above model, which assumes temperature continuity, is invalid. A thermal resistance model, which assumes a temperature jump at the interface is therefore more appropriate. The model assumes flux continuity across the interface and a thermal discontinuity [33]:

$$-k_1 \, {}^{\delta T_1}\!/_{\delta x} = -k_2 \, {}^{\delta T_2}\!/_{\delta x}, \qquad T_2 - T_1 = R_T \, {}^{\delta T_2}\!/_{\delta x} \tag{2.30}$$

$$\Gamma = \frac{1 - b_{21} + R_T k_2 \sigma_2}{1 + b_{21} + R_T k_2 \sigma_2} \tag{2.31}$$

where R_T is the interface thermal contact resistance. Interfaces of this kind have very similar properties to air gaps. Thermal wave interactions at semi-finite boundaries (as above) can be considered a good approximation for finite boundaries, which are found in reality, provided their dimensions are greater than the thermal wave length.

2.3.4 Semiconductors

When a semiconductor is irradiated with light whose photon energy is larger than the bandgap energy, E_g, both interband and intraband transitions can occur. These include excitations from the valence band to higher conduction bands, excitations across the energy gap, and excitations from imperfections, which occur from within the energy gap into the conduction band [33]. At very high frequencies (photon energies), high absorption and surface reflectivity are observed as a result of excitations by fundamental absorption processes. In the majority of materials the light absorption and the related heat generation is assumed to be localised in the absorption region, and can be treated as an instantaneous process relative to the modulation period of the laser [33]. However in semiconductors, near the band gap energy, three processes dominate resulting in heat generation being less localised and taking place over a longer time scale (Figure 2.18).

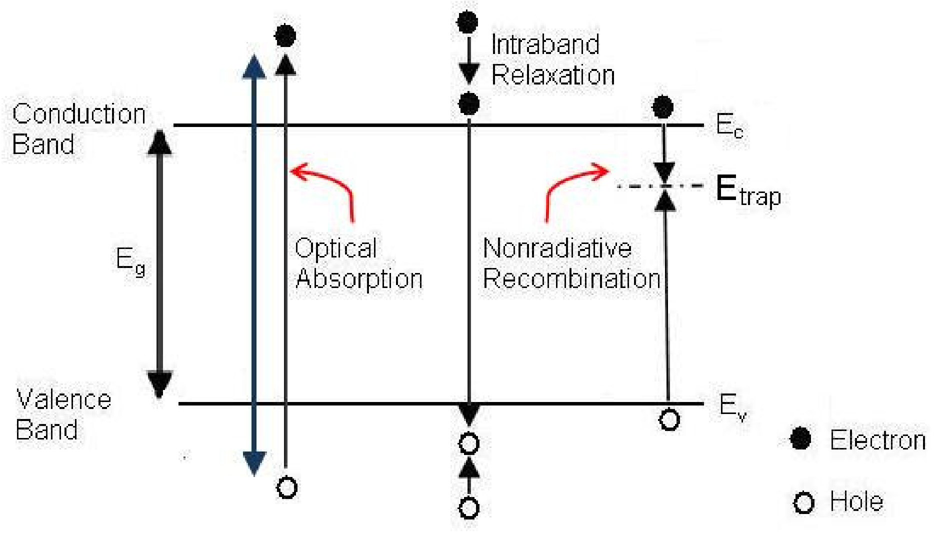

Figure 2.18: Schematic of Optical Absorption, Intraband Relaxation and Nonradiative Recombination via Traps in a Semiconductor.

The primary thermal wave source occurs when electrons are excited from the valence band into the conduction band with energy ($E - E_g$), greater than the bottom of the conduction band. Holes are then left in the valence band and the excess energy from the transition is transmitted into the lattice in the form of heat. Energy is transferred to the lattice via electron-phonon interactions. In the case of optical phonons this occurs almost instantaneously (~ps), close to the band edge acoustic phonons are involved, and the process is slower (~ns). The secondary thermal wave source is formed, when after the carrier lifetime, τ, the remaining energy is dissipated into the lattice. This occurs as a result of recombination of excited carriers in the conduction band with holes in the valence band. Electrons diffuse through the semiconductor, away from the original excitation point during the lifetime τ, resulting in a spatially extended thermal wave distribution. Some of the excited electrons diffuse through to the surface of the material, and recombine rapidly due to the high density of carrier traps. This results in a third thermal wave source at the surface.

2.4 Micro-Raman Spectroscopy

The scattering of light by materials was studied by the great physicists including Rayleigh and Einstein as far back as the late 1800s, but with the exception of Compton's studies on x-rays, no change in wavelength was observed [43]. The Austrian physicist Adolf G. Smekal in 1923 was the first to predict the inelastic scattering of light from a material, and the shift of the scattered light to higher and lower wavelengths [44]. However it was not until 5 years later that the Indian physicist, Sir C.V. Raman and colleague K. S. Krishnan proved the theory which now carries Raman's name. The theory was also proved independently at the same time, in quartz crystals by Grigory Landsberg and Leonid Mandelstam (1928) [45, 46]. The original experiments utilised sunlight focussed onto a sample of purified liquid, and with a telescope as the collector, and the eye as the detector [47]. Raman later won the Nobel Prize for Physics for his work in which he modified his first experiment to include a mercury vapour lamp as the light source, and placed a second lens near the sample to collect the scattered radiation, a system of optical filters was utilised to distinguish the scattered radiation and its frequency shift from the incident light [48]. Using this experimental setup Raman and Krishnan obtained line spectra for various liquids, and showed for each sample a small fraction of light is inelastically scattered at optical frequencies different from the frequency of the incident light – the basis of the Raman effect. Raman and Krishnan subsequently used the mercury lamp at 435 nm, and photographic film to record more detailed spectra of carbon tetrachloride exhibiting both the Stokes and anti-Stokes lines in 1929 [49]. G. Placzek later published a semi-classical theory of the Raman effect [45, 50], but work on the Raman effect lay largely undeveloped until after the advent of the laser in the 1960's.

As with similar early scientific discoveries, experimental configuration and calibration of the early Raman experiments were complex and time consuming. The invention of the laser in the 1960's brought about a renaissance in Raman spectroscopy studies. Lasers could be focussed on small samples, had increased detection sensitivity, allowed the study of low frequency vibrations, and eliminated some of the problems associated with sample fluorescence. Porto and Wood were the first to use lasers as a tool in Raman spectroscopy in their studies of organic liquids and gases [51], Townes suggested the HeNe laser as a Raman source in 1961, but it was not implemented in experiments until three years later [52].

Signal to noise ratio was improved by the integration into Raman systems in the 1950's of photon-counting photomultiplier tubes. However, it was not until the advent of new instrumentation including high quality holographic gratings, improved detectors and efficient data processing that Raman spectroscopy became more widely applied to the qualitative and quantitative analysis of chemical compounds [53]. Holographic gratings were largely defect free when compared to their predecessors, ruled gratings, and reduced stray light levels by orders of magnitude. Multiple stage monochromators or spectrographs were necessary in order to separate the signal of interest from the Rayleigh signal, and brought about the first easy to use analytical Raman Spectrometers [47]. Although charged coupled devices (CCD), were introduced in 1970 by Boyle and Smith [54], they were not used as detectors in Raman systems until 1987 [55].

Computers which integrate full acquisition control and sophisticated spectral analysis including fast Fourier transforms (FFT) have enabled the commercial systems that are now commonplace to be developed, and Raman Spectroscopy is now a powerful and widely used analysis technique in both research and industry. The first commercial micro-Raman system was designed around an optical microscope and incorporated single point and 2-dimensional Raman mapping. Use of micro Raman systems for quantification of local stresses in silicon down to device level was first published in 1983 [56], and since then has been widely used for strain analysis in semiconductors [57-59]. The use of different wavelength probe lasers in micro-Raman spectroscopy provides depth profiling capability, due to the dependence of wavelength on absorption coefficient, and penetration depth [60].

2.4.1 Rayleigh and Raman Scattering

When light interacts with matter photons can be absorbed, absorbed and re-emitted at a different wavelength, undergo scattering, or not interact with the material at all and pass straight through it. Elastic Rayleigh scattering, named after Lord Rayleigh who discovered it in the early 1900's, occurs when the scattering medium is composed of particles which are much smaller than the wavelength of the incident light. The photons do not gain or lose energy during the scattering process, and therefore there is no change in wavelength of the light. The majority of light passing through a transparent material undergoes elastic scattering, and so it is the most intense type of scattering. Inelastic scattering occurs when a small amount of the energy of the incident radiation is lost or gained. In the case of Raman scattering the incident photon is scattered, and there is an energy exchange between the incident photons and the semiconductor phonons. Inelastic, Raman scattering can take two forms: Stokes scattering occurs at longer wavelengths (lower energy) than the excitation wavelength; anti-Stokes scattering wavelengths are shifted to shorter wavelengths (higher energies). The magnitudes of Raman shifts are independent of the wavelength of excitation.

2.4.2 Raman Scattering in Solids

Raman spectroscopy involves the scattering of electromagnetic radiation by optical phonons in solids and molecular vibrations. Raman scattering occurs when light interacts inelastically with the lattice vibrations (phonons) of a material, which subsequently scatter the light. The frequency of the phonon Raman band is a function of the interatomic forces which are related to the bond lengths. In the case of the classical theory in crystalline materials the forces between the atoms are assumed to be linear and nearest-neighbour, and interatomic bonds can be modelled as springs, as described in Figure 2.19.

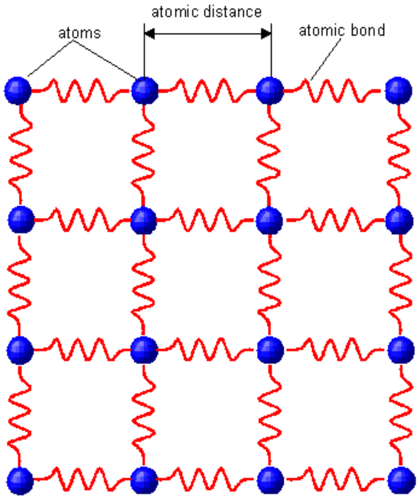

Figure 2.19: 2-dimensional crystal lattice with atomic bonds modelled as springs [70].

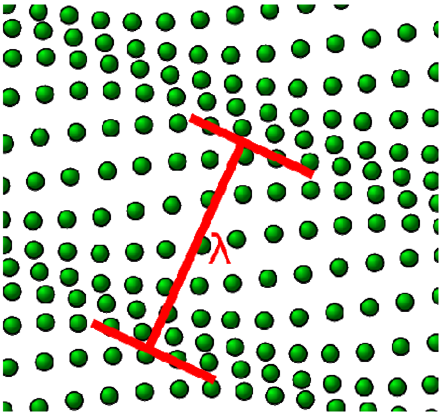

Figure 2.20: Vibrational wave travelling through crystal lattice with wavelength indicated. Amplitude of the wave is given by the displacements of the atoms from their equilibrium positions. λ is the wavelength of the wave [69].

The change of the spring constant (i.e. lattice spacing) under stress gives rise to shifts in the frequency of inelastically scattered Raman photons (Figure 2.20). Stokes scattering occurs when scattered photons lose energy by emitting a phonon, anti-Stokes scattering occurs when scattered photons gain energy. Thus scattered light has components with a different frequency than the incident light. A plot of the shifted light output versus frequency is a Raman spectrum.

Raman scattering can also be described in terms of the discrete energy states of each lattice vibration mode. This is a more exact theory, as unlike the classical theory it takes into account the quantized nature of vibrations. It also considers the relationship between lattice properties and Raman scattering, which classical theory omits [46]. In quantum mechanics the energy levels of a harmonic oscillator are quantized. Similarly, energy levels of lattice vibrations are quantized with a quantum of vibration known as a phonon. Inelastic scattering must satisfy conservation of energy and momentum. The scattering frequency, ω_S, is defined as: $\omega_S = \omega_i \pm \omega_j$ (2.32)

where ω_i is the incident photon frequency, and ω_j is the frequency of the excitation.

The scattering wave vector, $\overrightarrow{k_S}$, is defined as:

$$\overrightarrow{k_S} = \overrightarrow{k_i} \pm \overrightarrow{q_j} \qquad (2.33)$$

where $\overrightarrow{k_i}$ is the incident photon wavevector, $\overrightarrow{k_s}$ is the scattered phonon wavevector, and $\overrightarrow{q_j}$ is the wavevector for the elementary excitation.

The 3 scattering processes are illustrated in Figure 2.21. In equations 2.32 and 2.33 the plus sign represents the process in which an elementary excitation is generated (Stokes scattering), and the minus sign represents a process in which an elementary excitation is annihilated (anti-Stokes scattering).

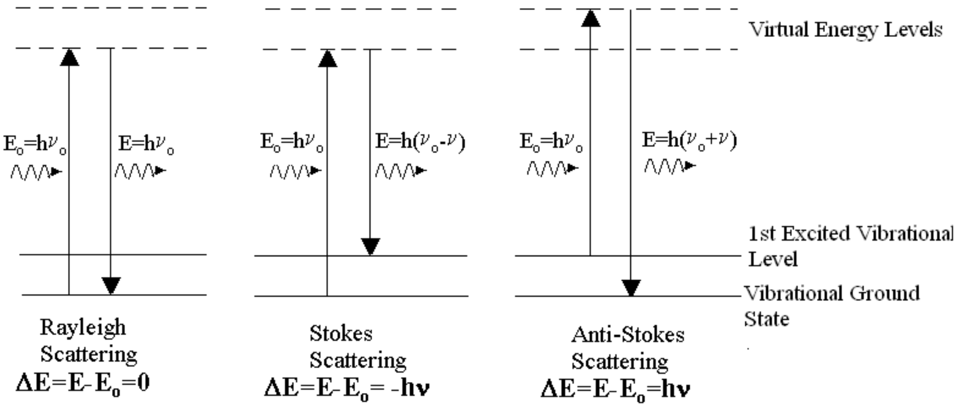

Figure 2.21: Diagram of Raman and Rayleigh Scattering. Raman scattering differs from Rayleigh by ΔE, the energy of the first vibrational level of the ground state. The energy of the virtual state is defined by the energy of the incoming laser and the phonon properties.

For the propagation of light of frequency ω_i in a plane-polarised homogeneous medium the electric field $\vec{E}$ in the crystal at position $\vec{r}$ is given as:

$$\overrightarrow{E_X} = \overrightarrow{E_0} \exp\left[i\left(\overrightarrow{k_i}.\vec{r} - \omega_i t\right)\right] \qquad (2.34)$$

where $\overrightarrow{E_X}$ is the electric field in the x-direction and $\overrightarrow{E_0}$ is the amplitude of the wave in the x-direction, and t is time.

The excitation of the crystal corresponding to the inelastic light scattering is given by the lattice vibration. For lattice vibrations with wavevector $\overrightarrow{q_j}$ and frequency ω_j, the vibrational amplitude at position $\vec{r}$ is expressed as:

$$Q_j = A_j \exp\left[\pm i\left(\overrightarrow{q_j} \cdot \vec{r} - \omega_j t\right)\right] \tag{2.35}$$

where Q_j is the normal co-ordinate of vibration and A_j is a constant [65, 66].

This quantised lattice vibration is known as a normal mode or a phonon, and can cause a variation in the electrical susceptibility of a crystal and give rise to Raman scattering.

When laser light with frequency ω_i and direction k_i is incident on a crystal the associated electric field $\vec{E}$ will induce a fluctuating electric moment in the crystal. $\vec{P}$, the electric dipole moment per unit volume (i.e. polarisation), may be defined as:

$$\vec{P} = \varepsilon_0 \chi \vec{E} \tag{2.36}$$

where χ is the susceptibility tensor and ε_0 is the permittivity in free space.

Electromagnetic radiation can induce microscopic polarizations of a material. A system's response to an electromagnetic field is known as the electric susceptibility. Susceptibility can change as a function of the lattice vibrations and thus can be expanded in a Taylor series with respect to the normal co-ordinate of vibration, Q_j, as:

$$\chi = \chi_0 + \left({}^{\delta\chi}\!/_{\delta Q_j} \right)_0 Q_j + \left({}^{\delta^2\chi}\!/_{\delta Q_j \delta Q_k} \right)_0 Q_j Q_k + \ldots \tag{2.37}$$

where the subscripts j and k refer to different vibration directions. Higher order terms can be neglected for small atomic displacements.

Thus equation 2.36 can be written as:

$$\vec{P} = \varepsilon_0 \chi_0 . \overrightarrow{E_0} \exp\left[i\left(\overrightarrow{k_i} . \vec{r} - \omega_i t\right)\right] + \varepsilon_0 A_j \overrightarrow{E_0} \left({}^{\delta\chi}\!/_{\delta Q_j} \right)_0 \times \exp\left[-i\left(\omega_i \pm \omega_j\right)t\right] \exp\left[i\left(\overrightarrow{k_i} \pm \overrightarrow{q_j}\right)r\right] \tag{2.38}$$

The first term in equation 2.38 represents the oscillation of the induced moment at the frequency ω_i of the incident light, resulting in Rayleigh scattering. The second term describes the induced moments at frequencies $\left(\omega_i - \omega_j\right)$ which lead to Stokes and at $\left(\omega_i + \omega_j\right)$ to Anti-Stokes first-order Raman scatterings. Inelastically scattered light is propagated in the directions $\overrightarrow{k_i} - \overrightarrow{q_j}$ and $\overrightarrow{k_i} + \overrightarrow{q_j}$ respectively. Raman scattering will only be observed when

$$\chi^{(1)} = \left({}^{\delta\chi}\!/_{\delta Q_j} \right)_0 \neq 0 \tag{2.39}$$

where the elements of $\chi^{(1)}$ are the Raman tensor components.

Assuming $\hat{e}_i$ and $\hat{e}_s$ to be the unit vectors of the polarisation of the incoming and scattered light, respectively, and R_j is the Raman tensor, the Raman scattering intensity is proportional to:

$$I \propto \left| \hat{e}_i . R_j . \hat{e}_s \right|^2 \tag{2.40}$$

Equation 2.40 determines whether a Raman-active phonon can be observed under certain experimental conditions regarding the incoming and scattered polarisation [65, 66].

Quantum Theory: Raman Intensities

Probabilities of Stokes and anti-Stokes processes strongly depend on the initial occupation number of the phonon state. From a quantum mechanical perspective the ratio of the intensities of Stokes and anti-Stokes scattering can be calculated from the Boltzmann equation [46, 47]:

$$\frac{N_n}{N_m} = \frac{g_n}{g_m} \exp\left[\frac{-\left(E_n - E_m\right)}{kT} \right] \tag{2.41}$$

where N_n is the population of phonons in the excited vibrational energy level (n), N_m is the population of phonons in the ground vibrational energy level (m), g is the degeneracy of the levels n and m, E_n-E_m is the difference in energy between the vibrational energy levels, and k is Boltzmann's constant. The Boltzmann distribution shows that at room temperature the ground state is more heavily populated, and thus Stokes Raman scattering is stronger than anti-Stokes Raman scattering. The ratio between Stokes and anti-Stokes intensities is given by:

$$\frac{I_{AS}}{I_S} = \exp\left(\frac{\hbar\omega}{k_B T} \right) \tag{2.42}$$

where I_{AS} is the intensity of anit-Stokes Raman scattering and I_S is the intensity of Stokes Raman scattering [65].

2.4.4 Polarizability and Raman Selection Rules

Raman scattering is dependent on the polarisation vectors of the incident and scattered light. This dependence is related to the symmetry properties of the derivative of the susceptibility, eqn (2.39) or of the equivalent Raman tensor, R_j [65-67]. For scattering of phonons in Si, which has the diamond cubic structure, the Raman tensors have the form [60]:

$$R_x = \begin{pmatrix} 0 & 0 & 0 \\ 0 & 0 & d \\ 0 & d & 0 \end{pmatrix} \qquad (2.43)$$

$$R_y = \begin{pmatrix} 0 & 0 & d \\ 0 & 0 & 0 \\ d & 0 & 0 \end{pmatrix} \qquad (2.44)$$

$$R_z = \begin{pmatrix} 0 & d & 0 \\ d & 0 & 0 \\ 0 & 0 & 0 \end{pmatrix} \qquad (2.45)$$

where x=[100], y=[010] and z=[001].

For back scattering from a (001) surface, i.e. the surface of a (100) Si wafer, only R_z is observed, which corresponds to the longitudinal optical (LO) phonon polarized along z. For back scattering from (110) surface of, for example, a cleaved wafer, as is the case with the stacked chips analysed in chapter 6 of this study, either the R_z or the R_x and R_y matrices can be involved. The R_x and R_y matrices correspond to scattering by transverse optical (TO), phonons polarized along x and y respectively [66]. For unstrained Si, the three optical Raman modes of Si have the same frequency of ~520 $\mathrm{Rcm^{-1}}$, where $\mathrm{Rcm^{-1}}$ refers to wave numbers relative to the frequency of the laser light.

2.4.5 Raman Peak Characteristics

The different characteristics of Raman peaks can reveal a range of information about the material being examined. Characteristic Raman frequencies can indicate the composition of the material, frequency shifts can indicate the stress/ strain state of the material, polarisation of the Raman peak can indicate crystal symmetry and orientation, the width of the Raman peak can indicate the quality of the crystal, and peak intensity can indicate the volume of material present.

The intensity of the Raman peak can provide information as to the crystalline disorder in the sample. Changes in the Raman polarizability tensors determine the Raman scattering intensity with decreases in intensity indicative of crystal disorder. Raman shift is the difference in wavenumbers (cm^{-1}), between the scattered radiation and the excitation (laser) radiation:

$$\Delta\omega_{Raman} = \Delta\omega_{Laser} - \Delta\omega_{Scattered} \tag{2.46}$$

The frequency of Raman phonon modes are always measured relative to the frequency of the laser light, and designated relative cm^{-1} (Rcm^{-1}). However the prefix is generally omitted and the popular labelling convention is cm^{-1}.

Peak Shape

The triply degenerate Transverse Optical (TO) phonon induced Raman peak shift of Si lies at 520.07 cm^{-1}[57, 61]. This peak is indicative of unstrained crystalline Si, and is due to the zero momentum state of the optical phonon with energy 64 meV [62]. In the case of amorphous Si (α-Si), a variety of phonon modes and energies are allowed, and a broad peak centred on 470 cm^{-1} is dominant. Nano-crystalline Si is characterised by a broad shoulder at 510 cm^{-1} [58]. Crystallite peak width and position is influenced by the crystallite size and shape, with micro-crystals smaller than approximately 300Å leading to a peak red shift and broadening [63], and peak shapes increasing in asymmetry for smaller crystallite sizes.

Strain Measurements

The extent of strain in a strained crystal can be quantified by the difference between the phonon energy of the relaxed (unstrained) crystal and the strained phonon energy [59]. The solution to the characteristic equation, gives the frequencies of the three optical modes in cubic crystals, in the presence of strain [57]:

$$\begin{vmatrix} p\varepsilon_{11} + q(\varepsilon_{22} + \varepsilon_{33}) - \lambda & 2r\varepsilon_{12} & 2r\varepsilon_{13} \\ 2r\varepsilon_{12} & p\varepsilon_{11} + q(\varepsilon_{33} + \varepsilon_{11}) - \lambda & 2r\varepsilon_{23} \\ 2r\varepsilon_{13} & 2r\varepsilon_{23} & p\varepsilon_{11} + q(\varepsilon_{11} + \varepsilon_{22}) - \lambda \end{vmatrix} = 0 \tag{2.47}$$

where p, q and r are material constants, known as the phonon deformation potentials, and ε_{ij} are the strain tensor components. The eigenvalues, λ_j, where j=1, 2, 3, denote the presence of stress, and ω_{j0} is the Raman frequency in the absence of stress. The strain shift can therefore be calculated from:

$$\Delta\omega_j = \omega_j - \omega_{j0} \approx \frac{\lambda_j}{2\omega_{j0}} \tag{2.48}$$

For backscattering from a (001) surface, only the third Raman mode is observed [64]. If a uniform biaxial stress model is assumed, the relationship between Raman shift and stress can be calculated from the equation [59, 64]:

$$\Delta\omega_3 = -4\times10^{-9}\left(\frac{\sigma_{xx}+\sigma_{yy}}{2}\right) \qquad (2.49)$$

where σ_{xx} and σ_{yy} are the stress components for biaxial strain in the x - y plane. Assuming, $\sigma_{xx} = \sigma_{yy}$ equation (2.49) can be written as:

$$\sigma_{xx} = \sigma_{yy} = \Delta\omega \big/ -4 \quad GPa \qquad (2.50)$$

Thus compressive uniaxial or biaxial stress results in a Raman peak shift to a higher wavenumber (blue shift), and tensile stress results in a Raman peak shift to a lower wavenumber (red shift).

2.5 Summary

In this chapter, principles underlying the theories of x-ray diffraction imaging, photoacoustic microscopy and micro-Raman spectroscopy have been presented. A basic introduction to SXRT/XRDI, and the principal image contrast mechanisms observed in the strained wafers and packages characterised in chapters 4, 5 and 6 have also been included. The photoacoustic effect in condensed matter samples has been reviewed, focussing on the established Rosencwaig–Gersho theory. The relationships between optical absorption coefficient, thermal diffusion length, laser wavelength and modulation frequency were also described. Finally, micro-Raman spectroscopy, a well established and widely used quantitative analysis technique, was introduced. Raman scattering theory in solids was discussed and the use of micro-Raman spectroscopy to measure stress and strain in semiconductor materials considered. Chapter 3 expands on the theories of XRDI, PAM and micro-Raman spectroscopy by describing in detail the experimental equipment, materials and methods behind each technique and their application in this study.

References

[1] Berg W.L., (1931) *Naturwissenschaften*, **19**, 391-396.

[2] Andre Authier et Al., X-Ray and Neutron Dynamical Diffraction Theory and Applications, Series B: Physics Vol. **357**.

[3] Ramachandran G.N., (1944) *Proc. Indian Acad. Sci*., **19**, 280-292.

[4] Wooster N.and Wooster W.A., (1945) *Nature*, **155**, 786-7.

[5] Barrett C.S., (1945) *Trans. Am. Inst. Min. Eng*., **161**, 15-65.

[6] Aroyo, Mois I.; Ulrich Müller and Hans Wondratschek (2006), *International Tables for Crystallography* (Springer) **A1** (1.1): 2–5.

[7] Lang A.R., (1959) *Acta Cryst*., **12**, 249-250

[8] T. Tuomi, N. Naukkarinen, and P. Rabe, *Physica Status Solidi (a)*, vol. **25**, pp. 93–106, 1974.

[9] A. Authier, *Dynamical Theory of X-Ray Diffraction*, pp. 546–549. Oxford Science Publications, 2001.

[10] K. Bowen, B. Tanner, *X-Ray Metrology in Semiconductor Manufacturing*, Taylor & Francis Group, 2006.

[11] T. Tuomi, *J. Synchrotron Rad*., (2002). **9**, 174-178.

[12] H. Wagenfeld, *Acta Cryst.* (1968). A24, 170-174.

[13] Jospeh B. Keller, *JOSA*,. Vol. **52**. No2, 1962.

[14] D. Lowney, T. S. Perova, M. Nolan, P. J. McNally, R. A. Moore, H. S. Gamble, T. Tuomi, R. Rantamaki and A. N. Danilewsky, *Semicond. Sci. Technol.* **17** (2002) 1081–1089.

[15] Darwin, C. G (1914a). *Phil. Mag*., **27**, 315-33.

[16] Darwin, C. G (1914b). *Phil. Mag*., **27**, 675-90.

[17] Ewald, P. P, (1920). *Z. Phys*., **2**, 332-42.

[18] William Hallowes Miller, *A Treatise on Crystallography*, Pitt Press, (1839).

[19] Jacqueline Heinrich, *ANKA Instrumentation Book*, October 1st, 2007.

[20] K. Bowen, B. Tanner, *High Resolution X-Ray Diffractometry and Topography*, 1998, CRC Press.

[21] B. Raghothamachar, G. Dhanaraj, J. Bai, and M. Dudley, *Microscopy Research and Technique*, **69**, 343 (2006).

[22] A. Lankinen *et al*., *Journal of Crystal Growth*, **283** (2005) 320–327.

[23] Alexander Graham Bell, *Am. J. Sci.* **20**, 205. 1880.

[24] Alexander Graham Bell, *Production of sound by radiant energy*, 1881.

[25] Tyndall, *J. Proc. R. Soc. Lond.*, **31**, 307.

[26] Roentgen, *W.C., Philos. Mag*. **11**, (5) 308.

[27] Lord Rayleigh, *Nature (Lond.)* **23**, 274. 1881

[28] W.H. Preece, *Proceeding of the Royal Society of London* (31), **506** (1881).

[29] Viengerov.M.L, *Dokl.Akad.Nauk, SSSR* **19**, 687 (1938).

[30] L. Kreuzer, *J Appl Phys*, **42**, 7, pp. 2934–2943, 1971.

[31] A. Rosencwaig, A. Gersho, *J Appl Phys*, **47**(1), 64 (1976).

[32] Allan Rosencwaig, *Chemical Analysis*, **Vol 57**, Photoacoustics and Photoacoustic Spectroscopy. John Wiley & Sons, 1941.

[33] D. P. Almond and P. M. Patel, *Photothermal Science and Techniques,* Chapman & Hall, 1996.

[34] A. Mandelis, P. Hess, *Progress in Photothermal and Photoacoustic Science and Technology*, SPIE Press, 2000.

[35] Haruo Endoh et Al., *Jpn. J. Appl. Phys*., Vol. **41** (2002) pp. 3361–3362

[36] Virginia Semiconductor, Inc., *Optical Properties of Silicon*. http://www.virginiasemi.com/pdf/Optical%20Properties%20of%20Silicon71502.pdf.

[37] Friedrich K., Haupt K., Seidel U., Walther H. G, *J. Appl. Phys*, **72** Issue: 8

[38] H. C. Chow, *J. Appl. Phys*., **51**, 4053 (1980).

[39] R. S. Quimby and W. M. Yen, *J. Appl. Phys*., **51**, 1252 (1980).

[40] F. Alan McDonald , *Appl. Phys. Lett.,* **36**, 123 (1980).

[41] Masanori Hangyo, et al*., Jpn. J. Appl. Phys*. 25 (1986) pp. 376-379.

[42] R.L. Thomas et al., *J. Appl. Phys.* 51, 1152 (1980).

[43] A. Compton, *Phys. Rev*., **21**, 483 (1923).

[44] Andreas W. Momber, *J. Mater. Sci*. (2010) **45**:750–758

[45] G. Turrell and J. Corset, *Raman microscopy : developments and applications,* (Academic Press, New York, NY ; London, 1996), p. 463.

[46] E. Smith and G. Dent, *Modern Raman Spectroscopy - A Practical Approach* (John Wiley & Sons Ltd., England, 2005), p. 71-92.

[47] Ferraro Nakamoto, *Introductory Raman Spectroscopy*, (Academic Press, 1994)

[48] C.V. Raman, *Indian J. Phys*., **2** (1928) 387

[49] C.V. Raman and K.S. Khrishnan, *Proc. Roy. Soc. (London),* **122**, 23, (1929).

[50] H.A. Bethe, G. Placzek, *Phys. Rev*., **51**, 450 – 484, (1937).

[51] Porto, S.P.S. and Wood, D.L., *Journal of the Optical Society of America*, **52** pp.251 (1962),

[52] C.H. Townes, *Advances in Quantum Electronics* (Columbia Univ. Press, 1961) p. 3.

[53] Baranska, H., Labudzinska, A.and Terpinski, J., *Laser Raman Spectrometry: analytical applications*, Ellis Horwood Limited, Chichester (1987).

[54] W.S. Boyle and G.E. Smith, *Bell System Tech. J.*, **49**, 587 (1970).

[55] S.B. Dierker, C.A. Murray, J.D. Legrange and N.E. Schlotter, *Chem. Phys. Lett.*, **137**, 453 (1987).

[56] Ian R. Lewis, Howell G. M. Edwards, *Handbook of Raman spectroscopy: from the research laboratory to the process line*, Marcel Dekker, New York and Basel, 2001.

[57] I. De Wolf, *J. Raman Spec.* **30**, 877 (1999).

[58] Jian Chen and Ingrid De Wolf, *Semicond. Sci. Technol.* **18** (2003) 261–268.

[59] Anastassakis, E. (1997), *J.Appl.Phys.*, **82** (4), pp. 1582-1591.

[60] Chen, J. and De Wolf, I., (2005), *IEEE Transactions on Components and Packing Technologies*, **28** (3), pp. 484-492.

[61] R. J. Needs and A. Mujica, *Phys. Rev. B* **51**, 9652 (1995).

[62] C. Smit et Al., *J. Appl. Phys.* **94**, 3582 (2003).

[63] I. H. Campbell and P. M. Fauchet, *Solid State Communications*, **58**, Issue 10, June 1986, pp 739-741.

[64] De Wolf, I. (1996), *Semiconductor Science and Technology,* **11** (2), pp.139-154.

[65] W. H. Weber, R. Merlin, *Raman Scattering in Materials Science* (Springer, 1996), p. 11-12.

[66] Gardner and Graves, *Practical Raman Spectroscopy*. Springer-Verlag 1989, pp 19 -24.

[67] Donnacha Lowney, "Analysis of the Structural and Optoelectronic Properties of Semiconductor Materials and Devices Using Photoacoustic Spectroscopy and Synchrotron X-ray Topography". M.Eng Masters Thesis, Dublin City University. April 2002.

[68] http://henke.lbl.gov/optical_constants/atten2.html

[69] http://en.wikipedia.org/wiki/File:Lattice_wave.svg

[70] http://en.wikipedia.org/wiki/Phonon

[71] A. Authier and C. Malgrange, *Acta Crystallographica Section A,* Volume **54**, Issue 6-1, November 1998, Pages: 806–819.

[72] Charles Kittel, *Introduction to Solid State Physics*, 7th Edition, Chapters 1&2, Wiley, 1996.

[73] http://halas.rice.edu/conversions

Experimental Methodology

3.1 Introduction

The aim of this chapter is to introduce the three main experimental techniques used in this study: X-Ray Diffraction Imaging (XRDI), 3-dimensional X-Ray Diffraction Imaging (3D-XRDI) and 3-dimensional surface mapping (3DSM). These methods are used as characterisation tools to qualitatively analyse strain fields in silicon, and in the case of 3D-XRDI and 3DSM to enable 3-dimensional visualisation of strain fields and lattice plane misorientation in bulk Si wafers and packaged chips. XRDI is used as a qualitative characterisation tool in conventional large area transmission (LAT), section transmission (ST) and large area back reflection (LABR) geometries. The main component of the two 3-dimensional imaging techniques, 3D-XRDI and 3DSM, is the 3-dimensional reconstruction of strain field and lattice misorientation data from X-Ray Diffraction Images using the widely available image processing and Computer Aided Design (CAD) packages *ImageJ*[1] and *SolidWorks*®. Two complementary non-destructive analysis techniques are also described: PAM and micro-Raman Spectroscopy.

3.2 Synchrotron X-Ray Diffraction (SXRT) / X-Ray Diffraction Imaging (XRDI)

Synchrotron X-Ray Topography (SXRT), also known as X-Ray Diffraction Imaging (XRDI) is a well established and powerful technique for the imaging of strain and defects in crystals such as dislocations, stacking faults, precipitates, voids, dislocations, strained layers and grain boundaries [1-3]. Analysis of topographs can also yield information on the density and distribution of dislocations, strain distribution caused by thermal processing, or introduced into a sample through strain engineering, and subgrain structures including misorientation angles [4 - 6]. XRDI is used in a range of geometries for the characterisation of materials, with each geometry providing information on a different part (surface, bulk, and cross-section) of the crystal. Three main XRDI experimental setups were used in this study: large area back reflection topography (LABR), large area transmission topography (LAT) and section transmission topography (ST) [3].

---

[1] *ImageJ* is also available as open source software known as *Fiji. Fiji* is *ImageJ* bundled with Java, Java 3D and many of the established plugins.

3.2.1 Image Geometries

SXRT provides much higher resolution topographs than conventional x-ray topography using a laboratory source and on a much shorter time scale, i.e. seconds versus hours. In addition to the geometric and spatial resolution of the synchrotron source, the resolution of the photographic film or ccd camera can also limit the spatial resolution of topographs. When taking topographs the two most commonly adjusted parameters are the sample to film/camera distance, L, and the angle of the sample holder with respect to the film/camera. The larger the sample to film/camera distance, the lower the resolution (eqn. 3.1), so smaller sample to film distances are preferable. However the film/camera should be located far enough away from the sample to avoid spot overlapping for large area topographs. Small adjustments of the sample holder orient different planes of the crystal with respect to the beam so as to position certain useful reflections optimally. For experiments discussed in this report the angle was typically between 0^0 and 20^0.

3.2.1.1 Large area transmission

The large area transmission (LAT) geometry setup is shown in Figure 3.1(a). Radiation passes through the back side of the sample, and reflections are recorded on the film. The incident beam is collimated to a maximum of ~4 mm x 4 mm, as larger beam sizes can lead to excessive fluorescence of the sample, which produces an unacceptable background x-ray intensity and hence poor contrast on the film. Topograph images represent the whole sample thickness and intensity variations are accumulated from defects through the bulk microstructure of the sample. In the case of good quality crystals, transmission images can be recorded through several mm of material.

3.2.1.2 Transmission section topography

Transmission section topography (ST), Figure 3.1(b), is similar to LAT except the beam is collimated into a narrow ribbon by a slit typically approximately 10 -15 μm in height. This enables sample cross-section images to be obtained, providing the Bragg angle is not too small. As in the case of LAT topography, ST images represent the whole sample thickness and intensity variations are accumulated from defects through the bulk micro-structure of the sample.

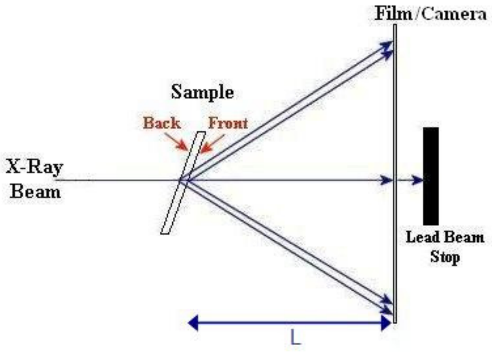

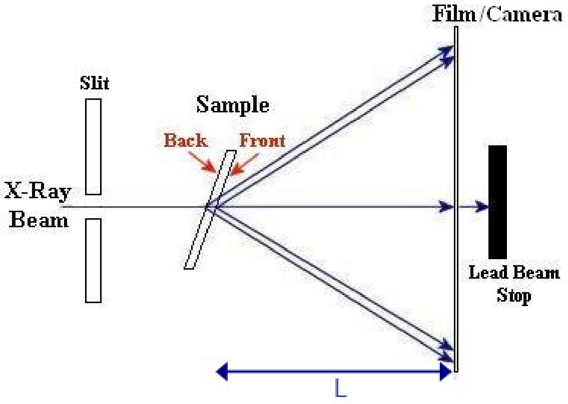

Figure 3.1(a): Large-Area Transmission Topography. Sample was typically tilted at 18^o to optimise the imaging of the 2 2 0 and 1 1 1 reflections. L is the sample to film distance.

Figure 3.1(b): Transmission Section Topography. Sample was typically tilted at 18^o to optimise the imaging of the 2 2 0 and 1 1 1 reflections. L is the sample to film distance.

3.2.1.3 Large area back reflection topography

Large area back reflection topography (LABRT) is illustrated in Figure 3.1(c). Radiation passes through a hole in the back side of the film, and impinges on the sample, perpendicular to its upper surface. As in LAT geometry, the incident beam is collimated to a maximum of 4 mm × 4 mm. LABRT is used to access information about the microstructure of the upper regions of the sample. Penetration depths can be calculated according to equations (3.1 – 3.2), and are typically within 1 μm – 10 μm of the sample surface.

3.2.1.4 Back Reflection Section Topography

Back Reflection Section Topography (BRST) is similar to LABRT except, like transmission section topography the beam is collimated into a narrow ribbon by a secondary slit, which is positioned between the main slits and the sample. A schematic of the BRST topography is shown in Figure 3.1(d).

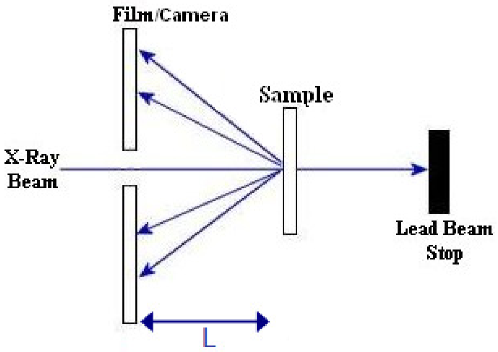

Figure 3.1(c): Large Area Back Reflection Topography. L is the sample to film distance.

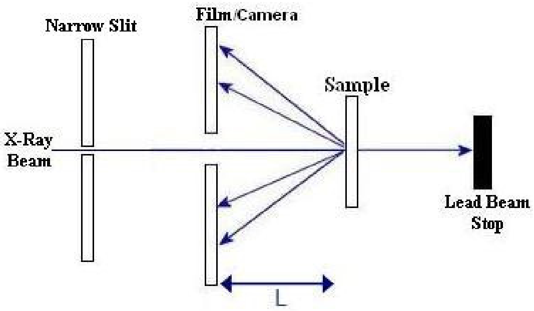

Figure 3.1(d): Back Reflection Section Topography. L is the sample to film distance.

3.2.2 Synchrotron Sources

Several synchrotron radiation sources are available for topography studies in Europe. The synchrotron sources used for this project were based at ANKA, Karlsruhe, Germany and HASYLAB-DESY, Hamburg, Germany. Both synchrotron sources have a similar beamline configuration, as described in Figure 3.2. The operation of a synchrotron source involves three main parts – a pre-accelerator, a booster synchrotron, and a storage ring. High energy electrons or positrons are generated by an electron gun (radioactive positron source) and accelerated to near the speed of light by a linear accelerator. For the sake of this discussion we will assume that the relativistic charged particles are electrons. The electrons are then transferred to a booster synchrotron, where their energy is increased. They are then circulated around an ultra-high vacuum storage ring, which contains a series of bending magnets. As the electrons pass through the magnetic field created by the magnets, electromagnetic radiation is created in accordance with relativistic electrodynamics [46, 47]. The straight sections of the ring contain insertion devices. These can be wigglers, or undulators, or a combination of the two.

Wigglers consist of a pair of arrays of bending magnets positioned perpendicular to the direction of motion of the electrons. The electron beam is periodically deflected by the alternating magnetic field, causing the electrons to wiggle or undulate about their nominal central position and thus radiate. The separation gap between the two arrays of magnets determines the magnetic field strength. By adjusting this gap, wigglers can be used to control certain properties of the radiation such as intensity and wavelength. Undulators are similar to wigglers in that they cause small electron or positron deflections; however the undulation of the particles is much weaker than in the case of a wiggler. This results in a longer pulse of light rather than a series of short bursts and enables high flux and brightness levels to be achieved.

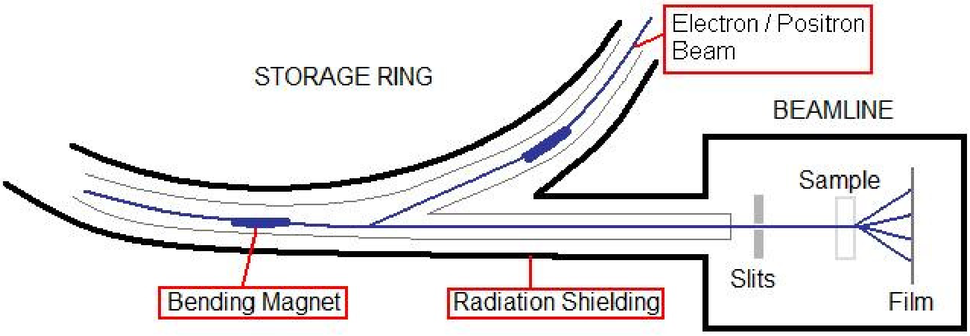

Figure 3.2: Topography Beamline at Synchrotron Radiation Facility [4].

The use of a synchrotron x-ray source enables excellent resolution topographs to be obtained. The maximum geometric resolution achievable for an image from a synchrotron source is dependent on the length of the beam line and the effective source size. The low divergence of the synchrotron beam is typically ≈ 10^{-4} rads in the vertical plane and ≈ 10^{-3} rads in the horizontal plane and the high intensity of the beam enables a high degree of spatial resolution to be achieved.

Smaller source sizes and longer beam lines lead to small angles subtended by the source at points in the specimen, and are preferable in order to obtain the best image resolutions [3, 7].

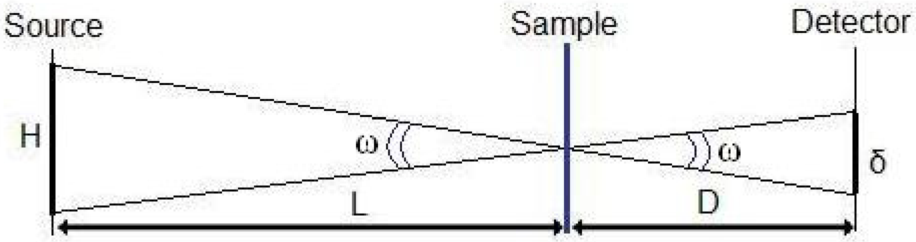

Figure 3.3: Schematic diagram showing the geometrical resolution set by the projected source height normal to the incident plane.

The geometric resolution, δ can be calculated from:

$$\frac{H}{L} = \frac{\delta}{D} \qquad (3.1)$$

where D is the sample to detector (film) distance, L is the source to sample distance, ω is the divergence of the beam received by the sample, and H is the size of the source (Figure 3.3).

$$\Rightarrow \delta = \frac{DH}{L} = \omega D \tag{3.2}$$

3.2.2.1 DESY

SXRT measurements were performed at HASYLAB-DESY, Hamburg, Germany (Hamburger Synchrotronstrahlungslabor am Deutschen Elektronen-Synchrotron), using the F-1 topography beamline at the DORIS III storage ring. The DORIS III ring operates at a positron energy of 4.450 GeV and typical beam currents of 80 – 150 mA, with a stored current lifetime of 10 – 18 hours [8]. The main parameters of the system are listed in the table below (Figure 3.4) [8]. For a typical sample to film distance of 80 mm, and the larger (horizontal) value for the source size, the geometrical resolution can be calculated from (3.2) to be ≈2.8 μm.

Parameter	Value
Circumference	289 m
Source – Sample Distance	35 m
Source Size	1.224 mm x 0.510 μm
Beam Divergence (horizontal)	0.4 mrad
Beam Divergence (vertical)	0.238 mrad

Figure 3.4: Main Parameters of the Synchrotron at DESY [8].

Figure 3.5 shows the setup for LABR topography imaging at DESY. In order to obtain LABR topographs the x-ray film is positioned between the incoming x-ray beam and the film holder. All images recorded at DESY were on high resolution *Slavich Geola VRP-M* Holographic Film, with a grain size of ~35 nm. The film holder has a hole of ~6 mm in diameter at the centre to allow the x-ray beam to pass through. X-rays pass through the back side of the film, and impinge on the sample, which is held at 0°. Samples were mounted on a sample holder, which is attached to dual high precision *Micos* LS-65 linear stages designed specifically for this study. This enabled movement of the sample in x and y directions with a step size down to 0.2 μm and unidirectional repeatability of 0.3 μm.

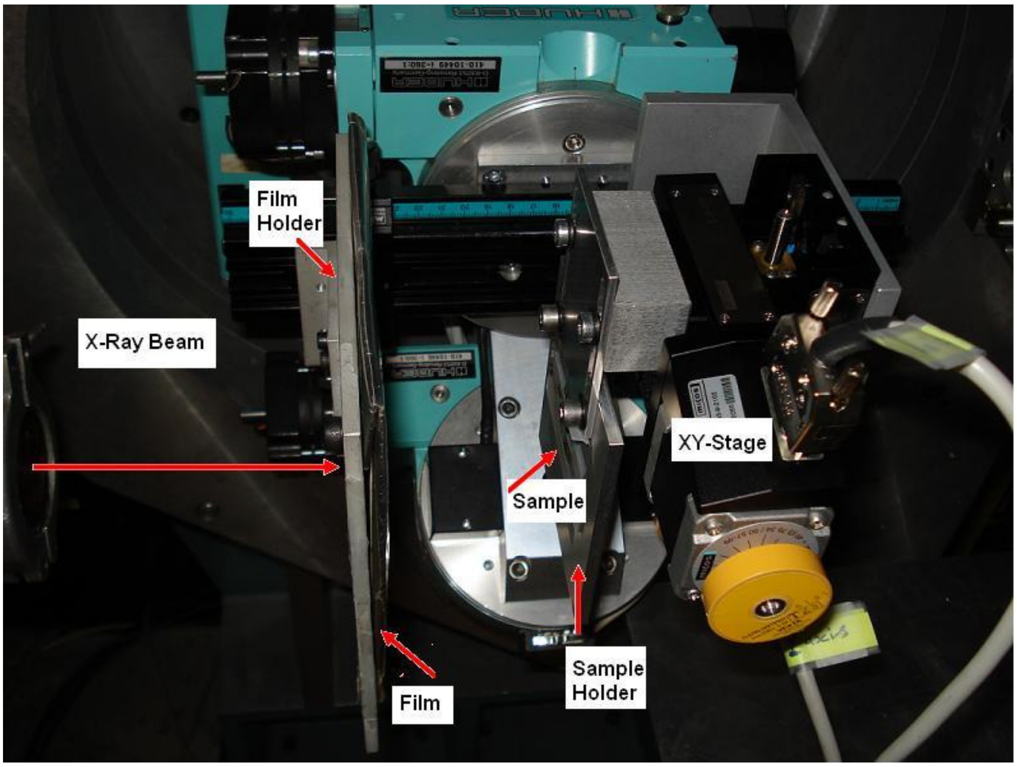

Figure 3.5: LABR Topography setup at DESY. Synchrotron X-Ray beam passes through the back of the film holder, and diffracts off the sample which is fixed to the sample holder. A Laue pattern of topographs is formed on the X-Ray Film.

3.3.2.2 ANKA

SXRT measurements were also performed at ANKA, Karlsruhe, Germany using the TopoTomo X-Ray Topography beamline. The ring operated at an electron energy of 2.5 GeV, with a typical beam current of 200 mA and a lifetime of around 20 hours. The main parameters of the system are listed in the table below (Figure 3.6) [9].

Parameter	Value
Circumference	110.4 m
Source – Sample Distance	30 m
Source Size	800 µm x 200 µm
Beam Divergence (horizontal)	2 mrad
Beam Divergence (vertical)	0.5 mrad

Figure 3.6: Main Parameters of the Synchrotron at ANKA [9].

There are two sets of slits at ANKA, one 6 m from the source, a secondary set 29 m from the source. The source size can be reduced down to a minimum of 5 µm x 5 µm by the first set of slits. A typical beam size for large area topography would be 4 mm x 4 mm, which would be controlled by the second set of slits. For a typical sample to film/camera distance of 80 mm, and the larger (horizontal) value for the source size, the maximum geometrical resolution can be calculated from (3.2) to be ≈2.1 μm.

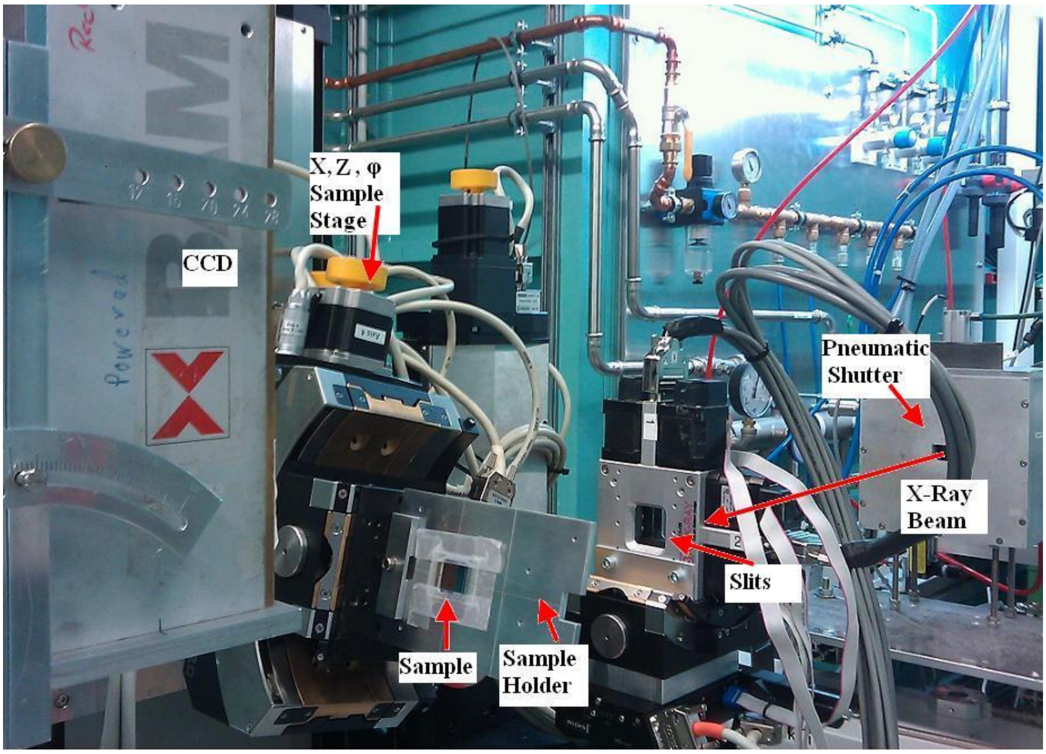

Figure 3.7(a): Image of the XRDI setup at ANKA showing the LAT geometry

Figure 3.7(a) shows the setup for ST topography imaging at ANKA. In order to obtain section topographs the X-rays are collimated into a narrow ribbon only 15 μm high using the second set of slits. The sample was mounted on a high precision goniometer capable of x-z translation movement and φ swivel movement. Utilising φ the sample was tilted to 12° to optimise the position of the 220 reflection (Figure 3.7(b)).

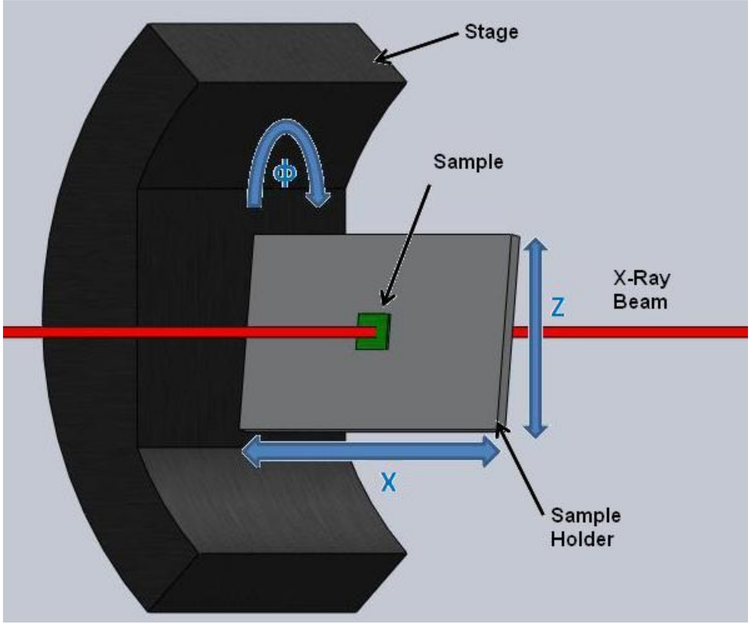

Figure 3.7(b): Schematic of stage and sample holder at ANKA showing x, z and φ axes.

Topographs collected at ANKA can be recorded on either high resolution film or using a CCD camera system. A pco.4000 14 bit cooled CCD camera system from PCO Imaging®, with a resolution of 4008 × 2672 pixels and pixel size of 9 μm × 9 μm was used in conjunction with a 300μm thick Ce doped $Lu_3Al_5O_{12}$ scintillating crystal for image acquisition at ANKA [10, 11]. The addition of 3.6x Rodenflex® "TV-Heliflex" magnification optics enabled an effective pixel size of 2.5 μm × 2.5 μm to be obtained. Where the CCD camera was used it was positioned approximately 16 cm from the sample to record only the 220 reflection from the Laue pattern of topographs.

3.3 3-Dimensional X-Ray Diffraction Imaging (3D-XRDI)

3D-XRDI is a high spatial resolution synchrotron based (<3 μm X-Y) diffraction imaging technique. 3D-XRDI provides an improvement over conventional XRDI in that it makes it easier to distinguish damage sites, identify stress / strain regions both above and below the surface, and gives a 3D analysis of defects in semiconductor wafers, most usefully when in kinematical diffraction mode. There are 4 key steps in the 3D-XRDI approach used in this study: XRDI image capture, XRDI image optimisation & registration, 3D rendering and 3D viewing. Image processing and analytical techniques (XRDI Image Optimisation, 3D rendering and 3D Viewing), and all post-rendering image enhancement, noise removal and analysis are performed utilising *ImageJ* software [21, 22].

Figure 3.8 below is a schematic of the 3D-XRDI image acquisition and processing steps. In the 3D processing steps (grey boxes) XRDI images are initially acquired via SXRT and imported into *ImageJ* as (tiff) stacks. The second step involves noise removal, stack registration and image cropping. Images are then rendered to form 3D representations, which can be viewed as volumes using the *3D Viewer*. There are numerous image processing options in *ImageJ*. For optimal visualisation of strain fields in 3D-XRDI all or some of the post-rendering image processing options, which are represented by the yellow boxes in the flow chart should be performed. Internal strain induced x-ray contrast fields can be viewed in the 3D model. The green boxes in the flow chart show the two options for internal strain field visualisation: - cutting away part of the 3D model, or rendering the stack as two parts.

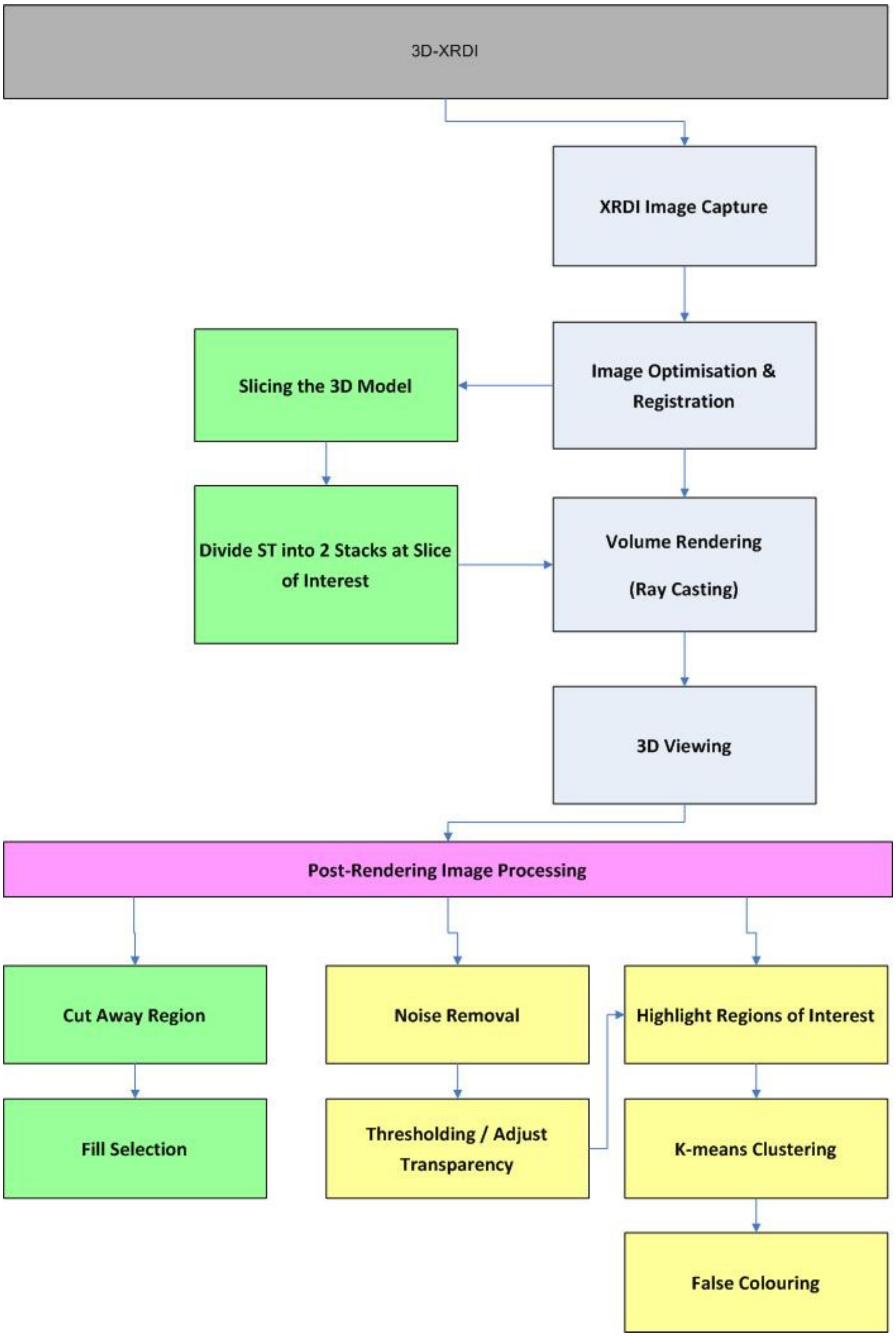

Figure 3.8: 3D-XRDI Image Acquisition and Processing Steps.

3.3.1 *ImageJ*

ImageJ, is a Java based image processing program written and developed by Wayne Rasband at the United States National Institutes of Health. *ImageJ* and its Java source code are freely available and in the public domain [21]. *ImageJ* can run on a number of platforms, either as an online applet or as a downloadable application. In addition to the sophisticated image editing and processing functionality available through its source code, *ImageJ* has extendable functionality via Java plugins. There are over 400+ plugins feely available online [23], which include advanced 3D volume reconstruction algorithms. *ImageJ* Version 1.44 for *Windows* operating system, bundled with 32-bit Java 1.6.0_20 [24] was used for this study. A number of plugins were added to supplement the basic functionality and expand 3D rendering capabilities. These included VolumeJ [25], StackReg[26], TurboReg [27], and K-*means clustering* [28].

3.3.2 3D Processing

3.3.2.1 XRDI Image Capture

3D-XRDI uses a stacked series of images obtained in the Transmission Section Topography (ST) geometry, [22]. These digital images were recorded at the ANKA Synchrotron, Karlsruhe, Germany using the TopoTomo X-Ray Topography beamline. Topographs were recorded using the *PCO.4000* high resolution 14 bit cooled CCD camera (Section 3.3.2.2). The setup for ST topography image capture at ANKA is shown in Figure 3.1(b) and described in Section 3.3.2.2. The sample to camera distance used was 60 – 85 mm, depending on the particular sample being examined. The sample was mounted on the goniometer, and aligned so that the region of interest was centred on the slits. The image acquisition time was optimised for a single ST topograph so as to capture the highest contrast image possible without saturating the image. Utilizing the z-translation the sample was stepped in 15 µm steps, from approximately 2 mm above the damage site to approximately 2 mm below the damage site, thus obtaining a series of ‘slices’ across the region of interest. A dark-field image was also captured at the beginning and end of the stepping sequence for later image normalisation.

3.3.2.2 XRDI Image Optimisation & Registration

The XRDI images obtained at the synchrotron were then loaded onto a desktop computer with a quad core processor and *ImageJ* open-source software installed [21]. Using the *Math* functionality in *ImageJ* the dark field images obtained at the synchrotron were subtracted from the topographs to remove any artefacts due to the scintillating crystal or ccd. Images were then stacked in sequence using the *images to stack* option. Images in the stack can be displaced from each other as a result of drift of the ccd sensor, and the stepping of the sample during image acquisition, the resultant 3-dimensional model from such a stack would be distorted, and not represent the true shape of the strain fields. Registration of the images prior to rendering is therefore essential. Two-dimensional image registration in *ImageJ* is supported by several plugins, which enable both manual and automatic registration. In the case of this study all image stacks were registered first using *StackReg [26]*, where registration of one or more images was inadequate, images were subsequently manually registered using *TurboReg [27]*.

XRDI ST topography images typically display cross sections across the entire sample. In order to focus on the region of interest, and reduce computational power needed, images were cropped to include only the damage site and surrounding strain fields using the *crop* function from the *ImageJ* menu.

3.3.2.3 Volume Rendering (Ray Casting)

The *ImageJ* 3D viewer is a plugin for *ImageJ*, which when combined with Java 3D and projection plugins enables image stacks to be rendered into a volume and viewed 3-dimensionally (Figure 3.9). Image stacks can be rendered using the *Projector* plugin [29] or by using the *volume reconstruction* plugin [30]. The projector plugin is utilized via the stacks/3D Project menus in *ImageJ*. The plugin offers three possible linear projection methods to render images: Nearest Point, Brightest Point or Mean Value projection. In the case of Nearest Point projection each pixel of a volume is projected onto a plane by a ray passing normal to the volume. The value of the nearest non-transparent point which the ray encounters is stored in the projection image [31]. *Brightest point* projection projects the brightest point encountered along each ray, while m*ean value* projects the average value of all transparent points encountered along a ray path. Interpolation can be applied by ticking the checkbox, and the volume can be rotated about x, y or z axes. In the case of 3D-XRDI the volume is rotated about the x or y axes and the slice spacing is input as the z-value. The *volume reconstructor* plugin performs the same function as the *projector* plugin while utilising trilinear interpolation algorithms [32]. Trilinear interpolation applies the weighted average of the nearest voxels to arrive at its final interpolated value. The z-spacing value (slice separation) is input as the *aspect-z* value in the *Volume Reconstructor* popup window.

In order to accurately construct a 3D image of the XRDI slices the distance between each successive ST topograph must be known, as well as the µm / pixel ratio. If accurate image dimensions are known, the *analyse/tools/scale* bar option in *ImageJ* allows the µm / pixel ratio to be calculated. The z-spacing can then be calculated according to the relationship below:

$$StepSize(\mu m) \Big/ \text{Im}ageScale\left({}^{\mu m}\!\!/_{pixel} \right) = \text{Z spacing} \qquad (3.3)$$

Although either of the volume rendering techniques described above may be used for volume rendering of XRDI, the method should be chosen carefully. The *projector* plugin is fast and memory efficient. However images can appear pixelated when interpolation is used. Where interpolation is not used both plugins gave similar results in the axial plane, however in the case of the *projector* plugin gaps can appear between neighbouring slices when the 3D volume is viewed from certain angles. When the resolution of the data set is low, tri-linear interpolation produces better quality 3D images. XRDI images can appear blurred, and thus the volume reconstruction plugin was used to generate the 3D images used in this study.

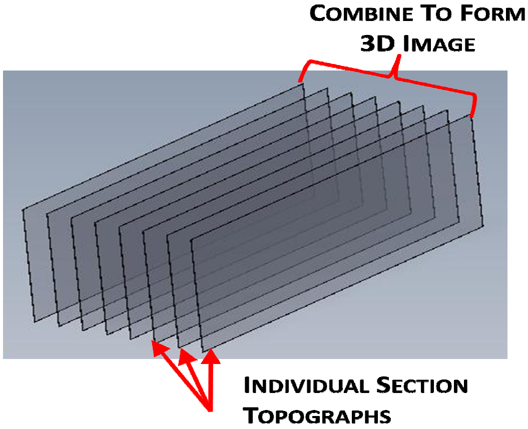

Figure 3.9: Series of Section Topographs (ST) which are rendered together to form 3D XRDI.

3.3.2.4 3D Viewing

The *ImageJ 3D Viewer* plugin enables stacks to be shown as volume visualisations in 3D XYZ-space. After rendering the hypervolume can be opened using the *3D Viewer* (*Plugins/3D Viewer*), and visualised in 3D. In the *3D Viewer* options *Color* should be set to *None* to use the default colour of the stack. The *resampling factor* is the factor by which the stack is resampled before it is rendered, this was set to two for all images rendered in this study. All other boxes should be left at their default values.

3.3.3 Post-Rendering Image Processing

Post-rendering 3D image quality can be enhanced by techniques such as noise removal, simple thresholding and transparency adjustments. Segmentation can also be performed via k-means clustering, and a variety of look up tables (LUT) can be applied to further enhance specific image features. Grey scale images can be segmented to separate features of interest from the background, and remove extraneous noise and image artefacts. The threshold slider sets the limit below which pixel values are set to black. Transparency of the 3D Volume can then be tuned so as to further remove noise, and enhance regions of interest. In an 8-bit greyscale image the transparency of each pixel is represented by a value between 0 and 1, with 0 as completely opaque, and 1 completely transparent. When used together thresholding and transparency are valuable tools in 3D-XRDI analysis as they enable uniform, outer layers (i.e. bare Si), to be stripped away and inner structures including highly strained regions, and defects to be highlighted. Figures 3.10 (a) and 3.10 (b) below show 3D-XRDI images with (a) no image processing applied (b) thresholding and transparency applied.

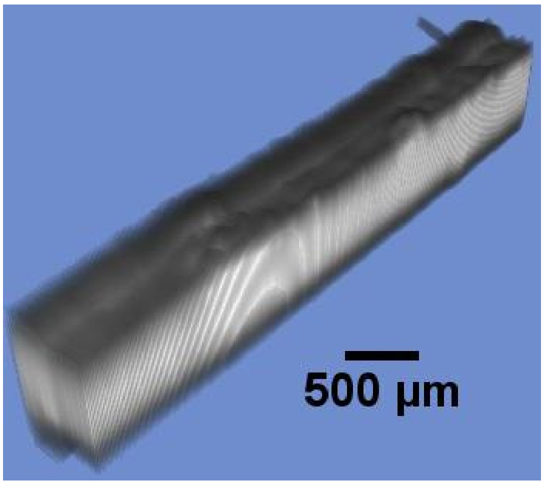

Figure 3.10 (a): 3D-XRDI 'raw' image showing Si sample damaged by arcing. Image was rendered using *volume reconstruction* plugin.

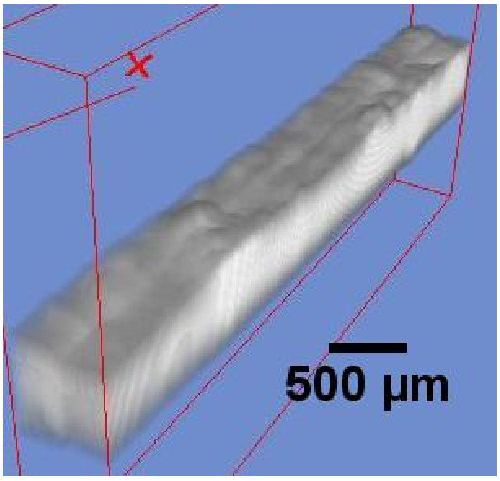

Figure 3.10 (b): 3D-XRDI image (Figure 3.10 (a)) after thresholding and transparency adjustments.

The black and white nature of the XRDI images and the subtle differences in grey levels make it difficult for the eye to distinguish changes in grey scale and the corresponding changes in strain field intensity. A K-means clustering can be used to separate the differences in strain field intensity, and enhance the analysis process. K-means clustering is available as a plugin at: http://www.ohloh.net/p/ij-plugins. A cluster is a region in which the density of objects is locally higher than in other regions. K-means clustering is a form of image segmentation where the number of clusters is initially decided by the user (K value).

The algorithm (Appendix A) initially selects K data points randomly. The remaining data points are assigned to one of the K clusters. The centroid of each of the K clusters then becomes the new mean and the steps are repeated until convergence is reached [29]. A false colour image is made from several grey scale images where each pixel value is mapped to a colour, according to the LUTs or function used, while restoring the default identity function. This ensures that grey values are modified so as to maintain the colour scaling of the input image. Over 100 LUTs are available in *ImageJ*, and they can be applied to greyscale images to highlight areas of interest or visualise regions of enhanced strain contrast. Figures 3.11(a)-(c) below show images with K-means clustering, and Spectrum and HiLo LUTs applied. Figure 3.11 (a) demonstrates K-means clustering applied to the Si arcing damaged sample in Figures 3.10 (a) & (b). The white regions correspond to areas where the strain field is the greatest, and the dark regions exhibit the least strain. Similarly, in Figures 3.11 (b) and (c) the regions of highest strain are indicated by the red and black areas, respectively. A plot of the active image's LUT, describing the colour that is displayed for the range of pixel values 0 – 255 can be obtained by accessing the menu command *Image/Color/Show LUT.* It can be useful to display the LUT plot, as in Figure 3.11(b), to relate specific colours to strain levels for a given image.

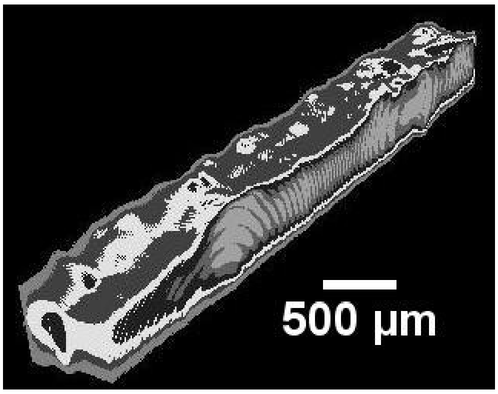

Figure 3.11(a): 3D-XRDI image of arcing damaged sample with K-means clustering applied.

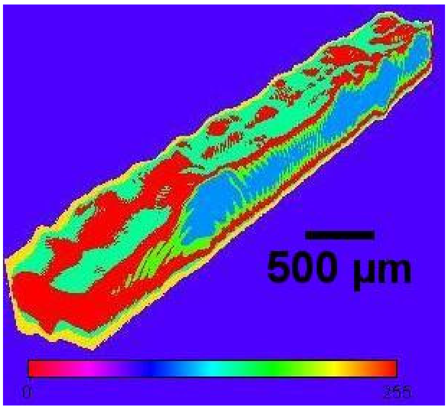

Figure 3.11(b): 3D-XRDI image of arcing damaged sample with Spectrum LUT applied after K-means clustering.

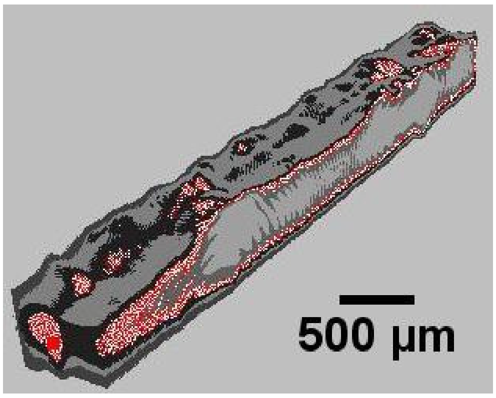

Figure 3.11(c): 3D-XRDI image of arcing damaged sample with HiLo LUT applied after K-means clustering.

3.3.4 Slicing the 3D model

The 3D-XRDI images can themselves be individually sectioned along any plane of choice in order to see detail of the internal damage, while continuing to preserve the 3D data. After image processing and registration steps the stack of images is separated into two stacks, with the ST topographs at the plane of interest at the end of the first stack and beginning of the last stack, respectively. Volume rendering, 3D viewing and subsequent image processing steps can then be performed on each stack, and the 3D volumes oriented in space so the planes of interest are visible.

Where the feature or area of interest does not lie in the plane of one of the original ST topographs 3D volumes can be sliced post-rendering. The volume is first positioned so as to orient the side of the face to be removed towards the user. The selection tool in *ImageJ* is then used to select the region that is to be cut away (discarded). Using the *Edit/Fill Selection* commands the volume is cut by removing any part of the volume which is within the selected region. The volume can then be oriented so as to view the feature/area of interest (Figure 3.12(a)) and K-means clustering applied to highlight regions of interest (Figure 3.12(b)).

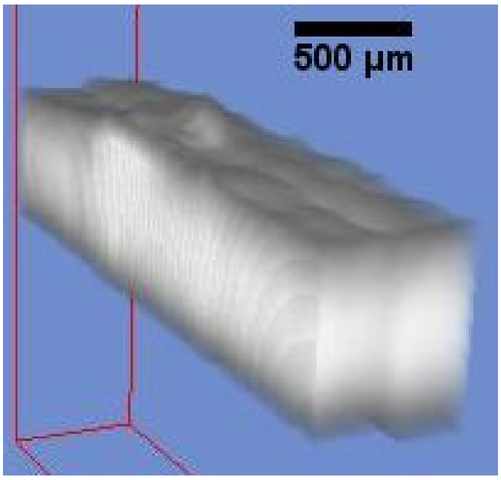

Figure 3.12(a): The arcing damaged sample from the side view after a region has been removed using the rectangular selection tool.

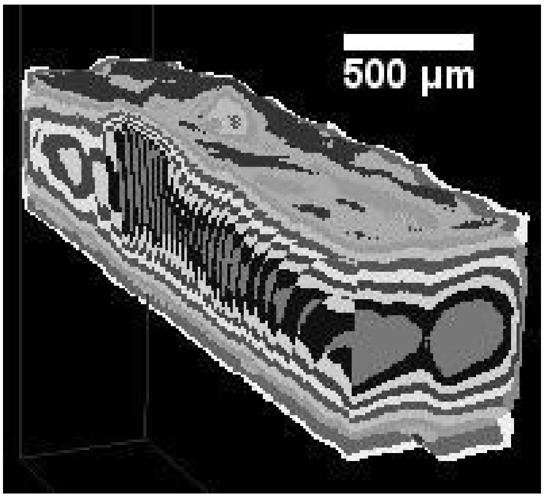

Figure 3.12(b): The arcing damaged sample from the side view after a region has been removed using the rectangular selection tool and K-means clustering has been applied.

3.4 3-Dimensional Surface Modelling (3DSM)

3-Dimensional Surface Modelling (3DSM) is a modelling technique which uses the high resolution (~3 µm) strain imaging capabilities of XRDI, combined with the advanced freeform modelling capabilities of *SolidWorks®* to build 3-dimensional profiles of crystalline misorientation across completely packaged chips. *SolidWorks®* is a 3D, parametric, solid modelling program. It enables the creation of free-form surfaces by the definition of an array of points on the surface. The position of the points can be optimised using algorithms available through the *SolidWorks®* user interface or through plug-ins which are freely available online. *SolidWorks®* can then fit a surface to these points using a number of proprietary algorithms. The XRDI/CAD based 3DSM process includes four main phases: XRDI image capture, importing XRDI into *SolidWorks®*, creating B-spline curves and constructing the 3D surface model (Figure 3.13).

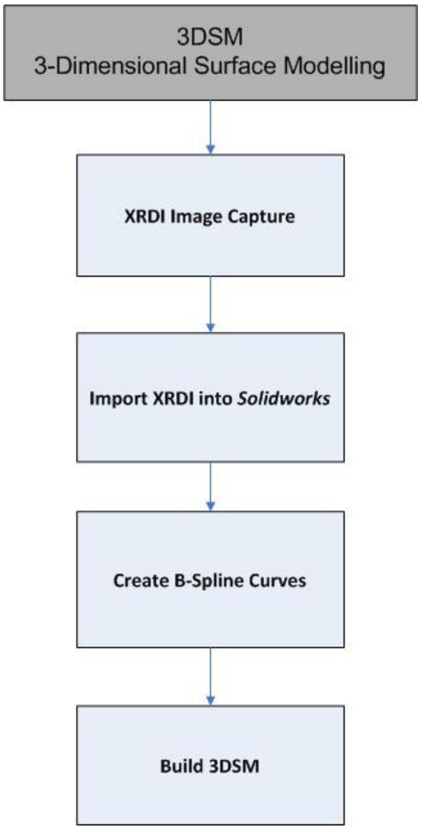

Figure 3.13: Process flow of 3DSM technique.

3.4.1 XRDI Image Capture

The X-Ray Difraction Imaging (XRDI) measurements were performed at ANKA, Karlsruhe, Germany using the TopoTomo beamline [2]. In order to apply the 3DSM technique the topographs were recorded in section transmission (ST) geometry. The experimental setup is described in Section 3.2. Briefly, the topographs were again recorded using the PCO.4000 high resolution 14 bit cooled CCD camera, with magnification optics, which enabled a pixel size of 2.5 µm to be obtained [9]. The sample to camera distance, L, was 80 mm. In order to obtain section topographs the X-rays are collimated into a narrow ribbon only 15 µm high. The CCD camera was positioned to record the 220 reflection from the Laue diffraction pattern of topographs. The sample was mounted on a high precision xy stage which enabled the user to step across the sample and thus obtain a series of section topographs across the packaged chip. ST topographs were taken at 1.0 mm steps from the pads at the top of the chip stepping sequentially until the bottom of the chip, was reached. The chip was then rotated at 90° and the process repeated; this enabled a grid of ST topographs, as illustrated in Figure 3.14(a), to be obtained.

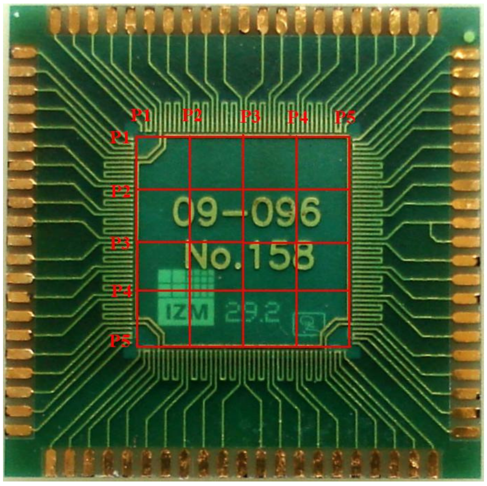

Figure 3.14(a): QFN-A package. Red lines show the approximate positions where ST topographs where obtained.

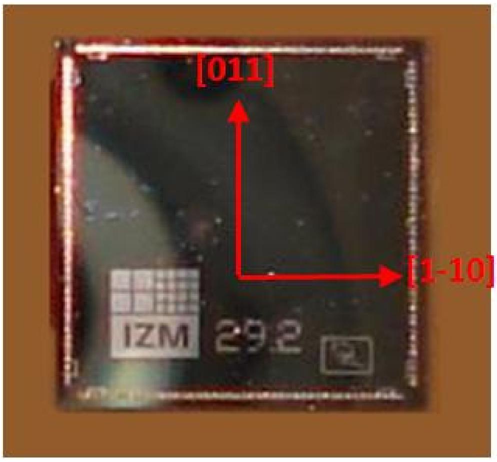

Figure 3.14(b): Unpackaged chip from QFN-A package. Red arrows show the [011] and [1-10] crystal directions.

ST topographs represent reflections from the [2 2 0] planes of Si. As topographs are obtained with the chip at 0° (horizontal ST topographs) and rotated 90° (vertical ST topographs), assuming the crystal axes as in Figure 3.14(b), reflections arise from either the (2 2 0)/(-2 2 0) or (2 -2 0)/(-2 -2 0) planes respectively.

3.4.2 Importing XRDI into *SolidWorks®*

The original ST topograph images were scaled and cropped so that the topograph filled the complete frame. A set of 4 sketch planes parallel to a reference plane (right plane) were created in *SolidWorks®*. Each sketch plane was positioned so that the distance between adjacent sketch planes was proportional to the distance between two corresponding ST topographs. Horizontal ST topographs were imported into *SolidWorks®* and positioned on the corresponding sketch planes so as to be centred with respect to the perpendicular front and side planes (Figure 3.15). The above process was then repeated in a new *SolidWorks®* file using the vertical ST topographs from the same chip rotated at 90^0.

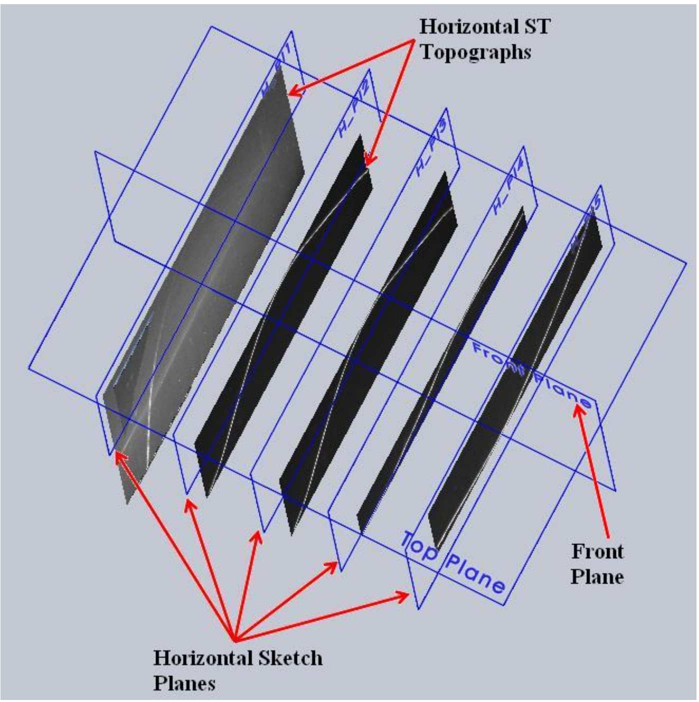

Figure 3.15: Construction of 3DSM showing 5 horizontal sketch planes with ST topographs intersected by front and top planes.

3.4.3 Creating B-spline curves

The next step in the modelling process was to create splines in *SolidWorks®*. *SolidWorks®* uses B-spline curves to define high resolution curves. B-spline curves are extended versions of Bezier curves, with each B-spline consisting of a number of Bezier curve segments. They use parametric modelling and are preferable to polynomial models due to their small size, automatic detail resolution and scalability [30]. B-spline curves are made up of an arbitrary number of control points which provide a basis for the contour to approximate. The mathematics behind B-spline curves are complex, and beyond the scope of this thesis [31, 32, 33], however the use of B-spline curves is relatively straightforward, and is further simplified by 3D parametric CAD software packages such as *SolidWorks®*.

In order to model the shape of the imported ST topographs the contours of the topographs were followed by positioning points along the exterior contours and using the point option of the spline mode in *SolidWorks®*. B-spline curves were filled to the points using the curve fitting technique, which utilises the least square fitting method. The B-spline curve was then adjusted further so as to fit the contours of the topograph more closely. This was carried out by adjusting the handles which control the tangent vectors at the spline points (Figure 3.16).

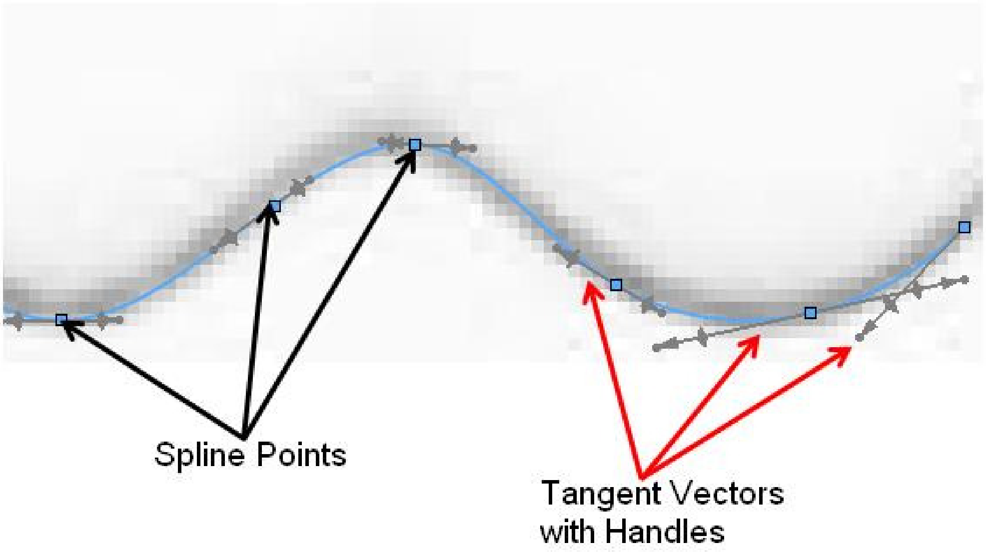

Figure 3.16: ST Topograph (black line) with b-spline curve fitted to the contour (blue line). Points which form spline and handles which control tangent vectors are indicated by black and red arrows respectively.

B-spline curves were created for each of the 5 horizontal and 5 vertical ST topographs. The imported topographs were then hidden, enabling a set of splines to be displayed as in Figure 3.17.

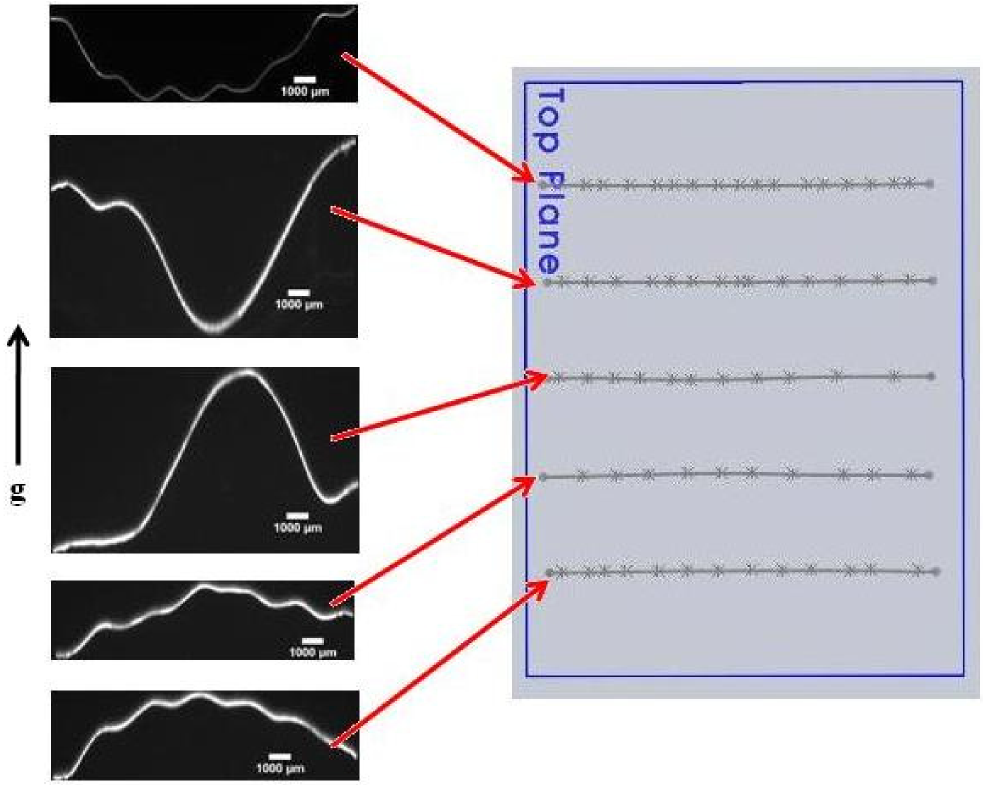

Figure 3.17: Horizontal topographs and corresponding horizontal B-Spline curves created in *SolidWorks®*.

3.4.4 Constructing the 3D Surface Model

The 3D surface model was created using the boundary surface feature in *SolidWorks®*. The boundary surface feature creates a solid surface model by connecting the splines created in the previous step. The splines were selected in sequence, from the P1 horizontal spline to the P5 horizontal spline, ensuring the same ends of the splines were selected to ensure surface continuity. Figure 3.18(a) shows the boundary surface mesh across 5 horizontal splines; no tangency constraint, i.e. zero curvature is applied in order to give the closest possible fit of the surface to the splines. Figure 3.18(b) is the same surface with curvature combs visible in two directions, combs cross the spline at inflection points which enable the boundary curve formation to be visualised. The surface can also be created by lofting between splines, however boundary surfaces are generally considered of higher quality as the surface created is continuous in all directions.

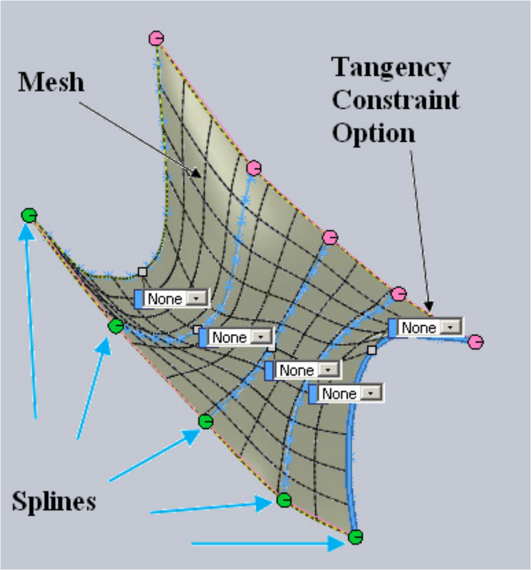

Figure 3.18(a): Boundary surface formation showing splines and mesh detail.

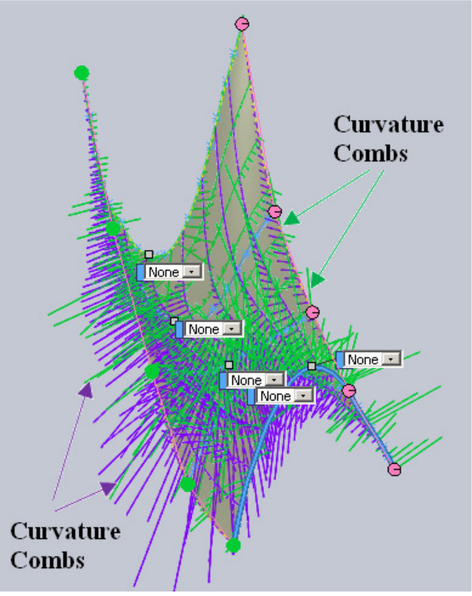

Figure 3.18(b): Boundary surface formation showing curvature combs.

SolidWorks® is a commercially available package, information is therefore not freely available on the algorithms used for surface modelling, however we know from their licensing [34], and other sources [35] that *SolidWorks®* primarily uses Parasolid. Computer Aided Three-dimensional Interactive Application (CATIA) based geometry and some 3D ACIS Modeler (ACIS) based geometry is also used by *SolidWorks®*, either explicitly as surfaces or as a component of applied features. All three of the above software kernels / suites use Non-Uniform Rational Basis Spline (NURBS) as the core surface representation [36, 37]. B-splines, which form part of NURBS curves, are straightforward to implement. As NURBS surfaces tend to have a large number of control points their implementation is more complex, and although *SolidWorks®* uses methods which simplify their complexity, in doing so it limits their capabilities. Further information on NURBS surfaces are given in [30-33].

3.5 Photoacoustic Microscopy (PAM)

The photothermal effect can be detected acoustically, optically, or thermally [38-40]. The cell used in this study was designed to detect the acoustic signal generated by the photothermal effect using gas condenser microphones. A photoacoustic microscope consists of five main elements: an excitation source, modulator, signal detector, signal processing and a display system. A low signal-to-noise ratio is inherent in all photoacoustic systems; in view of this the photoacoustic microscope must be designed to maximise the signal-to-noise ratio, and eliminate any superfluous noise caused by the mechanics / electronics of the system and its surroundings. The design of the current photoacoustic (PA) cell and system is based on Rosencwaig's principles [38]:

1. Acoustic isolation from the outside world.
2. Minimisation of extraneous photoacoustic signal arising from the interaction of the light beam with the walls, the windows, and the microphone in the cell.
3. Microphone configuration.
4. Means for maximising the acoustic signal within the cell.
5. The requirements set by the samples to be studied and the type of experiments to be performed.

3.5.1 PAM Schematic & Operation

Figure 3.19 shows a schematic of the photoacoustic microscope (PAM). The PAM can be divided into several sub-systems, each with specific functionality. The sub-systems include the cell and microphones, the light source and optics, the amplifiers, and lock-in amplifier and signal processing equipment including the computer.

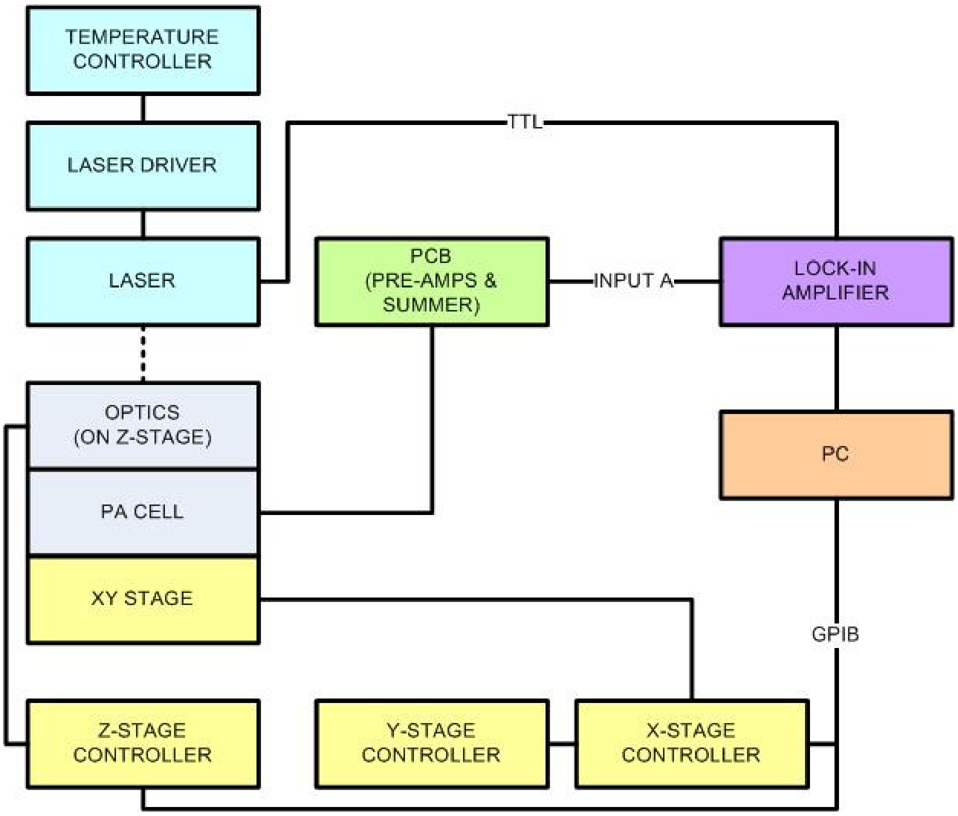

Figure 3.19: Schematic of Photoacoustic Microscope.

The sample is placed within the 15 mm diameter cell, which itself is mounted on a high precision *Micos VT-80 xy* stage having a minimum resolution of 5 µm and uni-directional repeatability of 0.5 µm. The laser and focussing optics are mounted directly above the cell window. The entire optical assembly is secured to a *Micos PLS-85* translation stage which allows movement in the +/- z-directions with a resolution of 0.5 µm and uni-directional repeatability of <0.1 µm, and thus allows optimum focussing of the laser on the sample. The 4 microphones in the cell are wired to 4 pre-amplifiers, which link to a summing circuit. The summer output goes directly to the input of the lock-in amplifier. The laser is controlled via the temperature controller and the laser diode driver. The output of the laser diode driver is linked to a TTL (transistor-transistor-logic) output via the lock-in amplifier. The entire photoacoustic system is mounted on an optical table with vibration isolation to isolate it from room vibrations.

The general operation of the photoacoustic microscope can be described by the process whereby light at 810 nm from the laser diode is focussed on the sample through the cell window. The laser is modulated via the TTL output of the lock-in amplifier. Light from the laser heats the sample and the resultant pressure variation in the surrounding air is detected by the microphones. The xy stage scans across the sample in a left-to-right, top-to-bottom raster pattern. The speed of the stage and the time constant of the lock-in amplifier, which are related to the resolution of the PAM image are user defined. The signal from the microphones is amplified, and then summed together in the pre-amp and summer printed circuit board (pcb). The signal is then input to the lock-in amplifier where it is detected, amplified and any out of band noise is removed. This increases the signal-to-noise ratio. Both the xy stage co-ordinates and the lock-in amplifier signal are transmitted via GPIB (General Purpose Interface Bus) and *LabVIEW®* software to the computer.

3.5.1.1 Cell & Microphones

The cell consists of a stainless steel body, which is highly polished to maximise the reflectivity. The light enters the cell through a *Spectrosil* ® (quartz) window. Spectrosil was chosen as it has a transmittance in excess of 99% for all incident light in the photon range 0.42 eV to 6.2 eV. The cell walls are relatively thick with respect to the size of the cell, and interfaces between the base plate and the cell, and the main chamber and the window are sealed by means of rubber o-rings to form a good acoustic barrier with the environment.

The volume of gas in the cell is a critical aspect of the PA cell design. For a solid sample, the PA signal in the cell is inversely proportional to the gas volume (equation 2.19). Therefore to increase the PA signal the volume of gas in the cell should be minimised. The layer of gas between the window and the solid forms a boundary layer, which acts as an acoustic piston, generating the signal within the PA cell. The thickness of the boundary layer must be greater than μ_g, the thermal diffusion length of the gas, in order for the signal to be produced [38-40, 48]. However the gas volume should not be too small as this could cause the signal to be dissipated through the cell walls and window before reaching the microphone.

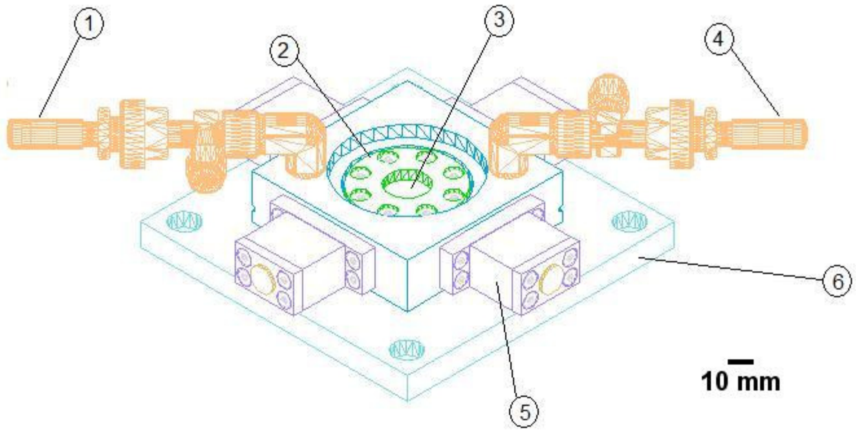

Figure 3.20: Photoacoustic Cell. 1 & 4, Gas inlet / outlet, 2, cell top plate, 3, spectrosil window, 5, microphone detector, 6, base plate.

The microphones used were 4 *Knowles* FG-3629 series electret microphones. The microphones are cylindrical in shape, which gives the advantage of a large surface area, and are designed so as to have a flat frequency response over a broad range 100 Hz – 10 kHz. This enables experiments to be undertaken at a range of modulation frequencies. In line with Rosencwaig's principles, the microphones were positioned at the end of long, narrow acoustic tubes within the cell so as to minimise the amount of scattered light, and hence background noise that could reach the microphone diaphragm. Figure 3.20 shows the microphone detector head. The detector head fits into the cell housing, and is held in place by screws. The PA signal travels to the microphone via a tunnel of diameter ~ 1 mm and enters via the small aperture (Figure 3.21 (1)), which is sealed with the cell housing by means of an o-ring. Further information relating to the signal-to-noise ratio (SNR) and noise analysis is given in Appendix B.

Studies show [41] that the signal-to-noise ratio can be improved by adding the signals from several microphones. Where several microphones are used, the signal increases with the number of microphones, used, whereas the noise from the microphones increases with the square root of the number. Four microphones are used in the current PA cell, however if an array of microphones were to be used, it should be possible to substantially increase the SNR ratio even further.

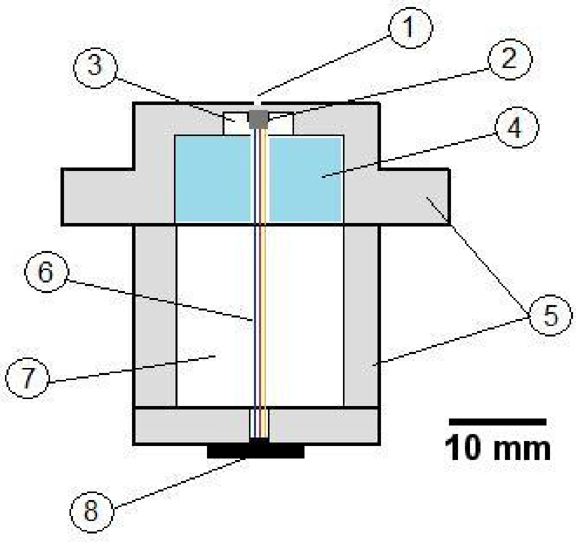

Figure 3.21: Microphone Detector Head.

1: entrance/exit aperture.
2: cylindrical microphone.
3: acrylic microphone holder.
4: hollow chamber, filled with blu-tac.
5: aluminium casings.
6: microphone wires.
7: empty chamber.
8: connector – to pre-amp.

3.5.1.2 Light Source & Optics

The excitation light source consisted of a *Spectra Physics* (model SFB100-810-D2-01) single emitter semiconductor laser diode of wavelength 810 nm and maximum output power of 1.2 W at a current of 1.5A. The laser is controlled by a temperature controller and laser driver. The laser driver is connected to the laser diode via a fiber optic, and the lock-in amplifier via a shielded cable and BNC connector.

An output beam from a laser diode is typically highly divergent. Collimating optics are therefore required to focus the beam to a small spot size. In addition to this, the beam profile should have an even intensity profile, ideally a Gaussian distribution. The design of the optics used in this PAM system is based on the use of a spatial filter. A spatial filter optimises the beam profile by removing the unwanted multiple-order energy peaks and passing only the central maximum of the diffraction pattern. The beam is first collimated by passing it through a lens with a low numerical aperture to ensure all the diffracted light is collected. It is then focussed through a pin hole to achieve a spot size of ~100 μm. The pin hole is positioned at the beam waist so as to allow only the central bright spot of the beam to pass. A second focussing and collimating lens further improves the beam profile, and reduces the spot size to enable focussing of a spot of ~50 μm diameter on the sample with an output power of ~ 1 W.

3.5.1.3 Amplifiers

A pre-amplifier is connected to the output of each of the four microphones (Figure 3.21, (8)). Each pre-amplifier consists of a low-noise operational amplifier chip connected to resistors and capacitors configured in an adjustable gain summing inverting amplifier mode (Appendix B). The op-amp used was a NE5534 chip with an input impedance of 100 kΩ.

For an inverting amplifier circuit, the gain,

$$A = {R_f}/{R_1} \tag{3.4}$$

where R_f is 100 kΩ (R2, Figure B2, Appendix B), and R1 is 1 kΩ (R1, Figure B2, Appendix B). A gain of 100 was therefore obtained for each one the pre-amplifiers connected to the microphones.

The signals from the four pre-amplifiers were summed together using a summing amplifier. The summing amplifier also used an operational amplifier chip in an inverting configuration, which enabled a gain of 100 to be achieved from the circuit. The gain could be adjusted using the potentiometer, which prevented the signal overloading at the lock-in amplifier. A circuit diagram of the summing circuit is given in Figure B3, Appendix B. The filtering is concentrated at the output of the summer.

$$f_c = {1}/{2\pi\tau} \tag{3.5}$$

where f_c is the frequency of the filter, and $\tau = RC$.

A 400 pF capacitor was used at the output, which drives a 10 MΩ load at the lock-in amplifier. This gives a high pass cut off at 40 Hz.

3.5.1.4 Lock-in Amplifier & Signal processing

The lock-in amplifier used in the PA setup is a *Stanford Instruments* SR830 DSP Lock-In Amplifier. The lock-in amplifier performs two major functions in the PA system:

- To act as an amplifier.
- To detect the very small (AC) microphone signal at a set frequency, from a noisy environment.

The lock-in amplifier consists of a phase sensitive detector with a very low pass filter. In the current PAM setup the lock-in amplifier modulates the output of the laser via its TTL output port. The port is linked to the internal oscillator of the lock-in amplifier, which outputs a square wave (Figure 3.19). The square wave is used as the reference signal of the lock-in amplifier, and is at the same frequency as the (unknown) input signal. The summer and pre-amp circuits are connected to the lock-in amplifier via signal input A (Figure 3.19), which acts as a single ended amplifier. A phase lock loop (PLL) in the lock-in amplifier locks the amplified input signal to the reference signal, and introduces a fixed phase shift. It then multiplies the signals using a phase-sensitive detector (PSD). The resultant signal is then passed through a low pass filter, which is very narrow band pass. The result is a DC output which is proportional to the amplitude of the input signal, without any noise superimposed on it. More information on the design and operation of lock-in amplifiers is available at [49, 50].

3.5.1.5 Data Acquisition

The phase and amplitude photoacoustic signals are simultaneously received by the lock-in amplifier, alongside the xy stage co-ordinates. The signals are reconstructed as amplitude and phase images by means of *LabVIEW®* code on the PC, which also controls the xy stage. A GPIB card interfaces between the hardware and the PC.

3.5.2 System Operation

The PAM system can be operated in microscope (scanning) mode, or by fixing the stage position and scanning the frequency. In the case of microscope mode the frequency is kept constant and the cell is moved in a raster pattern under the laser to enable an image of the sample to be obtained. The time constant of the lock-in amplifier and the velocity of the xy stage determine the image resolution and are user defined. In frequency scanning mode the stage position is kept stationary and the modulation frequency is scanned between limits which are user defined. Results are recorded for both amplitude and phase values and plotted using Origin 8 software.

3.6 Micro-Raman Spectroscopy

3.6.1 LabRam® HR800 System

The system used for this study is a Jobin-Yvon Horiba *LabRam® HR800* system with Labspec® 5 propriety software. It is an integrated Raman system with a microscope which is coupled confocally to an 800 mm focal length spectrometer. The sample is positioned on a high precision motorized XY(Z) table, which can be controlled by a joystick or directly by the software. A schematic of the Raman experimental setup is shown in Figure 3.22.

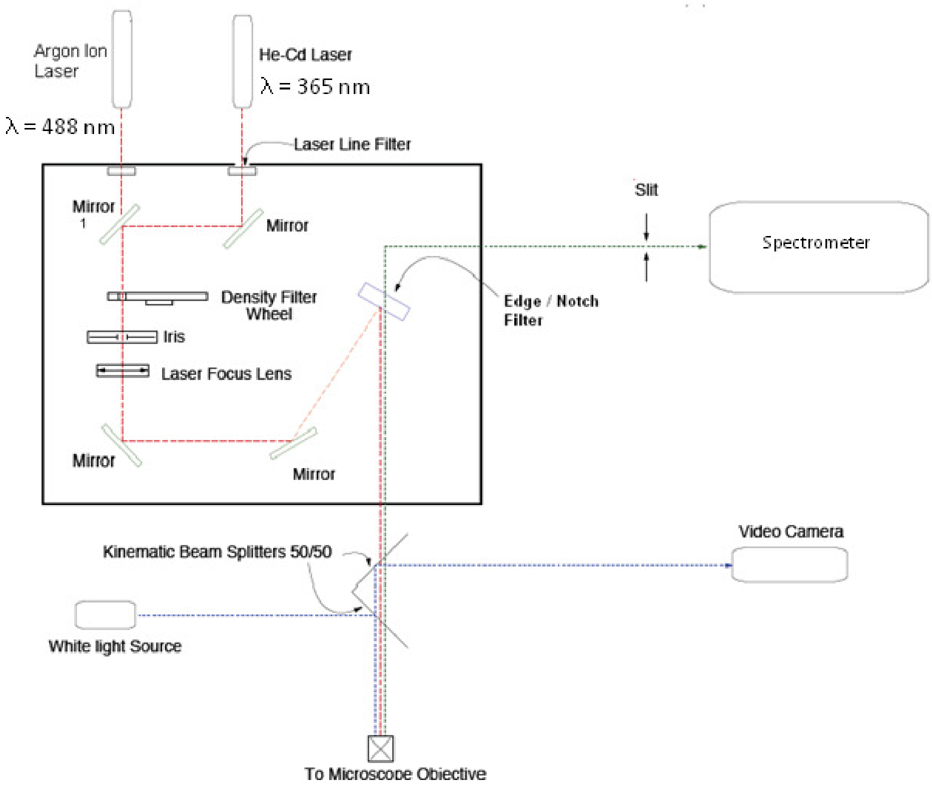

Figure 3.22: Schematic of Spectrometer System. Either Argon ion or HeCd laser can be selected, and Mirror 1 and Edge / Notch filter adjusted appropriately.

The spectrometer used is a dispersive spectrometer, 800 mm long. A diffraction grating enables splitting of the Raman signal into its individual wavelengths. The dispersed beam is then directed for detection by a liquid nitrogen cooled CCD detector as shown in Figure 3.23.

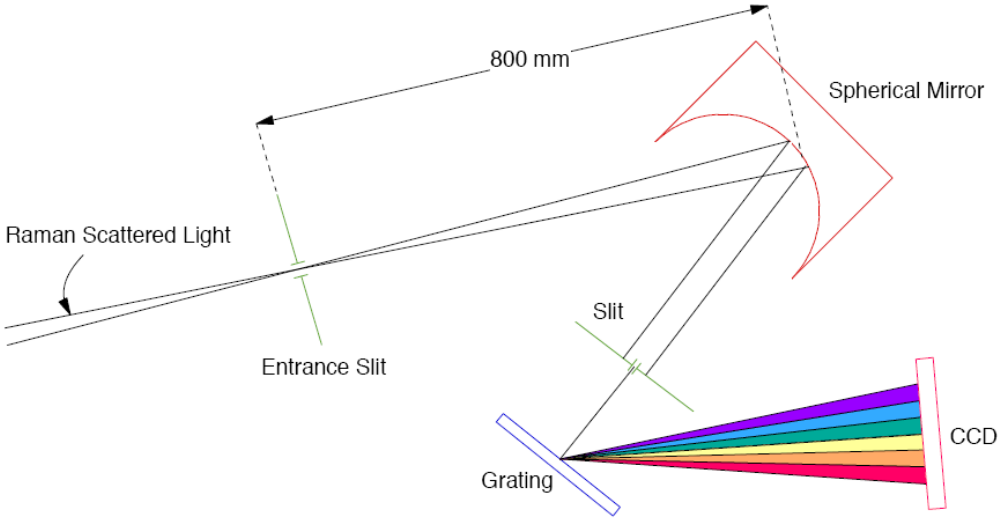

Figure 3.23: Raman Spectrograph Configuration.

The system is equipped with two lasers: a *Uniphase (model 2214)* Ar+ 488 nm air cooled laser, with an output power of 20 mW at 8A, and a 325 nm HeCd laser manufactured by *Kimmon Koha Co. Ltd*, with an output power of 22 mW [44]. Both lasers are mounted at the rear of the system, and light is reflected into the system via a periscope system. The 488 nm laser enables higher resolution and higher intensities than the 325 nm laser, as the shorter the excitation wavelength, the higher the dispersion required; also greater levels of stray light are introduced into the system with the 325 nm laser. However, the magnitude of the Raman peak shift is independent of the wavelength of excitation.

Laser Penetration Depth

Laser penetration depth can be varied by altering the wavelength of the excitation source. In the system used in these experiments two lasers were used in order to enable probing of the sample near the surface, and several hundred nm into the sample. The total intensity of the scattered light integrated from the surface of a sample to a depth d, is given by [43, 42]:

$$I_s = I_0 D \int_0^d e^{-2\alpha x} dx = \frac{I_0 D}{2\alpha}\left(1 - e^{-2\alpha d}\right) \qquad (3.6)$$

where I_0, D and α are the incident light intensity, the Raman scattering cross section and the absorption coefficient of the probed material at the wavelength of the laser source, respectively. The penetration depth, d_p can be defined as the depth which satisfies the relationship:

$$\frac{I_d}{I_s + I_d} = 0.1 \qquad (3.7)$$

where I_d is the total scattered light intensity integrated from d to infinity.

The penetration depth can therefore be defined as:

$$d_p = \frac{-\ln 0.1}{2\alpha} = \frac{2.3}{2\alpha} \qquad (3.8)$$

If α is taken as 1.225 x 10^6 cm^{-1} for Si at λ=325 nm and 20.61x10^3 cm^{-1} at λ=488 nm [43] the penetration depths can therefore be calculated as 9.33 nm and 556 nm for the 325 nm and 488 nm lasers, respectively.

A notch filter is used to pass a limited band which is centred on the wavelength of the laser being used, and to attenuate the background and secondary emissions which can interfere with the Raman spectra. The edge filter minimizes transmission below a given wavelength and maximizes transmission above it. A notch filter is used to filter the exciting line of the Ar^+ laser, and a holographic edge filter is used for filtering the exciting line of the HeCd laser. As the notch/edge filter is wavelength specific it must be manually swapped in / out according to the laser used.

Sampling is carried out through a high stability *BX 40* optical microscope with focus graduation of 1 µm and equipped with 10x, 50x, 100x objectives for use with the Ar^+ laser, and a 40x objective for use with the UV laser. The objective used to deliver the laser light affects the laser energy density, with the largest numerical aperture (NA) lenses giving the highest relative energy densities.

Minimum Laser Spot Size

The main system features which determine the laser spot size are the NA of the microscope objective and the laser beam quality factor (M^2). An ideal Raman system would have very high lateral spatial resolution, minimal depth of field and the highest possible laser energy density for a given laser power. If the laser beam quality is disregarded, the minimum spot size can be described by [51]:

$$d = \frac{1.22\lambda}{NA} \qquad (3.9)$$

where d is twice the Rayleigh criteria, the minimum resolvable detail required to spatially resolve the presence of identical size spots, and λ is the wavelength of the incident light. The objective used to deliver the laser light also affects the laser energy density. For the *LabRam® HR800* system used in these experiments, the measured peak energy density decreases by ~50% for the 50x objective when compared to the 100x objective.

The confocal Raman microscope design enables a very small sample area or volume to be analysed. Figure 3.24 is a schematic of the confocal focussing system. The laser beam is focussed onto the sample, and the returning beam is passed back into the system for analysis and deflection.

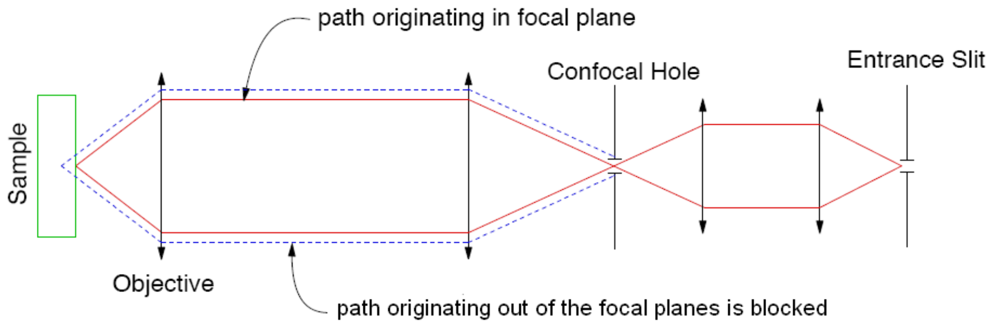

Figure 3.24: Micro-Raman confocal focussing system.

The microscope system also includes a confocal hole, which is adjustable between 0 and 1000 µm via the software interface, and scaled on the sample by a factor of 1.4x objective magnification. A black and white camera is used for the observation of the sample. Spectral resolution and coverage are directly proportional to the focal length of the focussing lens and the line density of the grating used. The *Labram HR800* system is equipped with 1800 l/mm, 3200 l/mm and 2400 l/mm gratings. The 3200 l/mm grating will disperse the spectrum almost 45 % more than the 1800 l/mm grating over the 800 mm length of the spectrograph, leading to the recording of higher resolution spectra.

3.6.2 System Calibration & Error Compensation

System calibration is of paramount importance if micro-Raman spectroscopy is to be used effectively to examine local mechanical stresses in silicon. In this study a number of calibration and correlation techniques were used to ensure the accuracy and repeatability of the Raman peak position measurement. These included allowing the system to stabilise before calibration, confirming the zero position of the spectrometer, calibrating to a known peak position and intensity on bare (undamaged) Si, and where possible cross correlating the results with the laser plasma peak to allow for temporal and thermal peak shifts.

Before commencing measurements the laser is switched on and allowed to stabilise, and the CCD is cooled using liquid nitrogen for at least an hour. The zero order position of the spectrograph is then set by allowing white light to scatter into the system, and with the spectrometer units set to nm, recording a spectrum. The position of the spectrum is then adjusted using the *Zero* parameter to be within +/- 1 pixel of 0. The smallest peak shift (equivalent to 1 pixel) that can be measured using the *Labram HR800* system is dependent on the laser and the grating used. In the case of the Ar^+ laser, which was used in conjunction with the 1800 l/mm grating a minimum peak shift of 0.02 Rcm^{-1} could be measured. The UV laser can be used with either the 2400 l/mm or 3200 l/mm grating, leading to a minimum peak shift measurement of 0.01 Rcm^{-1}. The laser shutter was then opened, and with the white light off and units set to cm^{-1}, the laser was focussed on the surface of a standard piece of (100) silicon. The system is then calibrated to the TO phonon mode Raman peak shift of 520.07 cm^{-1} by adjusting the *Koeff* value. Where possible the sample being studied was used to calibrate the system, ensuring that the position chosen was clean and far enough away from any damage or features and the sample edge so as not to be under strain. Spectra are then recorded for each sample, and fitted using a Gaussian-Lorentz function in order to accurately determine the peak positions. In addition to local stresses in the sample being measured, external factors such as temperature, laser stability and focus position can affect the Raman peak position. In order to compensate for these external influences plasma lines of the laser can be used for further calibration. Plasma lines are Rayleigh scattered and insensitive to stress in the material. Where spectra were recorded over long time periods (> 1 hour), the plasma filter was removed from the system. The position of a plasma line was monitored over the course of the experiment. For each point measured on the sample, shifts in the position of the plasma line were correlated against Raman peak shifts and any extraneous source of error removed. The focussing of the laser spot on the sample surface can lead to local heating of the sample. When thermal expansion occurs the Si TO phonon frequency typically shifts to lower energies with increasing temperature (~0.025 cm^{-1}/K) [45], suggesting tensile stress. Studies show that within the range of laser power used in this study the red shifts are less than the resolution of the spectrometer, and thus below the noise level of the system [45].

Summary

The development of three novel characterisation techniques for the non-destructive *in situ* identification and mapping of stresses, strains and deformations inside packaged chips, and bare Si wafers / die have been presented:

- 3-Dimensionsal X-Ray Diffraction Imaging (3D-XRDI): For high resolution 3-dimensional imaging of stresses and strains in Si wafers / die using a synchrotron source.

- 3-Dimensional Surface Mapping (3DSM): For high resolution 3-Dimensional mapping of strain fields and lattice misorientation in packaged die using a synchrotron source.
- Photoacoustic Spectroscopy (PAM): For non-destructive imaging of surface and sub-surface damage on Si wafers and die.

The advancements in XRDI / SXRT which were developed over the course of this project and enabled the development of 3D-XRDI and 3DSM have also been detailed. Micro-Raman spectroscopy is a well established technique for the quantification of strain in semiconductor materials. It is introduced here as a complementary analysis technique to the 3 above methods, and conventional XRDI.

References:

[1] A. Authier, *Dynamical Theory of X-Ray Diffraction*, pp. 546–549. Oxford Science Publications, 2001.

[2] K. Bowen, B. Tanner, X-*Ray Metrology in Semiconductor Manufacturing*, Taylor & Francis Group, 2006.

[3] T. Tuomi, *J. Synchrotron Rad.*, (2002). 9, 174-178.

[4] T. Tuomi, N. Naukkarinen, and P. Rabe, *Physica Status Solidi (a),* vol. **25**, pp. 93–106, 1974.

[5] K. Horan et al., *Materials Science and Engineering B*, 154-155 (2008) 118 – 121.

[6] J. Kanatharana et al., *Microelectronic Engineering*, **65** (2003) 209–221.

[7] *Applications of Synchrotron Radiation Techniques to Materials Science*, Materials Research Society, Vol 307, p213-247.

[8] http://hasylab.desy.de/facilities/doris_iii/beamlines/f1/specifications/index_eng.Html

[9] Jacqueline Heinrich, *ANKA Instrumentation Book,* October 1st, 2007.

[10] Danilewsky, A. N., Rack, A., Wittge, J., Weitkamp, T., Simon, R., Riesemeier, H., Baumbach, T., (2008), *Nuc. Instrum. Meth. Phys. Res. B*, **266**(9), 2035-2040.

[11] Nagornaya, L., Onyshchenko, G., Pirogov, E., Starzhinskiy, N., Tupitsyna, I., Ryzhikov, V. Galich, Y., Vostretsov, Y., Galkin, S., Voronkin, E. (2005). *Nuc. Instrum. Meth. Phys. Res. A,* **537**(1-2), 163-167.

[12] D. Noonan et al., *J. Mater. Sci.: Mater. Electron.* **10** (1999) 351–358.

[13] Kyoichi Haruta, *J. Appl. Phys.* **36** (1965) 1789–1790.

[14] A.R. Lang, *J. Appl. Phys*. **30** (1959) 11.

[15] W. Ludwig et al., *J. Appl. Cryst*. **34** (2001) 602–607.

[16] Seiji Kawado et al., *J. Synchrotron Radiat*. **11** (2004) 304–308.

[17] W. Ludwig et al., *Mater. Sci. Eng., A* **524** (2009) 69–76.

[18] V.V. Kvardakov et al., *Nucl. Instrum. Methods Phys. Res.* A **575** (2007) 140–143.

[19] Taihei Mukaide, Kentaro Kajiwara, Takashi Noma, Kazuhiro Takada, *J.Synchrotron Radiat.* 13 (2006) 484–488.

[20] R. Tanuma et al., *Phys. Status Solidi (a)* **204** (8) (2007) 2706–2713.

[21] Rasband, W.S., *ImageJ*, U.S. National Institutes of Health, Bethesda, Maryland, USA, http://*ImageJ*.nih.gov/ij/, 1997--2011.

[22] Abràmoff, M.D., Magalhães, P.J. and Ram, *Biophotonics International*, **11**(7):36--42, 2004.

[23] Tony J. Collins. *ImageJ for microscopy*, BioTechniques **43**:S25-S30 (July 2007).

[24] http://rsbweb.nih.gov/ij/download.html

[25] http://webscreen.ophth.uiowa.edu/bij/index.html

[26] http://bigwww.epfl.ch/thevenaz/stackreg/

[27] http://bigwww.epfl.ch/thevenaz/turboreg/

[28] http://www.nist.gov/lispix/imlab/flsclr/fcolor.html.

[29] Anil K. Jain, Richard C. Dubes, *Algorithms for Clustering Data*, Prentice Hall, 1988.

[30] Gerald Farin, Curves *and Surfaces for CAGD A Practical Guide*, 5th edition". p 431.

[31] Gerald E. Farin, *NURBS for Curve & Surface Design: From Projective Geometry to Practical Use*, A. K. Peters Ltd, (1999).

[32] D. Salomon, *Curves and Surfaces for Computer Graphics*, Springer (2005).

[33] David F. Rogers, *An Introduction to NURBS: With Historical Perspective (The Morgan Kaufmann Series in Computer Graphics*), Academic Press, (2000).

[34] *SolidWorks*® Student Edition 2010. Help/About.

[35] Guisheng Fang, Zengfang Li, *Development of a sketching CAD system based on Parasolid*, 9th International Conference on CAID/CD (2008).

[36] Siemens Parasolid XT Format Reference, Version 8.1, Rev. D. http://www.plm.automation.siemens.com/nl_nl/Images/JT_File_Format_Reference_Rev-D_tcm703-92072.pdf

[37] Manish O. *Freeform-Surface-Modelling-Using-NURBS*, Technical Seminar Report. Bangalore Institute of Technology, Mech. Dept., 2009-2010. http://www.scribd.com/doc/31529858/Freeform-Surface-Modelling-Using-NURBS-SEMINAR-REPORT

[38] Allan Rosencwaig, *Chemical Analysis*, **Vol 57**, Photoacoustics and Photoacoustic Spectroscopy. John Wiley & Sons, 1941.

[39] D. P. Almond and P. M. Patel, *Photothermal Science and Techniques*, Chapman & Hall, 1996.

[40] A. Mandelis, P. Hess, *Progress in Photothermal and Photoacoustic Science and Technology*, SPIE Press, 2000.

[41] I. Calasso and M. Sigrist, *Review of Scientific Instruments*, vol. **70**, no. 12, pp. 4569–4578, 1999.

[42] De Wolf, I. (1996), *Semiconductor Science and Technology*, **11** (2), pp.139-154.

[43] Takahashi J-I and Makino T., *J. Appl. Phys*. **63**, pp.87-91 (1988).

[44] HORIBA Jobin Yvon Ltd, *LabSpec v5 User Manual*.

[45] Kai F. Dombrowski, *Micro_Raman Investigation of Mechanical Stress in Si Device Structures and Phonons in SiGe,* p24, PhD Thesis (2000).

[46] Toshiyuki Shiozawa, *Classical Relativistic Electrodynamics: Theory of Light Emission and Application to Free Electron Lasers*", Chapters 2&3, Springer (2004).

[47] I. P. Grant, *Relativistic Quantum Theory of Atoms and Molecules: Theory and Computation,*(Springer Series on Atomic, Optical, and Plasma Physics, 2010.

[48] A. Rosencwaig, A. Gersho, *J Appl Phys*, **47**(1), 64 (1976).

[49] http://www.thinksrs.com/downloads/PDFs/Manuals/SR830m.pdf

[50] M. L. Meade, *Lock-in amplifiers principles and applications.* Trade paperback, Institute of Electrical & Electronic Engineer, 1983.

[51] S. Perkowitz, *Optical Characterization of semiconductors; Infrared, Raman and Photoluminescence Spectroscopy*, edited by N. H. March (Academic Press, London, 1993), p. 213.

Evaluation of Plasma Arc Induced Damage on Silicon Wafers using 3D-XRDI, Micro-Raman Spectroscopy, and PAM.

4.1 Introduction

Plasma etch and deposition processes such as Plasma-Enhanced Chemical Vapour Deposition, (PECVD), High Density Plasma-Enhanced Chemical Vapour Deposition, (HDPCVD), Reactive Ion Etch, (RIE) and anisotropic etching are widely used for device fabrication in high volume semiconductor manufacturing. Plasma charging damage, and in particular damage caused by wafer arcing is one of the important plasma process induced damage phenomena, and can take several forms including wafer edge sensitive structure induced wafer arcing, wafer arcing due to localised transient plasma instability, and plasma micro-arcing [1-5]. The resultant plasma arcing damage results in pits and non-uniformities on the wafer surface. Wafer arcing can lead to lost dies and yield reduction, as well as an escalation in the volume of particles on the wafer and increased operation costs [3]. Plasma damage due to arcing is predominantly observed in etch processes, with backend high RF power process with multiple underlying metal layers having the highest risk of wafer arcing [3]. Although the mechanisms for plasma arcing and microarcing have been studied widely, relatively few studies [6, 7] have been carried out on the type and extent of the physical damage caused by such arcing events.

Three samples were examined for this study: the first two samples are plasma arc damaged samples generated in a laboratory plasma chamber under slightly different process configurations; the third plasma damaged sample was obtained from industry, and is the result of an arcing event on the back side of a patterned Si wafer. Scanning Electron Microscopy (SEM), XRDI and PAM are initially used to locate and identify the arc damage sites. 3D-XRDI is presented here as a novel, non-destructive analysis tool in the characterisation of plasma arcing damage. Micro-Raman spectroscopy is used as a complementary analysis tool, and enables us to obtain a unique insight into the nature of damage caused by plasma arcing, and the levels of strain resulting from the damage. Further image analysis using *ImageJ* software and image processing algorithms is used to enhance the 3D-XRDI images and provide complementary information on the nature of the strain within the sample. This investigation demonstrates that the damage caused by wafer arcing can have a significant effect on wafer integrity and device structure and that 3D-XRDI has extensive capabilities for future non-destructive characterisation of process induced wafer damage.

4.2 Experiment

The plasma arcing damaged samples 1 and 2 were generated in the same plasma chamber with two slightly different process configurations. The plasma chamber consisted of a parallel plate design with the wafer on the grounded electrode, and was filled with Ar gas at approximately 3 mbar (2.25 torr). In the first of three damage regimes considered in this study the current drawn by the arc in the plasma was relatively high, ~200 mA, and resulted in a single damage site (Figure 4.1(a)). The second damage regime was caused by a low current of about 60 mA, and resulted in multiple arc damage sites (Figure 4.2(b)). The conditions for the third damage regime, (Figure 4.1(c)) are unknown, except that the arc was caused in an industrial plasma etch chamber.

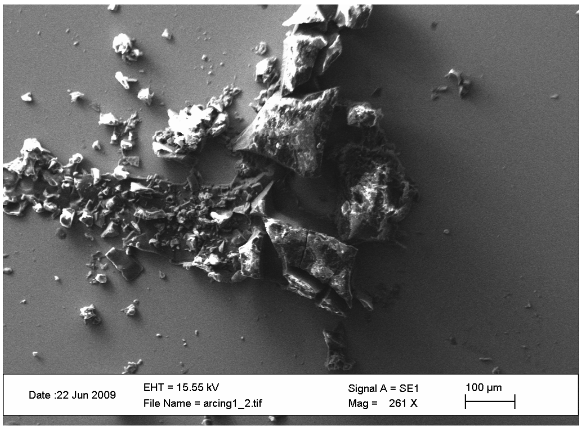

Figure 4.1(a): Scanning Electron Microscope (SEM) image of damage regime 1. Image shows an approximate 1000 µm × 800 µm area of arcing damage on Si substrate.

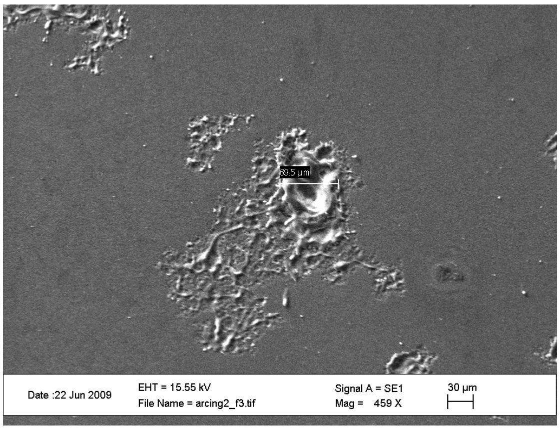

Figure 4.1(b): SEM image of damage regime 2. Image shows 100 µm – 250 µm islands of arcing damage on Si substrate. Note the difference in scale compared to Figure 4.1(a).

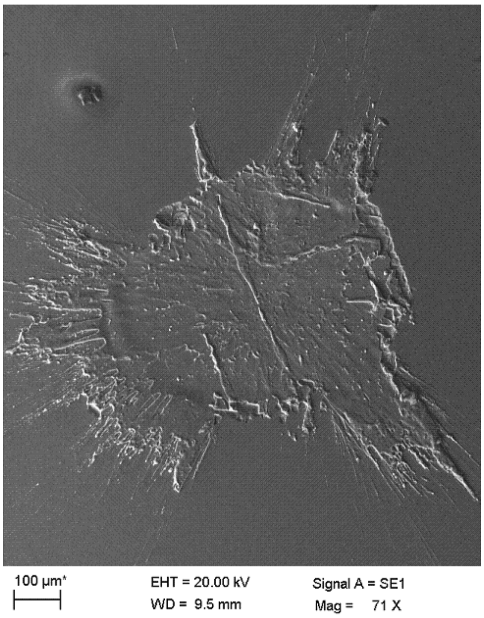

Figure 4.1(c): SEM image of damage regime 3. Image shows 850 µm × 750 µm area of arcing damage on back side of patterned Si wafer.

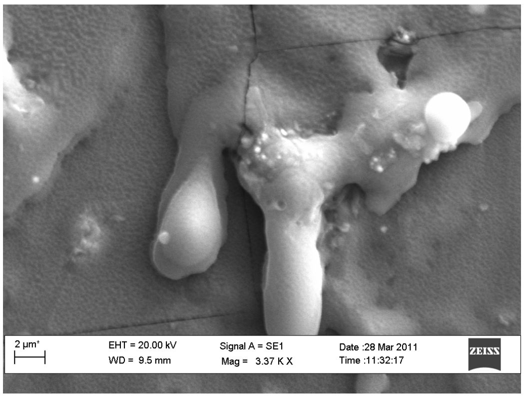

Figure 4.1(d): SEM image of damage regime 3. Image shows melting and cracks on arcing damaged region.

XRDI measurements were performed at HASYLAB-DESY, Hamburg, Germany using the F-1 topography beamline at the DORIS III storage ring, and at the ANKA Synchrotron, Karlsruhe, Germany using the TopoTomo X-Ray Topography beamline. In the case of the plasma arcing damage samples described in this section all topographs recorded on film were captured at the HASYLAB synchrotron and all topographs recorded on camera (CCD) were captured at the ANKA synchrotron. The HASYLAB topographs were recorded at high resolution using Slavich Geola VRP-M Holographic Film, with a grain size ~35 nm. The sample to the film distance, L = 80 mm, and a beam size of 2 mm × 2 mm was used. Images of the topographs were obtained from the original X-ray films using an imaging system comprising of a *Zeiss Axiotech* microscope equipped with a CCD camera, frame grabber, and image acquisition software. Images were recorded at room temperature for x100 and x50 magnifications. *LauePt* software [8] was used to simulate the Laue pattern for the geometry (Figure 4.2(a)). This enabled each reflection to be indexed and x-ray penetration depths to be calculated.

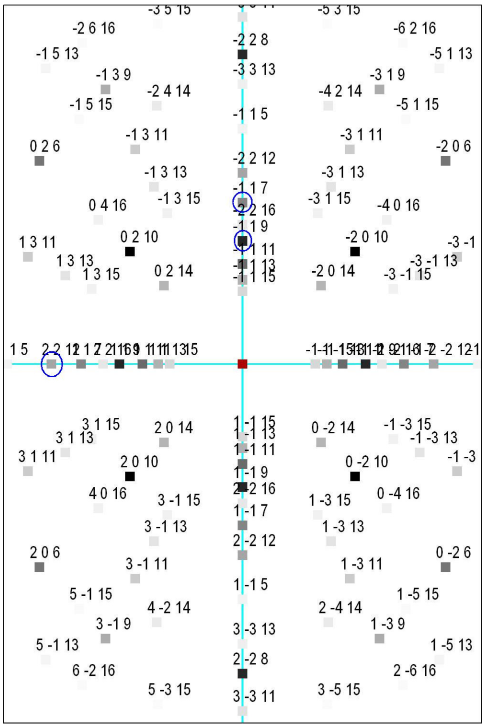

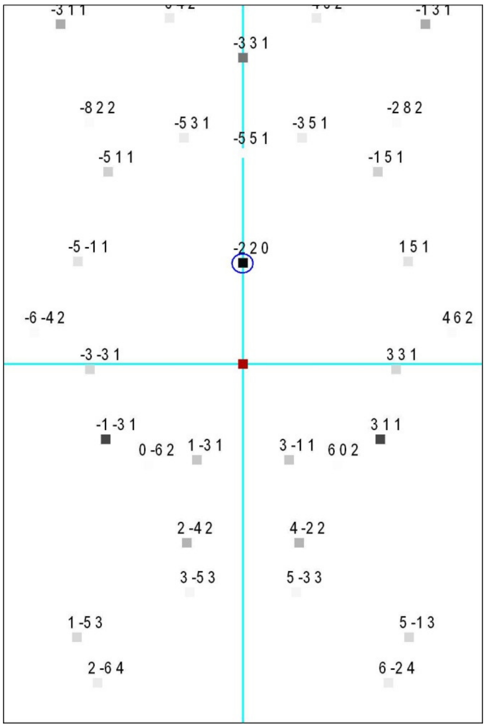

Figure 4.2(a): LABR Laue pattern for Si crystal with L=80 mm, θ=0°, spot size = 2 mm x 2 mm. Numbers show index of reflections. Laue pattern simulated using LauePt [8]. -1 1 7, -1 1 9 and 2 2 12 reflections are circled in blue.

Figure 4.2(b): LAT Laue pattern for Si crystal with L=80 mm, θ=12°, spot size = 2 mm x 2 mm. Numbers show index of reflection. Laue pattern simulated using LauePt [8]. 2 2 0 reflection is circled in blue.

3D-XRDI uses a stacked series of images obtained in the Transmission Section Topography (ST) geometry [9]. XRDI images for 3D rendering were recorded at the ANKA Synchrotron, using the CCD camera (section 3.2.2.2). A single reflection, the 2 2 0 reflection, was recorded using the CCD (Figure 4.2(b)). The sample was mounted on a high precision XY stage which enabled the user to step across the sample in ~15 μm steps and thus obtain a series of 'slices' across the damage site (Figure 4.3). In the example shown in Figure 4.3 the raw data consisted of a series of 17 ST images captured on the CCD. This stack of section topographs was then rendered into a 3D image using topographic algorithms from the *ImageJ* software suite [10, 11]. Regions of interest were highlighted using K-means clustering [12] and false colouring algorithms [12, 13]. The 3D image acquisition and processing steps are described in detail in Section 3.3.

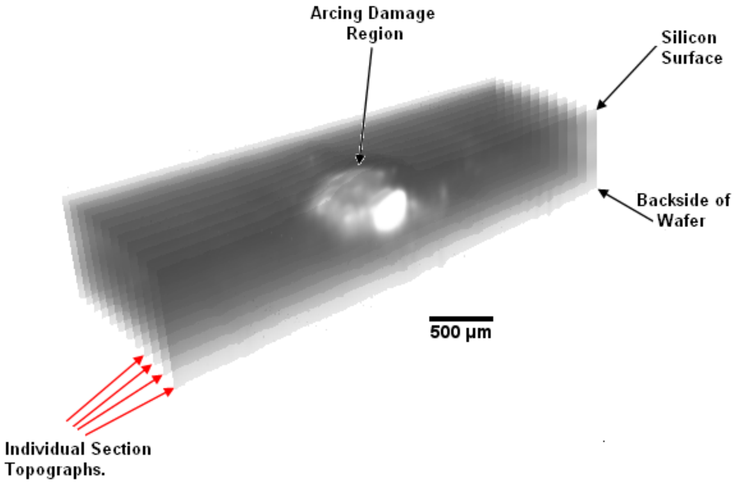

Figure 4.3: Series of Section Topographs (ST) which are rendered together to form 3D XRDI of damage regime 1. Changes in intensity and discontinuities at surface are a result of strain and related damage. Uniform grey area is bulk, unstrained Si.

The samples were also analysed by micro-Raman spectroscopy using both the 488 nm laser line of an argon ion (Ar^+) laser and the 325 nm laser line of a He-Cd UV laser on the JY Horiba *LabRAM HR800* High Resolution Raman Microscope. The system was equipped with a high precision X,Y(Z) motorized stage which enabled 2-dimensional (2D) scans of the damage sites to be obtained. Measurements were taken at 2.5 – 5 µm intervals, and results were cross correlated against a reference plasma peak to compensate for any temperature or intensity related peak shift. As micro-Raman 2D scans were run over the course of several hours the plasma filter was removed and any shift in the plasma line due to temporal, thermal or focussing effects was measured. Each point on the line scan was then normalised against the corresponding plasma line shift and thus errors in measuring the peak shift were minimised as described in section 3.6.2.

Photoacoustic measurements were undertaken using the photoacoustic microscope (PAM) described in Chapter 2. The system can be operated in microscope (scanning) mode, or by fixing the stage position and scanning the chopping frequency. In this study the microscope images were taken at a chopping frequency of 760 Hz, to coincide with the approximate peak signal of the cell. The time constant of the lock-in amplifier and stage velocity were varied to optimise the image resolution. In the case of the frequency scan the scanning range was set to 200 Hz – 2000 Hz. Plots are obtained for both amplitude and phase values recorded. For the arcing point scan (red line, Figures 4.22(a) & (b)) the stage was moved to the point where the arc point was seen on the PAM image and a frequency scan was taken.

For the Bare Silicon scan (black line, Figures 4.22(a) & (b)) the stage was moved to bare (undamaged) site on the same sample and a frequency scan was taken.

4.3 Results & Discussion

4.3.1 Damage Regime 1

SEM images of damage regime 1 (Figure 4.1(a)) show an area of arc induced damage on the surface of the wafer measuring approximately 1000 μm x 800 μm, and consisting primarily of what appears to be surface debris. Large Area Back Reflection (LABR) topographs of the (0 2 6) reflection exhibit several intermittently positioned dislocation cells, with non-uniform shape and ranging in diameter from approximately 50 – 175 μm, with darker voids or nodules between them.

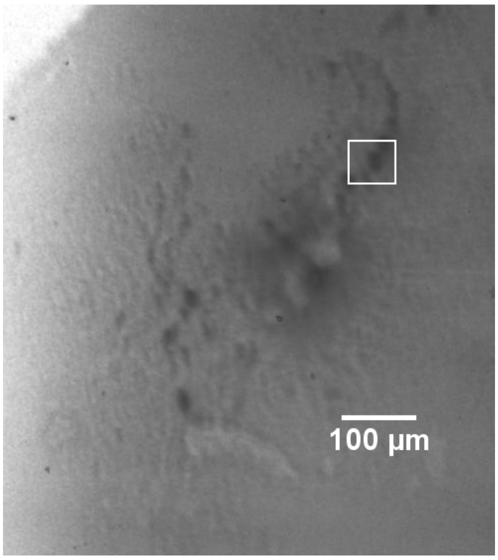

Figure 4.4: 0 2 6 LABR topograph of damage regime 1. Boxed area corresponds to region analysed by micro-Raman.

When the section topographs are rendered 3D images are obtained which (Figures 4.5-4.6) enable visualisation of the strain fields on all surfaces of the sample and also within any arbitrary location in its volume. Figure 4.5(a) is a 3D rendered XRDI using 17 ST topography slices; the main damage site is below the surface of the silicon sample. The raised grey region at the top of the sample can be attributed to strain in the Si substrate due to crystalline lattice deformations caused by the arc induced damage. The strain field contrast can be observed across a large volume of approximately 1500 μm x 1100 μm in the x and y-directions, respectively, and a depth into the Si wafer of ~⅔ the wafer thickness (see also Figure 4.6). Thus the damage regime extends into much larger volumes than can be observed solely by visual inspection.

A K-means clustering algorithm (section 3.3.3 and Appendix A), has been used to separate the differences in strain field intensity, and enhance the analysis process.

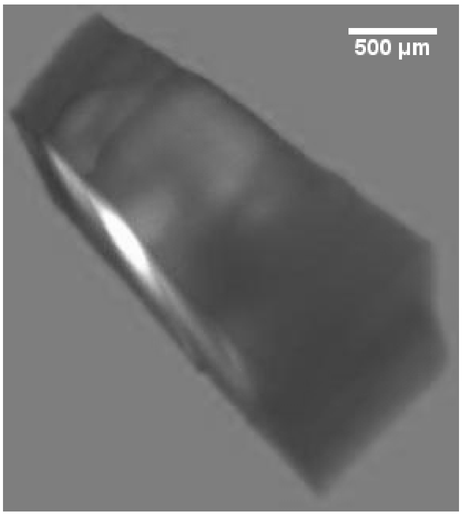

Figure 4.5(a): 3D-XRDI of damage regime 1. All 3D images are rendered from 220 Transmission Section Topographs.

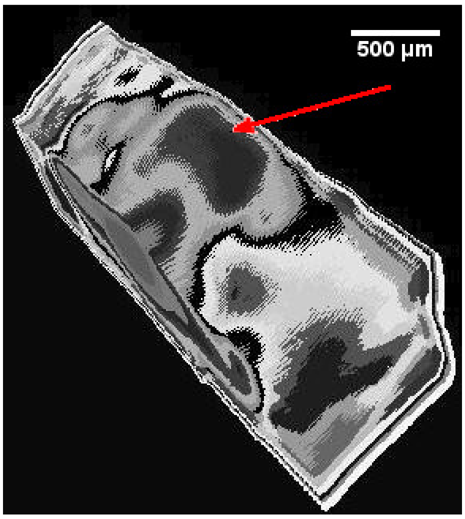

Figure 4.5(b): 3D-XRDI of damage regime 1 with K-means clustering applied.

Regions of similar strain field induced x-ray intensity can easily be distinguished in the clustered image (Figure 4.5(b)) when compared to the un-clustered image (Figure 4.5(a)). The black cluster on the surface directly at the damage site, indicated by the red arrow, appears to experience the largest imposed strains; the region measures approximately 850 μm wide and penetrates through 600 μm to the backside of the wafer. The strain fields propagating from the surface spread out to reach a maximum of ~1800 μm half way through the depth of the substrate, further illustrating that the surface condition gives only a small indication of the extent of the damage. The main advantages of this algorithm are its simplicity and speed, which allows it to run on large datasets.

The 3D-XRDI images can themselves be individually sectioned along any plane of choice in order to see detail of internal damage, while continuing to preserve the 3D data. Figure 4.6 illustrates a 3D-XRDI of damage regime 1 which has been 'cut' down the centre and false colouring has been applied in order to highlight areas of interest or visualize regions of enhanced strain contrast. A false colour image is made from several grey scale images where each pixel value is mapped to a colour, according to the table or function used. In Figure 4.6 the image has first been brightened, and the contrast enhanced before the *spectrum* colour scale in false colouring was applied.

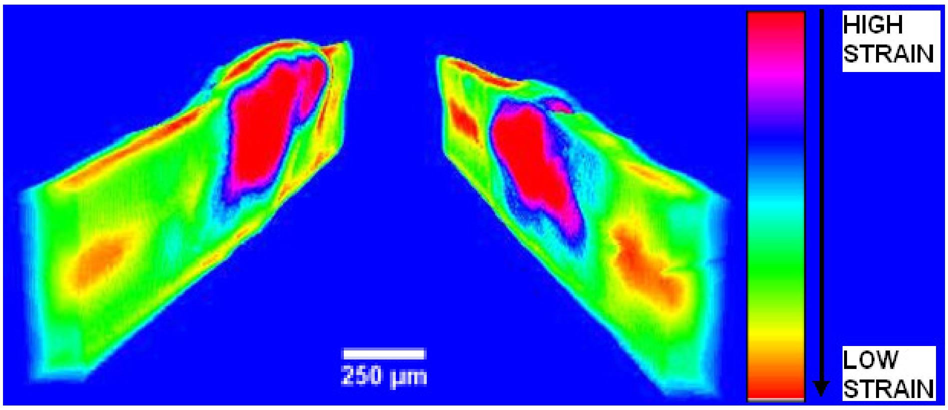

Figure 4.6: 3D-XRDI of damage regime 1 which has been 'cut' down the centre and false colouring applied. Scale bar shows look up table (LUT) with red region corresponding to area with highest strain levels and orange / yellow region corresponding to lowest strain levels.

Micro-Raman spectroscopy data for damage regime 1 was taken over an area of the sample approximately 80 µm x 80 µm, corresponding to the region highlighted (white box) in the large area back reflection topograph of Figure 4.4. This region was selected for study as it illustrates the effects of strain at both the inside and at the periphery of the damage site. Spectra were acquired with 3 accumulation times of 20 seconds and 10 seconds for the Ar^+ and UV lasers, respectively, to minimise noise effects. Previous micro-Raman data, taken at different locations on the same sample show these results to be indicative of what is happening on a larger scale at the interior and edges of the damaged region.

Figure 4.7(a) shows a 2D map of the main silicon Raman peak shift taken with a 325 nm UV laser, with a penetration depth, d_p, of ~9 nm in silicon, microscope image of the same location is shown in Figure 4.7(b). Micro-Raman spectroscopy results indicate crystalline silicon with some lattice disorder present. All the measured peaks on the damaged area are shifted due to stresses in the silicon (Figure 4.7(c)). A shift to higher wavenumbers indicates compressive stresses while shifts to lower wavenumbers are due to tensile stresses, indicating that the central part of the damaged region is in compressive stress and the periphery of the damage site is in tensile stress (Figure 4.7(a)). If a uniform biaxial stress model is assumed, the relationship between Raman shift and stress can be calculated from the equation [14]:

$$\Delta\omega = -4\times10^{-9}\left(\frac{\sigma_{xx}+\sigma_{yy}}{2}\right)(Pa) \qquad (4.1)$$

where $\Delta\omega$ is the change in Raman frequency from the calibration position at 520.07 cm^{-1}, and σ_{xx} and σ_{yy} are the stress components for biaxial strain in the X - Y plane,

Assuming, $\sigma_{xx} = \sigma_{yy}$ equation (1) can be written as:

$$\sigma_{xx} = \sigma_{yy} = {}^{\Delta\omega}\!/_{-4} \quad GPa \qquad (4.2)$$

The scale bar and corresponding arrows on the left side of Figure 4.7(a) indicate the calculated biaxial stress for the region of damaged silicon. Tensile stress at the surface ranges from 0 – 300 MPa, whereas compressive stress ranges from 0 – 600 MPa. Both tensile and compressive stress regions extend well beyond the visible damage site. Ar^+ laser results (Figure 4.8) show the levels of stress deeper into the damage site (d_p = 569 nm). In contrast to the results at the surface, they show the bulk of the damaged site to be in tensile strain, and the surrounding area to be in compressive strain. Tensile stress is also observed after high temperature annealing, when Si transitions from an amorphous to a crystalline state [15], which is a similar process to the phase transition at the plasma damage site. When such a phase transition occurs, it may also be assumed that a compensating layer in compressive stress must exist in proximity to this tensile layer, as illustrated in Figure 4.8.

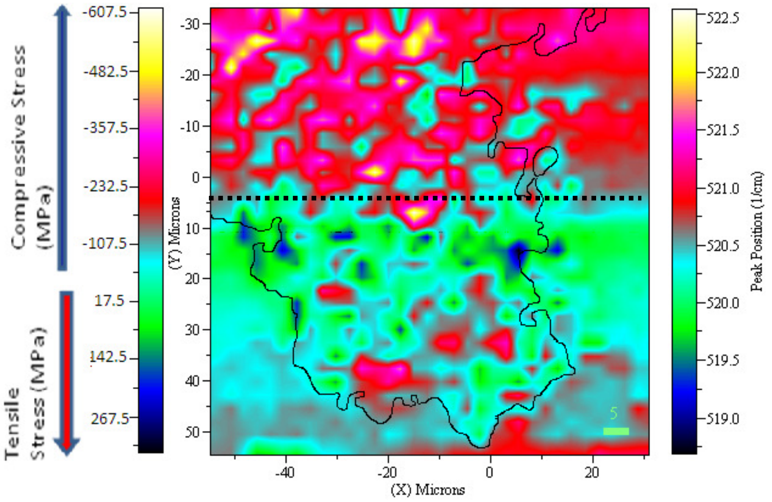

Figure 4.7(a): UV Micro-Raman 2D scan of region from damage regime 1 at d_p = 9 nm. Note area in compressive stress is above the dashed line, closest to main 'body' of damage site, and the area of tensile stress is largely below the

dashed line, on the periphery of the damage site. Edge of damaged region is bordered in black.

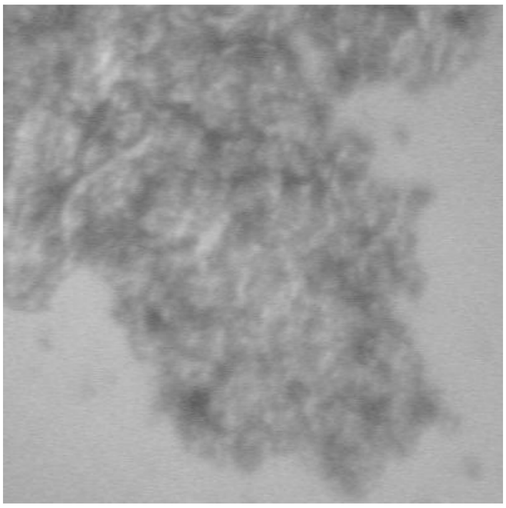

Figure 4.7(b): 40x optical microscope image of region in Figures 4.7(a) and 4.8. Note scale is the same for both images.

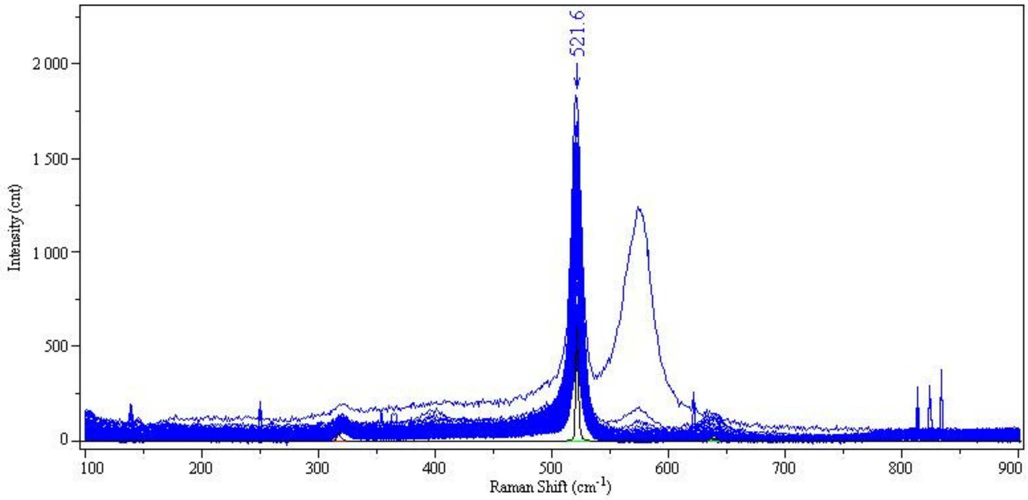

Figure 4.7(c): UV Micro-Raman spectra from damage regime 1 at d_p = 9 nm, corresponding to the 2D matrix scan in Figure 4.7(a). Spectra were collected over an 80 µm × 80 µm area at a spacing of 5 µm and with 3 accumulations. Blue shift of 520 cm^{-1} peak indicates compressive stress. Peak at 575 cm^{-1} is indicative of Boron doping, peak at 330 cm^{-1} is also a Si peak, however the phase is not known. Smaller, sharp peaks can be attributed to cosmic rays.

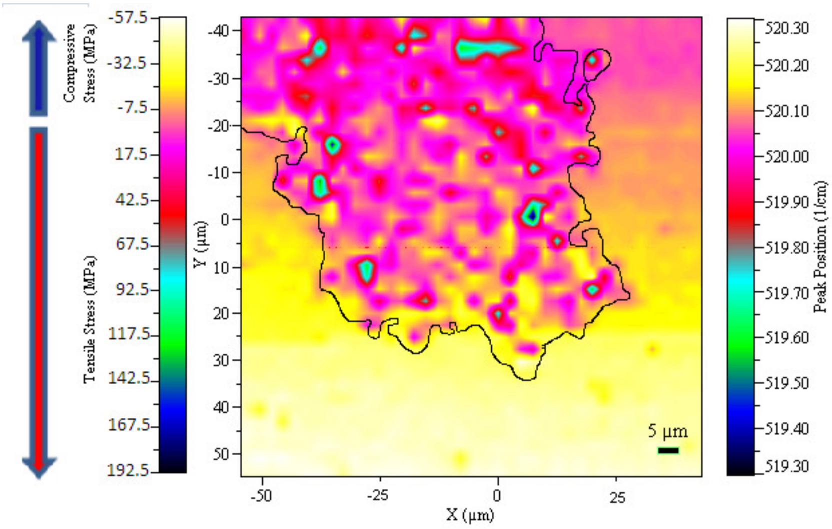

Figure 4.8: Ar^+ laser micro-Raman 2D scan of region from damage regime 1 at d_p = 569 nm. Spectra were taken over a 90 μm × 90 μm area at a spacing of 2.5 μm and with 3 accumulations. Note the bulk of the damage site is in tensile stress, and surrounding region is in compressive stress. Edge of damaged region is bordered in black.

4.3.2 Damage Regime 2

In most cases, for damage regime 2, the plasma induced damage on the wafer surface (using SEM) appears as a series of 100 – 250 μm diameter islands of microcrystalline Si. LABR topographs (Figure 4.9) show each island to contain a network of dislocations. Each dislocation cell measures approximately 20 μm wide, and extends over 250 μm into the substrate. The dislocation cells observed are very similar in size and form to dislocation cells observed in a previous study of laser micro-machining on Si [16]. This study showed that a UV laser with an output power of >20 W at 100 kHz repetition rate gave rise to a temperature increase of ~1.8 x 10^5 K at the surface of the Si, and resulted in strain magnitudes of the order of ~200 MPa. From this we can infer that the arcing event and high energy laser machining of Si induces similar damage in the substrate.

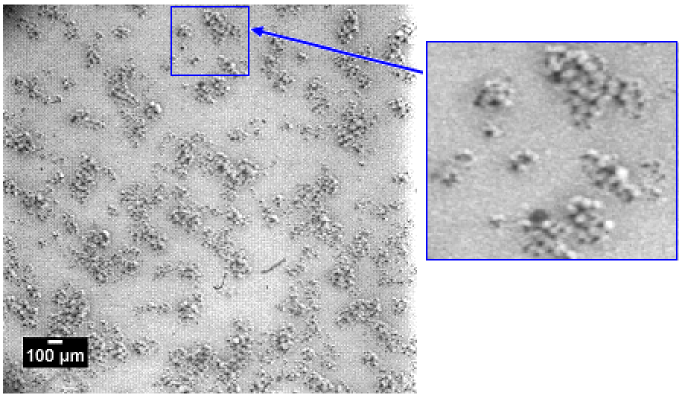

Figure 4.9: 0 2 6 LABR topograph of damage regime 2 showing arc induced islands containing networks of dislocation cells.

The 3D-XRDI image in Figure 4.9(a) is rendered from 12 stacked section topographs. The raised grey regions at the surface of the sample, which indicate an induced distortion of the underlying crystal Si lattice, can be attributed to the amorphous silicon regions identified by the micro-Raman spectroscopy results shown in Figures 4.11(a) and (b). As with damage regime 1, K-means clustering has been effectively used to highlight the different strain levels present within the sample (Figure 4.10(b)). The largest strain field present, corresponding to the circled region in both Figures 4.10(a) & (b) measures approximately 600 μm × 350 μm, and penetrates almost completely through the 450 μm thick substrate.

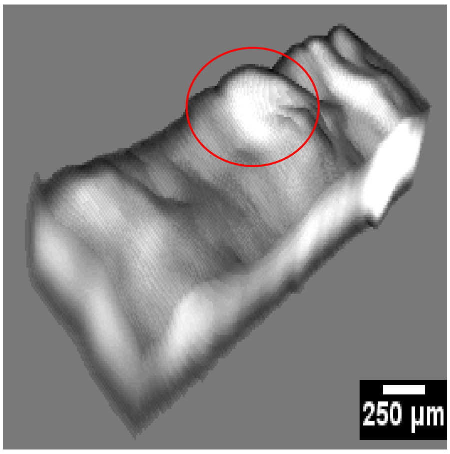

Figure 4.10(a): 3D-XRDI of damage regime 2. All 3D images are rendered from the 2 2 0 ST reflections. Region circled in red corresponds to largest area of damage which penetrates completely through the substrate.

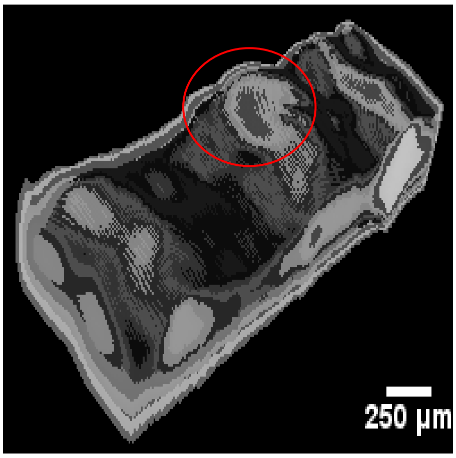

Figure 4.10(b): 3D-XRDI of damage regime 2 with K-means clustering applied.

Micro-Raman spectroscopy results, for the region shown in Figure 4.12(b), indicate the presence of both amorphous and crystalline Si. When a single arc-induced island of damage is examined using the UV laser the entire near surface region is shown to be in tensile stress, (Figures 4.11(a) & (b)), however when this is integrated to greater sample depths with the 488 nm Ar$^+$ laser with d_p = 569 nm, as in the case of damage regime 1 (Figure 4.12(a)), the data shows the damaged region to be in tensile stress, and the surrounding region in compressive stress. Lattice disorder remains, although to a lesser extent than at the surface. Figures 4.11(b) and (c) show that the main part of the damage site consists of Si-I, diamond cubic silicon, and a ring of α-Si is present at the edges of the damage site. At the centre of the island, where bulk cubic Si holds the area in tension, strains as high as 500 MPa are observed. Strain levels decrease towards the edges of the damage region, where the presence of amorphous Si, which has no long range order enables some strain relaxation. The presence of an inner crystalline region of Si, and an outer amorphous Si region, as seen in Figures 4.11 (b) & (c) is similar to the characteristic ring pattern which is observed in the femtosecond laser damage to Si [17, 18]. At the centre of the damage region the cooling rate is slow enough to allow crystalline Si to form, whereas at the edges of the damaged region the cooling rate is fast, and there is no time for the Si to return to the crystalline phase. It is likely that a similar two-zone ablation and cooling mechanism has occurred in the case of damage regime 2.

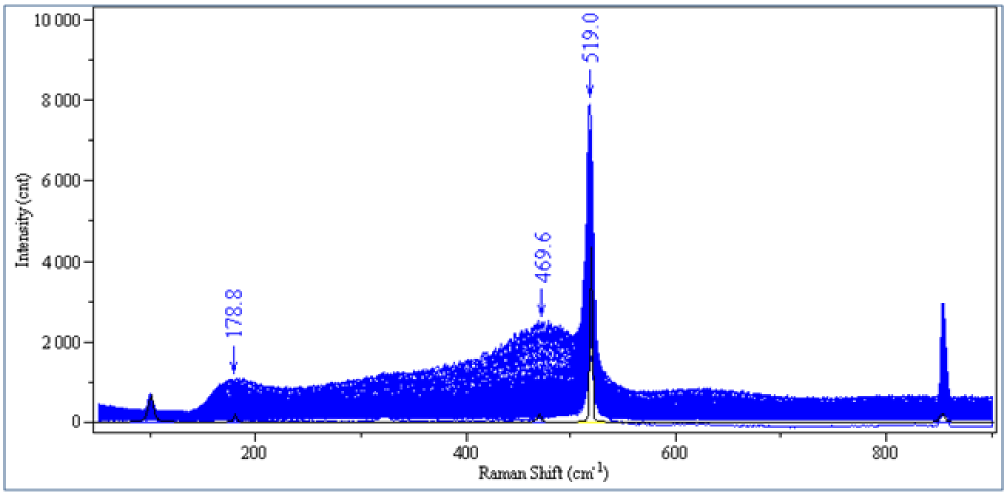

Figure 4.11(a): UV Micro-Raman spectra from damage regime 2 at $d_p = 9$ nm, corresponding to the 2D matrix scan in Figures 4.11(b) and (c). Spectra were collected over a 70 µm × 70 µm area at a spacing of 2.5 µm and with 3 accumulations. Red Shift of 520 cm^{-1} peak indicates tensile stress. Peak at 469 cm^{-1} is indicative of amorphous Si, peak at 178 cm^{-1} may also be due to amorphous Si. Sharp peaks at ~100 cm^{-1} and 850 cm^{-1} are plasma lines.

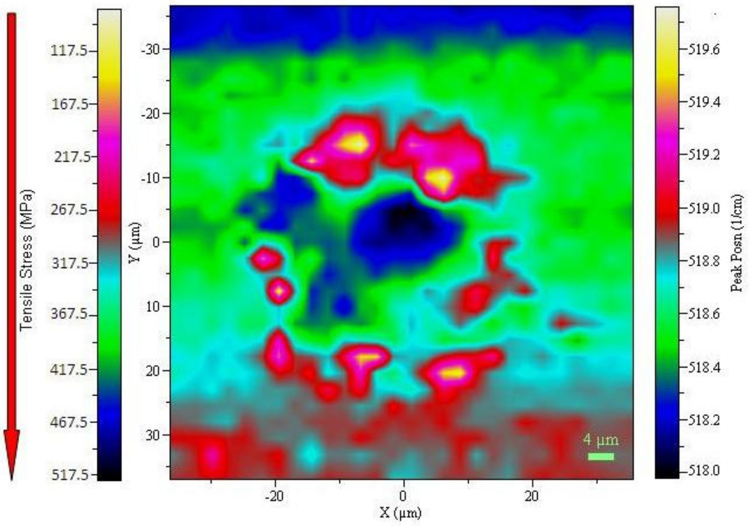

Figure 4.11(b): UV Micro-Raman 2D scan of region from damage regime 2 at $d_p = 9$ nm. Spectra were taken over a 70 µm × 70 µm area at a spacing of 2.5 µm and with 3 accumulations. Plot shows 520 cm^{-1} peak shift and related strain.

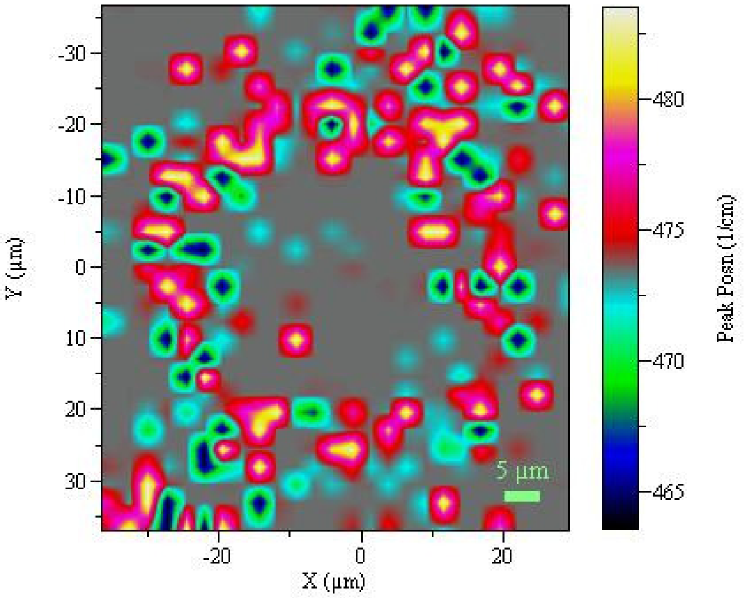

Figure 4.11(c): UV Micro-Raman 2D scan of region from damage regime 2 at $d_p = 9$ nm. Plot shows 470 cm^{-1} (amorphous Si) peak which forms a ring around the periphery of the damage site.

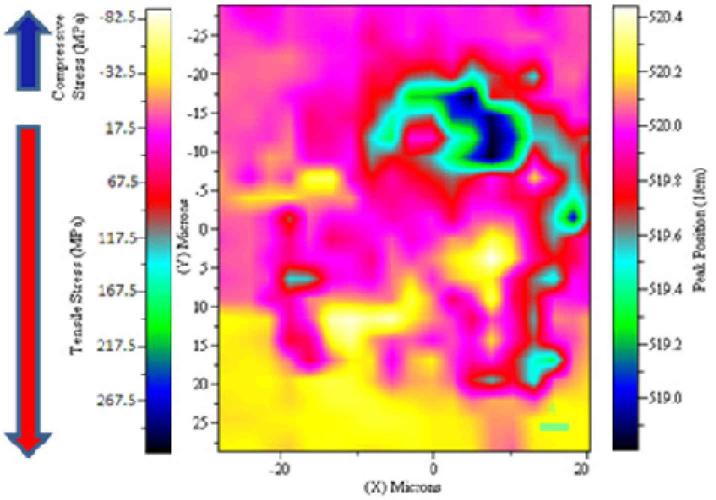

Figure 4.12(a): Ar$^+$ Micro-Raman 2D scan of region from damage regime 2 at d_p = 9 nm. Spectra were taken over a 50 µm × 60 µm area at a spacing of 2.5 µm and with 3 accumulations. Plot shows 520 cm^{-1} peak shift and related strain.

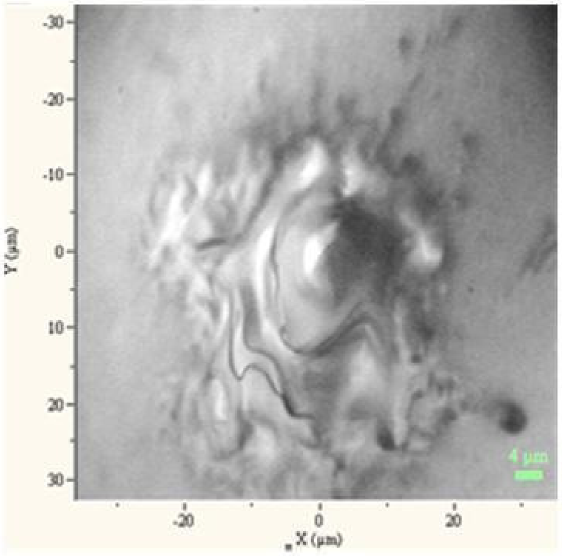

Figure 4.12(b): 50× optical microscope image of region in Figures 4.11-4.12.

4.3.3 Damage Regime 3

Optical images of damage regime 3 (Figure 4.1(c) and 4.13) show the impact of the arc on the Si surface, with rapid melting of the crystalline Si leading to an amorphous-type layer extending out from the centre of the damage site.

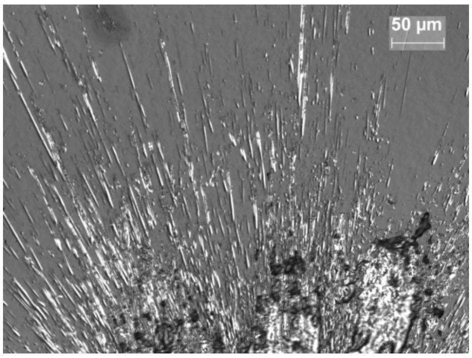

Figure 4.13: 20x Optical Microscope Image of the periphery of arcing damage on Sample 3.

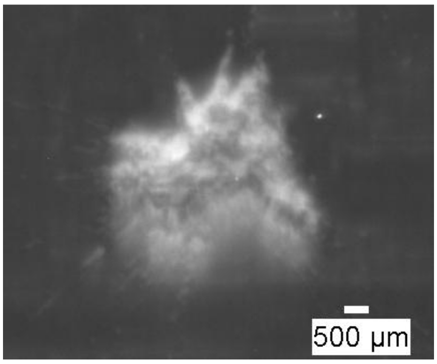

Figure 4.14: LAT topograph of the damage site, showing its distinctive shape. Image is recorded on CCD at ANKA.

The LAT topograph (Figure 4.14) of the damage site exhibits a distinctive shape, with the strain field due to the arcing damage measuring approximately 4200 µm × 2400 µm, almost twice the size of the surface damage when viewed using an optical microscope. LABR topographs of the arcing damage site shown in Figures 4.16(a)-(c) represent the distribution of strain-induced x-ray contrast present at x-ray penetration depths, t_p, of 40 µm, 75 µm and 190 µm, respectively. The topographs show small rounded regions throughout the damaged area ranging in size from ~80 µm–200 µm in diameter. These dislocation cells are similar to those seen in damage regime 2, however they are up to 10 times larger. It is likely that when the current discharges on the silicon surface local melting occurs, and the silicon volume expands and then contracts. The silicon later recrystallises, however the extreme heat load results in material damage which is apparent from the appearance of cells of single crystal Si bounded by walls of piled up dislocations (Figure 4.15), [19, 20]. In the -1 1 7 and -1 1 9 reflections, at t_p< 100 µm, there is a more random pattern of circular dislocation cells and a wider strain field, indicating an increased displacement of the lattice planes towards the surface, where the strain is the highest and the contribution of the damaged Si volume is greatest.

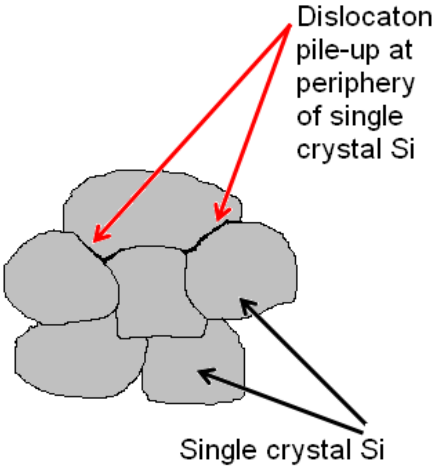

Figure 4.15: Diagram illustrating the dislocation pile-up present at the periphery of the cells of single crystal Si as seen in LATs Figures 4.16(a)-(c).

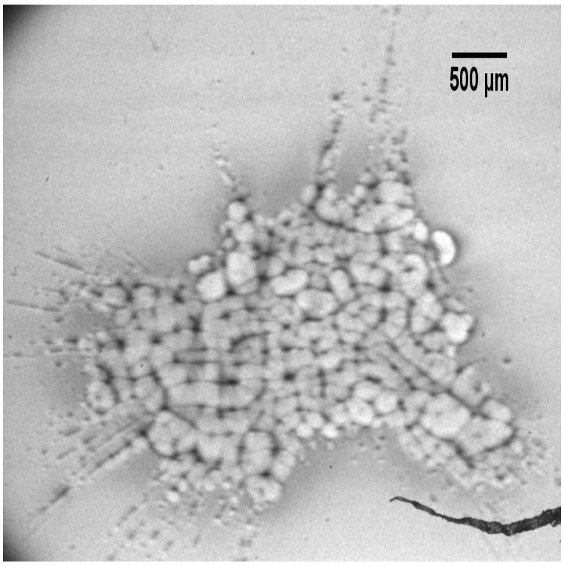

Figure 4.16(a): LABRT of damage regime 3, -1 1 7 reflection at 100x magnification. t_p, = 40 µm. Image recorded on high resolution film at HASYLAB Synchrotron.

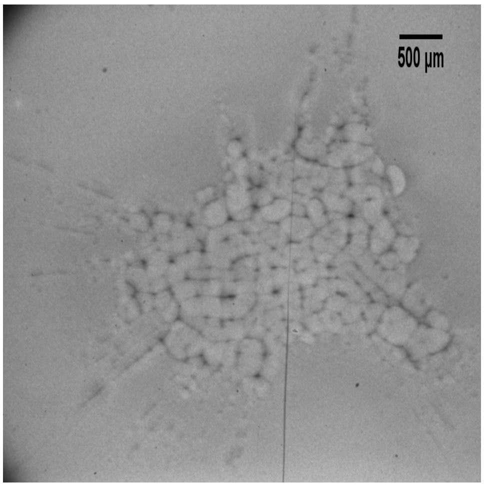

Figure 4.16(b): LABRT of damage regime 3, -1 1 9 reflection at 100x magnification. t_p, = 75 µm.

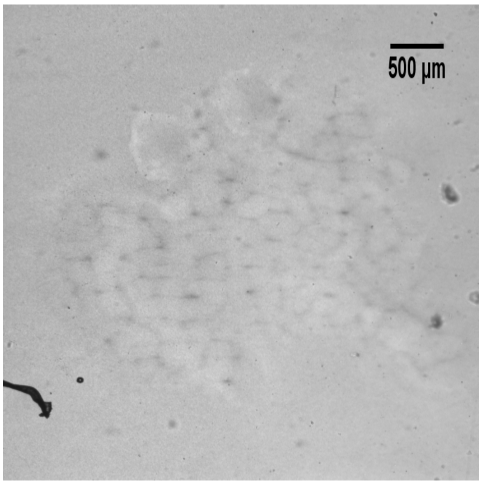

Figure 4.16(c): LABRT of damage regime 3, 2 2 12 reflection at 100x magnification. t_p, = 190 µm.

The 3D-XRDI data for *damage regime* 3 are comprised of over 130 ST topographs. The 3-dimensional image reproduces the distinctive shape of the surface strain fields observed in the corresponding LAT and LABR topographs (Figures 4.13 & 4.16 (a)-(c)). The 3D-XRDI highlights arcing damage extending approximately 100 µm upwards from the surface of the

Si, this may be a result of surface debris, or recrystallised Si sitting on top of the more uniform single crystal Si beneath it.

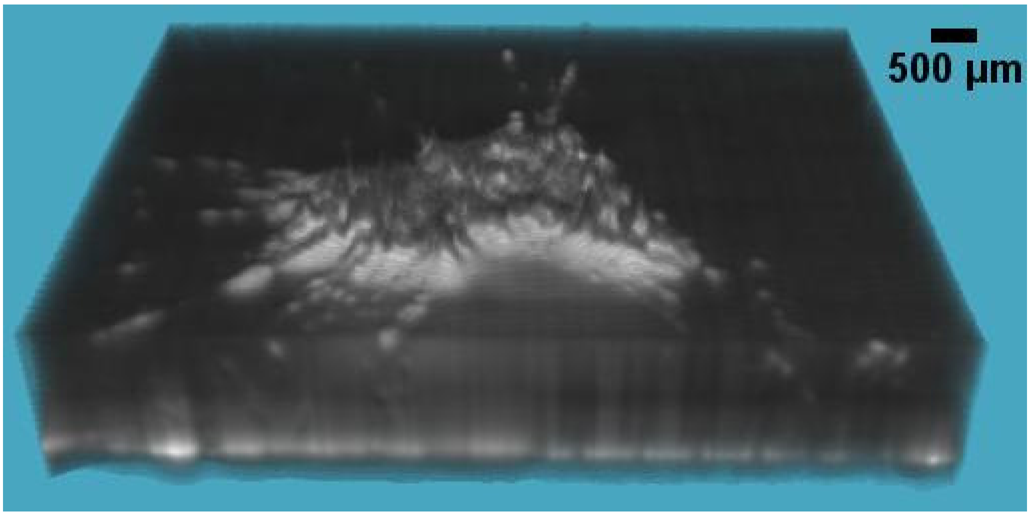

Figure 4.17: 3D-XRDI of damage regime 3. Image is comprised of over 130 ST topographs from 2 2 0 reflection.

When the 3D-XRDI is sectioned (Figure 4.18(a)) the strain field contrast can be seen to extend over a large volume of the wafer, and runs approximately 350 µm through from the back side into the 660 µm thick wafer, indicating that this form of arcing damage could impact the patterned IC structures on the surface of the wafer. In contrast to the previous two damage regimes, 3D-XRDI for this sample show most of the damage lies closer to the surface. Figure 4.18(b) shows the sectioned 3D-XRDI with the phase and HiLo look up tables (LUTs) applied. Application of the LUTs has enabled the regions of greatest strain field intensity to be clearly isolated in blue, demonstrating that the highest strain levels extend around the periphery of the damaged volume. The next highest regions of strain are shown in white/grey, with the relatively unstrained regions appearing almost black.

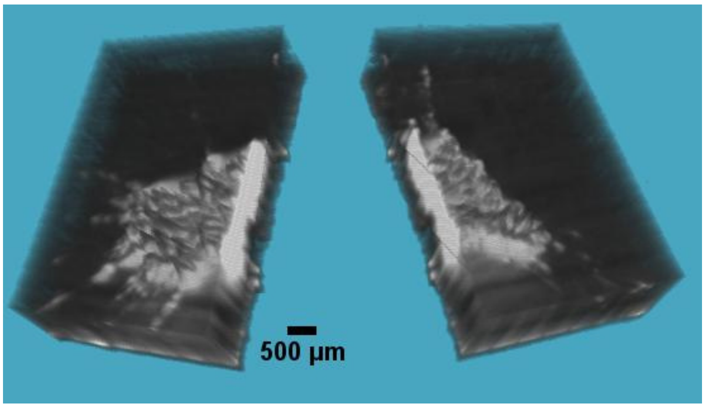

Figure 4.18 (a): Damage regime 3, which has been sectioned along central plane to enable internal damage to be viewed.

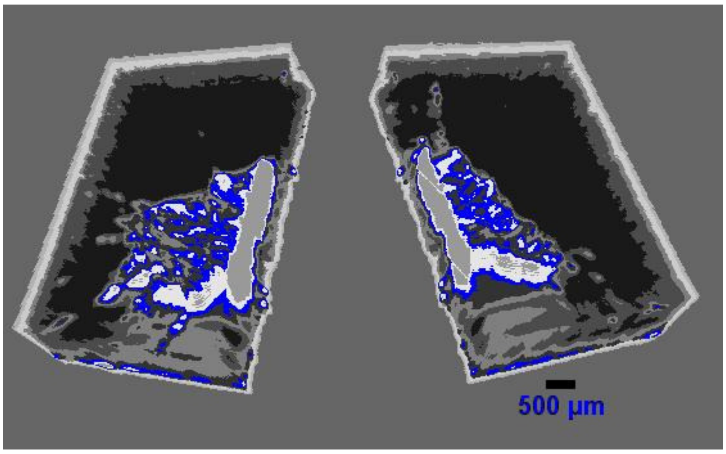

Figure 4.18(b): Damage regime 3, with phase and HiLo LUTs applied. Blue regions are regions of highest strain.

Micro-Raman measurements were undertaken using both Ar+ (488 nm) lasers and UV (325 nm) lasers, in order to obtain data at 556 nm and 9 nm laser penetration depths respectively. Ar+ measurements were taken with an accumulation time of 3 s, with 3 accumulations over a scan area of 60 µm × 60 µm (Figure 4.19), which enabled data to be obtained at the edge, and closer to the centre of the arc damaged region. The 1800 grooves/mm grating, a 200 µm hole size and 100% filter were also set to optimise the signal from the micro-Raman system.

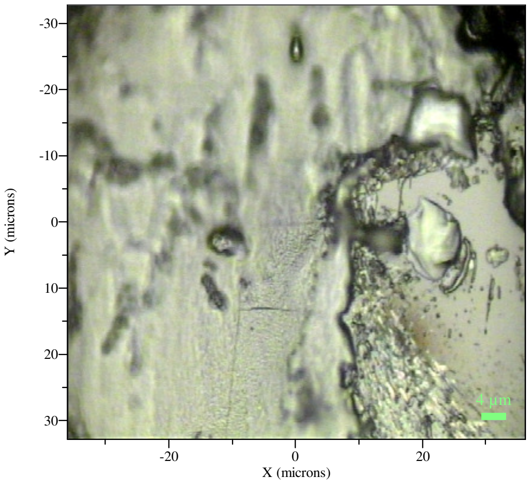

Figure 4.19 (a): Optical micrograph of region examined using Ar+ laser scan position image showing arcing from damage regime 3.

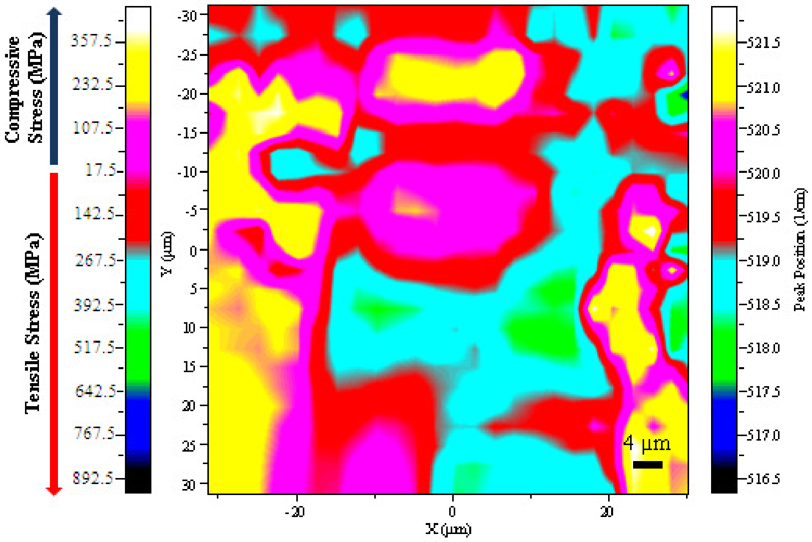

Figure 4.19 (b):Ar$^+$ Micro-Raman 2D scan of region from damage regime 3 at d_p=556 nm. Spectra were taken over a 60 µm × 60 µm area at a spacing of 2.5 µm. Plot shows 520.07 cm^{-1} peak shift and related strain in MPa.

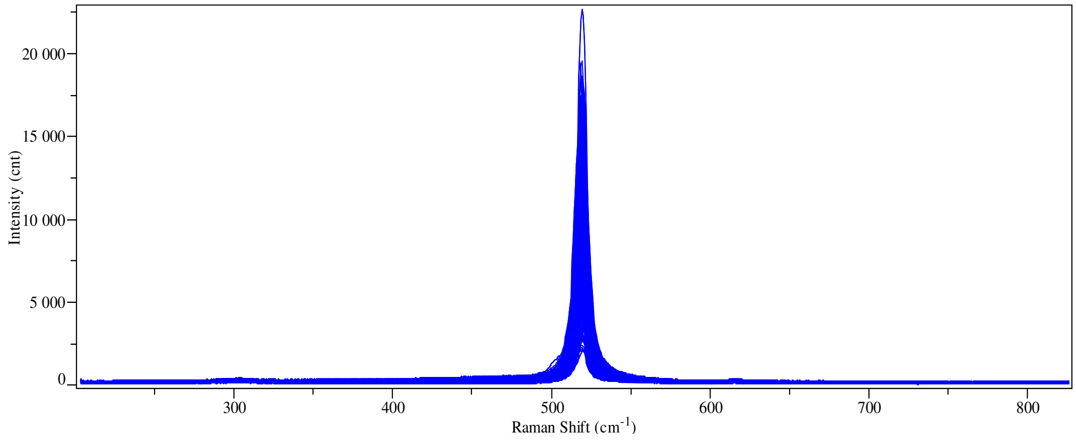

Figure 4.19 (c): Ar$^+$ Micro-Raman spectra from damage regime 3 at d_p=556 nm, corresponding to the 2D matrix scan in Figures 4.19(b) and (d). Spectra were taken over a 60 µm × 60 µm area at a spacing of 2.5 µm. Plot shows a single peak centred on 518.08 cm^{-1}.

Figures 4.19 (b)-(d) show the Raman spectra for a matrix scan taken with step size of 2.5 µm in x and y directions using the Ar$^+$ laser. In general the spectrum takes the form of a single symmetric peak centred on 518.8 cm^{-1}, with an average FWHM of 15 cm^{-1}. The 2D scan shows a pattern of a red peak shift at the edges of the damage region, indicating tensile stress, and a blue peak shift towards the centre of the damage region, indicating compressive stress. A downwards shift in peak position, accompanied by a reduction in peak intensity, as seen in Figures 4.19 (b) and (c) are indicative of confined micro-crystalline Si. The silicon peak intensity variation is also consistent with lattice disorder introduced by the heat and sub-surface damage caused by the arcing. The overall increase in peak width (FWHM) from that of crystalline Si at 3 cm^{-1} to between 7 and 16 cm^{-1} as seen in Figure 4.19 (d), can also be attributed to the presence of crystalline disorder, which decreases the phonon lifetime, thus generating an increase in the bandwidth [21]. It is not possible to clarify the exact origin of the Si peak shifts and intensity variations, as discussed above, small changes may be attributed to changes in crystallite type and strain, however stress levels enable a good understanding to be obtained of the general state of the damaged Si surface. If a biaxial stress model is assumed (equation 4.2), [14], tensile stress levels of over 400 MPa, and compressive stress levels of up to 400 MPa are apparent close to the surface of the damaged area, with the greatest tensile stress levels near the edges of the damage site, and the greatest compressive stress levels toward the centre of the damage site.

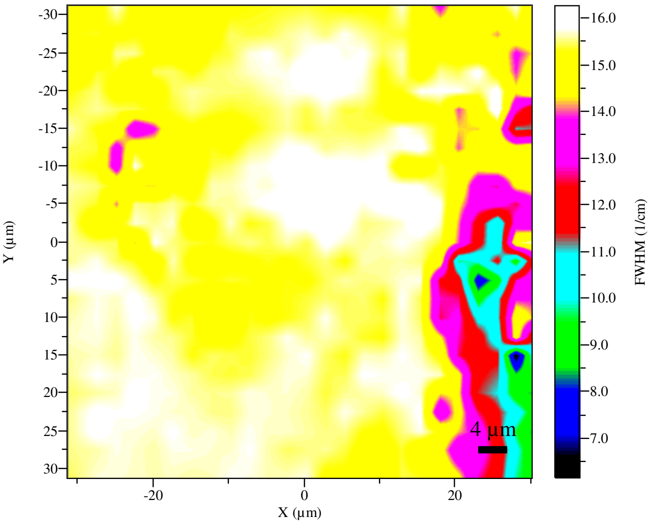

Figure 4.19 (d): Ar$^+$ Micro-Raman 2D scan of region from Figure 4.18(a), damage regime 3. Plot shows FWHM (cm^{-1}) measurements.

Spectra for the UV (325 nm) laser, taken with an accumulation time of 60s, and utilising the 3000 grooves/mm grating, are shown in Figures 4.20 (a) – (c). A single peak, centred on average at 520.50 cm^{-1} with a broad shoulder at 450 – 470 cm^{-1} is obtained across the entire scan area (Figure 4.20 (c)). The broad peak at 470 cm^{-1} is characteristic of amorphous Si Figures 4.16(a)-(c), this peak is not observed at ~560 nm, its presence in the UV micro-Raman data suggests a very thin layer of amorphous material above bulk crystalline Si.

The main peak decreases in intensity and increases in width as we move from the centre of the damaged region towards the edges, signifying less lattice disorder at the centre of the damage site. As with the results obtained using the Ar$^+$ laser a large red shift is apparent, indicating tensile stresses of 0 – 1768 GPa at the damage point. This tensile stress is much greater than that seen at deeper penetration depths (556 nm), demonstrating decreasing strain from the top 9 nm down to 556 nm of the surface damaged region. This is in agreement with the 3D-XRDI, where in Figure 4.18(b) we see the highest strain levels on top of, and surrounding the damaged volume.

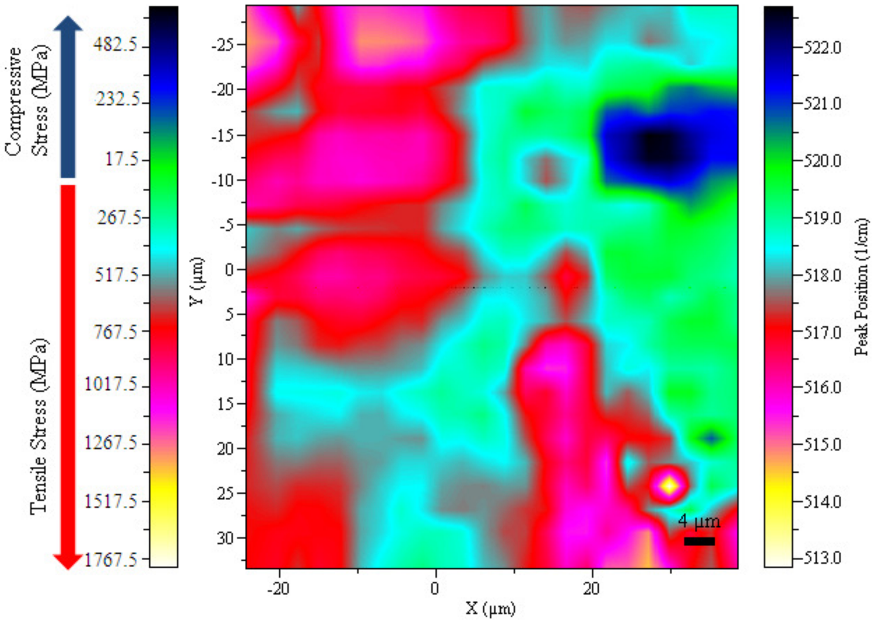

Figure 4.20 (a): UV Micro-Raman 2D scan of region from damage regime 3 at d_p=9 nm. Spectra were taken over a 60 µm × 60 µm area at a spacing of 2.5 µm. Plot shows 520.07 cm^{-1} peak shift and related strain.

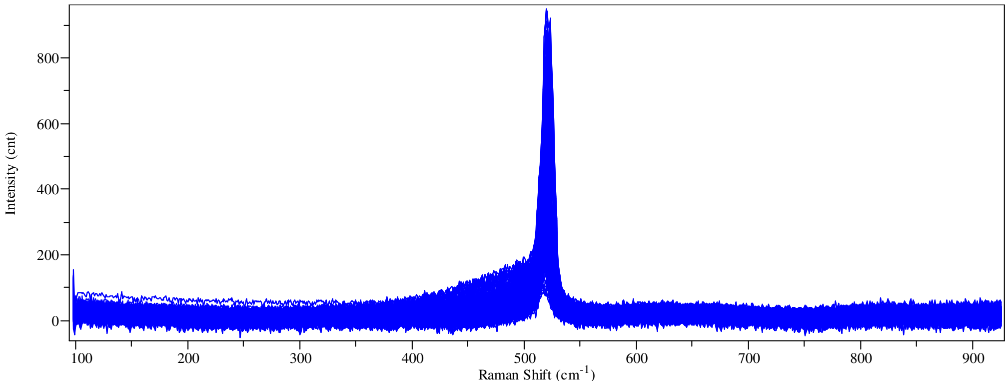

Figure 4.20 (b): UV Micro-Raman spectra from damage regime 3 at d_p=9 nm, corresponding to the 2D line scan in Figure 4.19 (b). Spectra were taken over a 60 µm × 60 µm area at a spacing of 2.5 µm. Plot shows a single peak centred on 520.50 cm^{-1}. Peak centred on 520.5 cm^{-1} and a broad shoulder at ~450 cm^{-1}.

Photoacoustic microscopy was initially used to identify the arc damage site on the 10 mm × 10 mm Si wafer sample. Scans were run using the PAM described in section 3.5, with the laser modulation frequency set to 760 Hz, a time constant of 30 ms and 0.1 mm resolution. PAM amplitude and phase images in Figures 4.21 (a) & (b) clearly indicate the damage to the silicon sample caused by arcing. Changes in contrast of the image at the arc point signify a variation in the depth and departure from good crystallinity at the location. The damage site appears to be smaller in the phase image (Figure 4.21 (b)) when compared with the amplitude image (Figure 4.21(a)). We know from section 2.3.3 that the amplitude image tends to be indicative of the state of the surface, whereas the phase image indicates the sub-surface state. In Figures 4.21 (a)-(d) the sample edge is indicated by an increase in the amplitude or phase signal. This occurs where the diameter of the laser beam is much less than μ_s, and l_s, and the 3D model of the PA effect is more relevant. Figures 4.21(c) & (d) show the spectral profile at the arc point for amplitude and phase images, respectively. The amplitude image shows a shift of ~0.35 mV at the arcing point, and the phase image shows a shift from ~+80° to -80°, which corresponds to a 20° phase difference at the arcing point. The minima are displaced from each other by approximately 500 μm, further suggesting that the amplitude and phase images are revealing different characteristics of the damage.

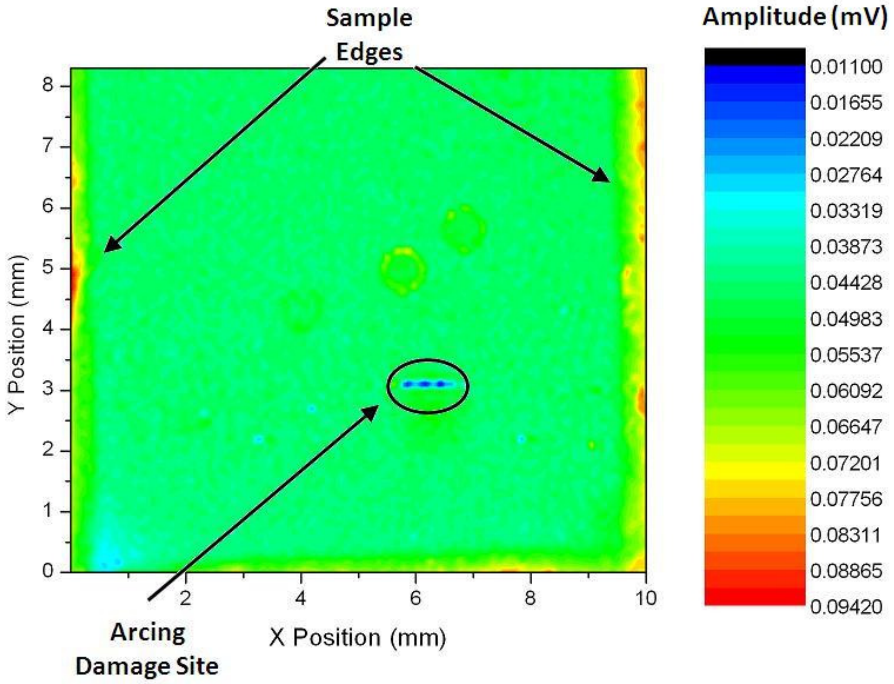

Figure 4.21(a): PAM Amplitude image of damage regime 3. Bright green area at edge of sample indicates the sample edge. Region circled in black is the arc damage site. Units are in mV, as recorded by the lock-in amplifier.

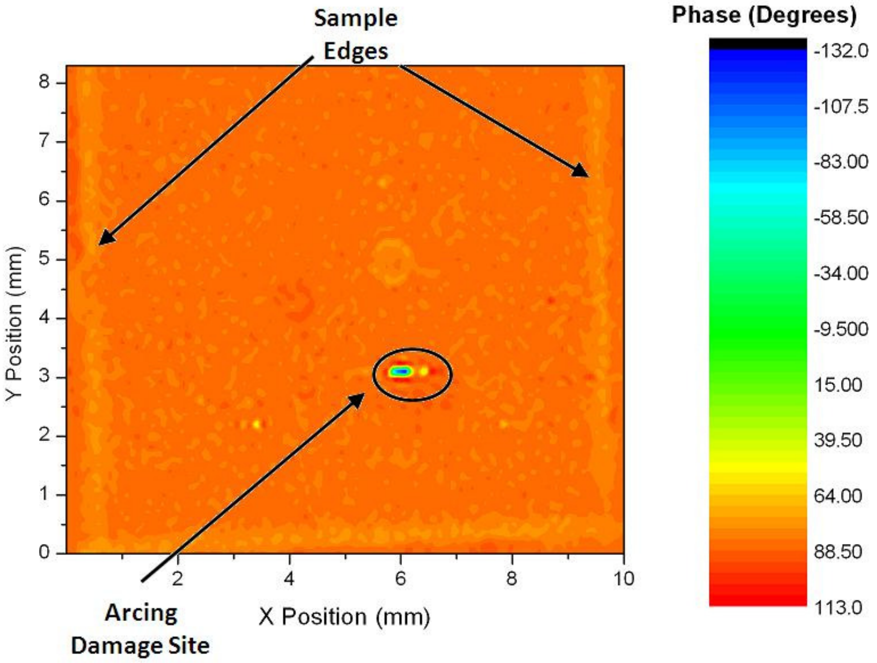

Figure 4.21 (b): PAM Phase Image of of damage regime 3. Lighter orange area at edge of sample indicates the sample edge. Region circled in black is the arc damage site. Units are in degrees, as recorded by the lock-in amplifier.

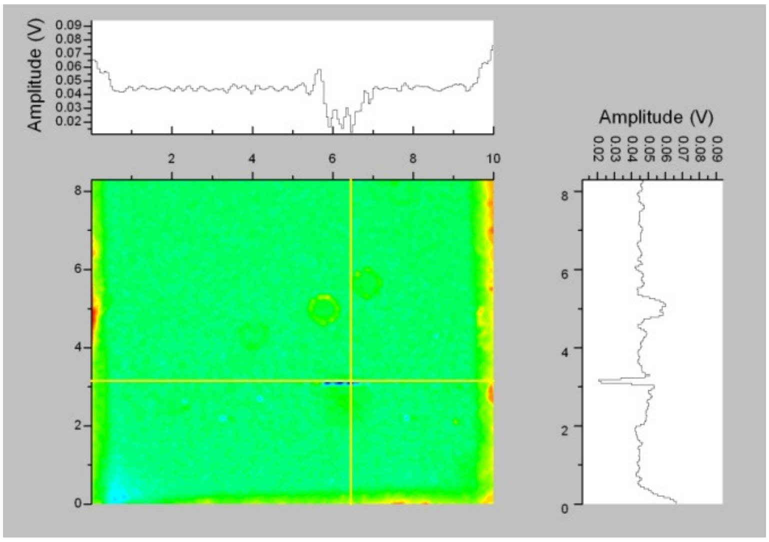

Figure 4.21(c): PAM amplitude image of damage regime 3, with profile at arcing point. Taken at 760 Hz, Time constant = 30 ms, 0.1 mm resolution.

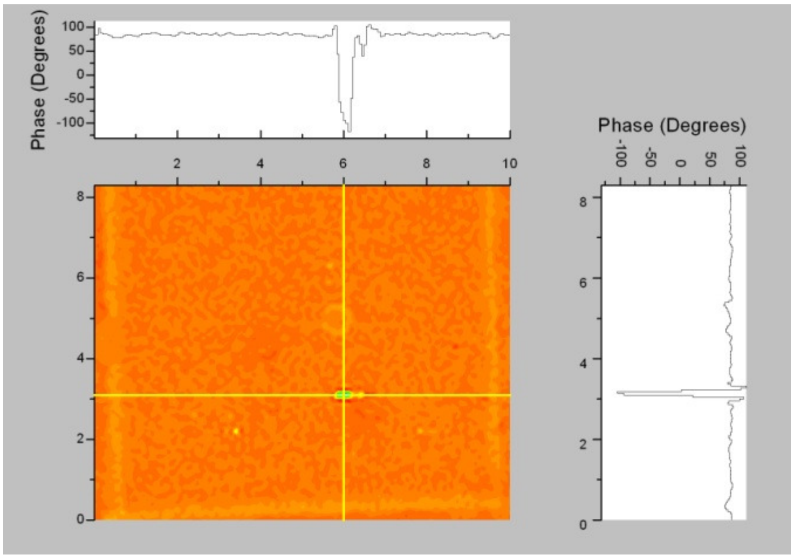

Figure 4.21(d): PAM phase image of damage regime 3, with profile at arcing point. Taken at 760 Hz, Time constant = 30 ms, 0.1 mm resolution.

The plots in Figure 4.22(a) and (b) show the photoacoustic (PA) signal amplitude and phase signals respectively versus the modulation frequency of the laser at two locations: the arcing point (red line), and bare, undamaged Si (black line). The amplitude and phase shifts for the PA frequency scans in Figures 4.22(a) and (b) correlate well with those in PAM images (Figures 4.21(c) & (d)), which show similar amplitude and phase differences. In Figure 4.22(a) the amplitude reaches a maximum at 720 Hz, which corresponds to the resonant frequency of the cell. The thermal wave generated as a result of the irradiation of the laser light propagates through the sample and interacts with the subsurface defects. The distance the thermal wave propagates into the sample is the thermal diffusion length, μ_s, where $\mu_s = \left(2\alpha_s / \omega \right)^{1/2}$ (see section 2.3.2) [1, 2].

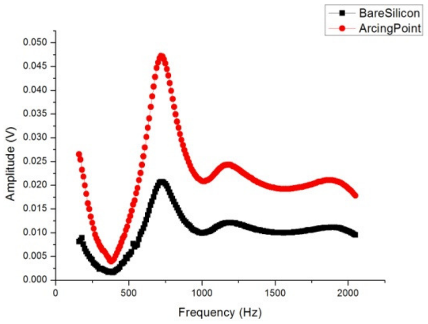

Figure 4.22(a): PA amplitude plot of damage regime 3 showing frequency scan at two different points.

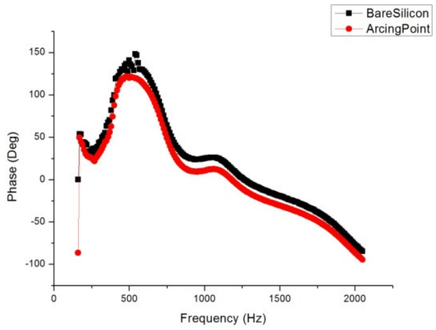

Figure 4.22(b): PA phase plot of damage regime 3 showing frequency scan at two different points.

At a modulation frequency of 720 Hz, the peak amplitude for the frequency scan in Figure 4.22(a) and (b), a theoretical thermal diffusion length of 200 µm was calculated. The total sample thickness is ~660 µm which equates the peak frequency to approximately the top third of the sample. From the 3D-XRDI we know the arcing damage extends approximately 350 µm deep into the sample, which is broadly in line with the PAM measurements. Figure 4.22(b) shows a plot of the PA signal phase, where the phase is the phase shift of the sound wave with respect to light pulse, versus modulation frequency for both the arcing point and bare silicon. The points chosen were identical to those chosen in Figure 4.22(a). In the case of the phase versus frequency graph the difference between the signals at the arcing point, and on the bare Si is not as well defined as the amplitude signal variation (Figure 4.22(a)). This is expected as it is known from previous experiments [22, 23] that at frequencies ~1 kHz, the PA amplitude signal is dependant on the optical absorption coefficient and morphology of the top surface, whereas the phase signal is dependant on the sub-surface structure (section 2.3.3).

Images 4.23(a) and (b) show the arc damage imaged with x-ray topography, (XRT). Figure 4.23(a) is an image of the arcing damage sample with the arcing damage circled in blue. Figure 4.23(b) shows the XRT image superimposed on the PAM phase image (Figure 4.21(b)). XRT results correlate well with those obtained from PAM and prove the efficacy of PAM as a non-destructive characterisation tool in the location and characterisation of defects on Si.

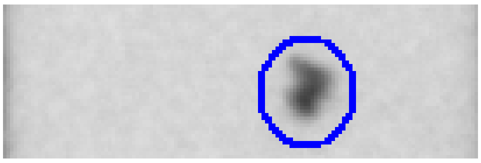

Figure 4.23(a): XRT image of damage regime 3. Damage site is circled in blue.

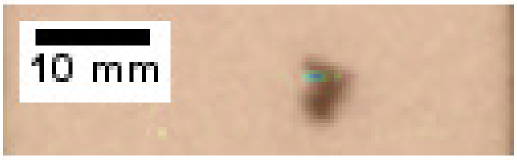

Figure 4.23(b): PAM Image of damage regime 3 (green dot) superimposed on XRT signal. Note scale is same in both images.

4.4 Summary

In this study we present a novel combined suite of metrology tools for 3D wafer strain imaging and analysis of process induced damage on Si. 3D-XRDI and micro-Raman spectroscopy have been successfully applied to non-destructively image the strain regions caused by three different types of plasma arcing induced damage on silicon, and to quantify the corresponding levels of strain. The 3-dimensional nature of the images enables strain information to be obtained throughout the entire volume of the measured silicon, presenting a unique opportunity for non-destructive semiconductor device process analysis. Further data on how the strain fields propagate through the crystal is obtained by splitting the 3D rendered stack of images at a plane of interest. The 3D images prove that for the damage regimes examined herein visual damage on the surface of the wafer is not wholly indicative of the levels of damage which lie beneath. Although considerable research has been undertaken examining the mechanisms behind plasma damage in semiconductor manufacturing, the majority of the research focuses on the electrical effect of such damage to oxide layers and thin films [24-26]. To date wafer and device characterisation tools have been limited to electrical measurements on purpose designed test wafers. Plasma arcing damage is one of the important plasma process induced damage phenomenon, the thermal mechanical properties of plasma damage and the impact of the damage on the surface and sub-surface of wafers and die is therefore key to the reduction of lost dies, yield, and operational costs.

3D-XRDI for damage regimes 1 and 2 are comprised of a relatively small number (<20), ST topographs, and are the first 3D-XRDI images published using the rendering techniques described in Section 3.3 of this report [27]. At the beginning of this project the image acquisition process took approximately 3 hrs for 45 ST topography images. Efficiency has been greatly improved over the course of this project by the automation of sample stage stepping, camera alignment and image capture sequences. It is now possible to obtain 600+

ST topography images in the same time, and the only limit to the amount of images which can be captured is the size of the storage media available. ST topographs used to create the 3D-XRDI for damage regime 3 were acquired using these new, more efficient techniques, enabling higher resolution 3D-XRDI to be created.

The K-means clustering algorithm used to enhance the 3D-XRDI images works well on data sets having isotropic clusters, and is therefore well suited to the highlighting and analysis of strain fields caused by plasma damage, together with appropriate false colouring. The disadvantage of the K-means algorithm is that it is not repeatable: as the clusters depend on the initial random assignments, each run can yield slightly different results.

Micro-Raman spectroscopy enables the levels of strain from the surface, down to depths of many hundreds of nm to be quantified. Results show the extension of strain fields beyond the visible surface damage area, and their correlation with the extended strain fields in the 3D-XRDI images.

PAM has been successfully applied to locate the arcing damage on sample 3 in both microscopy and frequency scanning modes. PAM and XRT results are in close correlation, proving that PAM can be successfully applied to the characterisation of surface and sub-surface defects on Si.

References

[1] Sychyi Fang and James P. McVittie, *IEEE Electron Device Letters*, Vol. **13**, No. 6, June 1992 347.

[2] K. Koski , J. Ho lsa, P. Juliet, *Surface and Coatings Technology* **115** (1999) 163–171.

[3] Shawming Ma, Neil Hanabusa, Brad Mays, Sergio Shoji, Michael Kutney, Troy Detrick, Bidu, Patada and Ralph Straube, 2003 IEEE.

[4] Y. H. Liou, Y. S. Chen, C. S. Wu, C. S. Tsai, M. Chi, 2001 6th International Symposium on Plasma Process-Induced Damage.

[5] Y Yin, D R McKenzie and M M M Bilek, *Plasma Sources Sci. Technol.* **15** (2006) 99–104.

[6] C.H.Yu, Y.H.Liou, Y.L.Tu, C.S.Wu,Y.S.Chen, C.Y.Pai, C.S.Tasi, M.H.Chi, 2001, IEEE.

[7] Qian Xue-Yu, Hills, Graham W., Chenming Hu , Hyungcheol Shin, Jha, Neeta, *Solid State Technology*, August 1993 v**36** n8 p29(6).

[8] X. R. Huang, NSLS: White-Beam X-Ray Diffraction Patterning (LauePt) Version 2.1 (2003).

[9] J. Kanatharana et al., *Microelectronic Engineering* **65** (2003) 209–221.

[10] Tony J. Collins, *ImageJ* for microscopy, BioTechniques 43:S25-S30 (July 2007).

[11] http://rsb.info.nih.gov/ij/index.html.

[12] http://sourceforge.net/projects/ij-plugins/files/.

[13] http://www.nist.gov/lispix/imlab/flsclr/fcolor.html.

[14] I. De Wolf, *Semicond. Sci. Tech.* **11**, 139 (1996).

[15] S. Hasegawa, S. Watanabe, T. Inokuma, and Y. Kurata, *J. Appl. Phys.* 77, 1938 (1995).

[16] J. Stopford, *Masters Research Project*, School of Electronic Engineering, DCU (2006).

[17] D.V. Tran, H.Y. Zheng, Y.C. Lam, V.M. Murukeshan, J.C. Chai, D.E. Hardt, *Optics and Lasers in Engineering*, **43** (2005) 977–986.

[18] Bonse, K. -W. Brzezinka, A. J. Meixner, *Applied Surface Science*, **221** (2004) pp.215–230.

[19] P.J. McNally et al., *J. Appl. Phys.,* Vol. **79**, No. 11, 1 June 1996.

[20] T. Fanning, M.B. Lee, L.G. Casagrande, D. Di Marzio, and M. Dudley, *Journal of Electronic Materials,* Vol. **22**, No. 8, 1993.

[21] I. H. Campbell and P. M. Fauchet, Solid State Communications Volume **58**, Issue 10, June 1986, Pages 739-741.

[22] Masanori Hangyo, et al*., Jpn. J. Appl. Phys*. **25** (1986) pp. 376-379.

[23] R.L. Thomas et al., *J. Appl. Phys.* **51**, 1152 (1980).

[24] Sychyi Fang and James P. McVittie, IEEE Transactions on Electron Devices, Vol. **41**. No. 6, June 1994, pp. 1034-1039.

[25] McVittie, J.P, *1st International Symposium on Plasma Process-Induced Damage*, 13-14 May 1996, pp. 7 – 10.

[26] Liou, Y.H., Chen, Y.S., Wu, C.S., Tsai, C.S., Chi, M., *6th International Symposium on Plasma- and Process-Induced Damage,* 2001, pp. 33 – 35.

[27] J. Stopford, D. Allen, O. Aldrian, M. Morshed, J. Wittge, A.N. Danilewsky, P.J. McNally, *Microelectronic Engineering* **88** (2011) 64–71.

Analysis of Strain in Packaged Chips using 3DSM, XRDI and Micro-Raman Spectroscopy.

5.1 Introduction

As the integrated circuit (IC) industry continues to push for improvements in chip performance and form factor while driving down costs, embedding of chips into organic substrates using printed circuit board (pcb) technology has emerged as a promising technology route for 3D component integration [2, 22, 23, 24]. Core technologies such as wafer thinning to the order of tens of microns, embedding by lamination, laser drilling, via metallization and vertical stacking technologies have become key enablers in the move towards high density, high functionality 3D integrated circuits. However the range of different materials used in chip embedding and packaging can lead to the build up of internal stresses and warpage of the embedded die. IC manufacturing and chip embedding processes can also induce stresses in the chip which have the potential to affect device functionality and reliability and ultimately lead to device failure. The management of mechanical stresses is therefore one of the key enablers for the successful implementation of 3D IC technology [23].

To date test methodologies for embedded chips have consisted of finite element modelling (FEM), micro-Raman spectroscopy, optical inspection, electrical testing and destructive testing such as shear testing [1, 2, 5, 6, 8]. Significant causes of strain, and hence failure of embedded chips are known to come from 3 major sources: materials induced stresses caused by differences in the coefficient of thermal expansion (CTE), wafer / chip warpage, and stress from the embedding / lamination processes [1, 2, 5, 13, 14,]. Materials induced failures are predominantly located at or near through silicon vias (TSV), where differences in the coefficient of thermal expansion (CTE) between the Si substrate and adjacent vias can lead to the formation of stresses in the surrounding substrate [12, 13, 14]. Wafer / die warpage increases greatly at thicknesses less than 100 μm, however bonding to the Cu substrate and subsequent lamination has been found to decrease warpage and relieve stresses. During lamination pressure and heat should be sufficiently high so as to provide sufficient adhesion and prevent voids occurring; however excess pressure and heat can lead to the formation of voids and delamination [2, 6]. With so many diverse challenges to the realisation of high volume 3D IC integration, advanced, non-destructive testing methodologies are fundamental to the development of embedded chip design and manufacture.

In this chapter X-Ray Diffraction Imaging (XRDI) is used in conjunction with 3D surface modelling (3DSM) to non-destructively obtain qualitative information on the nature and extent of the strain fields in thin, chip embedded Quad Flat Nonlead (QFN) packages at different stages in the manufacture, pre-conditioning and qualification processes, and to quantify the level of lattice warpage. Micro-Raman spectroscopy complements 3DSM data by quantifying the level of strain in unpackaged chips. 3DSM and the data obtained from XRDI techniques have the potential to improve process steps in chip packaging and reduce the major sources of warpage and in package stress that can lead to device failure.

5.1.1 IZM Fraunhofer Package

The packages examined in this study are QFN-A packages [1, 2], measuring 160 µm thick and 10 mm × 10 mm in size. Packages were produced in Berlin, under the EU HERMES project. The package consists of an active die bonded Si chip, 5 mm × 5 mm in size and 50 µm thick, with a peripheral bond pad pitch of 100 µm, embedded face up in a substrate. The chip is covered from the top side with a RCC (resin-coated-copper) dielectric layer 90 – 100 µm thick. A schematic of the chip assembly, processing and testing steps are shown in Figure 5.1 (a) and (b) [1, 2].

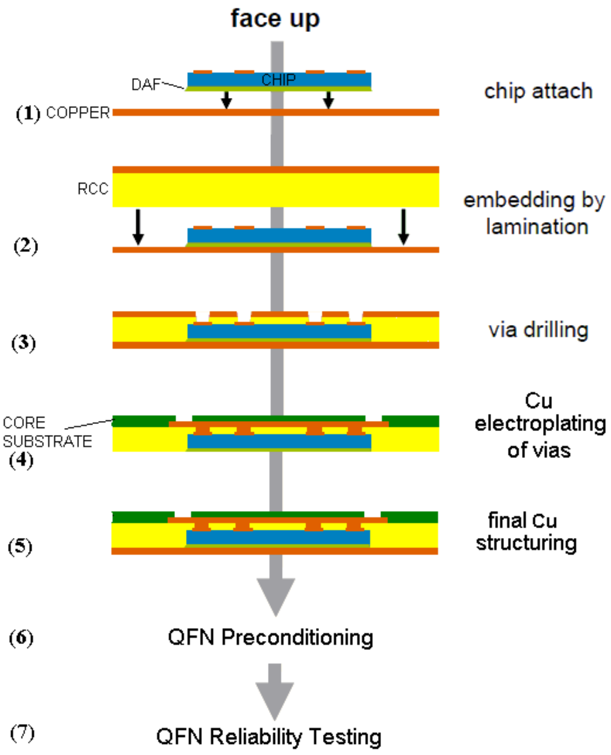

Figure 5.1(a): Schematic of 5 major chip embedding steps for QFN-A package. QFN-A chips underwent preconditioning and reliability testing after assembly.

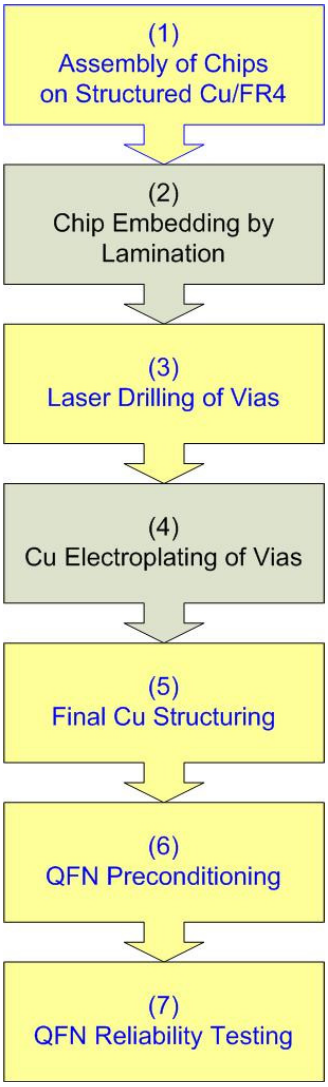

Figure 5.1(b): Process flow for 7 stages of chip embedding, preconditiong and test.

5.1.2 Chip Embedding Process

Face-up embedding was chosen for the QFN-A package as it offers the possibility of better heat dissipation via access to the back side of the chip. This is particularly important in the case of embedded power chips. Prior to embedding, chips were prepared by electrolytic deposition of 6-8 μm of Cu to the bond pads. Using a high precision (± 10 μm) die attach machine, double layered die attach film (DAF), an adhesive layer 20 μm thick was used to bond the chip to the Cu substrate (Figure 5.1 (1)). A resin coated copper (RCC) layer 90 – 100 μm thick was applied to the chip from the top side using a standard pcb multilayer vacuum lamination process [8], and the epoxy was then cured at ~185 °C for 60 min (Figure 5.1 (a) & (b), (2)). A pulsed 355 nm UV laser was used to drill the microvias through to the chip pads (Figure 5.1 (a) & (b), (3)). The vias were then cleaned to remove excess epoxy resin and improve Cu adhesion, and palladium was deposited on the epoxy surface prior to Cu metallization via electroplating (Figure 5.1 (a) & (b), (4)). Structured Cu conductor lines are required to connect the bond pads and capture pads on the chip. This was undertaken by means of laser direct imaging (LDI), which was used to expose a negative resist, which was subsequently acid etched to reveal the Cu line structure. The final step in the packaging process is Cu structuring on the bottom side of the package (Figure 5.1 (a) & (b), (5). Packages were processed in large panel format, and separated by cutting or sawing [1, 2] before undergoing pre-conditioning and qualification tests.

Samples were analysed after stages 1, 3 and 5 of the embedding process. Figure 5.2 below outlines the sample number and the corresponding process stage.

Process / Test Stage	Stage 1 Chip Attach	Stage 3 Via Electroplating	Stage 5 Post Production
Sample Reference Number	Sample 4	Atiotech 3a	09-096 No. 158
		Hitachi 3b	09-095 No. 136

Figure 5.2: Sample reference numbers and process stages for QFN-A package analysis.

5.1.3 Preconditioning and Qualification Tests:

The samples studied in this report underwent preconditioning and qualification tests in order to establish their reliability under a range of test conditions. Preconditioning tests were undertaken to simulate the effects of the board assembly process at component level. Preconditioning treatment was in line with the JESD22-A113-E [3] standard and consisted of 4 process steps. All packages were subjected to:

1. 5 temperature cycles from -40°C to 60°C, at a cycle rate of 1 to 3 cycles per hour (cph) [13], to simulate shipping conditions.
2. Dry bake for 24 hours at 125°C in order to remove all moisture from the packages.
3. Moisture soak level 2 (MSL3) (192 h, 30°C, 60% Relative Humidity), within 2 hours of the dry bake.
4. Solder reflow simulation, between 15 min and 4 hrs after removal from the temperature/humidity chamber. Three reflow passes at the established Pb free reflow temperature of 280°C, wherein cooling occurred between reflow cycles so that the reflow temperatures/times of the samples are not affected on the subsequent reflow cycles.

The second phase of testing involved 4 different reliability tests, with each package undergoing a different test. Test conditions are summarised below:

1. High temperature storage (HTS) at 150°C for 1000 hr, as defined by MIL-STD-883H [17], with the exception that HTS is done over a much longer period of time. This test is undertaken to determine the effect of high temperature storage on the packages without any electrical stresses applied.
2. Thermal cycling with 1000 cycles from -55°C to 125°C, in line with JESD22-A104D, Test Condition B [16]. The purpose of this test is to establish the resistance of the packages to extremes of high and low temperatures, and their ability to withstand cyclical stresses.
3. Temperature humidity storage, at 85°C with 85 % humidity for 1000 hr, with bias applied to the package, as defined by standard JESD22-A100C [15]. Corrosion of the package is promoted by high temperature and humidity, the corrosion process is triggered by the bias, which is applied to the package to simulate the bias conditions of the device in its real-life application. The bias can also drive mobile contaminants to areas of concentration on the die.
4. Pressure cooker test for 168 hr at 121°C, 100 % relative humidity, 2 atm pressure, as defined by standard JESD22-A102D [14]. This test is utilised to assess the ability of the package to withstand extreme temperature, humidity and vapour pressure conditions. It is used to accelerate corrosion in the metal parts of the product, including the metallization areas on the surface of the die.

Sample numbers and the corresponding reliability tests are outlined in Figure 5.3.

Process / Test Stage	Stage 6 After Preconditioning	Stage 7 After Phase 2 Reliability	Test Number
Sample Reference Number	09-095 No. 150	09-088 No. 241	1
	09-096 No. 008	09-089 No. 047	2
		09-089 No. 241	3
		09-088 No. 218	4

Figure 5.3: Table detailing sample numbers and the corresponding process stage / reliability test stages for QFN-A package analysis.

5.2 Experimental

X-Ray Diffraction Imaging (XRDI) measurements were performed at ANKA, Karlsruhe, Germany using the TopoTomo beamline [31, 32], and HASYLAB-DESY, Hamburg, Germany using the F-1 topography beamline at the DORIS III storage ring [25]. Topographs were recorded in large area transmission (LAT), large area back reflection (LABR) and section transmission (ST) geometries. The experimental setup for XRDI is described in Section 3.2.1. In the case of topographs recorded at ANKA, the PCO.4000 high resolution 14 bit cooled CCD camera, with magnification optics was used, which enabled a pixel size of 2.5 µm to be obtained [9]. The sample to camera distance (L) was 80 mm. In the case of topographs recorded at HASYLAB-DESY, images were recorded on high resolution film, (Section 3.2.2.1), and a sample to film distance, L, of 80 mm was used.

Initially ST topographs were taken at 1.0 mm steps from the pads at the top of the chip stepping sequentially until the bottom of the chip, was reached. The chip was then rotated by 90° and the process repeated, as described in section 3.4.1. In order to obtain higher resolution 3DSM topographs the image capture process was also tested using a step size of 0.5 mm, thus providing a greater number of points for definition of the 3DSM. A detailed explanation of image acquisition and building of 3DSM is available in section 3.4 of this study. With the exception of stage 3 samples 3DSM were shaded in order to enable the top and underside surfaces to be identified, with the top surface shaded in green, and the underside shaded in grey.

Micro-Raman measurements were used to quantify strain levels in the stage 1 samples. Using the 488 nm Ar^+ laser line on the *JY Horiba LabRAM HR800* high resolution Raman microscope (Section 3.6) scans were taken at 3 different positions on the chip, as described in Figure 5.4. The scan positions were selected so as to include regions on the chip which are prone to warpage, while avoiding the vias and patterning/symbols on the chip surface. Scans taken at positions 1 and 3 measured 1,400 µm wide × 25 µm high, with step sizes of 20 µm and 5 µm respectively. The central scan (Figure 5.4, position 2) measured 1,000 µm wide × 25 µm high, with step sizes of 20 µm and 10 µm respectively.

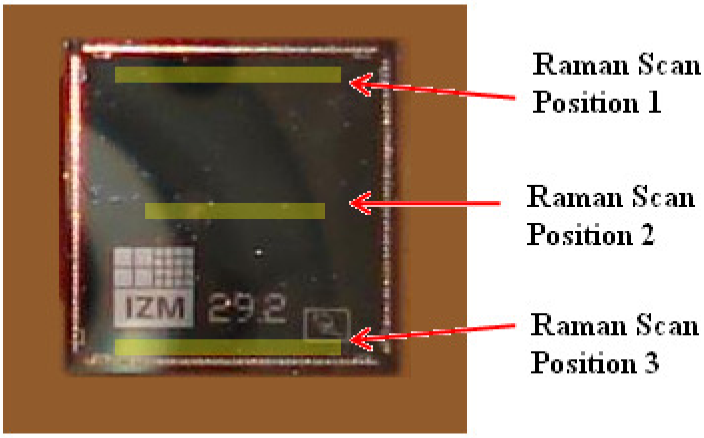

Figure 5.4: Positions of Raman matrix (2D) scans on Sample 4.

Before commencing measurements the laser was allowed to stabilise and the system was calibrated using a standard, unstrained piece of (100) silicon and calibrating to the triply degenerate Transverse Optical (TO) phonon induced Raman peak shift of 520.07 cm^{-1} in Si [19, 20]. As the total thickness of the chip, die attach film and Cu substrate measured less than 200 µm, flatness of the stage 1 chips was an issue. To compensate for any small deviations in flatness the chip-substrate structure was taped to a microscope slide and the optical auto-focus functionality on the micro-Raman system was used. This enabled signal intensity levels to be maintained across the width of the chip while using a short accumulation time (1s), to prevent heating of the sample. As the total scan time for each scan was less than one hour it was not necessary to correct for thermal and temporal peak shifts after data acquisition.

5.3 Results

Samples of the QFN-A packaged chips were characterised using both X-Ray Diffraction Imaging (XRDI) and 3-Dimensional Surface Modelling (3DSM) after 5 of the 7 processing stages described in Figure 5.1(b); chip attach, via drilling, final Cu structuring, preconditioning and reliability testing.

5.3.1 Stage 1: Chip Attach

After the first processing step, samples consisted of 5 mm × 5 mm squares of 50 μm thick Si embedded face up on a Cu substrate. A single chip, sample 4, was examined using XRDI, 3DSM, and the Ar^+ laser of the micro-Raman system. Initial tests on stage 1 chips showed them to be highly sensitive to the x-ray beam heat load from the synchrotron, which was estimated to raise the local chip temperature to ~40°C. As a result of this the acquisition time for ST and LAT topographs was set to 0.5 s, and the contrast of ST and LAT topographs was therefore compromised to a minor extent. Figure 5.5 (a) is a LAT topograph of the centre part of the sample. The sample shows some patterning along the left and right edges, and a grain running from the top right through to the bottom left corner of the image. Although several LAT images were taken they could not be patched together due to the lack of patterning / features on the topograph. The overall dimensions of the LAT topograph are approximately 5,000 μm × 12,700 μm, with the elongation of the topograph occurring parallel to projection of the diffraction vector, **g**. Elongation of LAT topographs is observed on several samples in the study. This phenomenon is most likely a result of the high degree of lattice curvature present in the chips / packages. We know that the greatest sensitivity to lattice displacement occurs when **g** is parallel to, or antiparallel to the reciprocal lattice vector **h**. This condition is satisfied in the case of sample 4, as shown in the LAT (Figure 5.5(a)).

3DSM showing the misorientation of the 2 2 0 planes in the Si chip (Figures 5.5(b) & (c)) have been normalised to reflect the square shape of the chip, and thus compensate for the geometric distortion observed in the corresponding LAT.

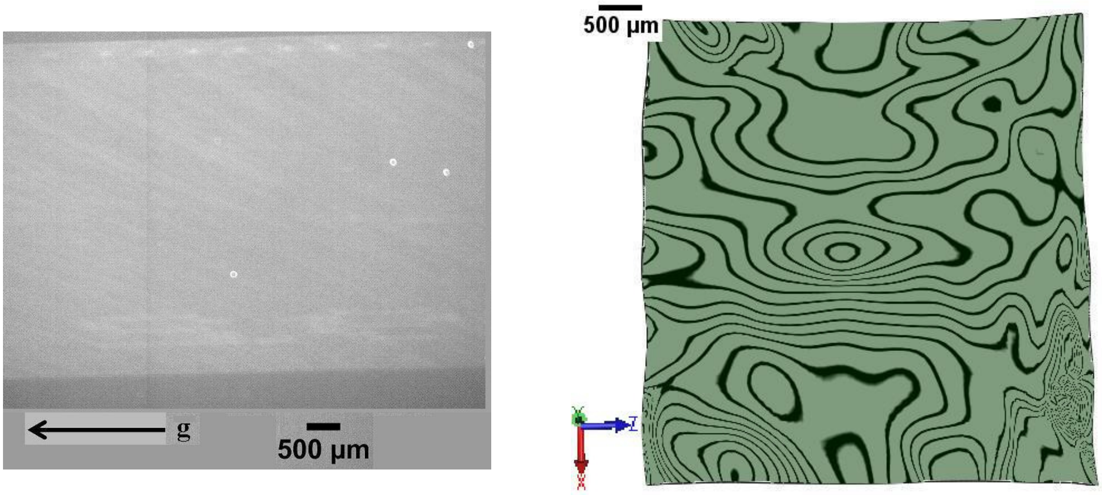

Figure 5.5 (a) & (b), (a) 2 2 0 LAT topograph from stage 1 chip showing central region of sample 4. White dots are artefacts from the CCD. The projection of the diffraction vector g onto the plane of the recording film is also indicated. (b) 3DSM of stage 1 chip showing misorientation of (2 2 0) Si planes of sample 4. Contours are shown to indicate degree of warpage of chip.

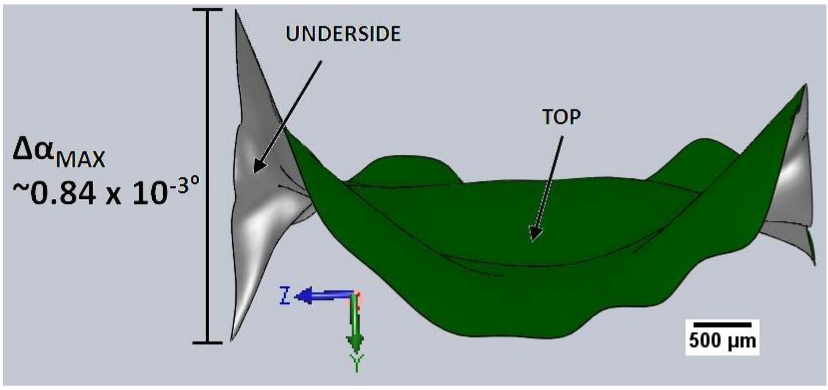

Figure 5.5 (c): 3DSM showing Δα, the relative misorientation of (2 2 0) Si planes of sample 4 viewed end on, with ST position corresponding to the upper edge of the chip facing the page.

The 3DSM are created from a series of 10 ST topographs as described in section 3.4. Distortion in the ST topographs is formed by the orientational contrast mechanism, where diffracted x-rays from highly strained and hence misorientated, regions in the Si lattice possess an altered Bragg angle. Deviations in the recorded position of the diffracted Si in the ST images (Figure 5.7) are seen as a result of the lattice planes being distorted either in compression or tension across the full width of the Si chip. Possible causes of lattice distortion are described in Figures 5.6 (a)-(c). During heteroepitaxal growth, if there is a large mismatch between the lattice constants of the two materials, and the layers are grown below the critical thickness, the upper layer may become strained with the lattice symmetry changing from cubic to tetragonal, (Figure 5.6 (a)). Overlayer deposition can also lead to strain, resulting in tension and hence distortion in the underlying Si lattice (Figure 5.6 (b)). The most likely cause of lattice misorientation seen in the ST topographs and 3DSM in this study is lattice distortion across the entire volume of the chip, resulting from chip warpage (Figure 5.6(c)). For a given chip/package the origin and extent of chip warpage depends on the processing/embedding stage.

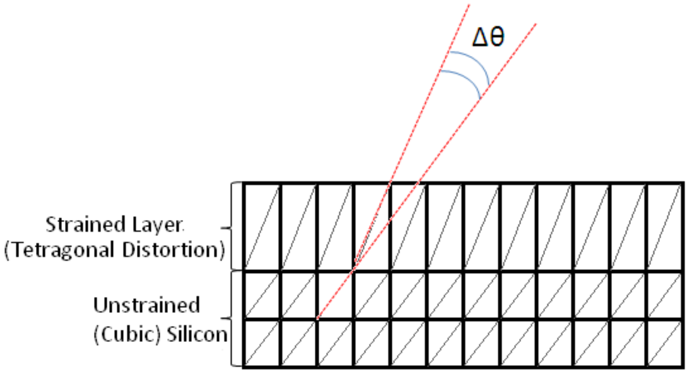

Figure 5.6 (a): Heteroepitaxial growth results in strained overlayer. Δθ changes, and the lattice symmetry alters from cubic to tetragonal.

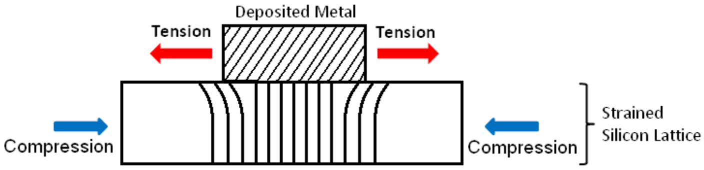

Figure 5.6 (b): Metal overlayer deposition causes tension in underlying Si leading to lattice distortion.

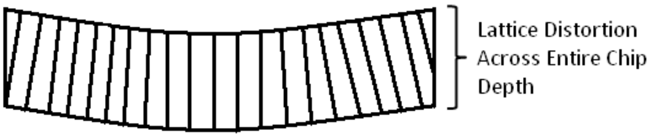

Figure 5.6 (c): Chip warpage results in lattice distortion through entire volume of chip.

For orientational contrast to occur, the lattice misorientation must exceed the x-ray beam divergence, which is a maximum of 2 mrad in the case of the ANKA synchrotron [17]. In a perfect crystal Bragg diffraction occurs according to the relationship:

$$\lambda = 2d_{hkl} \sin\theta_B \qquad (5.1)$$

where d is the interplanar spacing, θ_B is the Bragg angle, and λ is the wavelength of the incident beam. In a perfect crystal Bragg diffraction occurs at an angle of $180^0 - 2\theta_B$ relative to the incident beam.

$\Delta\theta_{MAX}$, the maximum shift in Bragg angle, given by the combination of the lattice dilation, ${\Delta d}/{d}\,\tan\theta$ and the lattice tilt, α;

$$\Delta\theta_{MAX} = {\Delta d}/{d}\,\tan\theta_B + \alpha \qquad (5.2)$$

where Δd is the deflection of planes parallel to $\overleftarrow{g}$.

$^{\Delta d}/_{d}\tan\theta$ cannot be obtained, as white beam radiation provides a large number of wavelengths, which give a diffracting wavelength for any dilated planes.

$$\therefore \Delta\theta_{MAX} \propto \alpha \qquad (5.3)$$

The magnitude of orientational contrast shift can be calculated from:

$$^{\Delta S}/_{2L} \cong \Delta\alpha \qquad (5.4)$$

where ΔS is the measured angular misorientation across the measured length of the sample, as shown in Figure 5.7, L is the sample the sample to film distance used in SXRT (80 mm), and Δα is the maximum apparent shift in the Bragg angle due to the strain-induced tilt of the diffracting planes [15, 16, 18]. $\Delta\alpha_{MAX}$, the maximum misorientation of the Si planes for the reflection imaged (using XRDI), is therefore measured relative to the points of greatest and least angular displacement in the relevant ST topograph, as shown in Figure 5.7.

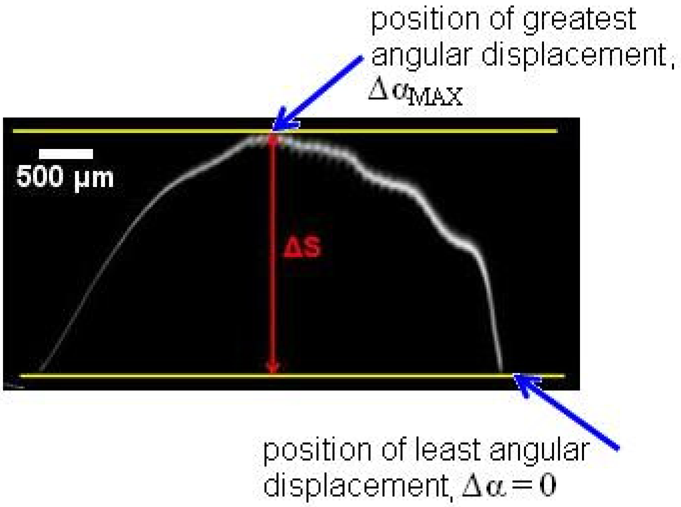

Figure 5.7: 2 2 0 ST topograph of sample 4, number 1 in series of 10 ST topographs which combine to form images 5.4 (b)-(d). Yellow lines show maximum deviation in ST topograph, which is equal to ΔS.

The greatest lattice distortion is observed in the final ST topograph, at the top of the chip, as seen in Figures 5.5 (c) and 5.7. $\Delta\alpha_{MAX}$, the maximum lattice tilt for Sample 4 is 0.84×10^{-3} (± 5%) degrees, considerably less than that seen at later processing / reliability testing stages. Figures 5.8 – 5.10 (a)-(b) show micro-Raman scans across 3 regions of the sample as described in Figure 5.4. Micro-Raman spectra were taken using the Ar^+ laser, which has a penetration depth of ~556 nm in Si, thus the data are therefore indicative of strain levels close to the surface of the chip. Scans 1 and 3, across the upper and lower regions of the chip respectively, show a single narrow Si peak, indicative of crystalline Si, centred on ~521.7 cm^{-1}. If a uniform biaxial stress model is assumed the stress corresponding to the Raman peak shift can be calculated from equations 4.1 and 4.2, Section 4.3.1 [21]:

$$\sigma_{xx} = \sigma_{yy} = \Delta\omega / -4 \quad GPa \qquad (4.2)$$

where Δω is the change in Raman frequency from the calibration position at 520.07 cm^{-1}, and σ_{xx} and σ_{yy} are the stress components for biaxial strain in the x - y plane.

Strain levels across the scans 1 and 3 (Figures 5.8 & 5.10, (a), (b)), range from 345 – 470 MPa, with both regions in tensile strain, and the highest strain levels are closest to the corners of the chip. The central micro-Raman scan 2, (Figure 5.9 (a), (b)), shows uniform strain levels of up to ~360 MPa from left to right across the chip, with changes in the strain occurring from the top of the scan downwards. As with scans 1 and 2 tensile stress is largely present, although low levels of compressive stress are also observed. Only a single phase of crystalline Si is present in scan 2, signified by a single narrow peak, with an average FWHM of 4.1 cm^{-1}. Multiple scans on the same region prove that the regular strain pattern is a genuine strain phenomenon rather than a temporal or thermal effect.

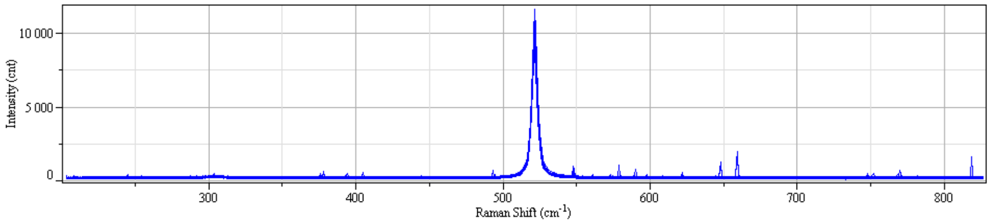

Figure 5.8 (a): Micro-Raman spectra for top section (Scan 1) of Sample 4 as shown in Figure 5.4. Main peak, indicative of crystalline Si is centred on 521.6 cm^{-1}.

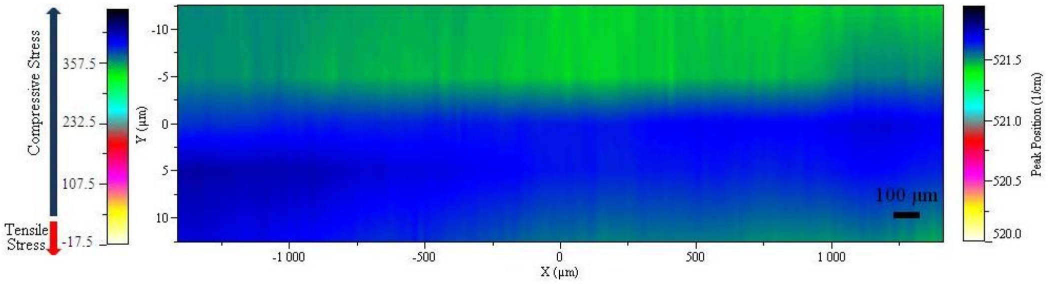

Figure 5.8 (b): Micro-Raman 2D scan for top section (Scan 1) of Sample 4 as shown in Figure 5.4. Entire region is in compressive stress, as indicated by scale

on left side of image. Highest levels of stress are indicated in blue/black, and present at the edges of the scan.

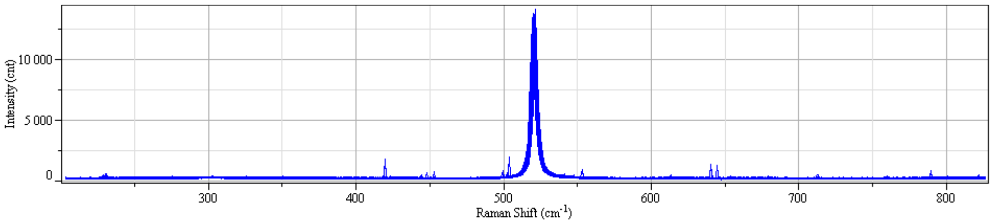

Figure 5.9 (a): Micro-Raman spectra for middle section (Scan 2) of Sample 4 as shown in Figure 5.4. Main peak, indicative of crystalline Si is centred on 520.75 cm^{-1}.

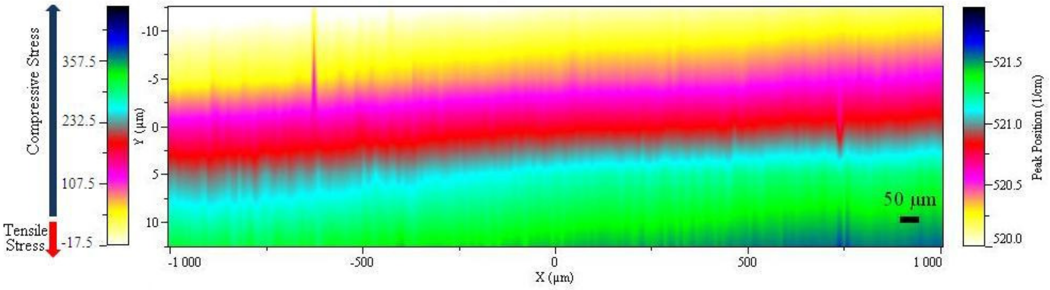

Figure 5.9 (b): Micro-Raman 2D scan for middle section (Scan 1) of Sample 4 as shown in Figure 5.4. Lower ~2/3 of scan is in compressive stress, with low levels of tensile stress also present, as indicated by scale on left side of image.

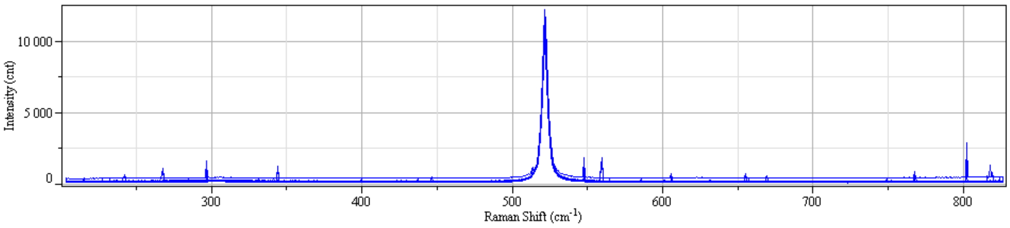

Figure 5.10 (a): Micro-Raman spectra for top section (Scan 3) of Sample 4 as shown in Figure 5.4. Main peak, indicative of crystalline Si is centred on 521.75 cm^{-1}.

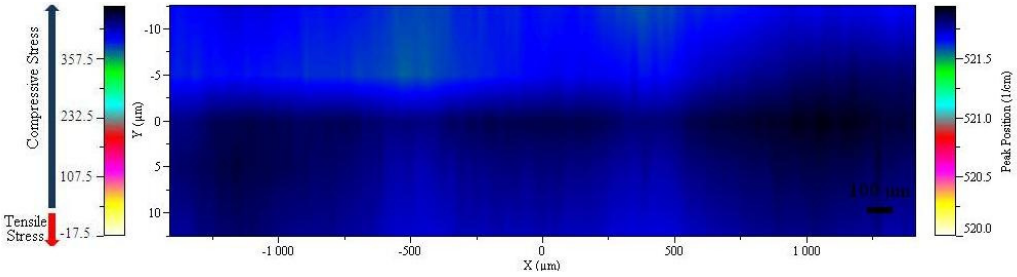

Figure 5.10 (b): Micro-Raman 2D scan for bottom section (Scan 3) of Sample 4 as shown in Figure 5.4. Entire region is in compressive stress, as indicated by scale on left side of image. Highest levels of stress are indicated in blue/black.

Micro-Raman spectroscopy is a well established and widely used characterisation technique for analysis of strain in Si die and packaged chips [20, 21, 27, 28]. As such it provides an appropriate platform from which to evaluate the efficacy of novel, qualitative techniques such as XRDI and 3DSM. Raman results show strain levels close to the surface of the chip of the order of 100's of MPa, the strain pattern shown in the 2D micro-Raman scans, with the greatest levels of compressive strain apparent at the edges and corners of the chip (Figures 5.8-5.10), compare well with the 3DSM (Figure 5.5(b & c)), which exhibit a uniform, relatively undistorted (warped) region at the centre of the chip, and warpage of the 2 2 0 lattice planes along all 4 edges of the chip. Although the magnitude of the induced lattice warpage, as seen in the 3DSM, and measured from the ST topographs is relatively small at this early processing stage, micro-Raman results prove that close to the surface, the induced strain levels are high and have the potential to affect device functionality and/or reliability [2, 14, 26]. The LAT topograph (Figure 5.5(a)), shows uniform strain across the chip, demonstrating that detailed information on lattice warpage is not always apparent from conventional XRDI, and that 3DSM is a valuable tool in characterisation of strain in packaged chips.

5.3.2 Stage 3: Via Electroplating

Two samples were anaylsed after Cu electroplating of the vias; Atiotech 3a and Hitachi 3b. As illustrated in Figure 5.1 (a), after stage 3 of processing die are completely enclosed in Cu and no part of the die is visible (Figure 5.11). Lasers used in Micro-Raman spectroscopy cannot penetrate Cu, and thus micro-Raman spectroscopy is not feasible beyond the first two stages of the packaging process (Figure 5.1 (a & b)). Likewise, none of the currently available IC characterisation metrologies can non-destructively measure or image stress/strain, warpage or defects beneath the SoC/SiP package lid [23]. This is a major drawback, since the electrical performance of the SoC/SiP is governed by the semiconducting Si (or SiGe, Ge, GaAs, InP, etc.) chips embedded in the system. XRDI, and in particular 3DSM are therefore an important tools in the analysis of major sources of die warpage and in-package stress, both techniques can be utilised at all stages of the chip embedding and packaging processes.

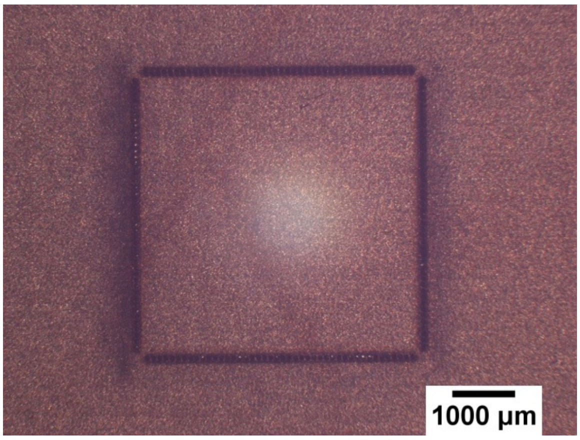

Figure 5.10: Stereo microscope image of die after stage 3, drilling of micro-vias to the Cu pads.

LAT topographs of both samples display a distinctive wave pattern, with a peak to peak pitch of 1050 – 1150 µm. As with the Stage 1 sample the LAT topographs (Figures 5.12 and 5.13), are elongated in the direction parallel to $\overleftarrow{g}$. The irregular pattern on the LAT images did not allow the topographs to be patched together to obtain a diffraction image of the complete chip, however the magnitude of the induced lattice warpage appears to be approximately two times greater parallel to the projection of the diffraction vector $\vec{g}$ onto the ccd than perpendicular to it (Figure 5.23 (a)).

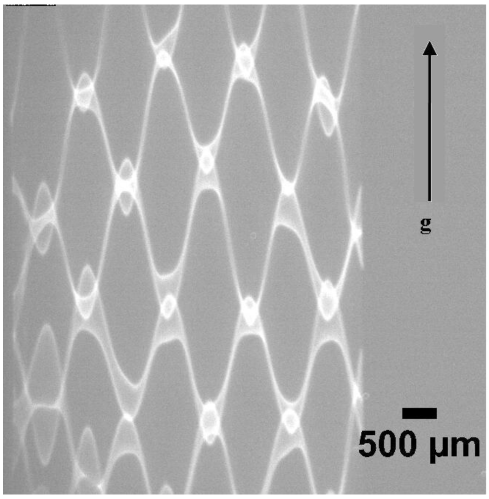

Figure 5.12: 2 2 0 LAT topographs reflection from central section of Atiotech 3a sample. Sample was oriented at 90° when LAT was recorded.

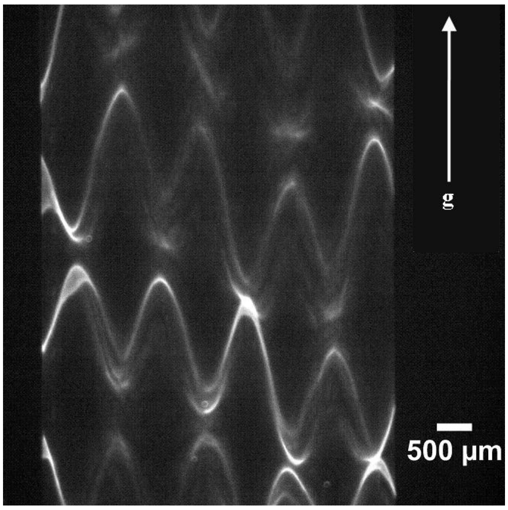

Figure 5.13: 2 2 0 LAT topographs from central section of Hitachi 3b sample. Sample was oriented at 90° when LAT was recorded.

The wave pattern is most prominent in the central region of the chip, with peaks smoothing out and becoming less pronounced towards the edges of the chip. Initial examination of the

LAT topographs in Figures 5.12 and 5.13 gives little information on the nature of the lattice distortion which would give rise to such a pattern, however the 3DSM clearly show the pattern of strain induced die warpage inside the packages (Figures 5.13 (a) – (f) and 5.15 (a) – (d)). As with the previous sample the shape of the 3DSM have been normailised to reflect the square shape of the chip. In addition to normalisation, additional connectors were added while constructing the 3DSM [30], to allow more precise control of the flow of the boundary surface. This was undertaken to ensure an accurate surface between adjacent splines with a large change in slope between them.

Two sets of 3DSM are shown for each sample, to represent topographs obtained from the chips at 0° (horizontal ST topographs) and 90° (vertical ST topographs). As reflections arise from different crystal planes (section 3.4.1), 3DSM for ST topographs recorded at 0° and 90° differ, with bumps more pronounced in vertical (90°) 3DSM in both the Atiotech 3a and Hitachi 3b chips. Figure 5.14 (f) demonstrates how the bumps on the 3DSM relate to the wave pattern on the LAT topograph, and further demonstrates the efficacy of the surface mapping process for packaged chips. Δα measurements for both chips at 0° and 90° show the relative angular lattice misorientations across the length of the sample to be approximately equal for both chips, with a $\Delta\alpha_{MAX}$ of ~0.9 × 10^{-3} (± 5%) degrees, for the horizontal ST topographs and ~0.65 × 10^{-3} (± 5%) degrees (Figures 5.14(b), 5.15(b)), for vertical ST topographs (Figures 5.14(d), 5.15(d)).

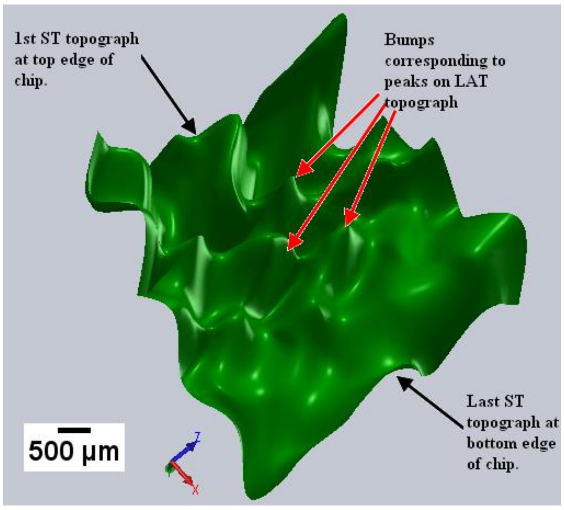

Figure 5.14(a): 3DSM of misorientation of (2 2 0) Si planes inside Atiotech 3a sample. 3DSM illustrates bumps corresponding to peaks on LAT topograph. 10 ST

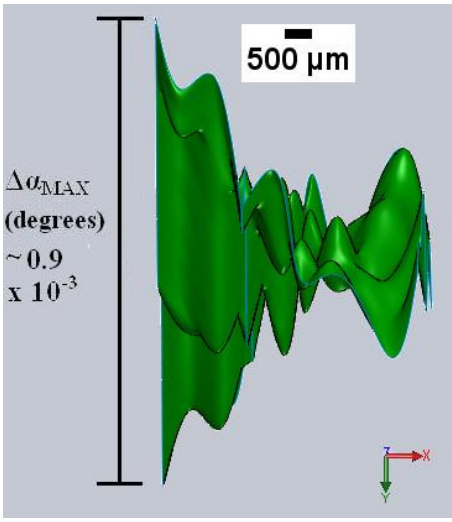

Figure 5.14 (b): 3DSM of misorientation of (2 2 0) Si planes inside Atiotech 3a sample, showing $\Delta\alpha_{MAX}$. Sample was

topographs were taken vertically across sample, beginning at the top edge of the chip. Sample was oriented at 0° when ST were recorded.

oriented at 0° when ST were recorded.

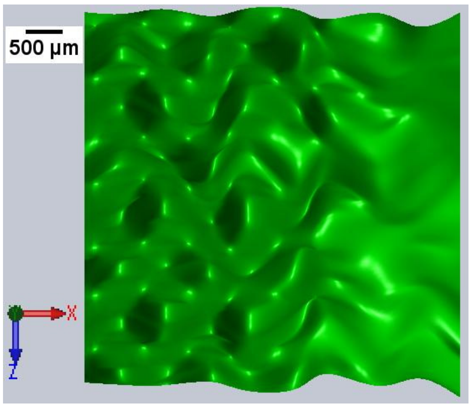

Figure 5.14(c): 3DSM of misorientation of (2 2 0) Si planes inside Atiotech 3a sample. Sample was oriented at 90° when ST were recorded.

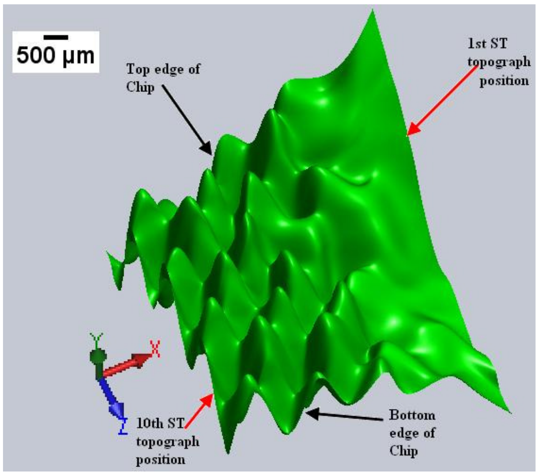

Figure 5.14(d): 3DSM of misorientation of (2 2 0) Si planes inside Atiotech 3a sample. Sample was oriented at 90° when ST were recorded.

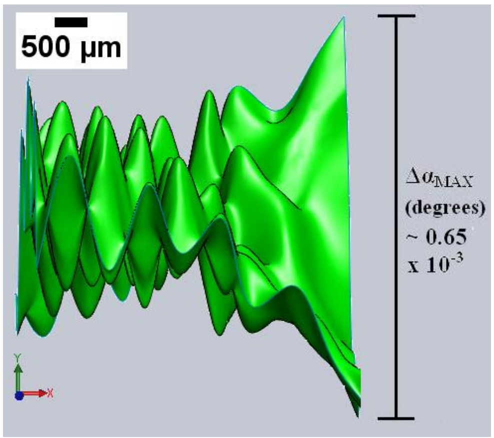

Figure 5.14(e): 3DSM of misorientation of (2 2 0) Si planes inside Atiotech 3a sample, showing $\Delta\alpha_{MAX}$. Sample was oriented at 90° when ST were recorded.

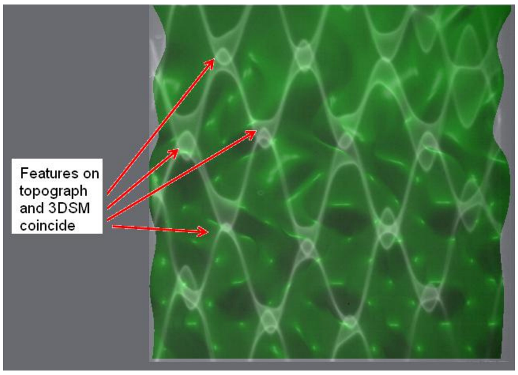

Figure 5.14(f): 3DSM of misorientation of (2 2 0) Si planes inside Atiotech 3a sample with LAT overlaid. For both images topographs were recorded with the sample rotated at 90°. Scale is same at that for Figure 5.11.

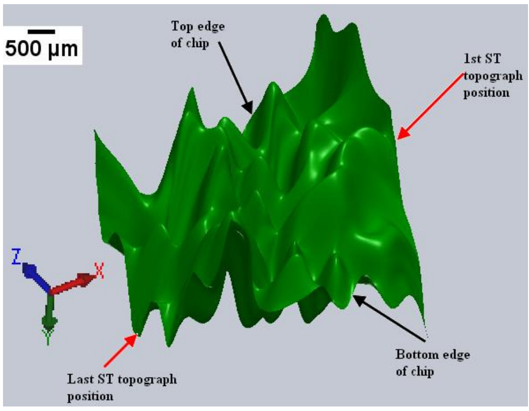

Figure 5.15(a): 3DSM of misorientation of (2 2 0) Si planes inside Hitachi 3b sample. 3DSM illustrates bumps corresponding to peaks on LAT topograph. 10 ST topographs were taken horizontally across sample, beginning at the top edge of the chip.

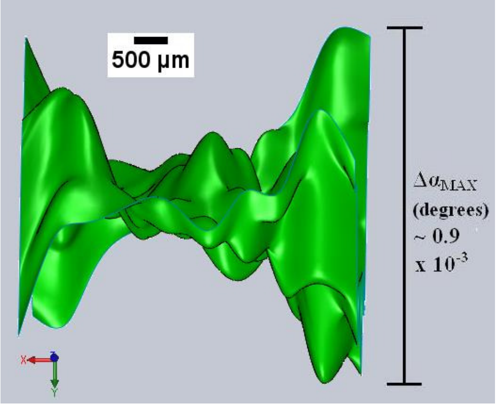

Figure 5.15(b): 3DSM of misorientation of (2 2 0) Si planes inside Hitachi 3b sample, showing $\Delta\alpha_{MAX}$. Sample was oriented at 0° when ST were recorded.

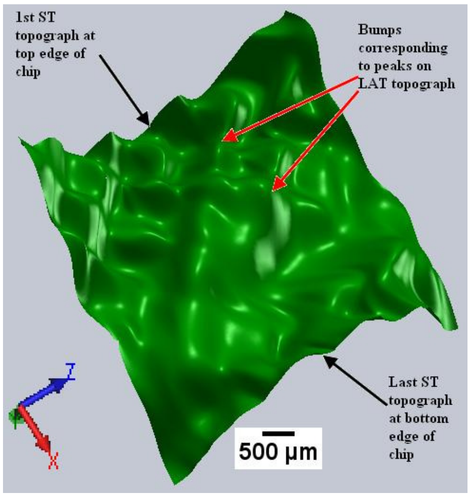

Figure 5.15(c): 3DSM of misorientation of (2 2 0) Si planes inside Hitachi 3b sample. 3DSM illustrates bumps corresponding to peaks on LAT topograph. 10 ST topographs were taken vertically across sample, beginning at the bottom edge of the chip.

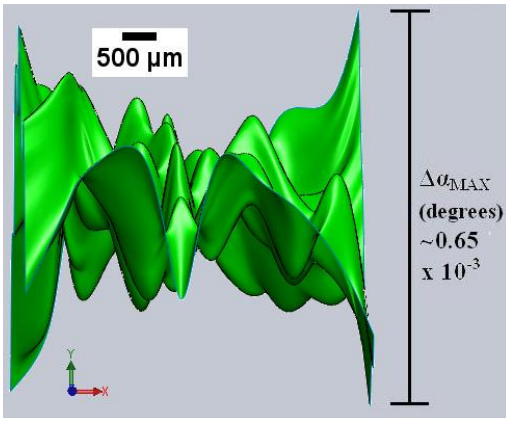

Figure 5.15(d): 3DSM of misorientation of (2 2 0) Si planes inside Hitachi 3b sample, showing $\Delta\alpha_{MAX}$. Sample was oriented at 90° when ST were recorded.

The development of the regular pattern of bumps / peaks at this stage in the process, and its absence at stages 1 and 5 suggests the phenomenon is linked to either the chip embedding by vacuum lamination or via drilling processes. TSVs are positioned along the edges of the chip, with 44 vias on each side placed 100 µm apart, the density and position of the bumps is therefore inconsistent with TSV drilling and placement. Previous laboratory based studies utilising FEM and SEM analysis [6, 29] on chips embedded in epoxy, have identified a region of high stress concentration between the chip and the epoxy, leading to cracking and delamination. The lamination process for QFN-A packages has undergone comprehensive development and optimisation [1, 2, 7, 8, 11] over the course of several projects. Heating rate and pressure are critical parameters with respect to lamination integrity. High heating rates at low pressures (5 – 10 bar) can lead to the occurrence of voids, and excessive epoxy fluid viscosity has the potential to cause insufficient epoxy coverage around the chip and influence package flatness [1, 2].

The distinctive pattern of lattice warpage seen after stage 3 processing is therefore most likely linked to vacuum lamination process, where the presence of voids or variations in epoxy coverage may lead to localised variations in strain in the crystal lattice, leading to the formation of bumps (Figures 5.14 & 5.15 (a) – (f)).

5.3.3 Stage 5: Post Production

Two post production samples were taken from batch 2 and examined prior to the preconditioning process. In the case of the first sample, 09-096 no. 158, the topograph of the 2 2 0 reflection in LAT topography (Figure 5.16(a)) is comprised of 6 camera images patched together. The topograph measures approximately 14,200 µm × 45,200 µm, illustrating stretching of the LAT topograph both parallel to, and perpendicular to the diffraction vector **g**. Although elongation occurs in all directions, it is over 3 times greater parallel to **g**, similar to the effect seen in LAT topographs in stages 1 and 3.

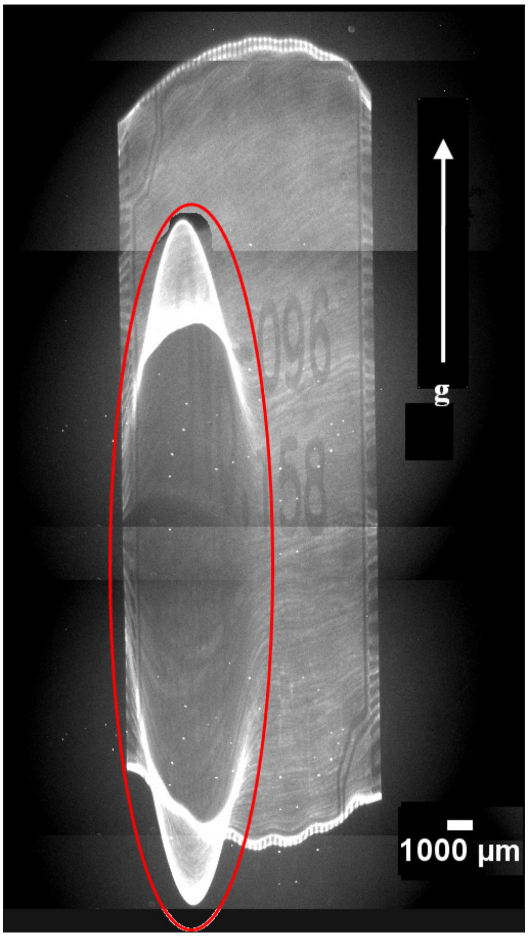

Figure 5.16(a): LAT topographs of sample 09-096, no 158. 2 2 0 reflection was recorded using a CCD camera. Region circled in red corresponds to region shown in Figure 5.16 (b).

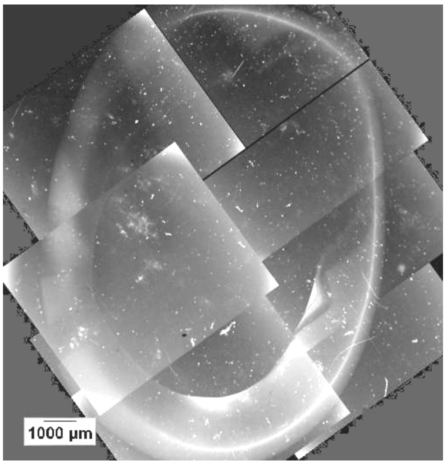

Figure 5.16(b): 0 2 10 LABR topograph of elliptical region circled in Figure 5.16 (a). Image was recorded on film and the contrast inverted for ease of comparison.

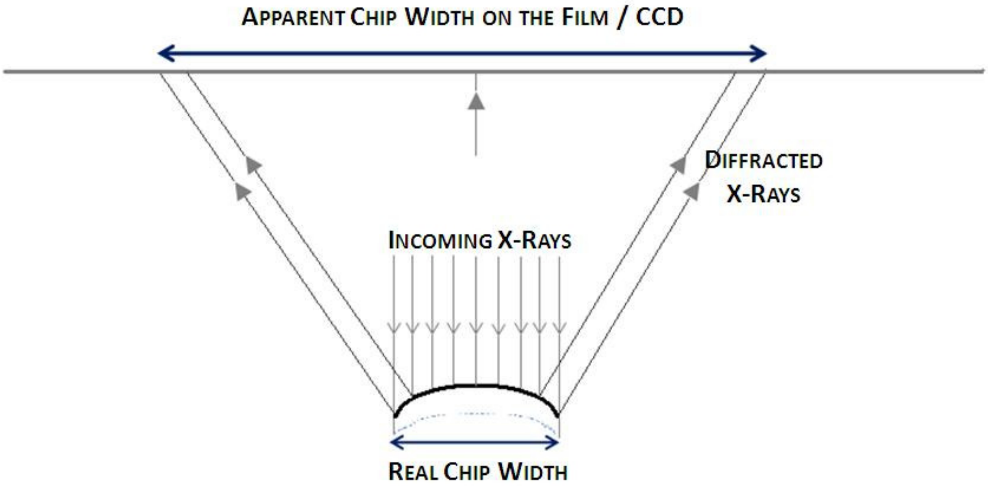

Figure 5.16 (c): Diagram illustrates how the x-rays diffract from the chip and diverge forming an elliptical shaped strain pattern.

In Figure 5.16 (d) the image has been normalised to compensate for this geometrical distortion, and the true square shape of the chip is reflected. The region circled in red, Figure 5.16(d), corresponds to the region shown in the 0 2 10 LABR topograph in Figure 5.16(b). Figure 5.16 (c) illustrates how the convex lattice planes interact with this highly stressed region and diffract the incoming beam, forming an elliptical shaped strain pattern. Orientational contrast occurs when diffracted beams overlap or diverge due to lattice misorientation. In the case of topographs recorded using a ccd camera the image contrast is inverted, and regions of low intensity, where loss occurs appear black. The greatest lattice distortion is therefore located towards the centre of the circled region.

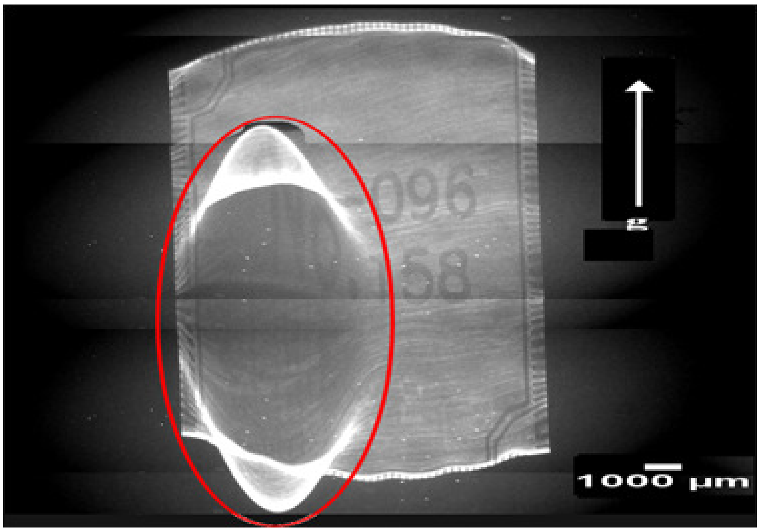

Figure 5.16(d): LAT topographs of sample 09-096, no 158, as shown in Figure 5.16 (a), with image normalised to compensate for geometric distortion parallel to $\vec{g}$.

Chip support and clamping in die bonding and chip placement processes are critical for die placement accuracy [1]. When support is insufficient warpage can occur [11, 1]. The LAT topograph of sample 09-096 no. 136 (Figure 5.22 (a)), measures approximately the same dimensions as LAT topograph of sample 09-096, no 158 (Figure 5.16 (a)) and shows a similar strain field pattern, with a corresponding elliptical region of high distortion at the same location. The uniform nature of the strain fields, and their presence on both packages, suggests they are linked to the manufacturing process. They may be due to the supports or clamps in die bonding and chip placement processes, perhaps where a die or substrate is supported on two sides, stress from processing can manifest itself in unsupported planes. The presence of vias can also lead to localised stresses in the package. Via drilling was undertaken using a pulsed 355 nm UV laser. We know that localised heating of the Cu surrounding very small diameter (15 μm) vias can lead to warpage [10], and can induce significant strain ~ MPa (Figures 5.17 (a), (b)) [4]. Die warpage may therefore be partially attributable to vias. TSV can also induce stress by squeezing / stretching the adjacent material leading to material deformation, debonding and delamination.

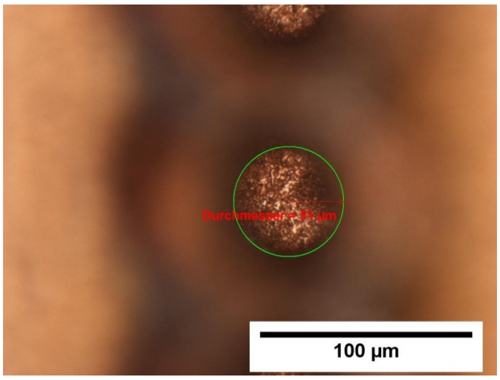

Figure 5.17 (a): Stereo-microscope image taken after drilling the vias to the copper pads with the UV laser. View shows drilled via focusing on the underliyng chip Copper pad. Scale bar is 100 µm, via diameter is 51 µm.

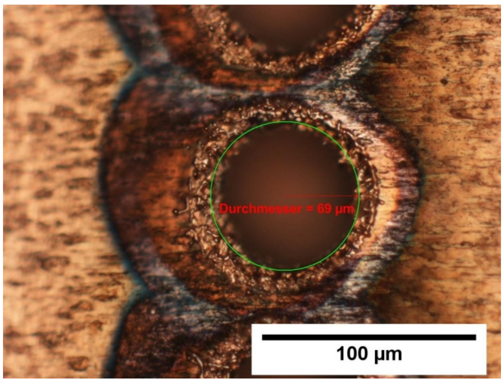

Figure 5.17 (b): Stereo-microscope image taken after drilling the vias to the copper pads with the UV laser. View shows drilled via focusing on the upper Cu layer of the package. Note distortion of via edges and surrpunding region, indicating the presence of stress and strain. Scale bar is 100 µm, via diameter is 69 µm.

The graphs below (Figures 5.18 and 5.19) show $\Delta\alpha_{MAX}$, the maximum measured strain induced lattice tilt, for ST topographs at positions 1-5 (Figure 3.14), in both horizontal and vertical directions. As the normal (unstrained) position of the ST image is not known, $\Delta\alpha_{MAX}$ is defined, as in Section 5.3.1, where $\Delta\alpha=0$ is the position of least deviation of the ST image, and $\Delta\alpha_{MAX}$ is the position of greatest deviation, as shown in Figure 5.7. The maximum lattice warpage ranges from ~ 1.69×10^{-3} - ~0.15×10^{-3} (± 5%) degrees for 09-096, no 158 and from ~2.89×10^{-3} - ~0.78×10^{-3} (± 5%) degrees for 09-096, no 136, and is dependent on the location on the chip.

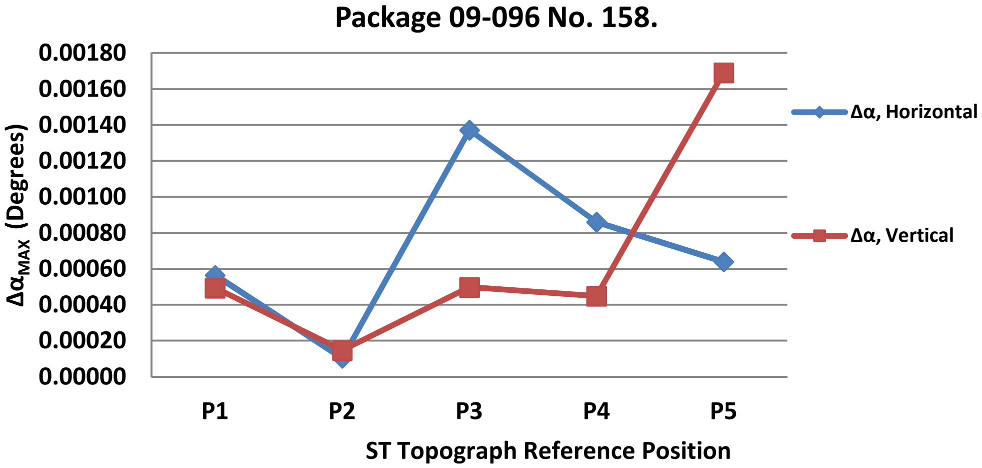

Figure 5.18: Angular displacement (warpage) data for package 09-096 No. 158. Horizontal and Vertical ST topograph positions (P1 – P5) correspond to red lines in Figure 3.14.

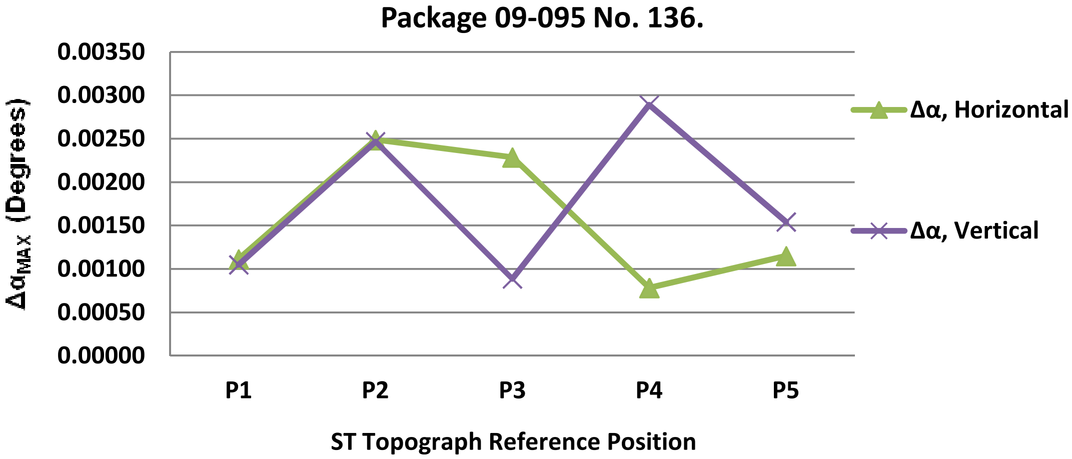

Figure 5.19: Angular displacement (warpage) data for package 09-095 No. 136. Horizontal and Vertical ST topograph positions (P1 – P5) correspond to red lines in Figure 3.14.

The 3DSM for both samples at stage 5, post production, are each comprised of 5 ST topographs placed 1 mm apart, they are therefore of lower resolution than the previous 3DSM from stages 1 and 3. The 3DSM of sample 09-096 no. 158 are shown in Figures 5.20 – 5.21(a) - (c) below. 3DSM formed from both the horizontal and vertical ST topographs again confirm the presence of the characteristic distorted region, circled in red, at the same position in the surface maps, and the magnitude of the measured angular misorientation is greatest in the case of the surface maps from the horizontal ST topographs. The images show the maximum apparent shift in Bragg angle due to the strain induced tilt of the diffracting (2 2 0) Si lattice planes inside the sealed package. The 3-dimensional surface models clearly pinpoint the highly distorted region (circled in red) corresponding to the same region highlighted in the topographs (Figures 5.16 (a) and (b)), and confirm that 3DSM can be used to produce accurate x-y maps of the location of the strain induced wafer warpage inside the packaged chip.

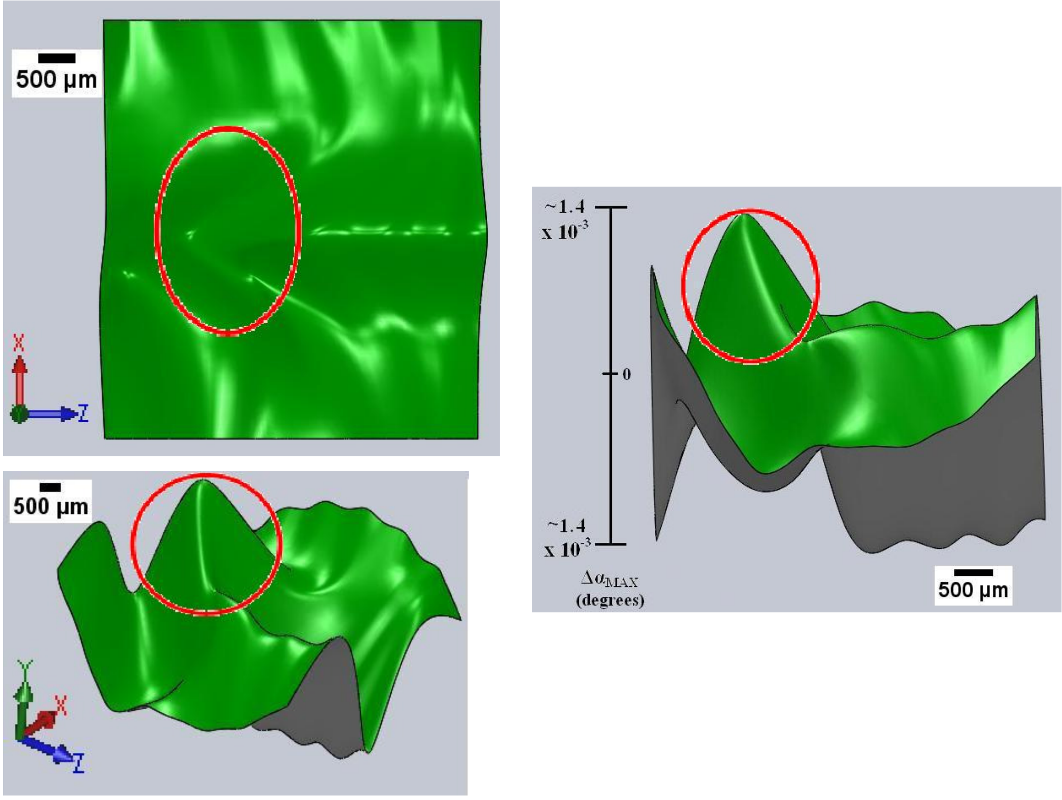

Figures 5.20 (a), (b), (c): 3DSM maps of misorientation of (2 2 0) Si planes inside a completely sealed package 09-096 no. 158. ST topographs were taken with the package orientated at 0°, i.e. in the horizontal position. Red circles correspond to the elliptical region in Figures 5.16 (a) & (b).

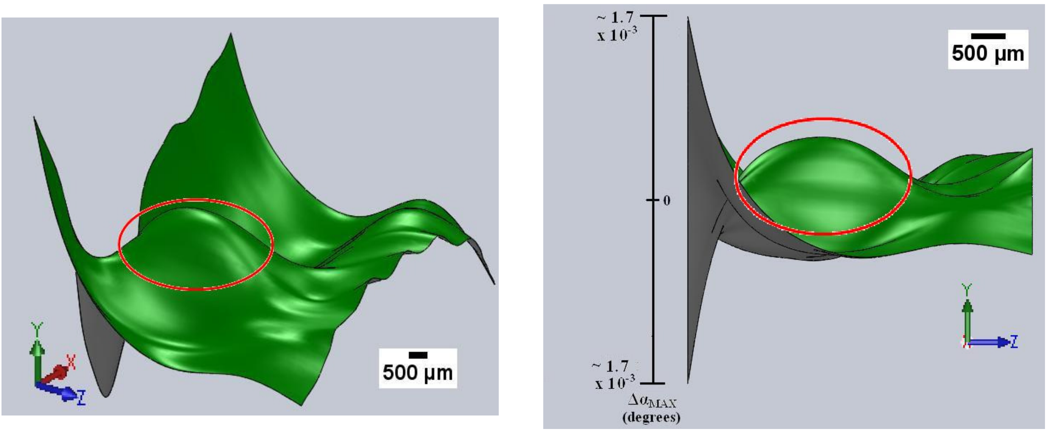

Figures 5.21 (a), (b): 3DSM maps of misorientation of (2 2 0) Si planes inside a completely sealed package 09-096 no. 158. ST topographs were taken with the package orientated at 90°, i.e. in the vertical position. Red circles correspond to the elliptical region in Figures 5.16 (a) & (b).

The 3DSM for sample 09-096 no 136 are shown in Figures 5.22 (c) and (d). As in the case of sample 09-096 no 158, the region of high lattice distortion seen in the LAT topograph (Figure 5.22 (a & b)) can be easily identified. In the case of the 3DSM comprised of vertical (90°) ST topographs the highly distorted region, circled in red in Figure 5.22 (d) is slightly displaced towards the top of the surface map when compared with the horizontal 3DSM and LAT topographs. This may be due to an insufficient number of ST topgraphs for the required resolution, and hence averaging or smoothing of points on the boundary surface formed between the splines (see Section 3.4.4). Δα, the strain induced lattice tilt is greatest in the case of the 3DSM with the chip in the vertical position, reaching a maximum of ~2.9 × 10^{-3} degrees (± 5%), at the position corresponding to the distorted region circled in red. For the 3DSM formed from horizontal ST topographs the highly distorted region circled in Figure 5.22 (c) has a measured strain induced lattice tilt of ~ 2.3 × 10^{-3} degrees (± 5%), less than the maximum value of Δα, ~ 2.5 × 10^{-3} (± 5%), degrees for the entire 3DSM of the 2 2 0 planes of the chip.

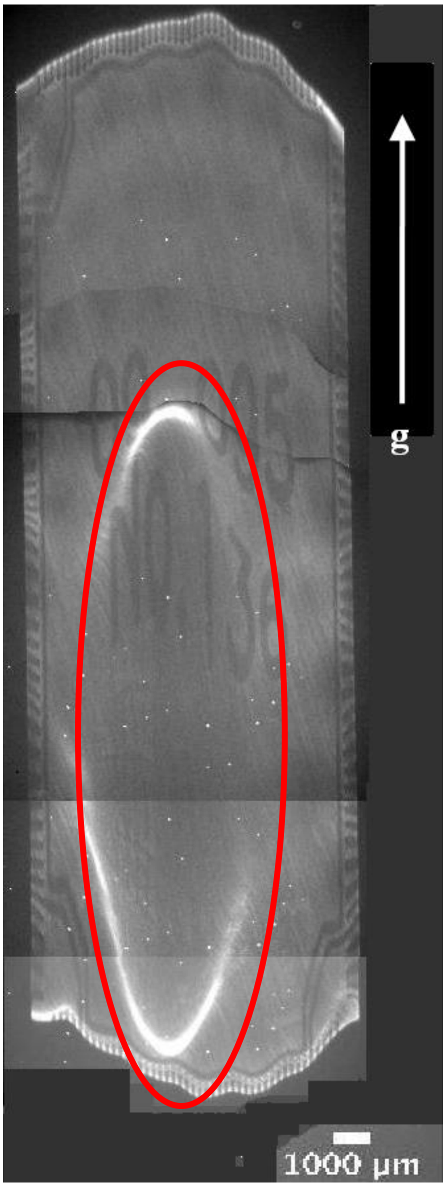

Figure 5.22(a): LAT topographs of sample 09-096 no. 136. 2 2 0 reflection was recorded using a ccd camera. Region circled in red corresponds to region of high lattice distortion.

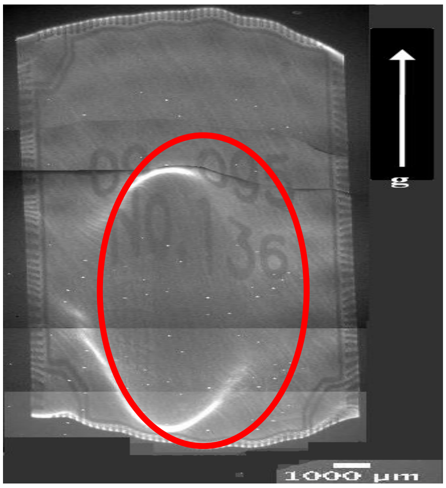

Figure 5.22(a): LAT topographs of sample 09-096, no 136, as shown in Figure 5.22 (a), with image normalised to compensate for geometric distortion parallel to $\vec{g}$.

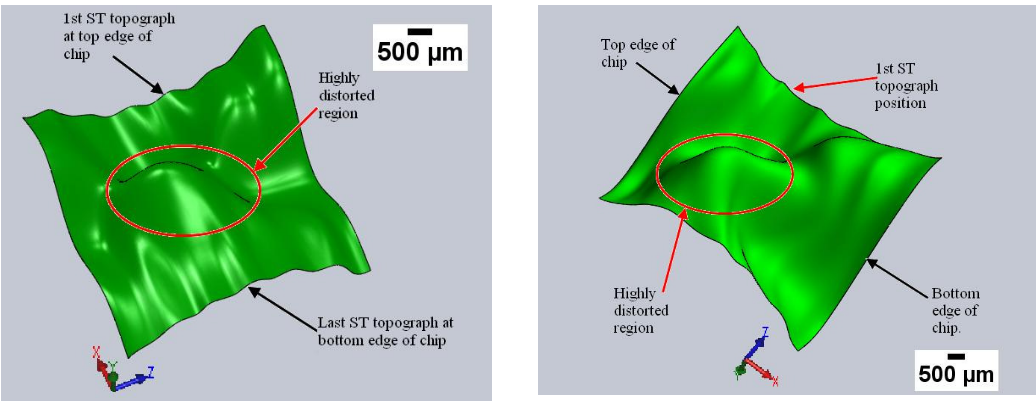

Figure 5.22(c) & (d): 3DSM maps of misorientation of (2 2 0) Si planes inside a completely sealed package 09-096 no. 136. ST topographs were taken with the package orientated at 0°, (Figure 5.20 (b)) and 90° (Figure 5.20 (c)). Red circles correspond to the elliptical region in Figure 5.20 (a). Relative positions of ST topographs which form basis of 3DSM are also shown.

5.3.4 Stage 6: Preconditioning

Two packages from batch 2, 09-095 no. 150 and 09-096 no. 008, were characterised after the preconditioning process, as described in Section 5.1.3. Preconditioning is undertaken in order to increase the likelihood of failure precipitation, and some degree of lattice warpage is expected [1]. LAT topographs of the 09-095 no. 150 package are shown in Figures 5.24 (a) – (d) below. The width of the x-ray diffraction images is the same for all three images, i.e. approximately 14,150 µm wide, and measures a maximum of 15,400 µm long. The slits for these experiments were set to 12 mm × 12 mm, and the divergent nature of the x-rays when diffracted by the highly missoriented (2 2 0) planes of the embedded Si chip, as seen with the post-production samples is evident. However geometrical elongation of the LAT topographs, as seen with stage 1, 2 and 3 samples is not observed after preconditioning. During the temperature cycle - dry bake – moisture soak phases of the preconditioning processes some strain relief may occur, allowing the strain fields to become more uniform in the (2 2 0) plane. LAT topographs differ depending on the position and orientation of the sample with respect to the x-ray beam, where x-rays diffract from a convex region on the crystal lattice x-rays diverge, and lead to an enlarged image, as described in Figure 5.23(a); conversely, when x-rays diffract from a concave region on the crystal lattice the x-rays converge, and a smaller, distorted image is formed, as described in Figure 5.23(b). The non-uniform changes in topograph shape seen in LAT topographs for samples 09-095 no. 150 (Figures 5.24 (a)-(c)) and 09-096 No. 008 (Figures 5.27 (a), (b), 5.29 (c)), can therefore be attributed to regions of differing lattice curvature and misorientation, observed in the corresponding ST topographs and 3DSM (Figures 5.26 (a), (b), 5.28 (a), (b), and 5.29 (a), (b)).

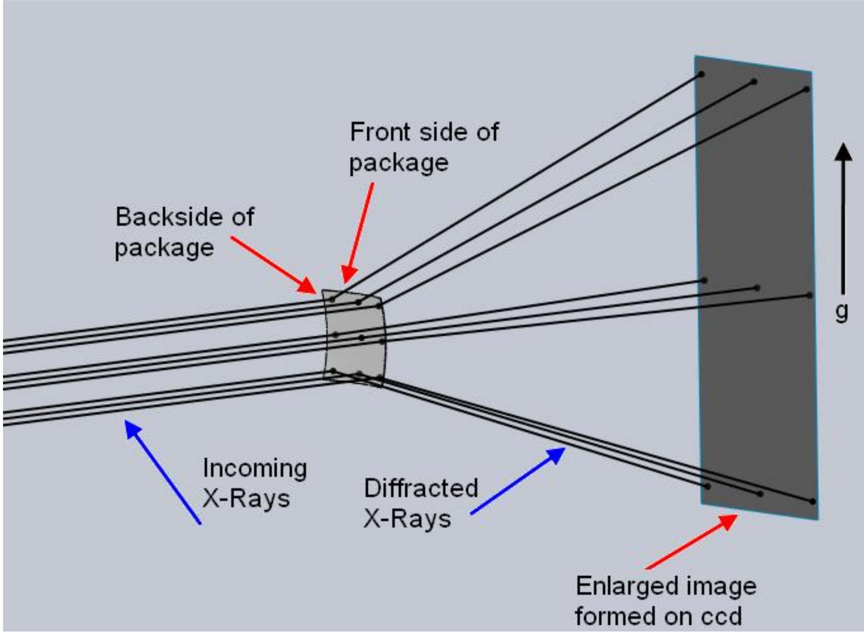

Figures 5.23(a): Formation of enlarged LAT topograph due to x-rays diffracting off convex lattice planes in the QFN-A package. Note diagram is to scale with the exception of lattice distortion, which has been exaggerated for ease of viewing.

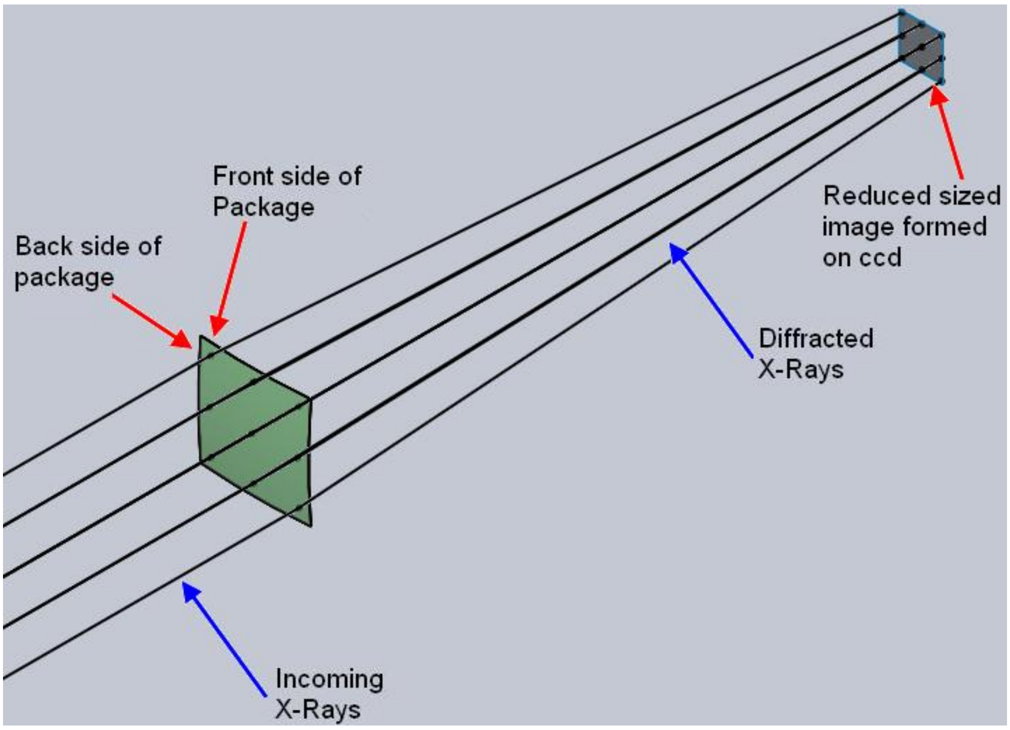

Figures 5.23(b): Formation of reduced size LAT topograph due to x-rays diffracting off concave lattice planes in the QFN-A package. Note diagram is to scale with the exception of lattice distortion, which has been exaggerated for ease of viewing.

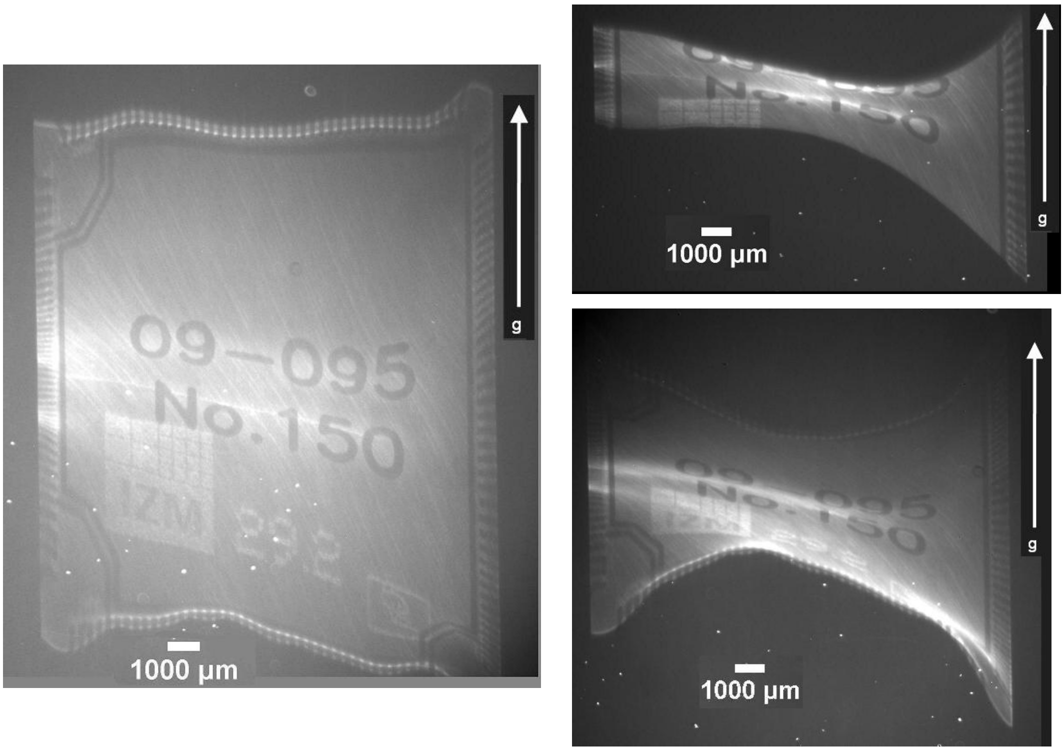

Figures 5.24 (a), (b), (c): 2 2 0 LAT topographs from package 09-095 No. 150. Topographs show how high levels of lattice misorientation can lead to distinct diffraction patterns when the package is moved up/down on the sample stage by ~1 µm.

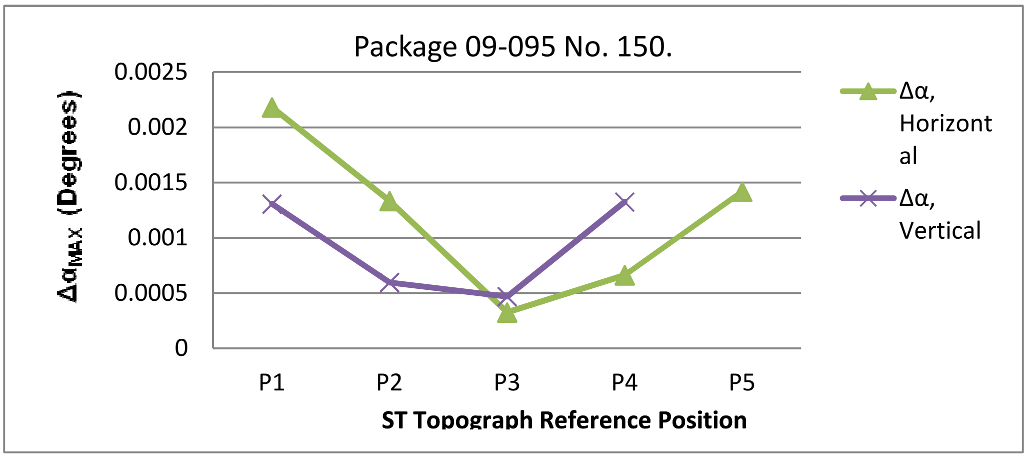

Figure 5.25: Angular displacement (warpage) data for package 09-095 No. 150. Horizontal and Vertical ST topograph positions (P1 – P5) correspond to red lines in Figure 3.14.

The lattice warpage for package 09-095 no. 150 ranges from ~2.18 × 10^{-3} - ~0.33 × 10^{-3} (± 5%) degrees (Figure 5.25). The 3DSM for both of the stage 6 packages display a distinct pattern of lattice distortion, with large, symmetrical curves at ST positions corresponding to the top and bottom edges of the chip (Figures 5.26(b), 5.28 (b), 5.29 (b)). Strain maps for both chips exhibit similar forms, with the maximum measured angular misorientation at the edges of the strain map and the central region of the strain map exhibiting the lowest levels of angular misorientation. Figures 5.26 (a) and (b) are low resolution (5 ST topographs) and high resolution (10 ST topographs) 3DSM for the same chip, 09-095 No. 150. Although the maximum Δα is the same for both 3DSM, the high resolution image shows almost identical values for the maximum lattice tilt, $\Delta\alpha_{MAX}$, at positions on the 3DSM corresponding to the top and bottom on the chip, whereas the low resolution 3DSM shows less lattice tilt at positions on the 3DSM corresponding to the bottom of the chip, ~1.4×10^{-3} (± 5%) degrees, than at the position corresponding to the top of the chip, ~2.2×10^{-3} (± 5%) degrees. This may be due to the wide spacing of the ST topographs, (1 mm), which combine to form the 3DSM. When fewer ST topographs are used to form the splines (Section 3.4.4), the point cloud which defines the boundary surface is of lower density. The boundary surface algorithm compensates for larger distances between points by approximating points on the surface to fill the empty space, resulting in a lower resolution 3DSM. Where the surface extends beyond the final ST topograph position averaging does not occur and the surface ends abruptly. Points beyond the final ST topograph position may therefore be missing in the lower resolution 3DSM.

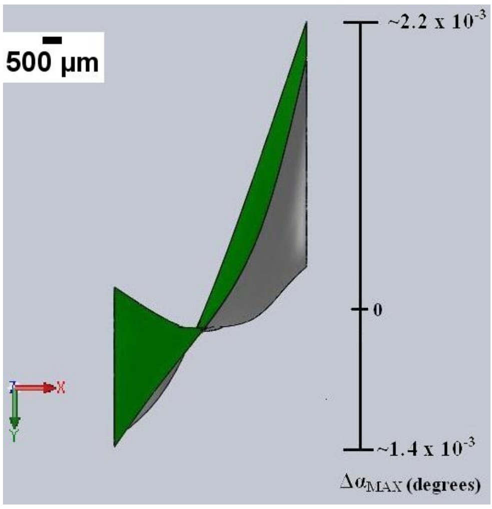

Figure 5.26(a): 3DSM of misorientation of (2 2 0) Si planes of package 09-095 No. 150 viewed side on. 5 ST topographs were taken with the package orientated at 0°.

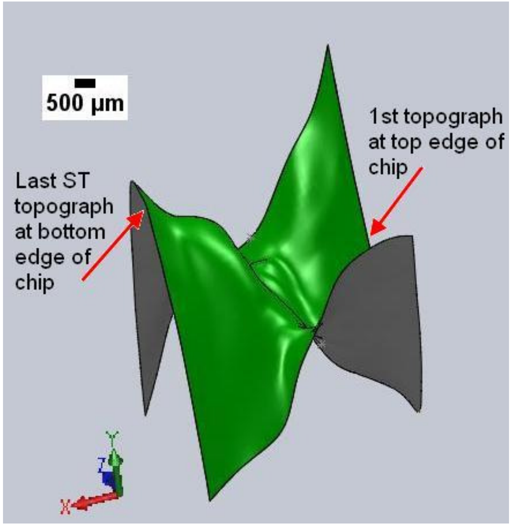

Figure 5.26(b): High resolution 3DSM of misorientation of (2 2 0) Si planes of package 09-095 No. 150 viewed side on. 10 ST topographs were taken with the package orientated at 0°.

LAT topographs for package 09-096 No. 008 are shown in Figures 5.27 (a) and (b). In the corresponding 3DSM (Figures 5.28, 5.29 (a)), the 3DSM maps are rotated in space so as to reproduce the geometrical perspective of the LAT topographs. The close correlation between the 3DSM and the topographs can easily be observed, and the fidelity of the surface modelling process appreciated.

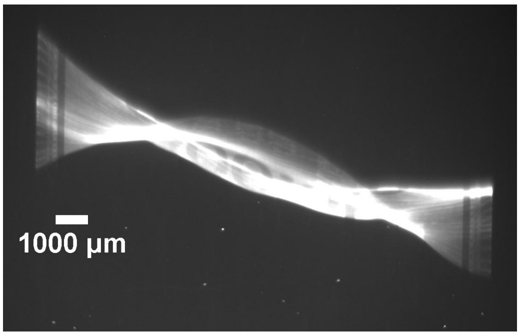

Figure 5.27(a): 2 2 0 LAT topograph of package 09-096 No. 008. Image is recorded with chip at 0°.

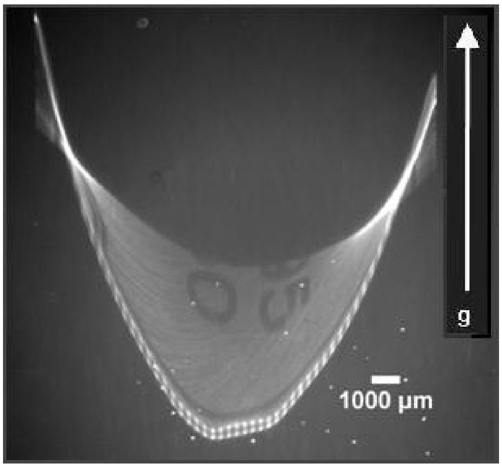

Figure 5.27(b): 2 2 0 LAT topograph of package 09-096 No. 008. Image is recorded with chip rotated to 90°.

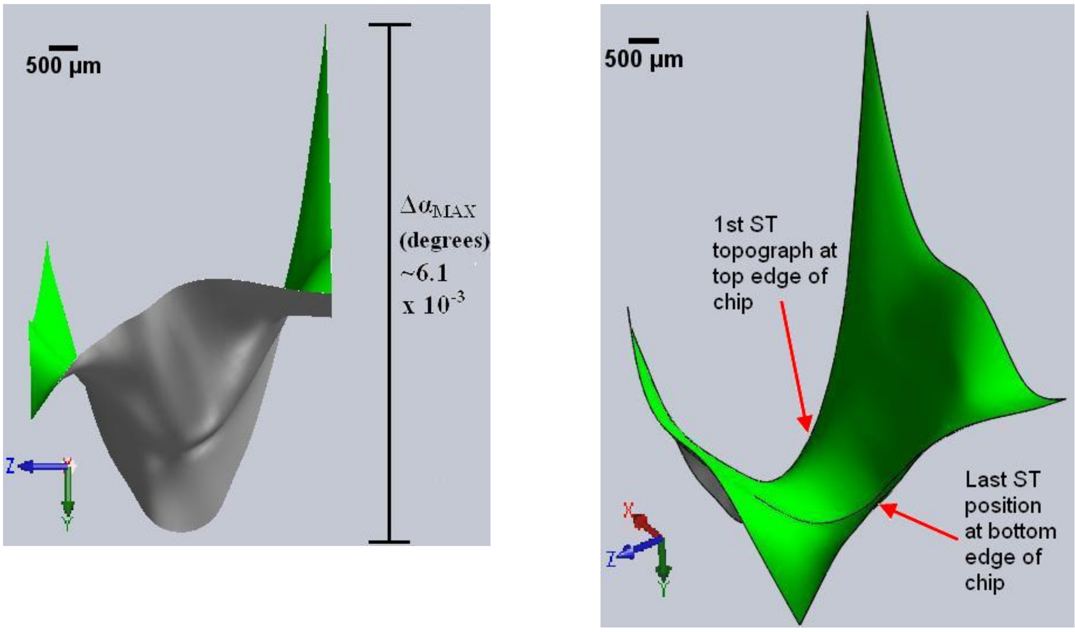

Figure 5.28(a) and (b): 3DSM of package 09-096 No. 008, showing misorientation of (2 2 0) Si planes. 5 ST topographs were taken with the package orientated at 0°. Relative positions of ST topographs which form basis of 3DSM are also shown.

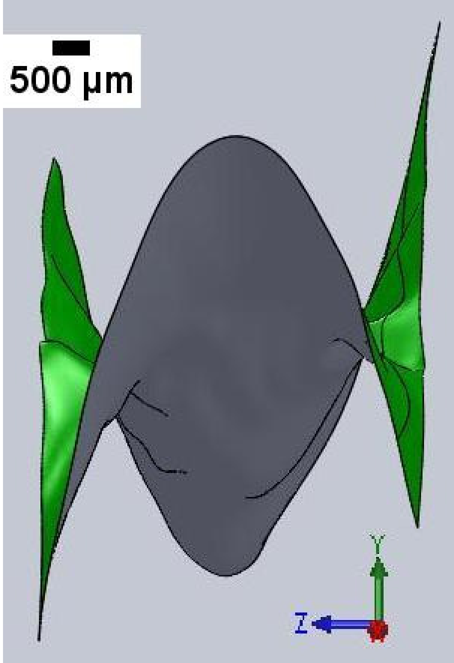

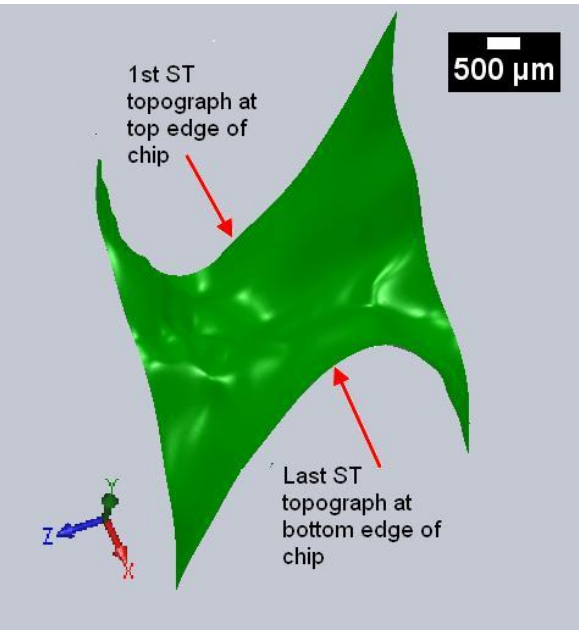

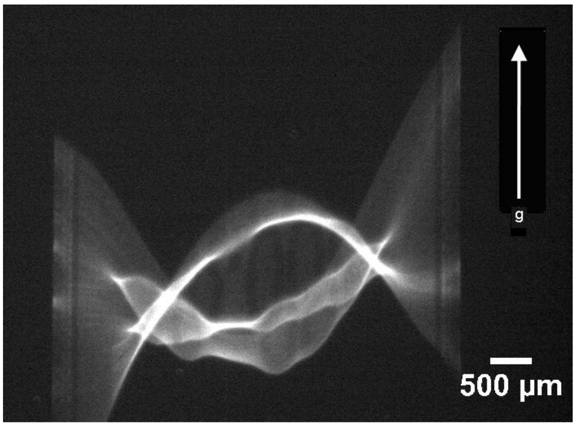

Figure 5.29 (a) & (b): High resolution 3DSM of package 09-096 N0. 008, showing misorientation of (2 2 0) Si planes. 10 ST topographs were taken with the package oriented at 0°. Relative positions of ST topographs wich form 3DSM are also shown. Figure 5.28 (c): 2 2 0 LAT topograph of package 09-096 N0. 008. Note correlation between LAT topograph and 3DSM as oriented in (a).

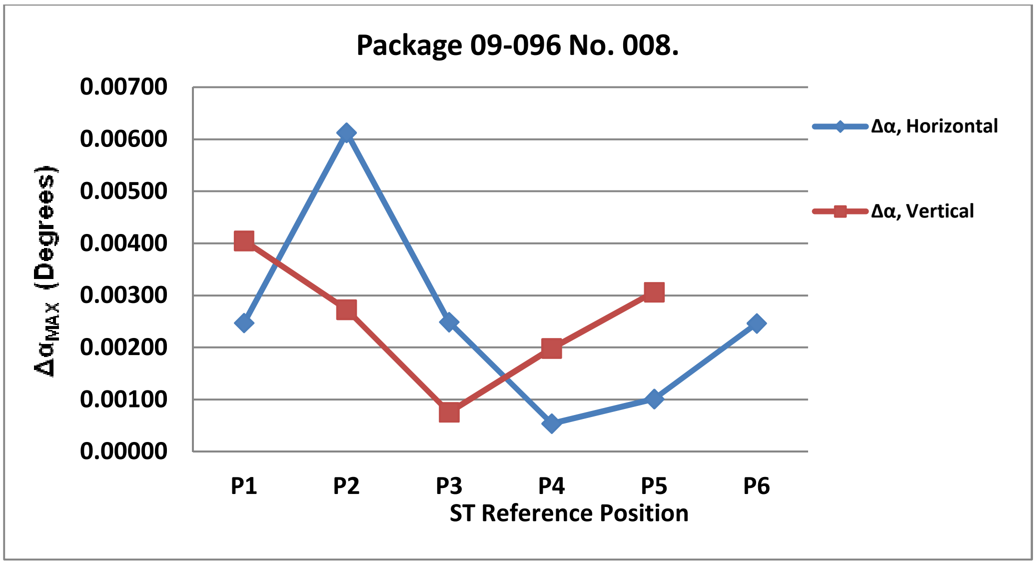

Figure 5.30: Angular displacement (warpage) data for package 09-096 No. 008. Horizontal and Vertical ST topograph positions (P1 – P5) correspond to red lines in Figure 3.14.

Lattice warpage for package 09-096 no. 008 ranges from ~6.13 × 10^{-3} - ~0.54 × 10^{-3} (± 5%) degrees (Figure 5.30). Package 09-096 no. 008 therefore has by far the greatest lattice warpage, and hence strain levels, of all the packages measured in this study. It is known that the expansion and bending of the epoxy during the reflow cycles can lead to bending of the package, and hence high stresses [2]. As the shape and profile of the 3DSM has a similar form to that of 09-095 no. 150, the other pre-conditioned sample in the study, this type of warpage is most likely a genuine result of the pre-conditioning process. Although the pre-conditioning process does appear to relieve lattice strain in the directions parallel and perpendicular to **g**, section topographs and 3DSM show that strain levels and warpage in the [2 2 0] direction, orthogonal to the (2 2 0) plane, are increased by pre-conditioning. This is in agreement with the results reported by Manessis et al. [1, 2], who observed warpage on the same packages after MSL3 testing, and when undertaking shear testing on the same packages at 1) resin/chip and 2) chip/DAF interfaces recorded decreased package strength by a factor of 3× to 4× [1].

5.3.5 Stage 7: Phase 2 Reliability Testing

Four samples underwent reliability testing as described in section 5.1.3 and Figure 5.3. Package 09-088 No.241 (Figures 5.31, 5.32 (a), (b)), underwent high temperature storage, and exhibits a similar form to the post-preconditioning samples, with the least lattice displacement at the centre of the package, ~0.41 × 10^{-3} (± 5%) degrees, and the greatest displacement at the edges of the package ~4.01 × 10^{-3} (± 5%) degrees (Figure 5.33). The centre horizontal profile of the chip reveals a similar ‘rippled’ appearance to that seen at the edges of the post production samples, the effect being illustrated in the ST topographs shown in Figures 5.34 (a) and (b). The rippled appearance may be related to voids, originating from the lamination process, and not directly resulting from the reliability test itself [2]. The rippled effect is revealed further in 3DSM of the package, Figures 5.32 (a) and (b). LAT topographs and 3DSM for package 09-088 No.241, measure ~14,450 µm wide, approximately the same size as the after preconditioning samples, further confirming that this high temperature reliability test does not have a significant effect on strain or warpage in the package.

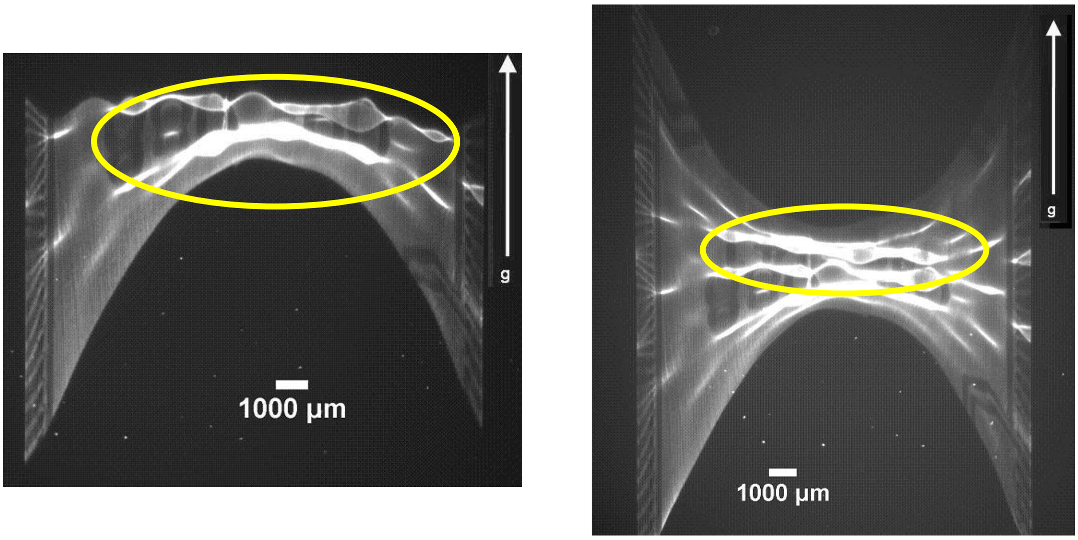

Figure 5.31 (a) & (b): 2 2 0 LAT topographs of package 09-088 No. 241. Yellow circled area indicates strained region most likely originating from the lamination process.

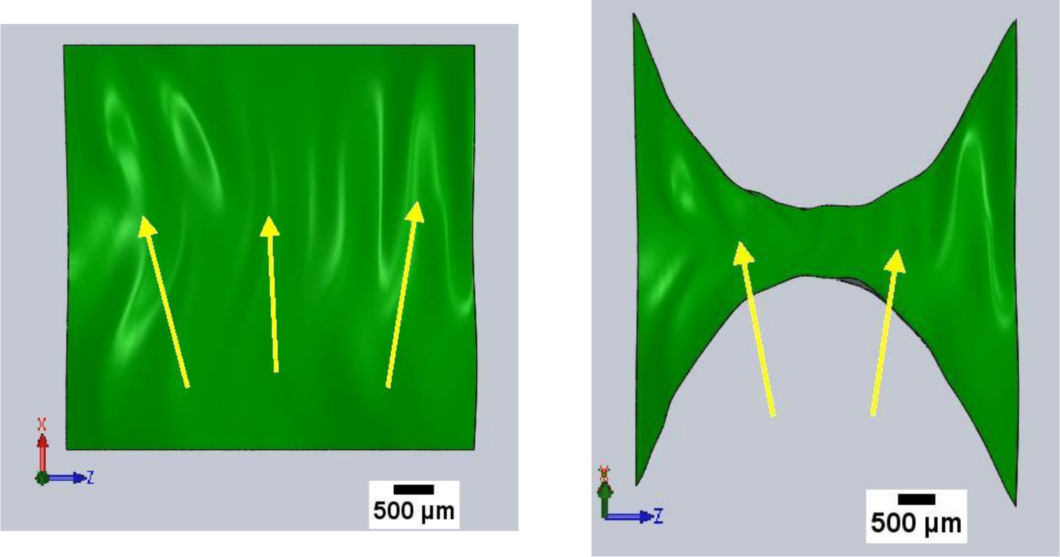

Figure 5.32 (a) & (b): 3DSM of package 09-088 No. 241, showing misorientation of (2 2 0) Si planes. Yellow arrows point to strained region most likely originating from the lamination process.

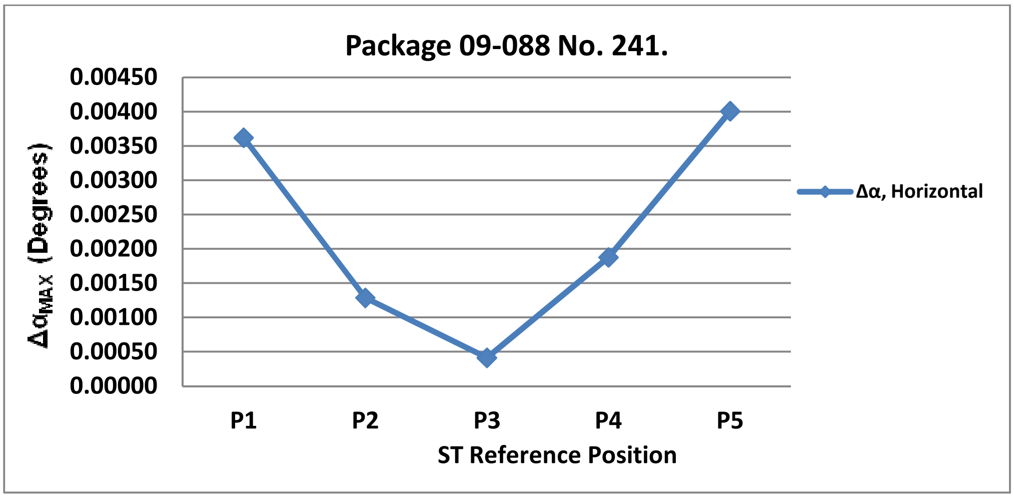

Figure 5.33: Angular displacement (warpage) data for package 09-088 No. 241. Horizontal ST topograph positions (P1 – P5) correspond to red lines in Figure 3.14.

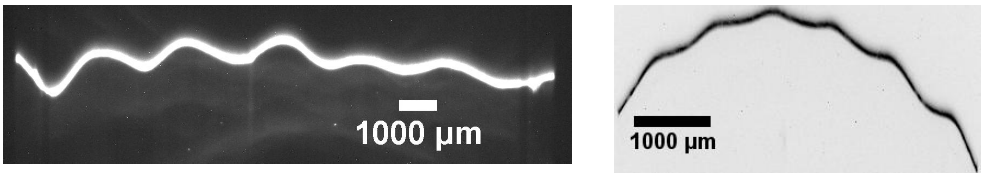

Figure 5.34(a): ST topographs of middle (P3) horizontal ST topograph from sample 09-088 No. 241, 2 2 0 reflection, showing distinctive 'rippled' profile Figure 5.33 (b): Top edge (P1) horizontal ST topograph from sample 09-096 No. 158 with similar 'rippled' features on profile.

Package 09-089 No. 047 underwent thermal cycling reliability testing. Although previous thermal cycling tests on similar packages have exhibited good results [2], this package demonstrates very high levels of lattice strain resulting in a fragmented LAT topograph due to extreme cases of orientational contrast and strongly suggests significant damage to the silicon in the package (Figures 5.35 (a) and (b)). Thin packages are more susceptible to humid conditions, and absorb moisture at a faster rate than thicker packages. During preconditioning, particularly MSL3 processing, moisture can become trapped within the package. At sudden elevated temperatures the trapped moisture can vaporise and exert immense internal stresses on the package. Figure 5.36 is a schematic of the LAT topograph image formation: misorientated lattice planes diffract incoming x-rays as shown, resulting in images at different spatial positions on film. Accurate angular data cannot be obtained from the ST topographs due to their fragmented nature.

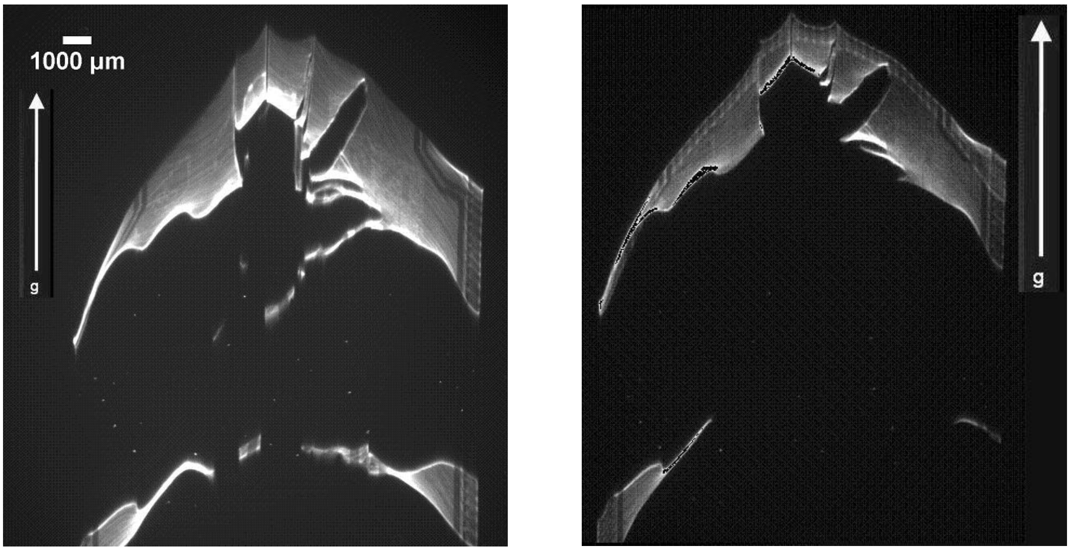

Figures 5.35 (a) & (b): 2 2 0 LAT topographs of package 09-089 No. 047 showing fragmented images resulting from high levels of strain. Scale is the same for both topographs.

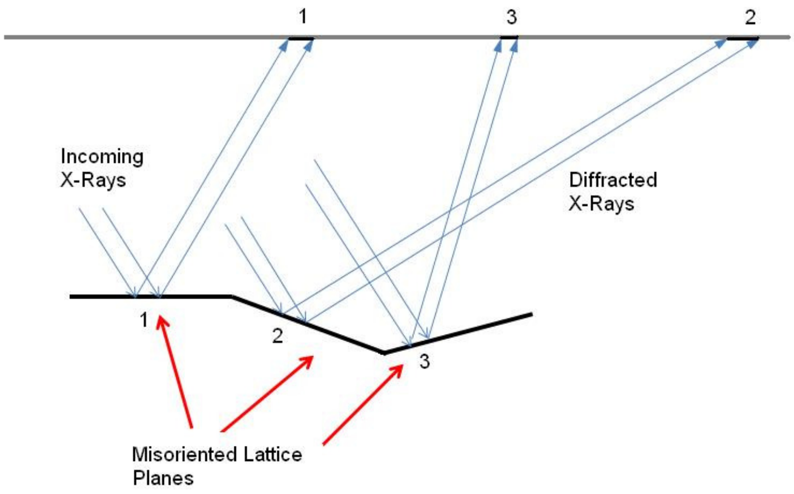

Figure 5.36: Diagram illustrating how topographic images of the areas of a sample with lattice planes misoriented with respect to “good” silicon appear at different spatial positions on film.

BRST topographs from three regions on the package, indicated by the red lines are shown in Figure 5.37 below. BRST show the areas at the edge of the chip to have very considerable lattice misorientation of up to ~0.95 × 10^{-3} (± 5%) degrees, across the regions shown in Figure 5.37 (red lines). There are significant variations in strain levels across the chip, with the corners of the chip, showing the least strain. This is most likely due to the presence of the pads which can relieve strain.

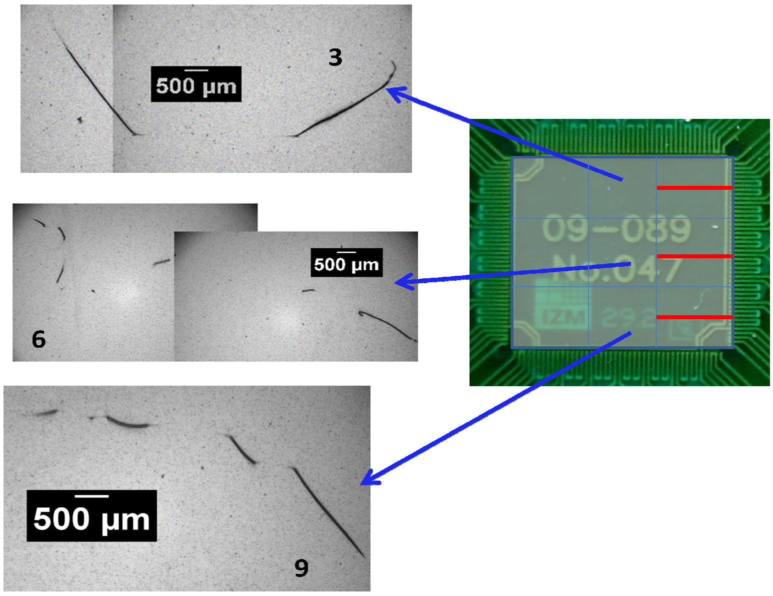

Figure 5.37: BRST from regions on package 09-089 No. 047, indicated by red lines. All ST shown are -1 1 9 reflections. Slit size was set to 4 mm long and ~15 µm high.

Packages 09-089 No. 241 and 09-088 No. 218 underwent temperature humidity storage and pressure cooker tests, respectively. Both packages show very large warpage/strain, (Figures

5.38 (a), (b), 5.39 (a)), indicated by the distorted shape and fragmented nature of the topographs. The ST topograph for 09-089 No. 241 appears as a broken line on the film. As with the previous sample, this indicates very high levels of lattice misorientation. The pressure cooker test is known to be the toughest of the phase 2 reliability tests, and damage is evident from visually examining the exterior of the package (Figure 5.39 (b)). The cause of failure could not be determined from XRDI, however when pressure cooker tests were carried out on similar packages in a 3D stack, SEM images showed the through hole interconnection failed at the interface between adjacent material layers , where the plating thickness was low [12]. ST topographs could not be recorded for this package as the lattice distortions were too large to allow enough commensurate regions to be imaged.

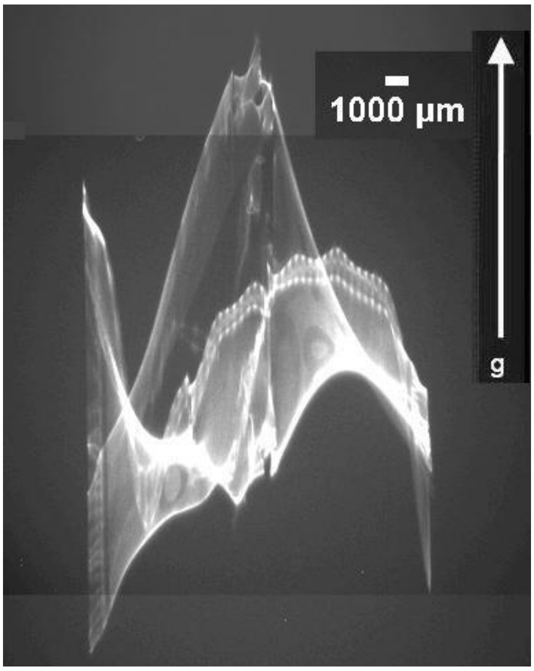

Figure 5.38(a): 2 2 0 LAT topograph reflection of package 09-089 No. 241. Image consists of 3 topographs patched together.

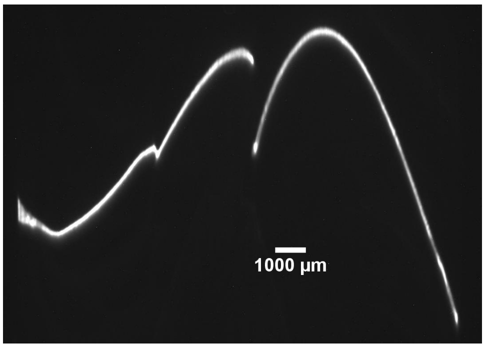

Figure 5.38 (b): 2 2 0 ST topograph of package 09-089 No. 241 at approximately the centre of the chip.

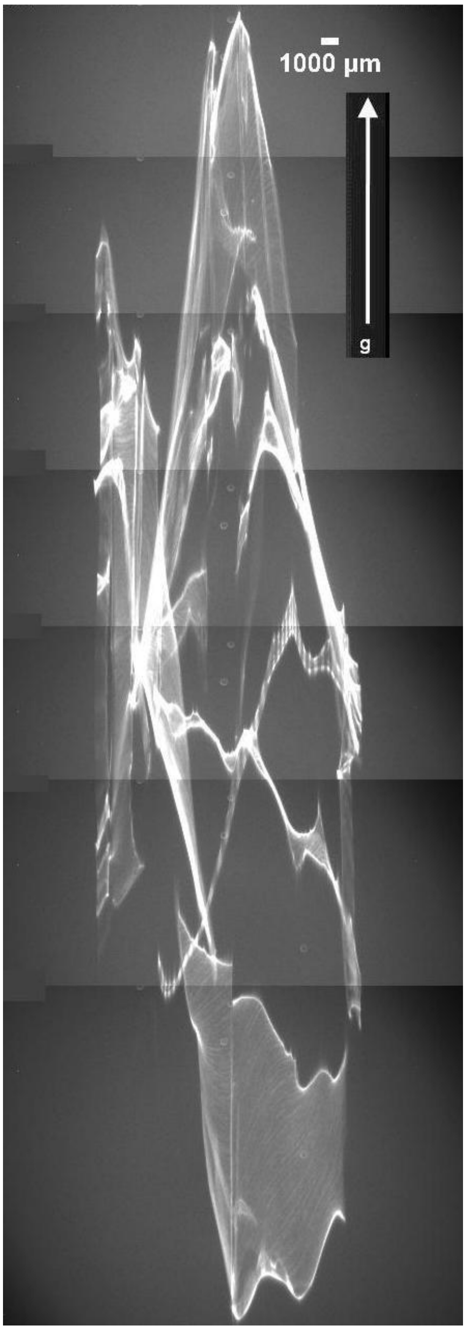

Figure 5.39 (a): 2 2 0 LAT topographs of package 09-088 No. 218. Image consists of 7 topographs patched together.

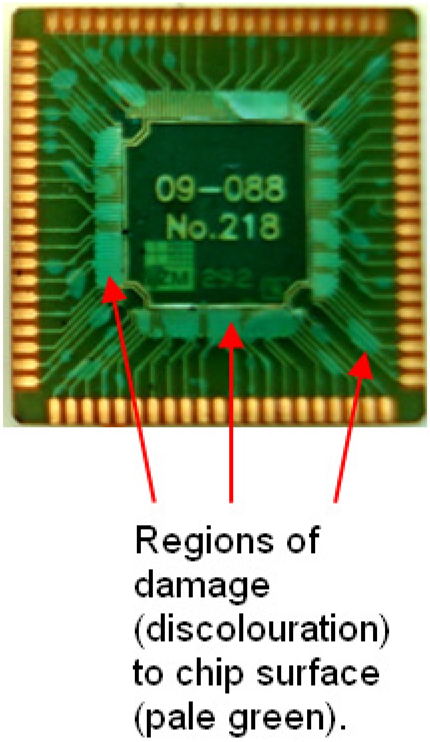

Figure 5.39 (b): Optical Image of package 09-088 No. 218 showing external damage, resulting from pressure cooker testing.

5.4 Summary

This chapter describes 3D surface modelling (3DSM), a novel technique for the non-destructive measurement of *in situ* strain and wafer die warpage in thin, chip embedded Quad Flat Nonlead (QFN) packages. 3DSM is used in conjunction with XRDI to obtain high resolution (~3 µm) strain/warpage maps and qualitative information on the nature and extent of the strain fields in completely packaged chips. Micro-Raman spectroscopy complements 3DSM data by providing quantitative information on the level of strain within the chips prior to the embedding process. Strain patterns in both the micro-Raman spectroscopy results and the 3DSM for Stage 1 chips correlate well, with the greatest levels of strain at the edges and corners of the chip, and a uniform, relatively undistorted (warped) region at the centre of the chip.

Chips / packages were examined at 5 different stages in the manufacture, pre-conditioning and qualification processes. Results show that the magnitude of strain induced lattice misorientation / warpage varies from chip to chip within the same process step; however the location of strain maxima and the strain pattern is characteristic of the particular process or reliability test being studied. 3DSM can be generated at each stage of production or reliability testing, and complemented by LAT topographs and angular displacement data. 3DSM data enables imaging of strain perpendicular to the plane of the topograph, (2 2 0) in this case, which is not easily observable or quantifiable using XRDI alone. Distinctive strain patterns can be identified from the surface maps, proving that the manufacturing and embedding process is stable. Initially this study used 5 ST topographs placed 1 mm apart to form the basis of the point cloud which defines the 3-dimensional surface. Later 3DSM are created using 10 ST topographs, 0.5 mm apart, enabling greater accuracy in the definition of the point cloud and hence the surface map to be obtained. Results comparing low and high resolution 3DSM show them to be in good agreement, with small differences attributed to loss in definition due to the lower number of points.

Lowest levels of strain are apparent before chip packaging/embedding, with strain levels increasing from stage 5, post production to stage 6 preconditioning and are at their greatest after Phase 2 Reliability testing, depending on which reliability tests are undertaken. Strain patterns observed using XRDI and 3DSM are not solely a result of the preceding manufacturing / testing stage. Underlying structures such as tracks, vias and metal layers can affect the levels of strain in the chip. LABR topographs and 3DSM show that all chips have lowest strain levels at the corners, irrespective of the processing stage. Analysis of strain patterns using XRDI and 3DSM agree well with the outcomes of FEM, shear testing, SEM and acoustic tomography on similar packages [1, 2, 5, 6, 8]. However, crucially, all these techniques are destructive (and of course FEM modelling is only as good as the assumed input data). The close relation between features observed on LAT and LABR topographs, and those reproduced in the 3DSM, particularly at via electroplating and post production stages prove that 3DSM is an effective technique for producing accurate maps of the location and magnitude of strain induced die/wafer warpage inside packaged chips.

The need to address non-invasive and non-destructive stress and strain metrology in Systems on Chip or System in Package (SoC/SiP) is recognised in the International Technology Roadmap for Semiconductors (ITRS 2009). 3DSM mapping provides the unique ability to non-destructively assess strain inside sealed packages post production, and after reliability testing, and complements other established characterisation / analysis techniques. Results prove the potential for this technique to examine non-destructively major sources of die warpage, and to provide quick feedback towards process improvement.

References

[1] Dionysios Manessis, Lars Boettcher, Andreas Ostmann, Rolf Aschenbrenner, and Herbert Reichl. *Electronic Components and Technology Conference (ECTC) 2010*, pp. 803 – 810.

[2] Dionysios Manessis, Shiu-Fang Yen, Andreas Ostmann, Rolf Aschenbrenner, and Herbert Reichl. *Proc. Electronics Components & Technology Conference (ECTC) 2007*, Reno, NV, May 29- June 1, 2007, pp. 278-285.

[3] Preconditioning of Plastic Surface Mount Devices prior to Reliability Testing. JESD22-A113E. http://www.jedec.org/Catalog/catalog.cfm

[4] J. Stopford, Masters Research Project, School of Electronic Engineering, DCU,2006.

[5] Fritzsch, T., Mrossko, R., Baumgartner, T., Toepper, M., Klein, M., Wolf, J., Wunderle, B., Reichl, H. *IEEE International Conference on 3D System Integration,* 2009, pp. 1-8.

[6] Ligang Niu, Yang, D., Mingjun Zhao., *International Conference on Electronic Packaging Technology & High Density Packaging*, (ICEPT-HDP), 2009, pp. 1229 – 1232.

[7] Andreas Ostmann, Dionysios Manessis, Johannes Stahr, Mark Beesley, Maarten Cauwe, Johan De Baets, *2nd Electronics System Integration Technology Conference*, Greenwich, UK. 2008, pp. 315 - 320.

[8] Dionysios Manessis, Lars Boettcher, Andreas Ostmann, Stefan Karaszkiewicz and Herbert Reichl, *4th International Microsystems, Packaging, Assembly and Circuits Technology Conference*, IMPACT 2009, pp. 174 - 177.

[9] A. Rack et al., *Nuclear Instruments and Methods in Physics* B, **267** (2009).

[10] Chien-Wei Chien, Li-Cheng Shen, Tao-Chih Chang, Chin-Yao Chang, Fang-Jun Leu, Tsung-Fu Yang, Cheng-Ta Ko, Ching-Kuan Lee, Chao-Kai Shu, Yuan-Chang Lee and Ying-Ching Shih, *Proceedings 57th Electronic Components and Technology Conference 2007*, ECTC '07, pp. 305 – 310.

[11] Dionysios Manessis, Lars Boettcher, Andreas Ostmann, Rolf Aschenbrenner, and Herbert Reichl. *59th Electronic Components and Technology Conference, 2009*. ECTC 2009, pp. 475 – 481.

[12] Thomas Löher, David Schütze, Wim Christiaens, Kristof Dhaenens, Swarnakamal Priyabadini, Andreas Ostmann, and Jan Vanfleteren, 3rd Electronic System-Integration Technology Conference (ESTC), 2010, pp. 1-5.

[13] Thenappan Chidambaram, Colin McDonough, Robert Geer, and Wei Wang, *IEEE Proceedings of 16th IPFA - 2009*, China, pp. 727 – 730.

[14] Daniel N. Bentz, Jing Zhang, Max Bloomfield, Jian-Qiang Lu, Ronald J. Gutmann, and Timothy S. Cale. Modelling thermal stresses of copper interconnects in 3D IC structures. Proceedings of the COMSOL Multiphysics User's Conference 2005 Boston.

[15] D. Noonan, P.J. McNally, W.-M. Chen, A. Lankinen, L. Knuuttila, T.O. Tuomi, A.N. Danilewsky, R. Simon, *Microelectronics Journal* **37** (2006) 1372–1378.

[16] J. Kanatharana, J.J. Perez-Camacho, T. Buckley, P.J. McNally, T. Tuomi, A.N. Danilewsky, M. O'Hare, D. Lowney, W. Chen, R. Rantamaki, L. Knuuttila and J. Riikonen, *Microelectron. Eng.* **65** (2003), pp. 209–221.

[17] Jacqueline Heinrich, *ANKA Instrumentation Book*, October 1st, 2007.

[18] J Kanatharana, J J P´erez-Camacho, T Buckley, P J McNally, T Tuomi, M O'Hare, D Lowney, W Chen, R Rantam¨aki, L Knuuttila and J Riikonen. J. *Phys. D: Appl. Phys.* **36** (2003)

[19] R. J. Needs and A. Mujica, *Phys. Rev. B* **51**, 9652 (1995).

[20] I. De Wolf, *J. Raman Spec.* **30**, 877 (1999).

[21] I. De Wolf, *Semicond. Sci. Tech.* **11**, 139 (1996).

[22] ITRS More than Moore White Paper. http://www.itrs.net/Links/2010ITRS/IRC-ITRS-MtM-v2%203.pdf

[23] ITRS SiP White Paper V9.0. *The next Step in Assembly and Packaging: System Level Integration in the package (SiP).* http://www.itrs.net/Links/2007ITRS/LinkedFiles/AP/AP_Paper.pdf

[24] M. Töpper et al., *IEEE Transactions on Advanced Packaging*, Vol.**23**, No.2, May 2000, pp 233-238.

[25] http://hasylab.desy.de/facilities/doris_iii/beamlines/f1/specifications/index_eng.Html

[26] Jing Zhang, Max O. Bloomfield, Jian-Qiang Lu, Ronald J. Gutmann, Timothy S. Cale., *Microelectronic Engineering* **82** (2005) 534–547.

[27] Jian Chen; De Wolf, I., *Proceedings 52nd Electronic Components and Technology Conference 2002*, Page(s): 1310 – 1317.

[28] Jian Chen and Ingrid De Wolf, *IEEE Transactions on Components and Packaging Technologies*, Vol **28**, No. 3, (2005).

[29] Xiuzhen Lu, Liu Chen, Zhaonian Cheng and Johan Liu, *2005 International Symposium on Electronics Materials and Packaging (EMAP2005),* December 11 -14, 2005, pp. 43 - 49.

[30] http://www.dezignstuff.com/blog/?p=3778

[31] Jacqueline Heinrich, ANKA Instrumentation Book, October 1st, 2007.

[32] Danilewsky, A. N., Rack, A., Wittge, J., Weitkamp, T., Simon, R., Riesemeier, H., Baumbach, T., (2008), *Nuc. Instrum. Meth. Phys. Res. B*, **266**(9), 2035-2040.

Study of Warpage in Stacked Chip Scale Package (CSP) using XRDI and Micro-Raman Spectroscopy.

6.1 Introduction

Chip scale packages (CSP's) were initially designed to meet the demands of portable electronic devices such as netbooks, smartphones, mobile internet devices, handheld games consoles and global positioning systems (GPS) units. By reducing the package size, when compared to traditional peripherally leaded packages, and using established ball grid array (BGA) technology, which requires little or no new investment in capital equipment, yields can be improved and assembly costs kept low.

3-dimensional (3D) integration technology used in stacked CSP’s involves vertically gluing together thinned Si wafers to form a stacked chip structure, and then interconnecting the layers to achieve the high level of silicon integration and area efficiency required in portable multi-media products. Stacked CSP’s, also known as Stacked System Integration Packages (SSIPs) [19], have many advantages over conventional, single die CSP’s and unstacked chips, enabling chip size to be condensed, reducing track length, improving speed, and decreasing interconnect power and crosstalk. Furthermore, stacked CSP’s can be multifunctional, integrating multiple applications such as SRAM and flash memory, which are important to the mobile phone industry. A number of advanced materials and processes are used in stacked CSP technology including high density, thin core substrates, advanced materials (die attach film, epoxy mould compound) and die attach, wire bonding, and moulding processes. Wafer thinning, alignment, interconnection, bonding and encapsulation are critical steps in the manufacture of 3D integrated circuits (ICs), and can all lead to strain and hence damage in the large scale integration (LSI) structures.

Previous attempts to analyse packaged or processed integrated circuits have been limited by the thickness of the metallization and the outer packaging itself. Early attempts on delidded packages [22] enabled 5-10 μm resolution imaging of strain fields, and the basic analysis of warpage.

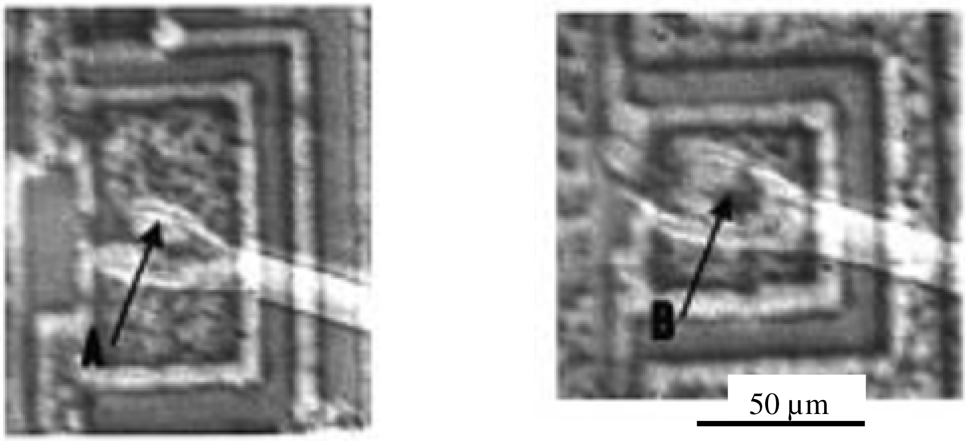

Figure 6.1 (a) & (b): 620 Large Area Back Reflection X-Ray Topographs (penetration depth into Si = 27 µm) showing the different strain fields and damage under two Au wedge bonds, (a) and (b), in a delidded 2764 8Kx8 EPROM [22].

More success has been achieved in the examination of the strain fields under bump metallisation, ball grid array solder bumps and on the impact of under bump metallisation on solder bump reliability [13-15, 23, 24]. In all of these cases a powerful combination of XRDI, micro-Raman spectroscopy and finite element modelling has been applied in order to elucidate the impact of these processes on bump, device and package reliability. However the packages, devices and/or bonds under test could not be examined in their actual processed state and the samples had to be prepared for scanning electron microscopy and thinned down for XRDI through the wafer back sides.

This study examines the strain induced post assembly in triple stacked CSP's by the manufacturing process, using two established, non-destructive characterisation techniques: synchrotron x-ray topography (SXRT) and micro-Raman spectroscopy.

6.2 Stacked Chip Scale Package (CSP)

A diagram of the triple stacked CSP characterised in this study is shown in Figure 6.2. The package consists of 3 silicon die stacked on top of each other and individually separated by an insulator. Cu foil is bonded to one side of the substrate using a polymide adhesive and then patterned to form the required circuitry. The die stack is bonded to a thick, rigid bismaleimide/triazine (BT) laminate substrate, which maximises the separation between die and pcb surface and thus decouples the stresses caused by the differences in the coefficient of thermal expansion (CTE) of the silicon die and the pcb material during thermal processing [19, 28, 29]. Large eutectic solder balls with 0.8 mm pitch are used to route the chips to the pcb. The entire package is encapsulated in an epoxy mould compound.

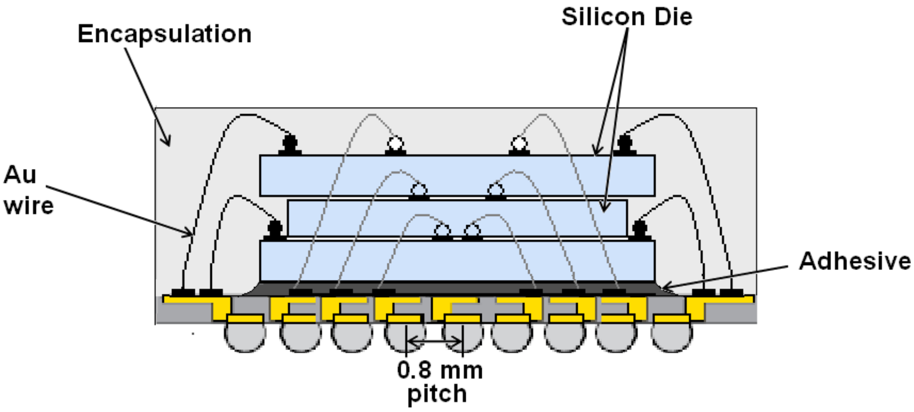

Figure 6.2: Diagram of triple stacked CSP (not to scale) showing main components including silicon die, adhesive, gold wire and solder balls with 0.8 mm pitch.

6.3 Experiment

SXRT measurements were performed at the ANKA Synchrotron, Karlsruhe, Germany using the TopoTomo X-Ray Topography beamline (section 4.3.2.2). Topographs were recorded in large area back reflection (LABR) geometry at high resolution using Slavich Geola VRP-M Holographic Film, with a grain size ~35 nm. A sample to film distance, L = 85 mm, and a beam size of 2.5 mm × 1.5 mm was used. Images of the topographs were obtained from the original X-ray films using the *Zeiss Axiotech* microscope equipped with a CCD camera, frame grabber, and image acquisition software. Images were recorded at room temperature for x100 and x50 magnifications. *LauePt* software was again used to simulate the Laue pattern for the geometry [16], which enabled each reflection to be indexed and penetration depths to be calculated.

The triple stacked CSP was cross sectioned and enclosed in a resin material (Figure 6.3(a)).

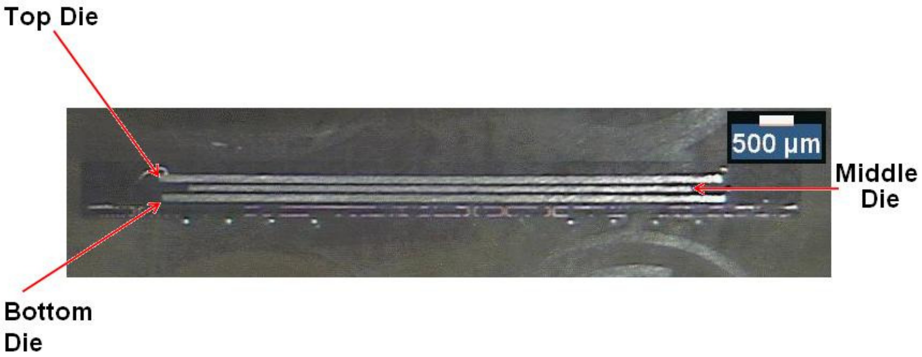

Figure 6.3(a): Optical cross section of stacked CSP enclosed in resin, showing 3-layer structure. Total package height ~675 µm (excluding BGA), die thickness ~100 µm. Die stack thickness ~350 µm. Bottom die is attached to substrate by adhesive.

Micro-Raman spectroscopy measurements were performed using the *JY Horiba LabRam HR800* micro-Raman system (section 3.6.1) with the 488 nm Ar+ laser. A 10× objective was used to focus the laser source to a diameter of about 10 μm on the sample surface. A confocal hole of 200 μm and a grating of 2400 g/mm were chosen for the experiments. Before commencing measurements the system was calibrated as described in section 3.6.2. A line scan consisting of 11 points, 5μm apart was set up to measure each layer, as described in Figure 6.3(b). Line scans were taken at the same position for each layer, with 3 accumulation times for each scan to surpass noise effects. As scans could be performed in a relatively short time (<10 mins) it was not necessary to compensate for peak shifts resulting from thermal or temporal changes.

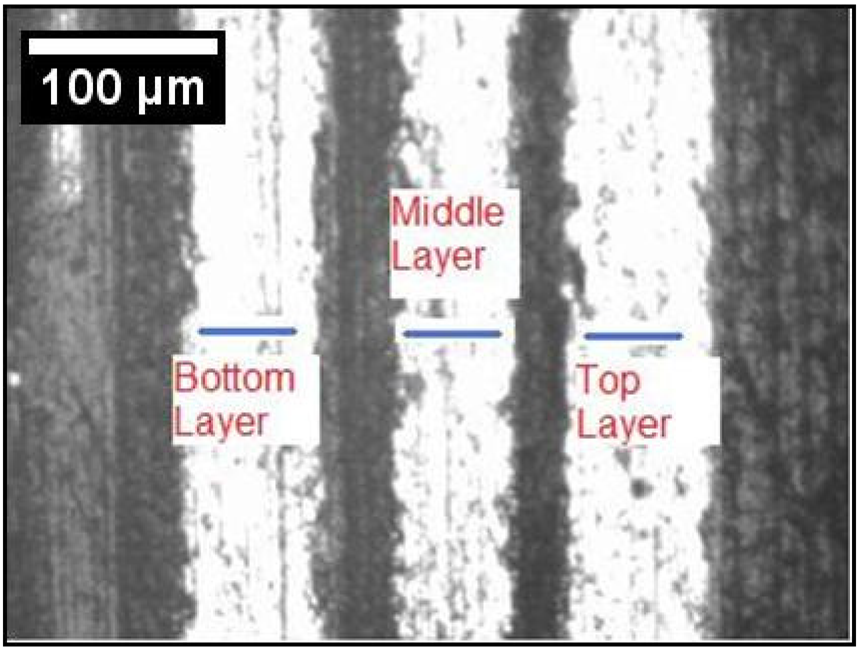

Figure 6.3(b): Position of Raman line scan for each layer (die) on triple stacked CSP. Layers (die) are labelled with respect to Figure 6.3(a).

6.4 Results

Analysis of the stacked CSP was undertaken in order to qualitatively and quantitatively examine the lattice displacement in each of the Si chips in the package. Due to the size of the package, and in order to minimise fluorescence from the resin material in which the package was mounted, the x-ray beam was kept to a maximum of 2.5 mm wide × 1.5 mm high. The package therefore had to be imaged in parts. Using the x-y stage the package was stepped across in 2mm steps, and images were recorded on the film after each step. A 0.5 mm overlap was allowed for each step to ensure no region of the package was omitted (Figure 6.4).

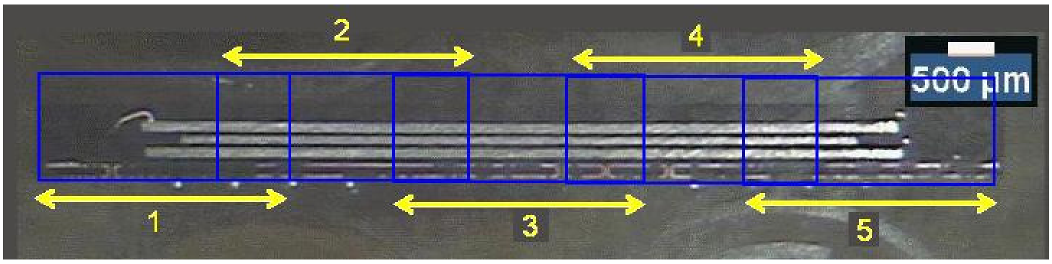

Figure 6.4: Image of package illustrating approximate positions of x-y stage steps (blue boxes) and corresponding topograph positions (yellow numbers).

Warp is a measure of the angular misorientation of a set of planes. A qualitative estimate of the amount of strain and lattice warpage in the chip can be obtained by comparing LABR topographs at different x-ray penetration depths. Figures 6.5 (a) and (b) show LABR topographs of the 2 0 10 and 2 0 6/4 0 12 reflections from the stacked CSP. Harmonics occur when there are several orders of diffraction in a single diffraction spot, which leads to diffraction from lattice planes corresponding to (hkl), (2h2k2l), (3h3k3l), etc. The calculated x-ray penetration depth for the 2 0 10 reflection, t_p ~107 µm. t_p for the 2 0 6 / 4 0 12 reflection is either ~18 µm or 206 µm. The image on the film corresponding to either the 2 0 6 / 4 0 12 reflection is comprised of a 64 % 2 0 6 intensity contribution plus a 36% 4 0 12 intensity contribution and it is therefore not possible to determine exactly which reflection or x-ray penetration depth the image has arisen from. Warpage can vary from smiling (edges up) to frowning (edges down) depending on the stack configuration, die size, and materials. Typically warpage of the bottom package is smiling [27]. In general, both sets of topographs show a similar pattern, with the greatest lattice displacement apparent at the extremities of the chip. The 2 0 6/4 0 12 images appear to exhibit slightly greater warpage than the 2 0 10 images, further indicating that the level of lattice warpage varies according to position on the die.

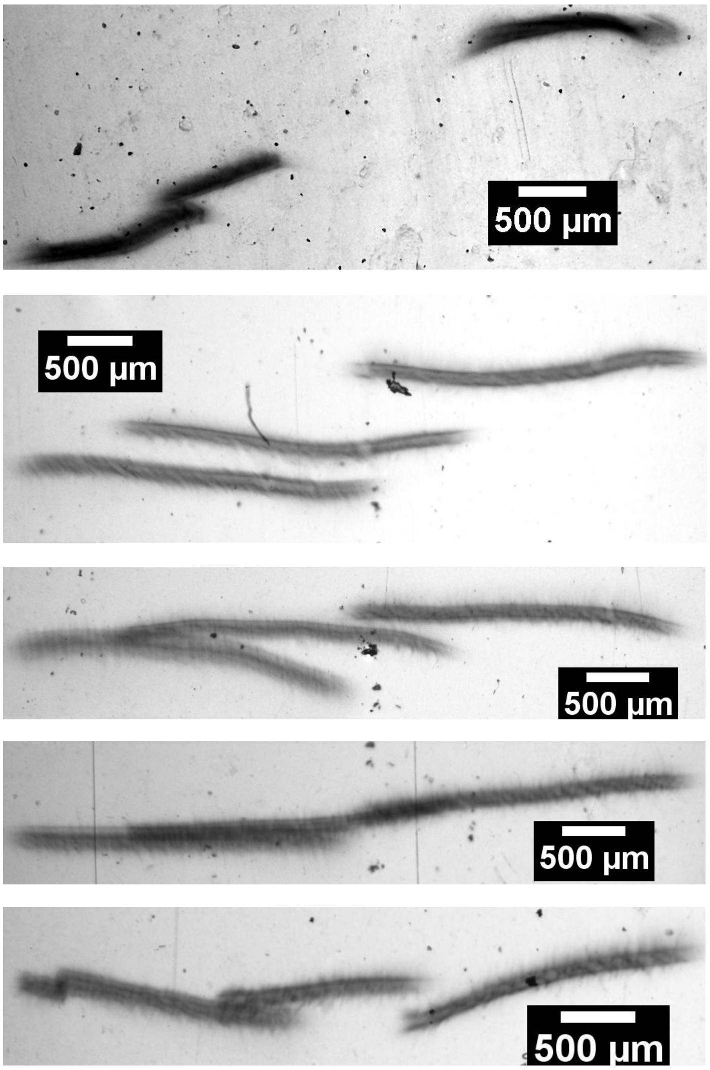

Figure 6.5(a): 2 0 10 LABR topographs, t_p ~107 µm from stacked CSP. The first image (uppermost position) corresponds to position 1 in Figure 6.4, and the image second from the top to position 2, etc.

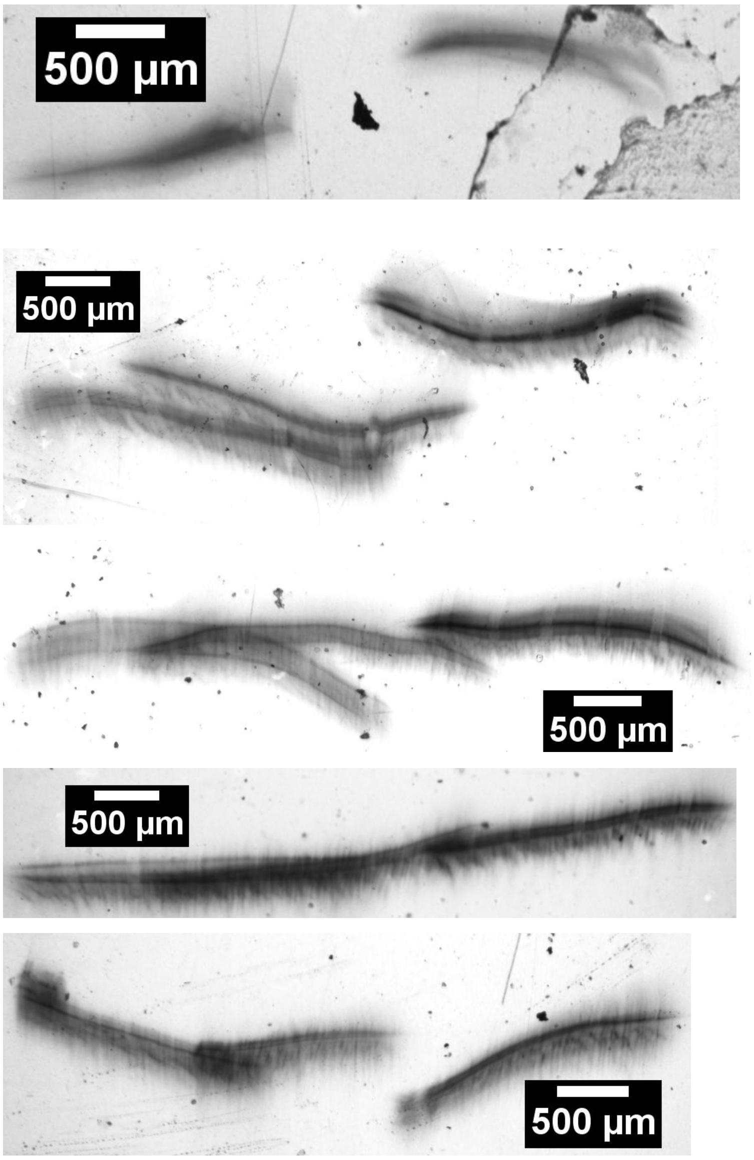

Figure 6.5(b): 2 0 6 / 4 0 12 LABR topographs, t_p ~18/206 µm from stacked CSP. The first image (uppermost position) corresponds to position 1 in Figure 6.4, and the image second from the top to position 2, etc.

To obtain a quantitative estimate of the stress in the chip one can in the first instance measure the warpage from topographic images. We know from Section 5.3.1 that:

$$\therefore \Delta\theta_{MAX} \propto \alpha \tag{6.1}$$

where $\Delta\theta_{MAX}$ is the maximum shift in Bragg angle, and α is the lattice tilt.

The magnitude of orientational contrast shift can be calculated from:

$$\Delta S \big/ 2L \cong \Delta\alpha \tag{6.2}$$

where ΔS is the maximum angular misorientation across the measured length of the sample, L is the sample to film distance used in SXRT (80 mm), and Δα is the maximum apparent shift in the Bragg angle due to the strain-induced tilt of the diffracting planes [1, 13, 14].

Plots of the maximum displacement (warpage) of each die (Figure 6.6), show the greatest amount of lattice displacement in the middle Si die, ranging from about 81 to 364 arcsec, with the top silicon die exhibiting slightly less warpage, ranging from approximately 245 to 120 arcsec. Misorientation in the Si due to the package is lowest for the bottom die; this is most likely due to its attachment to a substrate, providing greater stability [19].

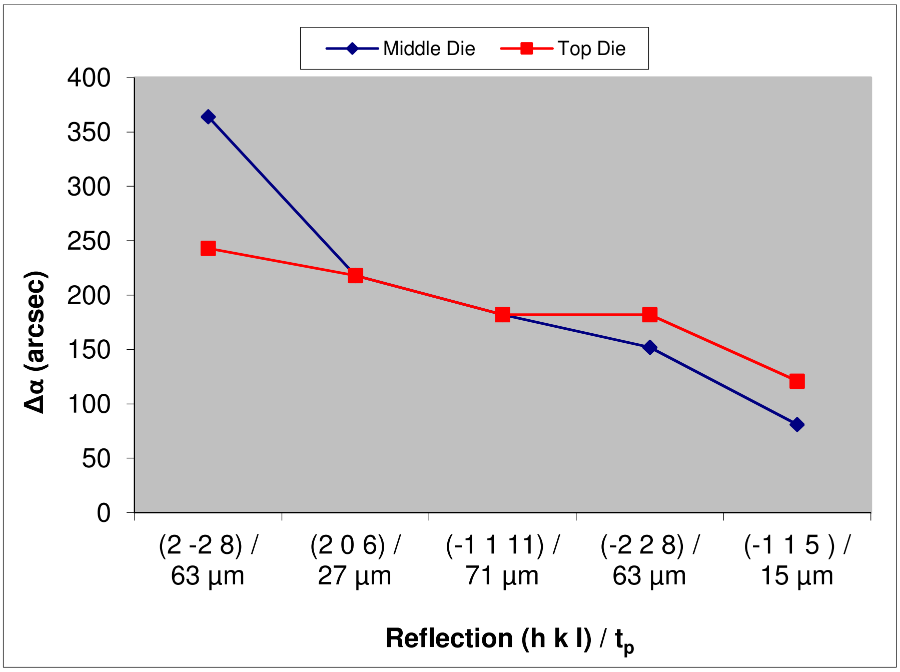

Figure 6.6: Maximum lattice tilt, Δα, for diffracting planes for reflections (h k l), and x-ray penetration depths (t_p) shown.

As stated earlier, micro-Raman spectroscopy is a well established non-destructive, high resolution analysis tool for the measurement of local mechanical stresses in semiconductor materials [1, 5-8, 13, 14]. Lattice strain can change the frequencies of the phonons in a material, which results in a shift of the Raman peak frequency. The peak frequency of the Raman line of single crystal silicon has been reported to lie at approximately 520 cm^{-1} [4, 5]. The calibrations undertaken during this study, on a clean sample of (100) silicon at room temperature, show the peak to lie at 520.07 cm^{-1}. A positive or negative shift in the Raman peak position from the unstressed value corresponds to a compressive or tensile stress, respectively [6].

We know from Section 2.4.2 that due to polarisation rules, only peaks that meet the conditions:

$$I = C\sum_j \left[\hat{e}_i.R_j.\hat{e}_s\right]^2 \qquad (6.3)$$

can be observed, where $\hat{e}_i$ and $\hat{e}_s$ are the unit vectors of the polarisation of the incoming and scattered light, respectively, R_j is the Raman tensor, I is the Raman scattering intensity, and C is a constant.

When measuring in backscattering on the (001) surface of Si, which is the crystal orientation of most Si chips, only the LO peak can be observed [7]. Assuming biaxial stress σ_{xx} along (100) and σ_{yy} along (010), the relationship between Raman shift and stress is given by equations 2.48 – 2.50 (section 2.4.5), [5, 6, 25]:

$$\Rightarrow \Delta\omega_3 = \frac{\lambda_3}{2\omega_0} = -1.93\times10^{-9}\left(\sigma_{xx} + \sigma_{yy}\right) \qquad (6.4)$$

where ω_3 is the Raman frequency of the third optical mode of Si.

Although equation 6.4 has been previously used to calculate the stresses in cross-sections and in packaged chips and MEMS [17, 18], the equation is only valid when performed on the (001) surface [6-8]. When interpreting micro-Raman results for packaging induced stress in Si chips, where chips are cleaved and results are collected from a cross-section of each silicon layer, equation 6.4 is not strictly correct, due to the anisotropic nature of Si.

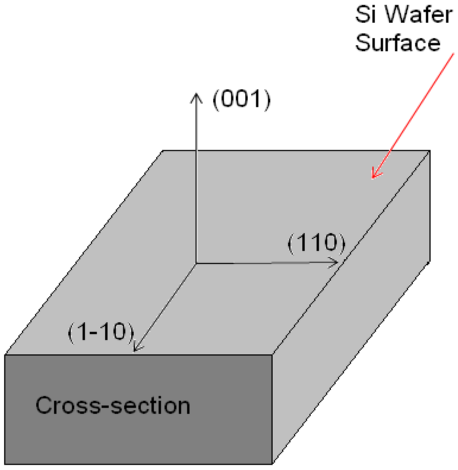

Figure 6.7: (1 –1 0) Cross-sectional surface of Si wafer / chip.

When backscattering from the (1-10) surface of Si (Figure 6.8), only the second TO peak is observed, and the relationship between Raman shift and stress is given by [6-8, 20]:

$$\Delta\omega_2 = -0.365\times10^{-9}\sigma'_{xx} - 2.31\times10^{-9}\sigma'_{yy} \qquad (6.5)$$

where σ_{xx}' is on the cross-section parallel to the surface of the chip, i.e. along [110], and σ_{yy}' is perpendicular to the surface of the chip, i.e. along [001]. From equation 6.5 we can see that Raman peak shift is dominated by stress along the [001] direction. In addition to stresses induced in the CSP from wafer processing, and packaging, the cleavage of the package for analysis also affects the local cross-sectional stress distribution [21]. Raman measurements for the CSP in this study therefore consist of a combination of stresses from the σ_{xx}' and σ_{yy}' directions, and from at least three processes. It is not possible to isolate the different stress components for the micro-Raman measurement or determine which process from which the strain has originated. Thus in the case of the packaged CSP described in section 6.2, micro-Raman measurements can only estimate approximate levels of stress in the chip. This approximation is in line with previous similar studies [17, 18], where equation 6.4 has been used to calculate the levels of strain in the packaged die.

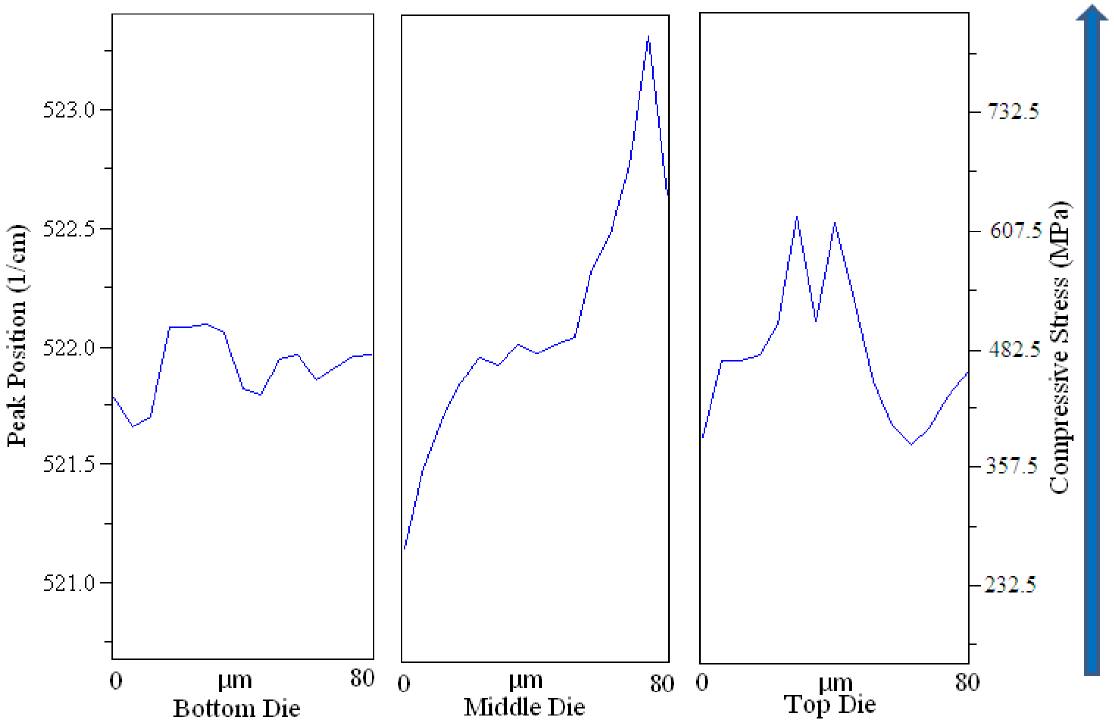

Figure 6.8: Summary of micro-Raman peak shift data for each die in layer stack. Data shows each layer to be in compressive stress.

Figure 6.8 shows micro-Raman peak position and compressive stress levels versus relative scan position across each die in the stacked CSP. Raman scans show the greatest change in strain levels from the bottom (left side) to the top (right side), of the middle die, with a relatively small variation in strain levels in the top and bottom die.

Micro-Raman spectra for the bottom die, (Figures 6.9 (a) and (b)), show the cubic Si peak lying between 521.65 cm^{-1} and 522.20 cm^{-1}, $\Delta\omega$, the peak shift from the unstrained position, is >0, indicating compressive strain. The strain is at its lowest value at the very bottom of the Si die, where the Si is attached to the substrate, and is at its greatest in the centre of the line scan, which corresponds to the middle of the bottom die. At the upper edge of the bottom die the strain decreases again, with levels corresponding to about 480 MPa. The strain pattern is in agreement with the XRDI results, which show the least lattice warpage in the bottom die. Table 6.1 shows the average CTE for materials in the CSP layer stack/package. The CTE for the pcb is much greater than the CTE of Si, resulting in the epoxy resin/solder mask shrinking as it cools, and inducing compressive stress in the Si. This undesirable effect is minimised by the presence of the BT substrate and large solder balls, which buffer and maximise the separation between Si die and pcb board.

Material	CTE (ppm/°C)	Comments
Si (100)	2.6-3.3	Average values, dependant on axis [12]
Cu	16.4	Average values, dependant on axis [11]
Epoxy Resins	50-125	Average value [10].
Polymide Adhesive	28	Average value [10].
bismaleimide/triazine (BT)	13 - 55	Pre-glass transition temperature (180°C), dependant on axis [9].

Table 6.1: Average CTE for materials in the triple stacked CSP (Figure 6.1).

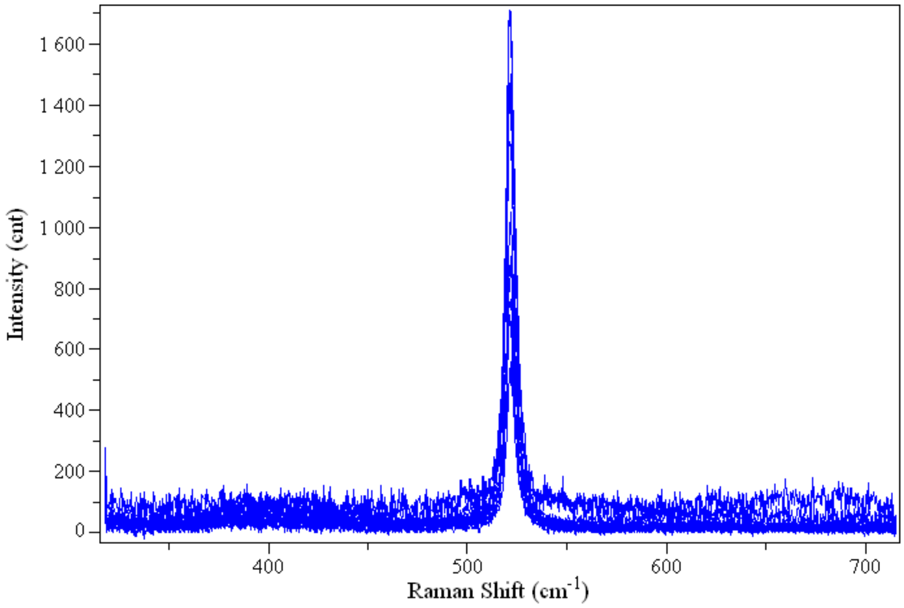

Figure 6.9(a): Ar+ Laser Micro-Raman Spectrum for line scan with 5 micron steps. Bottom layer of sample.

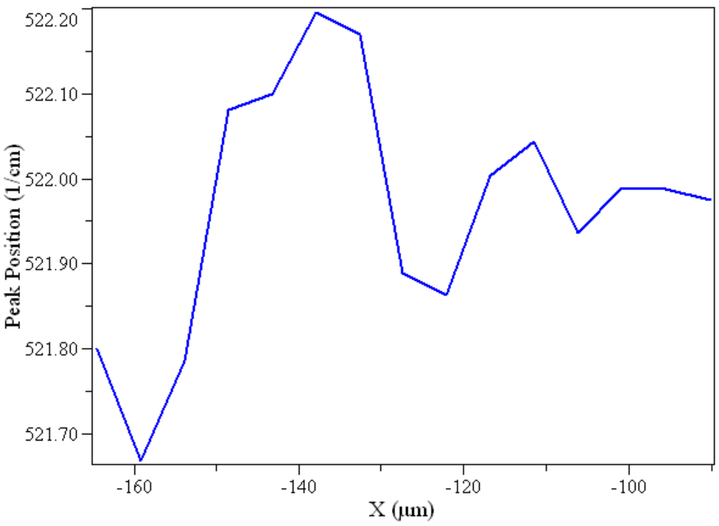

Figure 6.9(b): Ar+ Laser Micro-Raman Plot of Peak Position versus Scan Position for Line Scan in Figure 7.3.6 above, Bottom layer of sample.

Line scans of the middle die (Figures 6.10 (a) and (b)), show spectra in the range 521.25 cm^{-1} to 523.25 cm^{-1}. The strain gradually increases from a minimum of 295 MPa towards the bottom of the middle layer, to a maximum of 795 MPa close to the top of the layer. The middle layer shows the greatest range in strain values, as well as the largest spectral blue shift, which correlates with the LABR topographs (Figure 6.5, (a) and (b), Figure 6.6), where the strain maps show the largest amount of strain for this layer, with the measured angular misorientation across the width of the die at a maximum closest to the top die.

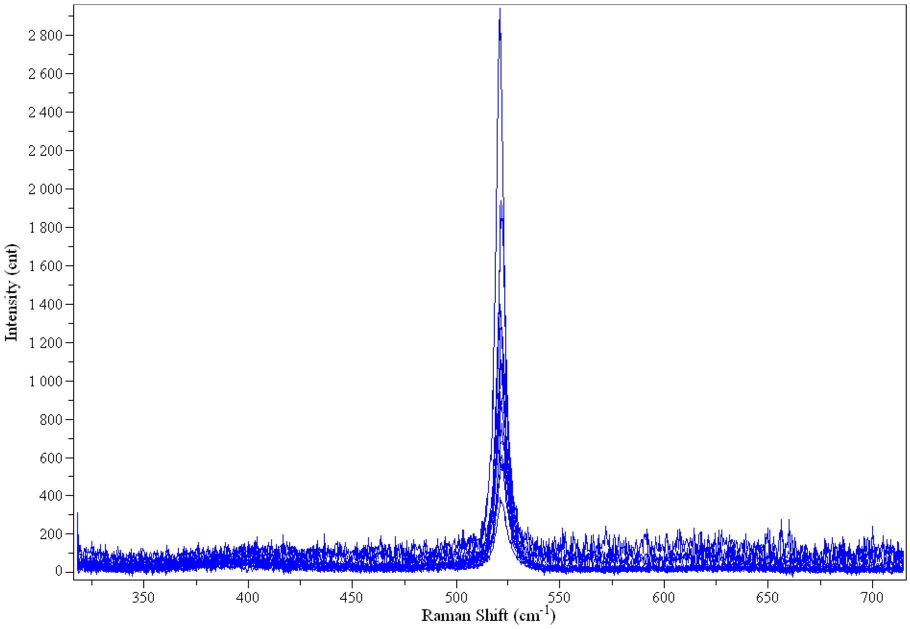

Figure 6.10(a): Ar+ Laser Micro-Raman Spectrum for line scan with 5 micron steps. Middle layer of sample.

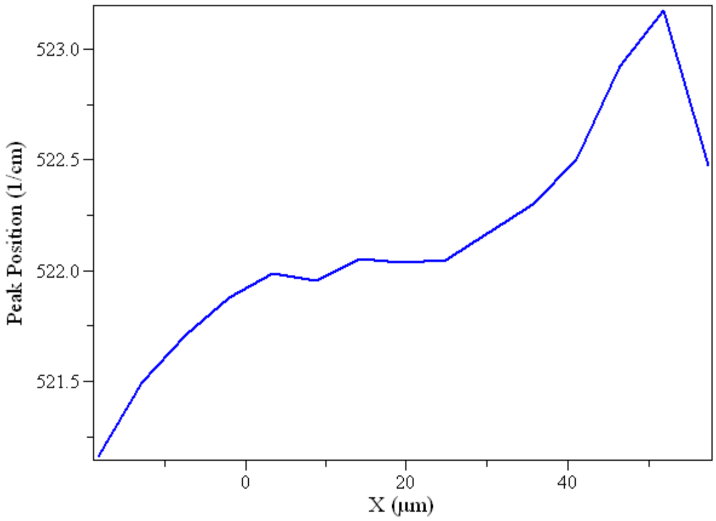

Figure 6.10(b): Ar+ Laser Micro-Raman Plot of Peak Position versus Scan Position for Line Scan in Figure 7.3.8 above, Middle layer of sample.

For the top Si die, (Figures 6.11 (a) and (b)), Raman peak shifts of 1.53 cm^{-1} to 2.38 cm^{-1} are present with associated stress values of 382 MPa to 595 MPa. As with the bottom die, the top die shows the least amount of strain at the upper and lower surfaces, with a large increase in strain in the centre of the line scan, corresponding to the middle of the silicon die. Encapsulation processes can lead to warpage of the chip, where the asymmetry between the encapsulated layers and the bottom die leads to an imbalance and hence the build up of stresses. Although large stresses are seen in both the XRDI and micro-Raman results for all die, the disparity is reduced, particularly in the case of the top die, by the presence of the rigid substrate on which the bottom die is mounted.

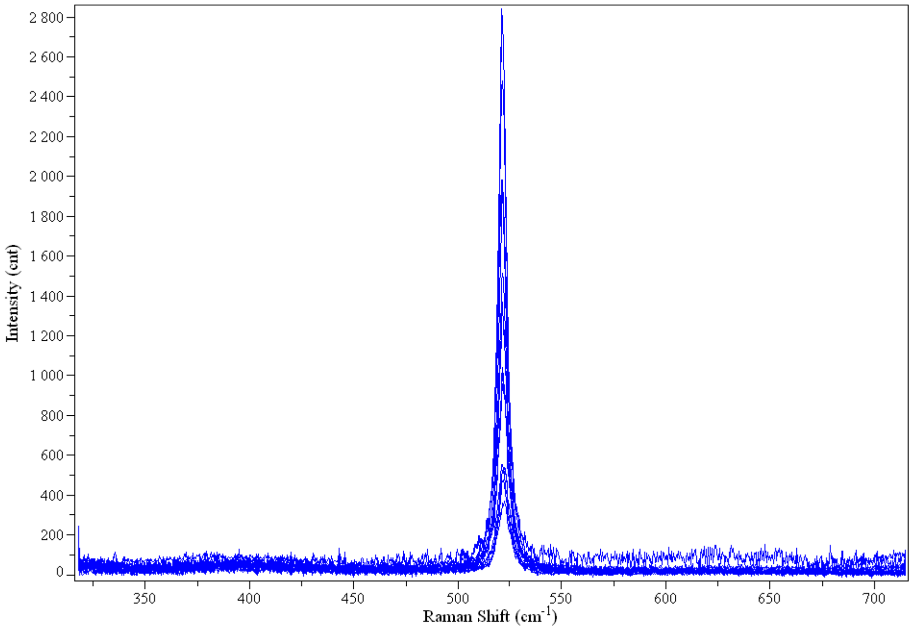

Figure 6.11(a): Ar+ Laser Micro-Raman Spectrum for line scan with 5 micron steps. Top layer of sample.

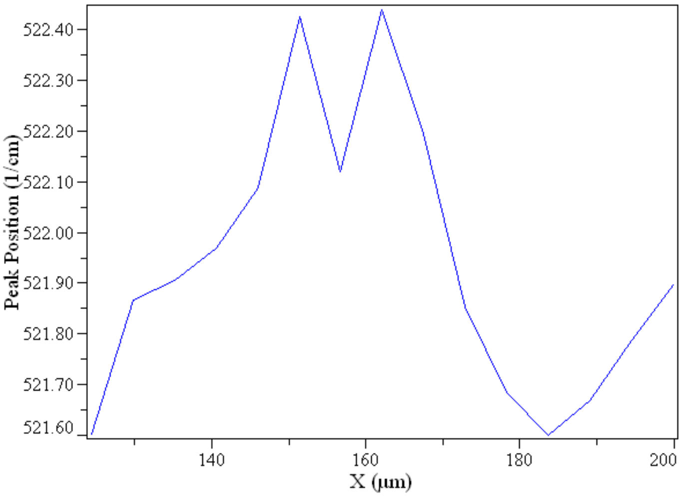

Figure 6.11(b): Ar+ Laser Micro-Raman Plot of Peak Position versus Scan Position for Line Scan in Figure 7.3.10 above, Top layer of sample.

6.5 Summary

This chapter introduces the basic technologies utilized in triple-chip stacked CSP's, and the materials and processes involved in their construction. Thermal-mechanical stress induced in the Si die by packaging are examined using two non-destructive, high resolution characterisation techniques: XRDI and micro-Raman spectroscopy.

The stresses which are built into 3D chips as a result of the manufacturing process can lead to yield, electrical performance and reliability issues. Regions with high concentrations of strain are prone to debonding, voiding and cracking [19]. Compressive die stresses up to 795 MPa in magnitude, as observed in the middle layer of the 3D structure examined in this study, and the warpage visible in the synchrotron x-ray topographs would be well capable of doing such damage. Micro-Raman results correlate well with those obtained from the XRDI images, Figures 6.5 (a) and (b), which show increased stresses in the middle and top Si layers relative to the bottom layer.

References

[1] J Kanatharana, J J Pérez-Camacho, T Buckley, P J McNally, T Tuomi, M O'Hare, D Lowney, W Chen, R Rantamäki, L Knuuttila and J Riikonen. *J. Phys. D: Appl. Phys*. **36** (2003), A60-A64.

[2] A. Rack et al., *Nuclear Instruments and Methods in Physics* B **267** (2009), pp. 1978-1988.

[3] http://www.ccp14.ac.uk/ccp/web-mirrors/xianrong-huang/

[4] R. J. Needs and A. Mujica, *Phys. Rev. B* **51**, 9652 (1995).

[5] I. De Wolf, *J. Raman Spec*. **30**, 877 (1999).

[6] Ingrid De Wolf, *Semicond. Sci. Technol.* **11** (1996) 139–154.

[7] Jian Chen; De Wolf, I., *52nd Proceedings Electronic Components and Technology Conference (ECTC), 2002,* Page(s): 1310 – 1317.

[8] Jian Chen and Ingrid De Wolf, *IEEE Transactions on Components and Packaging Technologies*, Vol **28**, No. 3, (2005).

[9] http://www.insulectro.com/content_media/file/isola_DSG20051608.pdf

[10] Charles A. Harper, *Electronic Packaging and Interconnection Handbook.* McGraw-Hill, 4th Edition.

[11] Sinha, A., Mihailovic, J.A., Morris, J.E., Hua Lu, Bailey, C., *Nanotechnology Materials and Devices Conference (NMDC), 2010 IEEE*, Page(s): 262 - 266 (2010).

[12] *ASM Ready Reference: The Thermal Properties of Metals*. ASM International (2002).

[13] D. Noonan, P.J. McNally, W.-M. Chen, A. Lankinen, L. Knuuttila, T.O. Tuomi, A.N. Danilewsky, R. Simon, *Microelectronics Journal* **37** (2006) 1372–1378.

[14] J. Kanatharana, J.J. Pérez-Camacho, T. Buckley, P.J. McNally, T. Tuomi, A.N. Danilewsky, M. O'Hare, D. Lowney, W. Chen, R. Rantamaki, L. Knuuttila and J. Riikonen, *Microelectron. Eng.* **65** (2003), pp. 209–221.

[15] J. Kanatharana, J.J. Perez Camacho, P.J Buckley, P.J. McNally, T. Tuomi, J Riikonen, A.N. Danilewsky, M. O'Hare, D. Lowney, W. Chen, R Rantamäki and L. Knuuttila, *Semicond. Sci. Technol.*, **17**, 1255 – 1260 (2002).

[16] X. R. Huang, *NSLS: White-Beam X-Ray Diffraction Patterning (LauePt),* Version 2.1 (2003).

[17] I. De Wolf, J. Chen, and W. M. van Spengen, *Optics Lasers Eng*., vol.

36, pp. 213–223, 2001.

[18] Murugesan Mariappan, Ohara Yuki, Bea Jichoel, Lee Kang-Wook, Fukushima Takafumi, Tanaka Tetsu, Koyanagi Mitsumasa, *3D Systems Integration Conference (3DIC)*, 2010 IEEE International, Page(s): 1 – 5, (2010).

[19] Fukui, Y., Yano, Y., Juso, H., Matsune, Y., Miyata, K., Narai, A., Sota, Y., Takeda, Y., Fujita, K., Kada, *50th Proceedings M. Electronic Components and Technology Conference (ECTC)*, pp.385 – 389, (2000).

[20] Anastassakis E, Pinczuk A, Burstein E, Pollak F H and Cardona M 1970 *Solid State Commun.* **8** pp.133–8.

[21] Atsushi Yagishita, Tomohiro Saito, Saito Matsuda, Yukihiro Ushiku, *Jpn. J. Appl. Phys*. Vol. **36** (1997) pp. 1335-1340.

[22] P.J. McNally, R. Rantamäki, T. Tuomi, A.N. Danilewsky, D. Lowney, J.W. Curley and P.A.F. Herbert, *IEEE Trans. Comp. Packag. Technol.,* **24** (1), pp. 76-83 (2001).

[23] P. Ratchev, B. Vandevelde and I. De Wolf, *IEEE Trans. Device and Materials Reliability*, **4,** 5-10 (2004).

[24] W. Chen, P. McCloskey, J.F. Rohan, P. Byrne, and Patrick J. McNally, *IEEE Trans. Comp. Packaging Technol.,* **30,** 144-151, (2007).

[25] Anastassakis, E. (1997), *J.Appl.Phys*., **82** (4), pp. 1582-1591.

[26] Akito Yoshida et al., Proceedings 56th Electronic Components and Technology Conference(ECTC), 2006 pp. 6.

[27] ITRS SiP White Paper, “The next Step in Assembly and Packaging: System Level Integration in the package (SiP)”, 2007, http://www.itrs.net/links/2007itrs/LinkedFiles/AP/AP_Paper.pdf

[28] Amkor 3D Packaging Technology Datasheet, http://www.amkor.com/

[29] Amkor Flip Stack CSP Technology Datasheet, http://www.amkor.com/

Conclusions & Further Research

7.1 Conclusions

This study is driven by the needs of industry. Progress goals in integrated circuit manufacturing are defined by the International Technology Roadmap for Semiconductors (ITRS) [http://www.itrs.net/]. The most recently published, 2009 ITRS states that there is *"… a need to develop metrologies that can be used to efficiently measure either stress or strain under both thermal and mechanical loading conditions in thin films (for example in layers within Silicon) in packaged form.*" Advanced SoC/SiP systems are still not as reliable as conventional packaged integrated circuit systems and meeting the reliability requirements of future SoC/SiP components and systems will require tools and procedures that are not yet available. Further SiP/SoC metrology requirements are detailed in the ITRS SiP White Paper V9.0, [http://www.itrs.net/papers.html]:

1. Identification of failure mechanisms
2. Improved non-destructive failure analysing techniques and methods
3. Electrical/thermal/mechanical simulation
4. Test vehicles for specific reliability characterisation
5. Lifetime models with defined acceleration factor
6. Failure classification standards.

This study directly addresses the metrology gap listed in items 1 and 2 on the list, and in the ITRS through the development beyond proof-of-concept stage of a novel combined suite of metrology tools: 3-Dimensional X-Ray Diffraction Imaging (3D-XRDI) and 3-Dimensional Surface Mapping (3DSM) for the analysis of packaged chips at all stages, from bare die through to completely packaged chip. Conventional XRDI / SXRT techniques are also implemented, to this author's knowledge, for the first time in the analysis of warpage and strain in stacked chips. A further, innovative technique, photoacoustic microscopy (PAM), is effectively used in this study to image defects in silicon wafers / dies.

3D-XRDI has been successfully developed and employed in the study of defects / strain due to plasma arcing inside semiconductor wafers/die from the top of the wafer through to the back side, enabling full 3D strain profiles to be obtained. Furthermore, the unique imaging capabilities of 3D-XRDI allows sub-surface defects and features that were previously only apparent to experts in the field of x-ray topography, through the analysis of individual section transmission topographs, to be identified by a relatively inexperienced user. The use of post-rendering image processing techniques to enhance 3D-XRDI images, and simplify the analysis process is demonstrated through the use of thresholding, transparency and K-means clustering algorithms, and the application of LUTs on 3D-XRDI of plasma arc damaged samples. Details of internal damage of the wafer/die can be viewed by sectioning the 3D-XRDI along any plane of choice, or slicing the 3D model at any chosen position. Image capture and integration times at the ANKA synchrotron have been greatly improved over the course of this project, leading to more than an order of magnitude decrease in the time required to take a series of section transmission topographs. Initially the image capture process took ~4 min per topograph, currently the process takes ~10 s per topograph, and further order of magnitude speed improvements are expected over the coming year or so. The efficacy of the XRDI technique is validated by micro-Raman spectroscopy, a well established and widely used technique for the analysis of strain in semiconductors.

3DSM is an entirely novel, non-destructive x-ray diffraction imaging technique, developed in this study to produce x-y mapping of the deformations and strain fields in packaged SiP. 3DSM is applied to the analysis of 5 of the 7 stages of typical embedded QFN manufacturing and test processes, from bare die through to packaging and reliability testing, enabling possible process-related sources of die warpage to be identified, and hence providing valuable feedback towards chip improvements in embedding technology. Validation of 3DSM is undertaken through the comparison with known characterisation techniques, namely conventional XRDI and micro-Raman spectroscopy. Stage 3 via electroplating results demonstrate the close correlation between the wafer pattern on the LAT topographs, and the bumps on the 3DSM. A similar correlation is seen at stage 5, post production, where an elliptical region of high distortion seen in the LAT and LABR topographs is reproduced in the 3DSM

Modern packages are now thin enough to be easily penetrated by x-ray photons, making XRDI possible on single and stacked packages. In this study XRDI is used as a qualitative characterisation tool in conventional LAT, ST and LABR geometries, on single and stacked die packages. It also functions as a foundation for the generation of 3D-XRDI and 3DSM. XRDI is effectively used to characterise warpage in a triple stacked CSP for the first time. Quantitative values are also obtained for the level of warpage in the middle and top dies in the package. Results show that the use of a BT laminate substrate is effective in reducing die warpage in the bottom die, and that when combined with a suitable encapsulating material, warpage of the top die is also minimised. However the middle die appears to have the greatest levels of warpage, and further study is required to understand the origin of this warpage. Overall results prove that XRDI is an extremely adaptable quality evaluation tool for semiconductor IC process development, and that it has the potential for the analysis of complex stacked packages.

PAM has been used for the location and depth probing of process related defects in silicon, which are located several hundred microns beneath the chip surface. Further research is required to improve the resolution of PAM measurements, and the reliability and repeatability of the PAM system.

The current trend for increasing device integration (SoC, SiP, MCP, 3D packaging), and 3 dimensional multi-die and multi-layer packages has introduced many challenges for the future of IC manufacturing. This study contributes directly to the state-of-the-art by developing a suite of novel techniques which can be applied to the analysis of advanced packages from bare die/wafers all the way through to fully encapsulated packages, and thus fulfilling one of the challenges of the ITRS. The data obtained in this project has the potential to enable research groups and industrial end users to:

- improve process steps,
- reduce the major sources of die warpage and in-package stress,
- produce faster-to-market products with greater reliability and performance.

The above techniques have a great deal of potential for the non-destructive analysis of strain / warpage in wafers, die and packaged chips. However a significant weakness of XRDI based techniques is the need for a synchrotron source, and thus the inability to integrate them into a fab environment. Techniques such as 3D-XRDI and 3DSM are therefore currently more suited to process research and development.

7.2 Further Research

The primary focus of further research should be to establish the limitations of XRDI, 3D-XRDI, 3DSM and PAM, particularly with respect to the analysis of 3D packages. There is a limit to the thickness of Si, or the number of layers/chips the synchrotron beam can penetrate. Similarly, the maximum number of layers the PAM laser beam and induced thermal waves can penetrate should be established.

As discussed in the conclusions, the time to capture section transmission topographs has been improved by more than an order of magnitude over the past 3 years by the introduction of a high resolution CCD camera and implementation of automated image capture software. Image resolution was also improved by the introduction of a second set of slits close to the beam exit. Further hardware and software improvements and automation should be pursued to further reduce image acquisition time. Hardware improvements at the ANKA synchrotron include redesign of the sample holder to enable several samples to be mounted alongside each other, and the addition of a second set of section topography slits in the vertical position to enable the capture of a grid pattern of topographs without the need to rotate the sample by 90°. Software improvements at the synchrotron include automatic stage stepping and image capture sequences, similar to those applied in the 3D-XRDI process. Due to the high degree of orientational contrast in the packaged chips ST topographs can appear at different places on the CCD camera. Automatic pattern recognition algorithms would therefore be required to ensure that complete ST images are always captured.

In the case of 3D-XRDI the 3D rendering and image processing steps are tedious, and time consuming. A straightforward way to improve the efficiency of the image processing stages is to write an *ImageJ* plugin, which includes all the processing steps from image registration through to post rendering image processing. As 3D-XRDI uses standard, open source image processing algorithms, more robust and sophisticated software could be written using C++/Java, and developed in line with a GUI interface.

The minimum resolution of 3DSM is dependent on a number of factors: synchrotron and image acquisition (CCD) resolution limits, the spacing of the ST topographs used to construct the 3DSM, and the surface modelling algorithms used to reconstruct the surface models. Initial proof-of-concept work on 3DSM was undertaken with ST topographs captured at 1 mm steps across the package, with the package rotated at 0° and 90°. Resolution was later enhanced by reducing the step size to 0.5 mm. Further resolution improvements may perhaps be achieved by reducing the spacing of ST topographs to ~15 μm, as in the 3D-XRDI image capture process. As discussed in Section 3.4.4 *SolidWorks®* uses a simplified form of NURBS surface in its boundary surface algorithm. Improved resolution may be achieved through the implementation of more complex boundary constraints, and additional connectors may be added, to allow control of the flow of the boundary surface and to ensure an more accurate surface between adjacent splines with a large change in slope between them (Section 5.3.2). Another option would be to add splines going in the direction of the connectors. These splines could then be used to define the second direction of the boundary surface. Although both these techniques are effective, implementation in every 3DSM may be too time consuming. A new surface construction technique may therefore be needed to improve accuracy of surface modelling, within practical time constraints. A possibility is the *SolidWorks®* add-in called *ScanTo3D*, which enables the importation of point cloud data, and its conversion into a NURBS surface.

Using the current PAM system scan of a 10 mm × 10 mm surface area takes approximately 10 mins. Improvements in the laser focussing, amplifier electronics and software design of the PAM should enable increased scanning speed and image resolution. The PAM chamber should also be redesigned to facilitate larger die and full wafers.

Appendix A

K-Means Clustering

For a given data set $X = \{x_1, \ldots x_N\}, x_N \in R^d$ which is partitioned into M distinct subsets (clusters) $C_1, \ldots C_M$ such that the clustering criterion is optimised. The most common k-means clustering algorithm uses the sum of the squared Euclidean distances between each data point, x_i and the centroid m_k of the subset C_k which contains x_i [1, 2]. The clustering error depends on the clustering centers, $m_1, \ldots m_M$.

$$E(m_1, \ldots m_M) = \sum_{i=1}^{N} \sum_{k=1}^{M} l(x_i \in C_k) \| x_i - m_k \|^2$$

where $l(X) = 1$ if X is true, and 0 otherwise.

To solve the problem with two clusters (k=2), the initial positions of the cluster centre k=1 is at the centroid of the data set X, and the initial position of the second cluster is at the data point $x_n (n = 1, \ldots N)$. N iterations of the k-means clustering algorithm are then performed, with k clusters where each iteration, n, starts from the state $(m_1^*(k-1), \ldots, m_{(k-1)}^*, (k-1), x_n)$. The best solution obtained is considered as the solution for k=2 with $(m_1^*(k), \ldots, m_1^*(k))$.

[1] Aristidis Likas, Nikos Vlassis, Jakob J. Verbeek, "The global k-means clustering algorithm", Pattern Recognition **36** (2003) 451 – 461.

[2] Vance Faber, "Clustering and the Continuous k-Means Algorithm". Los Alamos Science Number 22 1994.

Appendix B

Noise in PAM Microphones.

Figure 3.2.1(b) shows a plot of the noise levels obtained from the PAM system for an empty cell, with laser modulation at 720 Hz. The signal was measured using the existing pre-amp. circuitry, which was fed directly into the sound card of a PC and recorded using igarage ™ software. The total noise in the system ranges between -80 dB and -33 dB, (99 μV – 22 mV), and shows two significant peaks at approximately 473 Hz and 1550 Hz.

Studies of the noise in this system show that the main source of noise is electronic noise from the microphones. The noise at the microphones can be approximated by:

$f = {}^{1}\!/_{2\pi\tau}$, where f is the bandwidth of the signal, and τ is the time constant set at the lock-in amplifier. The bandwidth is therefore equal to 53 Hz. Noise at the summer output = $\frac{0.5}{\sqrt{f}} = \frac{0.5}{\sqrt{53}}$, = 69 μV/Hz$^{1/2}$. The factor of 0.5 in this calculation assumes the lock-in amplifier uses a single side band, i.e. that half the energy is dumped, and half is converted to DC. Gain is achieved in both the pre-amplifier and the summer circuits. Total gain, $g_{total} = g_{summer} \times g_{pre\text{-}amp}$. g_{total} = 100 V × 100 V = 10,000 V^2. The peak noise at the microphone can therefore be obtained from Noise at the summer output / total gain, which is equal to 6.9 nV/Hz$^{1/2}$. The theoretical expectation for the noise value is given by $\sqrt{4kTR}$, where T is room temperature, and k is Boltzmann's constant. This gives a value of approximately 40 nV/Hz$^{1/2}$. The difference between the theoretical and the calculated results may be due to the estimation of the noise at the summer output.

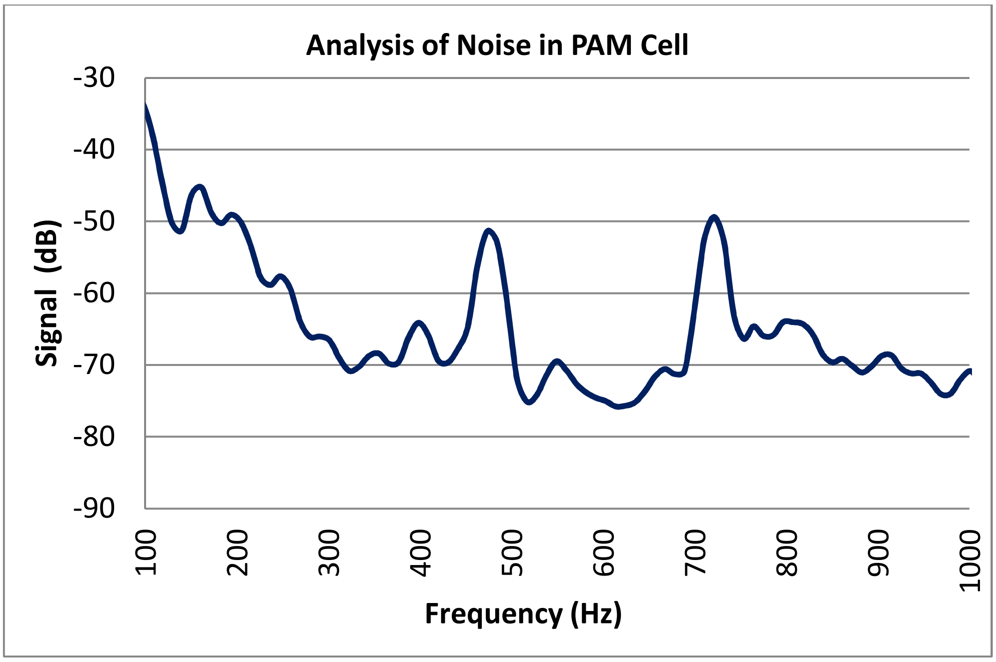

Figure B1: Graph plotting the PA signal obtained from the empty PAM cell with laser modulation frequency of 720 Hz.

PAM Pre-Amplifier Circuit Diagrams

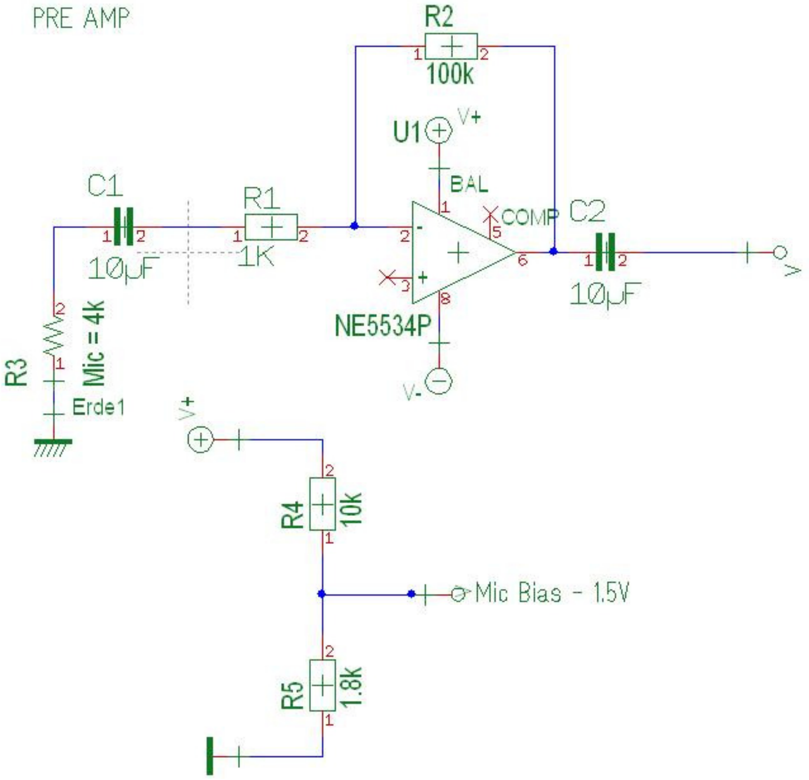

Figure B2 : Pre-amplifier circuit diagram

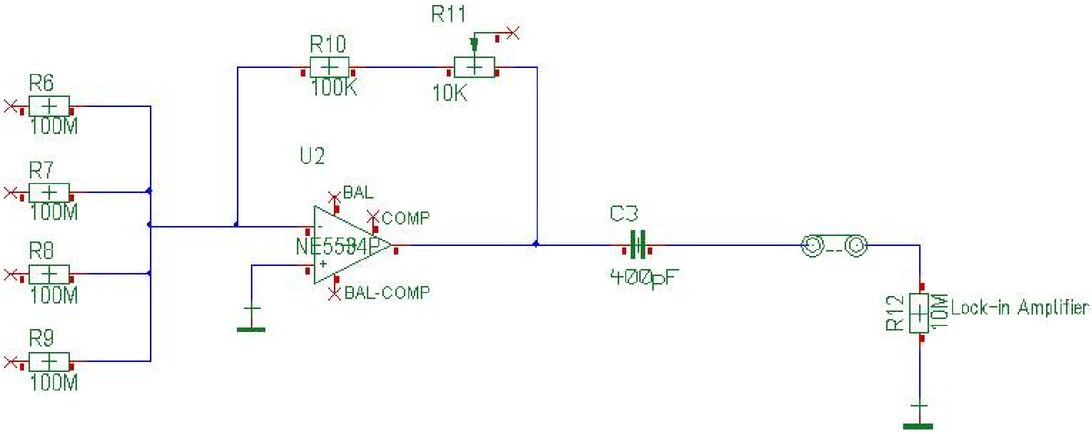

Figure B3 : Summer circuit diagram

List of Publications

Jennifer Stopford, Arthur Henry, Dionysios Manessis, Nick Bennett, Ken Horan, David Allen, Jochen Wittge, Aidan Cowley, and Patrick J. McNally. "Non-Destructive X-Ray Mapping of Strain and Warpage of Die in Packaged Chips", EMPC 2011, Brighton, England. (Pending publication).

J. Stopford, D. Allen, O. Aldrian, M. Morshed, J. Wittge, A.N. Danilewsky, P.J. McNally, "Combined use of three-dimensional X-ray diffraction imaging and micro-Raman spectroscopy for the non-destructive evaluation of plasma arc induced damage on silicon wafers", *Microelectronic Engineering* **88** (2011) 64–71.

David Allen, Jochen Wittge, **Jennifer Stopford**, Andreas Danilewsky and Patrick McNally. "Three-dimensional X-ray diffraction imaging of process-induced dislocation loops in silicon", *J. Appl. Cryst.* (2011), 44, 526–531.

D. Allen, **J. Stopford**, J. Wittge, M.C. Fossati, J. Garagorri, E. Gorostegui-Colinas, P.J. McNally, T. dos Santos Rolo, P. Vagovic, M.M. Morshed, O. Aldrian, A.N. Danilewsky, M.R. Elizalde, D.K. Bowen, and B.K. Tanner, "3-Dimensional X-Ray Diffraction Imaging Study of Damage to Silicon Wafers", ANKA Annual Report 2010.

J. Wasyluk, T.S. Perova, D.W.M. Lau, M.B. Taylor, D.G. McCulloch, **J. Stopford**, "Ultraviolet and visible Raman analysis of thin a-C films grown by filtered cathodic arc deposition", *Diamond & Related Materials* **19** (2010) 514–517.

Horan K., **Stopford J.**, McNally P., Bennett N., Cowern N.E.B., "Photoacoustic spectroscopy at the nanoscale for ultra-shallow implanted silicon". International Workshop on INSIGHT in Semiconductor Device Fabrication, Metrology and Modeling 2009. Napa, California.

Conference Presentations

J. Stopford, A. Henry, D. Allen, O. Aldrian, D. Manessis, N. Bennett, M. Morshed, K. Horan, J. Wittge, A.N. Danilewsky, A. Cowley, and P.J. McNally. "Novel Applications of X-Ray Diffraction Imaging (XRDI) in the Non-Destructive Imaging of

Strain and Defects in Semiconductors", ICMAT Singapore June 2011, Invited Talk; Symposium on Microelectronic Process, Package and Reliability Analysis.

J. Stopford, D. Allen, J. Wittge, M.C. Fossati, J. Garagorri, E. Gorostegui–Colinas, P.J. McNally, M.M. Morshed, O. Aldrian, A.N. Danilewsky, M.R. Elizalde, D. Jacques, R. Bytheway, D.K. Bowen and B.K. Tanner, "Three-dimensional x-ray diffraction imaging of damage to silicon wafers", *10th Biennial Conference on High Resolution X-Ray Diffraction and Imaging, (XTOP2010)*, University of Warwick, UK, 20-23 September 2010.

Jennifer Stopford, Ken Horan, David Allen, Andreas Danilewsky, Muhammad Morshed and Patrick McNally, "Prevention of Si Wafer Breakage Via Non-destructive Evaluation of Plasma Arc Induced Damage", MRS Fall Meeting, Boston, USA, 2009.

D. Allen, **J. Stopford,** J. Wittge, M.C. Fossati, J. Garagorri, E. Gorostegui-Colinas, P.J. McNally, A.N. Danilewsky, D.K. Bowen, B.K. Tanner, M.R. Elizalde, D. Jacques and R. Bytheway, "Three Dimensional X-Ray Diffraction Imaging of Slip Bands in Silicon", E-MRS 2011 Spring & Bilateral Meeting, Nice (France), May, 2011.

Posters

Jennifer Stopford, Arthur Henry, Dionysios Manessis, Nick Bennett, Ken Horan, David Allen, Johan Wittge, Aidan Cowley, and Patrick McNally, "3D Surface Modelling of Strain in Packaged Chips", Nanoweek Conference, Co. Kildare, Ireland, 2011. Winner of Best Poster Prize.

Jennifer Stopford, Arthur Henry, Dionysios Manessis, Nick Bennett, David Allen, Jochen Wittge, Aidan Cowley, and Patrick McNally, "3D surface modelling of strain in packaged chips", Hasylab Users' Meeting, Hamburg, Germany. Jan. 2011.

D. Allen, **J. Stopford**, J. Wittge, M.C. Fossati, J. Garagorri, E. Gorostegui-Colinas, P.J. McNally, A.N. Danilewsky, D.K. Bowen, B.K. Tanner, M.R. Elizalde, D. Jacques and R. Bytheway, "Three Dimensional X-Ray Diffraction Imaging of Slip Bands in Silicon", Nanoweek Conference, Co. Kildare, Ireland, 2011.

Ken Horan, **J. Stopford**, P.J. McNally, N. Bennett, N.E.B. Cowern, “Photoacoustic Imvestigation of Nanoscale Ion Implant Damage in Silicon”, Nanoweek Conference, Co. Kildare, Ireland, 2011.

J. Stopford, D. Allen, O. Aldrien, M. Morshed, J. Wittge, A.N. Danilewsky, P.J. McNally, “3D X-Ray Diffraction Imaging (3D-XRDI) of Plasma Arc Induced Damage in Silicon Wafers”, European XFELD, DESY, Hamburg, 2010.

J. Stopford, D. Allen, O. Adrian, Dr. M. Morshed, Dr. A. Danilewsky, Dr D. Reid, Prof. P. McNally, “Novel Metrology Techniques for the Non-destructive Evaluation of Plasma Arc Induced Damage”, Nanoweek, 2009.

Brian Tanner, Jochen Wittge, Andreas Danilewsky, David Allen, **Jennifer Stopford**, Patrick McNally, David Jacques, Matteo Fossati, Eider Gorostegui–Colinas, Jorge Garagorri, Reyes Elizalde, Daniel Haenschke, Zi-Juan Li, Tilo Baumbach and Keith Bowen, “Thermal Slip and Silicon Wafer Breakage”, Intel ERIC Conference, Dublin 2010.